APPROVAL SHEET

Title of Dissertation: Infrared Spectral Lineshapes of Water Vapor and Carbon Dioxide

Name of Candidate: David Charles Tobin
Doctor of Philosophy, 1996

Dissertation and Abstract Approved: ______________________

Dr. L. Larrabee Strow
Associate Professor
Physics Department

Date Approved: __________

Curriculum Vitae

Name: David Charles Tobin.

Permanent Address: 3702 Bay Drive, Edgewater, MD 21037.

Degree and date to be conferred: Ph.D., 1996.

Date and Place of Birth: March 30, 1968. Annapolis, MD.

Secondary education: South River Senior High School, Edgewater, MD, June, 1986.

Collegiate institutions attended:

Dates	Institution	Degree	Date of degree
1986-1991	University of Maryland Baltimore County	B.S.	May, 1991
1991-1993	University of Maryland Baltimore County	M.S.	May, 1993
1993-1996	University of Maryland Baltimore County	Ph.D.	May, 1996

Major: Physics, Applied Physics.

Professional publications:

1. D. C. Tobin, L. L. Strow, W. J. Lafferty, and Wm. B. Olson, Experimental Investigation of the Self- and N_2- Broadened Continuum within the ν_2 Band of Water Vapor, Appl. Opt. *accepted* 01/24/96.

2. L. L. Strow, D. C. Tobin, S. E. Hannon, A Compilation of First-Order Line Mixing Coefficients for CO_2 Q-branches, J. Quant. Spectrosc. Radiat. Transfer **52**, 281-294 (1994).

3. R. M. Sova, M. E. Thomas, D. C. Tobin, D. Byrum, and L. L. Strow, Characterization of Candidate DIAL Lidar Water-Vapor and Carbon Dioxide Absorption Lines in the Two Micron Region, SPIE Proc. **2366**, 383-393 (1994).

4. D. C. Tobin, Carbon Dioxide Lineshapes in $\Pi \leftarrow \Sigma$ and $\Pi \leftarrow \Delta$ Vibrational Transitions, Master's Thesis, University of Maryland Baltimore County (1993).

5. X. -G. Zhang, M. A. Van Hove, G. A. Somorjai, P. J. Rous, D. C. Tobin, A. Gonis, J. M. MacLaren, K. Heinz, M. Michl, H. Lindner, K. Muller, M. Ehsasi, J. H. Block, Efficient

Determination of Multilayer Relaxation in the Pt(210) Stepped and Densely Kinked Surface, Phys. Rev. Lett. **67**, 1298-1301 (1991).

Professional positions held:

Dates	Position	Institution
1991-present	Research Assistant	UMBC, Physics Department, Baltimore, MD
1989-1991	Physical Science Trainee	NIST, Radiometric Physics Division, Gaithersburg, MD

ABSTRACT

Title of Dissertation: Infrared Spectral Lineshapes of Water Vapor and Carbon Dioxide

David Charles Tobin, Doctor of Philosophy, 1996

Dissertation directed by: Dr. L. Larrabee Strow, Associate Professor, Physics Dept.

Spectral lineshapes are investigated for pressure broadening conditions where the standard treatments fail. Emphasis is placed on the physical mechanisms responsible for the lineshapes, the overall accuracy of the results, and applicability to line-by-line radiative transfer codes.

A phenomenological lineshape which includes the transfer of intensity between neighboring transitions (*line- mixing*) and includes duration of collision effects is developed for CO_2. Parameters representing the magnitude of line-mixing and the mean collision time are adjusted to obtain agreement with measured transmission spectra throughout and beyond the $\Sigma \leftarrow \Sigma$ ν_3 R-branch at 4.3μm. Assuming a vibration independent collision time, the model is applied to the 15μm region where perpendicular bands are dominant. For both regions, line-mixing is responsible for the majority of the observed sub-Lorentzian behavior. Good agreement with data is obtained for all pressures, temperatures, and perturbers. Another version of the model having a simpler form for the duration-of-collision effect is optimized for use directly at the ν_3 R-branch band-head, an important region for remote sensing applications.

An experimental study of the “continuum" absorption within the ν_2 band of H_2O is presented. High and low optical depth self-, N_2-, and O_2-broadened transmission spectra were recorded using a Fourier transform spectrometer and long path absorption cell. Analysis of the continuum in the microwindows between lines shows general agreement with the laboratory results of Burch *et.al.* and with recent atmospheric measurements. N_2-broadening results agree best with the CKDv0 model of Clough *et.al.* at

band center and with CKDv2.1 in the band wings. N_2-broadened widths of over 150 $H_2^{16}O$ transitions are measured in order to better characterize the H_2O lineshape. Our widths are systematically ~10 % greater than values reported by Toth for $H_2^{18}O$, suggesting an isotopic dependence. Direct least-squares fits to the observed spectra were performed to determine the lineshape from near to far-wing. Results clearly show that the intermediate N_2-broadened lineshape is extremely super-Lorentz, suggesting that dispersion and/or inductive forces are important for medium range intermolecular separations.

Infrared Spectral Lineshapes of Water Vapor and Carbon Dioxide

by

David Charles Tobin

Dissertation submitted to the Faculty of the Graduate School
of the University of Maryland in partial fulfillment
of the requirements for the degree of
Doctor of Philosophy
1996

Preface

This dissertation outlines research performed to understand and accurately characterize the spectral lineshapes of carbon dioxide and water vapor. Particular attention is paid to spectral regions that are useful in remote sensing and in which the current treatments are not sufficiently accurate. In general, it is my experience that many lineshape studies are either parameterizations that are too simple, or are attempts at *ab-initio* calculations that are too complex to produce results which are accurate enough for remote sounding applications. Ab-initio calculations must make a number of severe approximations, resulting in lineshapes that are not always applicable to the original problem. On the other hand, very simple empirical models do not contain the necessary physics to produce realistic lineshapes. The approach taken in this work is to provide better understanding of the physics responsible for the lineshapes while also providing models which are as accurate as possible. These two goals are not mutually exclusive.

I have tried to present this research in a clear and concise manner. In most cases, however, I have erred on the side of saying too much rather than not enough. To aid the reader, a brief road-map is given here. The dissertation is composed of two independent but related studies. The presentation is divided into four chapters and several appendices. Chapter 1 is a general introduction, providing background information and the significance of this work. Chapter 2 is an introduction specific to spectral lineshapes. It includes a review of the standard lineshapes and also outlines more advanced approaches to collisional broadening. Its goal is to provide enough background information such that readers can easily follow the approaches and results of this work, as well as the limitations and advantages of other studies. The actual research is then presented in Chapters 3 and 4. Combined with Chapter 2, these are each stand-alone works that can be read separately.

Chapter 3, a study of CO_2 lineshapes, begins with a brief introduction outlining the research, followed by a description of previous studies. A lineshape model including the effects of line-mixing and collision durations is proposed in Section 3.3. The line-mixing theory is based on research performed for my Master's thesis: *Carbon Dioxide Lineshapes in* $\Pi \leftarrow \Sigma$ *and* $\Pi \leftarrow \Delta$ *Vibrational Transitions*. Appendices A and B review the molecular spectroscopy of CO_2 and the model developed previously for line-mixing in CO_2 Q-branches, respectively. These may be helpful in understanding the proposed model. The model contains two adjustable parameters (which have physical meanings) that allow the model to be rather flexible. These parameters are adjusted by obtaining optimum agreement with measured transmission spectra. Details of calculations performed for the ν_3 band at $\sim 4.3\mu$m are then presented, along with comparisons to measured spectra and other calculations. The model is then applied to the 15μm region in Section 3.6. A version of the model which is easier to parameterize and more accurate at the ν_3 R-branch band-head is also proposed. Lastly, a summary and suggestions for future work are given.

An experimental study of the H_2O lineshape is presented in Chapter 4. This also begins with an introduction and a review of previous studies. Compared to CO_2, the behavior of the H_2O lineshape is not well understood or characterized experimentally, especially in the near and intermediate line wing. As a result, this study concentrates on the experimental retrieval of the H_2O near-wing lineshape from an extensive set of high optical depth spectra. We believe this represents the first time the H_2O lineshape in the $\sim$0.5–30 cm^{-1} region has been directly retrieved from observed spectra. The experimental set-up and data collection are outlined in Section 4.3. The rest of the chapter deals with the analysis of these data to extract the information they hold about the lineshape. Sections 4.4, 4.5, and 4.6 are concerned with issues such as transmission baseline errors, water vapor pressures, and the accuracy of the line parameters used in the data reduction. Since the derived lineshapes are related directly to the line parameters, these are discussed at some length – the main goal is to evaluate the accuracy of the parameters and their effect on the retrieved lineshapes. In particular, a rather detailed analysis of the nitrogen broadened line widths is given. The spectra are then analyzed in the microwindows in Section 4.7 by determining continuum coefficients. This completely empirical continuum is used widely in many applications because it provides a relatively simple way to represent the cumulative effects of all lines. In Section 4.8, the spectra are analyzed closer to the line centers. A small super-Lorentz effect is observed in the near-wing, although it is highly dependent on the line widths used in the analysis. Because there are no previous reports of this behavior, several attempts to quantify it are presented. In Section 4.10, a method for extracting the lineshape from the spectra is presented. This method treats the data in a consistent manner and provides a lineshape from near to far-wing determined purely from experiment. Comparisons to theoretical and empirical results are presented. A summary and suggestions for future studies are then given.

Most analysis was performed using *MATLAB* on a Silicon Graphics Indigo workstation although some line-by-line calculations were performed with *GENLN2*. This document was produced with LaTeX.

Acknowledgments

It is my pleasure to acknowledge those who have made this research possible.

Foremost, I am endebited to Larrabee Strow for giving me the opportunity to pursue my education, for serving as my advisor, and providing scientific, financial, and personal support for the past five years. It has been a pleasure to work with and know him.

Secondly, I need to thank Scott Hannon for answering several years worth of genuinely stupid questions, for help in running GENLN2, and for his useful comments and insights into the research presented here.

I am grateful to the Molecular Physics Division of NIST and the Johns Hopkins Applied Physics Laboratory for use of their facilities. I especially want to thank Walter Lafferty (NIST) for sacrificing much of his time to help with the data collection and for many useful comments concerning the data analysis. Thanks also to Bruce Olson (NIST) for designing and building the absorption cell. Mike Thomas and Ray Sova of APL gave up much of their 1993 Christmas and New Year's breaks to teach me how to run the BOMEM software and collect transmission spectra – thank you.

Thanks are due to several individuals including George Birnbaum (NIST), John Johns (NRC, Ottawa), Qiancheng Ma (NASA GISS), Richard Tipping (U. Alabama), Bob Gamache (U. Mass. Lowell), Tony Clough (AER, Inc.) and Bob Toth (JPL) for their contributions to this research. Thanks to Wallace McMillan and Bob Benson of UMBC for their help.

Finally, I thank my fiance Aimee Powell, my parents, and the rest of my family for their support and understanding throughout this dissertation.

This work was supported by the National Aeronautical and Space Administration under grant NAG 05-5-28045.

D. Tobin

Contents

List of Tables

List of Figures

Chapter 1

Introduction

How does the temperature of the Earth's atmosphere vary in space and time? What is the distribution of water vapor in the atmosphere? How can we measure the intermolecular potential between a water and nitrogen molecule? What is the spectral lineshape of vibration-rotation transitions in water and carbon dioxide? All of these questions have intimate connections that guide the research described in this dissertation.

One description of this dissertation is the study of the infrared spectral lineshapes of water vapor and carbon dioxide. In the case of carbon dioxide, this research replaces purely empirical models of the far-wing spectral lineshape with a physically based lineshape model based on rotational relaxation and collision durations. This model can describe many of our observations with one or two parameters that represent simple physical processes. In the case of water vapor, we experimentally determine parts of the water vapor lineshape for the first time, providing information needed for advances in molecular lineshape theory, and providing new information on the water-water, and water-nitrogen intermolecular potential functions.

Lineshape studies of these gases provide a very useful tool for probing the nature of molecular interactions and collisions. For example, predicting an accurate spectral lineshape under pressure broadening conditions implies that one has determined an accurate description of how the molecules interact during collisions. Accurate representations of intermolecular potentials for all separation distances, however, exist for only the simplest of colloid systems, such as rare gas mixtures and diatom–rare gas mixtures. Some attempts at CO_2-rare gas and H_2O-rare gas systems have been made, but these unfortunately do not approach the accuracy required for spectroscopic applications. Unlike most measurements which are sensitive to only short and/or long range molecular interactions, lineshape studies provide a severe test for the potentials because they probe their behavior for all separation distances, including the important potential well region. More complex systems such as CO_2–CO_2, CO_2–N_2, H_2O–H_2O, and H_2O–N_2, which are investigated in this work, are even less well known. Due to these limitations, coupled with the need for high accuracy for remote sounding applications, the approaches taken in this research do not attempt to calculate lineshapes directly from intermolecular potentials. Rather, more phenomenological and observational approaches are used to extract information about the molecular interactions from measured transmission spectra. This, in turn, provides useful information for further development of accurate potentials.

What about our questions related to the Earth's atmosphere? A spectrum of the Earth from space in the thermal infrared is characterized almost totally by atmospheric emission by water vapor and carbon dioxide vibration rotation spectral lines. Although we understand the frequency (wavenumber) and strength of these lines quite well, we have limited understanding and only gross models of the shapes of these lines, especially for water vapor. For example, in Figure 1.1, existing parameterizations of water vapor spectral lineshapes result in errors of up to 4K in brightness temperature. This is quite large compared to accuracies on the order of 0.2K of future satellite spectrometers. So, another description of this dissertation is the development of atmospheric radiation models that can predict the Earth's outgoing thermal radiation at high spectral resolution. These models, in turn, are needed to invert satellite measurements of infrared radiances and determine atmospheric profiles of temperature and water vapor. These models may also be important for understanding radiation cooling of the atmosphere, which can vary quite strongly as water vapor redistributes itself in response to global climate change.

A partial impetus for this research is the requirement for high accuracy infrared radiation models for the Atmospheric Infrared Spectrometer (AIRS) [1] which is scheduled for launch in the year 2000 on the Earth Observing System (EOS) PM-1 satellite. As part of NASA's Mission to Planet Earth program, the EOS program was initiated as a system of space- and surface-based instruments to provide the scientific basis to answer questions related to global climate change. AIRS will globally monitor the temperature and humidity of the atmosphere. AIRS is also the prototype of future NOAA operational weather satellites. It is a polar orbiting high resolution grating spectrometer which will measure up-welling thermal radiation in over 2,300 spectral channels and provide twice-daily global coverage of the Earth. The inverse problem of determining atmospheric temperature and water profiles from the observed radiances is another major research topic that is not considered in this work.

The importance of this work is highlighted in a recent AGU report [2] which concludes that much of the uncertainty in our present understanding of the Earth's radiation budget for clear sky conditions is due in part to (1) the inaccurate characterization of how atmospheric gases emit radiation and (2) simply not knowing the amount of these gases present in the atmosphere precisely enough. This is particularly true for water vapor which varies widely both spatially and temporally and whose spectroscopy is not well characterized, especially with regard to the lineshape. With a better knowledge of these processes, remote sounding satellite projects can then monitor atmospheric profiles more accurately.

A brightness temperature spectrum typical of the Earth's atmosphere is shown in Figure 1.1. This figure shows the equivalent Planck brightness temperature of the

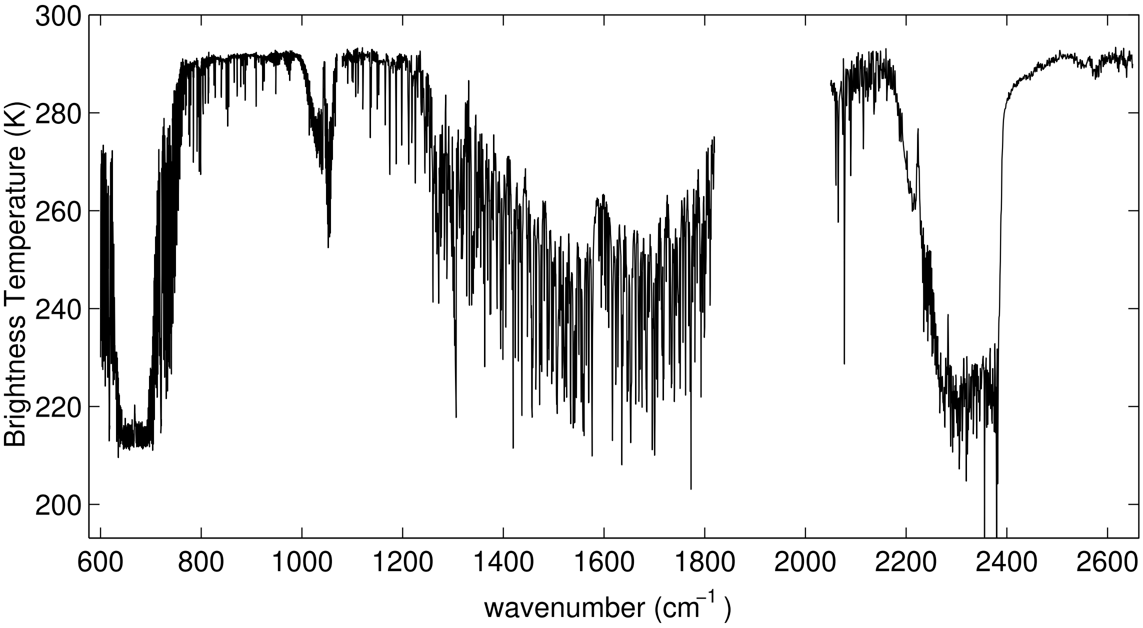

Figure 1.1: An infrared brightness temperature spectrum of the Earth's atmosphere showing the effect of absorption and emission by atmospheric molecules. Retrieval channels for AIRS are located almost continuously throughout the spectrum.

radiance at the top of the troposphere (∼20km) as measured by the University of Wisconsin's High–Resolution Interferometer Sounder (HIS) during a NASA field campaign in Wallops Island, Virginia in 1993. Visible in the figure are the signatures of the strong ν_2 bands of CO_2 from 600 to 800 cm^{-1}, the fundamental ν_2 band of H_2O spanning the entire region from 1200 to 2100 cm^{-1}, and the fundamental ν_3 band of CO_2 from 2150 to 2450 cm^{-1}. Ozone also has a strong signature at ∼1100 cm^{-1}. Given the atmospheric state (surface characterization, temperature and density profiles) at the time of this measurement, this spectrum can, in principle, be calculated to the accuracy of the data if the molecular spectroscopy and the correct spectral lineshapes are known. In the satellite community, this is known as the "forward model". The reverse is also somewhat true. That is, if the molecular spectroscopy and the lineshapes are known, the atmospheric state can be determined to within certain tolerances using inversion processes.

Forward model calculations commonly use spectral line databases such as the Air Force's HITRAN database [3] for the relevant line strengths, widths, frequencies, and lower state energies of the infrared active molecules in the Earth's atmosphere. HITRAN has improved considerably in the last several years to the point where many of the standard line parameters of the stronger bands of the major molecules have accuracies approaching those needed for remote sensing. In most cases, errors in spectral lineshapes are now the major uncertainty in the forward calculations, especially since many key sounding channels are located precisely in between lines and in the wings of bands where a knowledge of the spectral lineshape is most critical.

Two independent studies of pressure broadened lineshapes are presented in this dissertation. In Chapter 3, a lineshape model which takes the effects of line-mixing and non-zero collision durations into account is developed for carbon dioxide. Using spectra in the 4.3μm and 15μm regions, the model is fine-tuned and information about the these processes is obtained. In Chapter 4, the water vapor lineshape is investigated using measured transmission spectra within the fundamental ν_2 band. For both studies, much of the research has involved the careful extraction of spectral lineshape information from large data sets of high optical depth spectra of water vapor and carbon dioxide. This process is wrought with difficulties and errors. I have attempted to characterize and remove these errors as well as possible, and in the end, extract the true lineshape. Emphasis is placed on physical insight into the mechanisms responsible for the observed spectra, the overall accuracy of the models, and their applicability to operational line-by-line radiative transfer codes. The lineshapes should be accurate from the line center to far-wing and over a wide range of atmospheric pressures and temperatures.

Further introductory material specific to carbon dioxide and water vapor are presented at the beginnings of Chapters 3 and 4. A review of the general approaches and approximations involved in lineshape studies referred to in this work is found in Chapter 2.

Chapter 2

Introduction to Spectral Lineshapes

Before proceeding to the specific lineshape studies of CO_2 and H_2O, it is useful to review some basic information on spectral lineshapes. This chapter examines the basic lineshape parameters, including line centers, shifts, widths, and strengths. The standard lineshapes for natural and Doppler broadening are then presented, followed by a more detailed review of collisional lineshapes. This begins with the standard Lorentz/Michelson treatment. Commonly used assumptions and more advanced techniques for approaching this problem are then outlined.

2.1 Molecular Absorption and Beer's Law

Molecular absorption occurs when a molecule absorbs light and simultaneously makes a transition to a higher level of internal energy. The absorption of incident photons decreases the outgoing radiation, and a spectral line is produced. The shape or frequency dependence of this absorption is often called the lineshape. Because of various factors, the absorption occurs not only at the resonant frequency of the transition (determined by the difference between the upper and lower energy levels), but over a spread of frequencies. These broadening factors lead to a finite width of the spectral line. While the resonant frequency and the intensity of the absorption are determined primarily by the structure of the molecule, the lineshape is determined by the molecules' environment.

The frequency dependence of the absorption coefficient, $k(\nu)$, determines the shape of a spectral line. Beer's law relates the absorption of radiation through a gaseous medium linearly to the incident radiation (see Figure 2.1):

$$-dI = k(\nu)I_0Pdl \tag{2.1}$$

with the absorption coefficient, $k(\nu)$ being the constant of proportionality. $-dI$ is the decrease in radiation flux over a path length of dl through a gas of constant and uniform pressure P. Integrating this equation over a homogeneous path length of L yields the integrated form of Beer's law:

$$T(\nu) = \frac{I_f(\nu)}{I_0(\nu)} = \exp\left(-k(\nu)PL\right). \tag{2.2}$$

$T(\nu)$ is is the transmission at frequency ν. $I_0(\nu)$ and $I_f(\nu)$ are the initial and final radiation intensities. Thus, the absorption coefficient is related to the observed transmission by

$$k(\nu) = -\frac{1}{PL}\ln\left(T(\nu)\right). \tag{2.3}$$

It should be noted that deviations from the linear form of Beer's law are only observed at extremely high photon densities. Under atmospheric conditions, however, the linear dependence of the extinction on the amount of absorbing material and incident radiation is valid.

2.2 Line Parameters

The lineshape of a single (non-interacting) transition is commonly characterized by several parameters including the line *center* (ν_0), line *strength* (S), and line *width* (γ). These are illustrated in Figure 2.2.

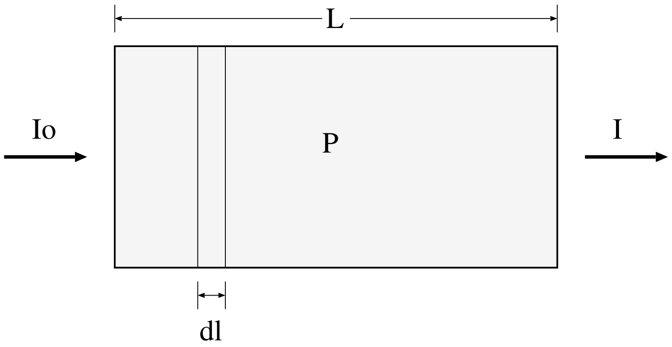

Figure 2.1: A gas cell of pressure P and length L with incident radiation, I_0, from the left. The amount of absorption at frequency ν is determined by the magnitude of the absorption coefficient, $k(\nu)$, the gas pressure, and the path length according to Beer's law.

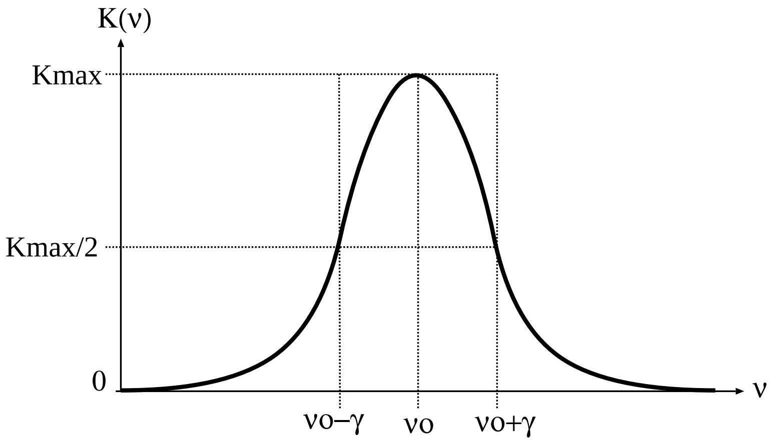

Figure 2.2: A spectral line depicting the line center, ν_0, and half-width, γ. The line strength, S, is the absorption coefficient, $k(\nu)$, integrated over all wavenumbers ν.

Several spectral line databases are available which provide a compilation of the line positions, strengths, and widths as well as several other important parameters such as the lower state energy, pressure induced line center shifts, isotopic abundances, rotational and vibrational quantum indexing, width-temperature exponents, and transition probabilities. HITRAN [3, 4] (the high resolution transmission molecular absorption database) is one such database used in this work which is maintained by the Phillips Laboratory Geophysics Directorate . It currently lists the parameters of over 700,000 rotation and vibration-rotation spectral lines for 31 molecules of atmospheric importance from 0–23,000 cm^{-1}. This database represents the most accurate compilation of line parameters. However, due to its size, it is only updated every two to four years and thus recent state-of-the-art measurements and calculations are not always in the database and must be obtained elsewhere.

2.2.1 Line Centers

The line *center*, or position, of a spectral line is determined by the molecular structure, just as the allowable vibrational-rotational energy levels of the molecule are determined by its structure. Planck's relation:

$$\nu_0 = \frac{\Delta E}{h} \tag{2.4}$$

relates the transition frequency, ν_0 (cm^{-1}), to the change in internal energy, ΔE, where h is Planck's constant. The line centers are thus determined by the structure and allowed energy levels of the molecule and by transition selection rules. The energy levels of CO_2 and H_2O are reviewed in Appendices A and D. Since the line centers do not depend critically upon the interactions with other molecules, or upon the population of various states, they do not vary significantly with temperature or pressure. One common exception to this are the very small shifts in line center with increasing pressure. Just as molecular collisions can disturb optical transition leading to increased line widths (discussed later), these disturbances can also lead to an apparent change in the resonant frequency of the molecule's wave-train. Computationally, the shifted position is given by

$$\nu_0(P) = \nu_0 + P \cdot \delta_\nu \tag{2.5}$$

where P is the total pressure and δ_ν is the pressure induced frequency shift and is determined either theoretically or experimentally. A more theoretical explanation of line shifts which are due to distant collisions was first given by Lenz and more recently by Breene [5].

2.2.2 Line Strengths

The line *strength* or line intensity is a direct measure of the ability of a molecule to absorb photons corresponding to a given transition. It depends upon both the properties of the single molecule and the relative number of molecules in the upper and lower states. The strength, S, is defined as

$$S = \int k(\nu_0, \nu)d\nu \tag{2.6}$$

where the integral is over all ν. Experimentally, S can be determined using Equation 2.6 if $k(\nu_0, \nu)$ is measured. Alternatively, if the functional form of $k(\nu_0, \nu)$ is known, regression techniques can be used to determine S.

By far the strongest interaction between matter and an incident filed of electromagnetic radiation involves the molecule's electric dipole moment. The intensity of a dipole transition is proportional to the square of the matrix element of the dipole moment operator M:

$$R_{i,j} = \int \Psi_i^* M \Psi_j dV \tag{2.7}$$

where dV is a volume element in configuration space and the integral is over all space. Ψ_i and Ψ_j are the wavefunctions of the lower and upper levels of the transition. The wavefunctions are orthogonal and therefore, if M is unchanged during the transition, $R = 0$. Consequently, for a dipole transition to occur, the electric dipole moment must change between the initial and final energy levels of a transition. Otherwise, the molecule is not linked to the incident radiation and no absorption occurs. Weaker transitions can occur, however, for quadrupole transitions even if there is no change in the dipole moment, although these are not considered in this work.

The line strength is also proportional to the relative populations of the upper and lower transition levels. In thermodynamic equilibrium the probability of a molecule being in a specific energy level is given by

$$\frac{N_i}{N} = g_i \exp(-\frac{hc}{kT}E_i)/Z(T) \tag{2.8}$$

where h is Planck's constant, c is the speed of light, k is Boltzmann's constant, T is the temperature, N is the total number of molecules, N_i is the number of molecules in energy level E_i, g_i is the statistical weight of the level, and $Z(T)$ is the partition function given by:

$$Z(T) = \sum_i g_i \exp(-\frac{hc}{kT}E_i) \tag{2.9}$$

In this work, the partition functions are computed using Gamache's [6] convenient parameterization:

$$Z(T) = a + bT + cT^2 + dT^3 \tag{2.10}$$

where a, b, c, and d have been tabulated for most molecules found in the lower atmosphere. Combining Equations 2.8 and 2.9, the relative population of the upper and lower energy levels is given by:

$$\frac{N_j - N_i}{N} = \frac{g_j \exp(-\frac{hc}{kT}E_j) - g_i \exp(-\frac{hc}{kT}E_i)}{Z(T)} \tag{2.11}$$

The line strength is then expressed as

$$S_{i,j} = \sigma_{i,j}\frac{N_j - N_i}{N} \tag{2.12}$$

where $\sigma_{i,j}$ are integrated absorption cross sections and are given by

$$\sigma_{i,j} = \frac{8\pi^3}{3h}\nu_{i,j}|R_{i,j}|^2. \tag{2.13}$$

Combining these results yields the full expression for the line strength:

$$S_{i,j} = \frac{8\pi^3}{3h}\nu_{i,j}|R_{i,j}|^2\frac{g_i \exp(-\frac{hc}{kT}E_i)}{Z(T)}[1 - \exp(-\frac{hc}{kT}\nu_{i,j})] \tag{2.14}$$

Using line strengths determined either theoretically or experimentally at some reference temperature T_{ref}, the strength can be converted to other temperatures using

$$S_i(T) = S_i(T_{ref})\frac{Z(T_{ref})}{Z(T)}\frac{\exp(-hcE_i/kT)}{\exp(-hcE_i/kT_{ref})}\frac{[1 - \exp(-hc\nu_i/kT)]}{[1 - \exp(-hc\nu_i/kT_{ref})]} \tag{2.15}$$

2.2.3 Line Widths

The line *width*, or halfwidth, is defined as half the frequency interval between ν_0 and the frequency at which $k(\nu)$ has fallen to one half of its maximum value. Values of line widths in the Earth's atmosphere can range from 0.0002 cm^{-1} for conditions where the molecules are isolated to 0.5 cm^{-1} for conditions of extreme pressure broadening. Under pressure broadening conditions, the resulting lineshape near line center is well approximated as a Lorentzian with a nominal line width of

$$\gamma = \frac{2r^2}{m}\frac{P}{R_m T}\left(\frac{3kT}{m}\right)^{\frac{1}{2}}, \tag{2.16}$$

which has been derived from classical Kinetic theory using the Equipartition theorem and the Ideal gas law. r s the effective radius of the molecule, m is the molecule's mass, P is the total pressure, R_m is the gas constant, and T is the temperature. A typical time between collisions for an atmospheric gas at room temperature and pressure is $\sim 10^{-10}s$, which leads to a Lorentz width of $\sim$0.05 cm^{-1}. If the line width, γ_0, is determined at a given pressure, temperature combination (P_0, T_0), the line width at other conditions is

$$\gamma = \gamma_0 \left(\frac{T_0}{T}\right)^{\frac{1}{2}} \left(\frac{P}{P_0}\right) \tag{2.17}$$

Thus, the line width increases linearly with pressure and decreases with temperature. Although this kinetic theory does not result in accurate values of γ_0, the pressure dependence is observed in most cases. More commonly, γ_0 is determined either experimentally or calculated with more realistic theories when accurate measurements are not available. Furthermore, the temperature exponent, $\frac{1}{2}$, is generally replaced with a parameter n, which is also determined experimentally. The accuracy of n was investigated by Lui Zheng and Strow [7] for both $CO_2 \leftrightarrow CO_2$ and $CO_2 \leftrightarrow N_2$ collisions: $n \simeq 0.69$ for $CO_2 \leftrightarrow CO_2$ collisions and $n \simeq 0.75$ for $CO_2 \leftrightarrow N_2$ collisions. In general, n can vary with transition for the same molecule. For example, accepted values of n for H_2O range from 0.5 to 1. When n is unknown, default values of 0.64 and 0.68 are generally used.

For mixtures of gases, the total line width is the sum of the individual partial widths:

$$\gamma_{TOT} = \sum_i \gamma_{0,i} P_i \tag{2.18}$$

From quantum Fourier transform theory calculations, the line width for the $f \leftarrow i$ transition is calculated using [8]

$$\gamma_i = \left(\frac{n\nu}{2\pi c}\right) \sum_{J_2} \rho(J_2)\sigma_{if,J_2} \tag{2.19}$$

where n is the perturber density, c is the speed of light, ν is the mean relative thermal velocity ($\nu = \sqrt{8k_B T/\pi\mu}$), μ is the reduced mass of the perturber/absorber system, and $\rho(J_2)$ is the density of the perturber state J_2. σ_{if,J_2} are the absorption cross sections and are dependent upon which type of interactions are dominant. For example, for H_2O-N_2 collisions, the strongest interaction is dipole-quadrupole, yielding

$$\sigma^{DQ}_{if,J_2} = \pi b_0^2 \left(1 + s_{if,J_2}(b_0)\right) \tag{2.20}$$

where b_0 is an impact parameter related to the minimum distance between absorber and perturber during the interaction and s_{if,J_2} is related to the dipole moment of H_2O, the quadrupole moment of N_2, and the impact parameter. For self-broadened H_2O, the main interaction is dipole-dipole and similar calculations can be performed. This quantum treatment of line widths represents a large improvement over simple kinetic theory calculations. Such calculations, however, are most often scaled to agree with experimental results to obtain the highest degree of accuracy and are included in spectral line databases whenever accurate measurements are not available or possible.

Experimental studies of line widths can become surprisingly complicated for several reasons. One common complication is due to the overlapping and blending of adjacent spectral lines. Others include excessive experimental noise, badly-characterized instrument functions, incorrect "background" absorptions, and lack of characterization of the optical path. Some of these concerns have been reviewed by Gamache *et.al.* [9]. Furthermore, for some gases such as water vapor, experimental results from different investigators for the same spectral line lie well outside quoted uncertainties. Larger systematic and analysis errors, not inaccurate experimental spectra, are most likely responsible for these disagreements. The case for N_2-broadened water vapor line widths is investigated in detail in Chapter 4.

2.3 Lineshape Theories

The frequency dependence of the absorption coefficient is determined by the molecule's physical state and its environment. Broadening factors can be divided into three general classes. They are (1) natural broadening, (2) Doppler broadening, and (3) collision broadening. While natural and Doppler broadening can be described with relatively simple theoretical models, providing an accurate generalized collision broadening theory is a very challenging problem. Each of these are addressed below.

2.3.1 Natural Broadening

The *natural* lineshape is best described by considering a stationary, isolated molecule. If such a molecule is allowed to absorb radiation, undisturbed by any other form, it will eventually make a transition back to a lower level of internal energy. Consequently, the molecule has a limited lifetime at any given energy level. The resulting lineshape is given by

$$k_{nat}(\nu) = \frac{S}{\pi}\left(\frac{\gamma_{nat}}{(\nu - \nu_0)^2 + \gamma_{nat}^2}\right) \qquad (2.21)$$

where $\gamma_{nat} = 1/\tau_{nat}$ is the "natural" line width. Due to the relatively long lifetimes of these undisturbed molecules, γ_{nat} is very small, with values on the order of 10^{-5} cm^{-1}. For this reason, natural lineshapes are not observable under atmospheric conditions or with spectrometers of average resolution.

2.3.2 Doppler Broadening

The inhomogeneous *Doppler* lineshape is applicable to conditions encountered in the upper troposphere and stratosphere. In these cases, the temperature is assumed to be high enough to produce molecular motion, but the pressure is low enough so that the molecules experience no collisions; or at least are not subject to *strong* collisions which terminate the dipole moment oscillation. At pressures of about 5 Torr or less, the Doppler lineshape is predominant, with a typical line width of 0.001 cm^{-1} at 296 K. The molecular motion produces an apparent shift in the observed frequencies and such broadening is called Doppler broadening.

The shifted Doppler frequency, ν', for a molecule moving with a speed $\mathcal{V}_m$ along the direction of observation, relative to the observer, is given by

$$\nu' = \nu_0 \frac{\sqrt{1-(\mathcal{V}_m/c)^2}}{1+\mathcal{V}_m/c} \tag{2.22}$$

where ν_0 is the un-shifted frequency. For $\mathcal{V}_m \ll c$, ν' can be approximated with a binomial expansion as

$$\nu' = \nu_0 \left(1 - \frac{\mathcal{V}_m}{c}\right) \tag{2.23}$$

Therefore, for each $\mathcal{V}_m$, there exists a corresponding shifted frequency. Given a Maxwell distribution of velocities within the gas, the density of molecules with velocity $\mathcal{V}_m$ is given by

$$dn = N\left(\frac{m}{2\pi kT}\right)^{\frac{1}{2}} \exp\left(-\frac{m}{2kT}\mathcal{V}_m^2\right) d\mathcal{V}_m \tag{2.24}$$

N is the total number of molecules, m is the molecular mass, T is the temperature, and k is Boltzmann's constant. The corresponding absorption coefficient, $k_D(\nu)$, like the Boltzmann distribution, has a Gaussian form:

$$k_D(\nu) = \frac{S}{\gamma_D}\sqrt{\frac{\ln 2}{\pi}}\, e^{-\ln 2\left(\frac{\nu-\nu_0}{\gamma_D}\right)^2} \tag{2.25}$$

γ_D, the line width of the Doppler lineshape, is given by $\nu_0\sqrt{\frac{2kT\ln 2}{mc^2}}$. Notice how quickly the Doppler lineshape goes to zero far from the line center due to the negative exponential.

Another lineshape which is sometimes applicable for Doppler-type conditions is the *Rautian* lineshape [10]. It considers cases in which collisions cause a change in velocity of the oscillator, but with no simultaneous change in the internal quantum state of the molecule. In the extreme, if many of these collisions take place during one cycle of the wavetrain, the Doppler shifts average out to zero and a narrowing of the Doppler lines is observed. This effect is generally seen for cases with a light absorber with widely spaced energy levels (H_2) and a heavy perturber (Xe, Kr). In the systems studied here, collisions are more likely to induce infrared rotation-vibration transitions than to simply produce changes in translational motion.

2.3.3 Collision Broadening

At pressures greater than $\sim$ 5 Torr, the collisions between molecules must be addressed. Collisions are the most important phenomenon to contribute to broadening at these higher pressures. In 1906 Lorentz showed that line broadening takes place when absorbing molecules or atoms collide. If one assumes that a collision takes place during the time in which radiation is being absorbed, the coherency of the wave train is interrupted. This interruption results in a broadening of the spectral line. Quantum mechanically, pressure broadening is caused by the broadening of the molecules' energy levels by fields produced by the colliding molecules. This is a complex subject, and exact solutions for the absorption coefficient are found only under certain approximations. The exact treatment of this problem requires the knowledge of the time-dependent quantum mechanical wavefunction of an ensemble of colliding molecules. In general, this has not been achieved to date and therefore the problem is often approached by developing empirical or semi-empirical models which simulate the system. In the following sections, a model leading to the standard Lorentz lineshape is presented, followed by descriptions of more complex techniques of dealing with collisional broadening.

2.3.3.1 Lorentz Lineshape

In the simplest treatment, the collisional lineshape is that of a Lorentzian. At high pressures, collisions occur often and it is unlikely that a molecule is allowed to oscillate undisturbed for its entire natural lifetime. Instead, the molecule is usually perturbed by many collisions. This model makes several assumptions which lead to a simple solution for the absorption coefficient. The molecule's dipole moment is assumed to be oscillating with frequency ν_0. When a collision occurs at time t, the oscillation terminates instantaneously. No natural damping is included because the time between collisions, t, is much less than the natural lifetime, τ_{nat}. In other words, $\exp(-t/\tau_{nat}) = 1$ for all times considered.

It is important to understand the assumptions which have been made for this model. One of the assumptions is called the *impact approximation*, which assumes that the time between collisions is much greater than the duration of a collision, τ_{dur}, and therefore, the behavior of the dipole moment during the collision is negligible. In this case, τ_{dur} is taken to be zero, corresponding to an instantaneous phase shift in the dipole moment. These types of collisions are also sometimes called *adiabatic* in that the system has no time to react to the collisions. The opposite of the impact approximation is called the *quasi-static* approximation, in which the collision durations are essentially assumed to be much larger than the time between collisions. This point is addressed when statistical lineshapes are discussed. Another assumption made here is that of *strong collisions*. A strong collision is taken to be an interaction which terminates the oscillation, leaving no memory regarding its orientation or other properties before the collision. On the other extreme, *weak* collisions are those which have little or no effect in disturbing the molecule. In this case, collisional effects are only felt as a damping effect after a large number of weaker impacts. Collisions are also assumed to involve only two molecules, and such collisions are referred to as *binary collisions*. One final assumption is that the molecules follow classical straight line trajectories between collisions. So in the Lorentz model, which is often called the billiard-ball model, colliding molecules can be thought of as quickly moving hard spheres which do not interact with one another until they actually touch each other.

Fourier analysis of this model wavetrain leads to a spectral distribution of the form

$$\mid \mathcal{F}\{\mu(t)\} \mid^2 = \frac{\sin^2[2\pi(\nu - \nu_0)t/2]}{[2\pi(\nu - \nu_0)]^2} \tag{2.26}$$

This expression must be averaged over all possible values of t. From the kinetic theory of gases, the distance traveled between collisions, l, by a molecule of average velocity v_m has a Poisson distribution:

$$p(l)dl = \frac{dl}{l_m} e^{-l/l_m} \tag{2.27}$$

where l_m is the mean free path. Using $dt = \frac{dl}{v_m}$, the distribution for the time between collisions is

$$p(t)dt = \frac{dt}{\tau_{col}} e^{-t/\tau_{col}} \tag{2.28}$$

where τ_{col} is the mean time between collisions. Using this distribution, the absorption coefficient, $k_L(\nu)$ is found to be

$$k_L(\nu) = \frac{S}{\pi} \left(\frac{\gamma_L}{(\nu - \nu_0)^2 + \gamma_L^2} \right) \tag{2.29}$$

where $\gamma_L = 1/\tau_{col}$ is the Lorentz line width. Within this billiard-ball model, τ_{col} is calculated as l_m/v_m and has an average value of about 1.5×10^{-10} seconds [5]. This corresponds to a Lorentz line width of approximately 0.02 cm^{-1}, which is much larger than a typical Doppler width. Thus, whenever collisions are present, they provide the primary form of broadening.

This absorption coefficient is called the *Lorentz* lineshape. It has the same form as the natural lineshape; the only difference being the value of the line widths. It is useful to compare the Doppler and Lorentz lineshapes. The Doppler model assumes a Boltzmann velocity distribution, which goes smoothly to zero at large velocities. Its corresponding spectral distribution, therefore, also decays quickly in the far-wing (far from line center). This is not the case for the Lorentz model, which assumes instantaneous behavior during collisions. The effect of this unphysical temporal behavior is the placement of extremely high frequency components in the lineshape's spectral distribution. Consequently, $k_L(\nu)$ is too large in the far-wing, and the Lorentz model predicts too much absorption in this region.

Despite the apparent shortcomings of the model used for the Lorentzian line shape, it is very accurate for many applications. The Lorentz lineshape is accurate as long as two conditions are satisfied: (1) the spectral region of interest is not too far removed from the line center where the impact approximation results in the prediction of too much absorption, and (2) there exists no significant overlapping of adjacent spectral lines. The latter of these two conditions arises because the Lorentz theory assumes no transfer of intensity from one spectral line to another (often called "line mixing"). Experimental deviations from the Lorentz lineshape within $\sim$2–4 γ_0 of line center of isolated lines have not been confirmed for systems of atmospheric interest.

2.3.3.2 Van Vleck - Weisskopf Lineshape

When describing the procedures used to calculate the Lorentz and natural lineshapes, the assumption that transitions occur at relatively high frequencies (i.e. infrared) was made. When computing the Lorentz lineshape, the Fourier transform of the dipole moment actually yields two terms – one centered about ν_0 and the other about $-\nu_0$. The lineshape should be written as [11]

$$k(\nu) = \frac{S}{\pi}\left(\frac{\gamma}{(\nu-\nu_0)^2+\gamma^2} + \frac{\gamma}{(\nu+\nu_0)^2+\gamma^2}\right). \tag{2.30}$$

This shape is more often used in the microwave region of the spectrum, where the second term of the sum is not negligible. For molecules active in the infrared region, however, ν_0 is large enough such that $(\nu-\nu_0) \ll (\nu+\nu_0)$ and the resulting lineshape can most often be safely approximated as Lorentzian. An exception is in "window" regions (far from any line centers). Another modification to the Lorentz model involves the behavior of the molecule directly after a collision. In the Lorentz model, we essentially assumed the wave-function experienced *random* phase shifts during collisions and immediately began oscillating again at its resonant frequency. The wave-function, however, does not experience a random reorientation, but should be distributed according to the Boltzmann distribution of the field when the collision occurs [12]. Following this approach leads to a slight modification of Equation 2.30:

$$k(\nu) = \frac{S}{\pi}\left(\frac{\nu}{\nu_0}\right)^2\left(\frac{\gamma}{(\nu-\nu_0)^2+\gamma^2}+\frac{\gamma}{(\nu+\nu_0)^2+\gamma^2}\right) \tag{2.31}$$

which is commonly called the *Van Vleck-Weisskopf* lineshape [11]. Equation 2.31 is an improvement over Equation 2.30 in that (2.30) predicts no absorption in the limit of zero resonant frequency, which is not observed experimentally. Equation 2.31 is also more acceptable in that it agrees with Debye's [12] relaxation theory in the same limit.

2.3.3.3 Van Vleck - Huber Lineshape

Another similar lineshape which was developed to satisfy the principle of *detailed balance* (discussed below) is [12]

$$k(\nu) = \frac{S}{\pi}\left(\frac{\nu}{\nu_0}\right)\frac{\tanh(hc\nu/2kT)}{\tanh(hc\nu_0/2kT)}\left(\frac{\gamma}{(\nu-\nu_0)^2+\gamma^2}+\frac{\gamma}{(\nu+\nu_0)^2+\gamma^2}\right) \tag{2.32}$$

which is called the *Van Vleck-Huber* lineshape.

2.3.3.4 Voigt Lineshape

Before going on to explain more elaborate models, the *Voigt lineshape* should be introduced. It does not introduce any new physical insight into broadening phenomenon, but is very useful computationally. The Voigt lineshape is the convolution of the Doppler and Lorentz lineshapes. For this reason, it assumes Doppler characteristics at low pressure and Lorentz characteristics at higher pressures. Therefore, one single expression for the lineshape can be used throughout a wide range of pressures. The

Voigt lineshape, $k_V(\nu)$ is given by

$$k_V(\nu) = \frac{k_0 y}{\pi} \int_{-\infty}^{\infty} \frac{e^{-t^2}}{y^2 + (x - t)^2} dt \tag{2.33}$$

with

$$k_0 = \frac{S}{\gamma_D}, \quad y = \frac{\gamma_L}{\gamma_D}\sqrt{\ln 2}, \quad x = \left(\frac{\nu - \nu_0}{\gamma_D}\right)\sqrt{\ln 2} \tag{2.34}$$

The Voigt lineshape does assume there is no correlation between collision cross sections and the relative speed of the colloids. Again, for atmospheric systems this approximation appears to be quite accurate.

2.3.4 General Techniques for Calculating Collisional Lineshapes

So far, the lineshape models have admittedly been presented in an informal style in order to provide general physical insight. However, for more advanced approaches, it is useful to understand the more formal techniques in which absorption coefficients are calculated. This is needed to help understand the deviations from Lorentz lineshapes examined in this thesis. There are many ways in which this is accomplished, but only the most common are described here. This begins with a description of the correlation function treatment of lineshapes, which helps relate the collision separation distance to the frequency displacement from line center. A review of the intermolecular forces pertinent to line broadening is then given, with attention paid particularly to the characteristics of the potentials used in lineshape calculations. The *ab-initio* and statistical approaches are then presented. Except for the basic information, these sections are oriented toward H_2O lineshapes. Aspects of lineshape theory peculiar to rotational relaxation and CO_2 line-mixing are introduced separately in Chapter 3.

2.3.4.1 Correlation Functions

A common way in which lineshapes are calculated is through the use of autocorrelation functions. Qualitatively, the autocorrelation function describes how long some physical quantity of a complicated system exists before its average value becomes zero.

Since dipole interactions are strongest, this method generally involves modeling the molecule's changing dipole moment, $\mu(t)$, as a function of time. The autocorrelation of $\mu(t)$ is given by $\phi(t) =< \mu(0) \cdot \mu(t) >$, where $<>$ denotes a statistical average over the entire system. Because the net dipole moment has contributions from many different elements of the system, $\phi(t)$ will, in general, involve a complicated sum. Using physical intuition, expressions for $\phi(t)$ can be developed. Fourier analysis is then used to calculate the spectral distribution. Formally, this is justified by the Weiner-Kchichstine theorem, which states that the power spectral density of a temporal function $f(t)$ at frequency ν is the square of the Fourier transform of $f(t)$ divided by π. The absorption coefficient at frequency ν (cm^{-1}) and temperature T of a gaseous sample is given by [13, for example]

$$k(\nu) = \frac{4\pi^2}{3\hbar c}\nu \tanh(\hbar\nu/2kT)[F(\nu) + F(-\nu)] \tag{2.35}$$

where the spectral densities $F(\pm\nu)$ are the Fourier transforms of the autocorrelation function $\phi(t)$. Thus, if $\phi(t)$ is known or can be modeled, the absorption coefficient may be calculated. The lineshape then tells us what the power spectrum of $\mu(t)$ is like on average. Because $\phi(t)$ is an average over all absorber–perturber configurations, however, there is not a direct relationship between the lineshape and $\mu(t)$.

Correlation function approaches are commonly used because of their simplicity and generality. For instance, the Doppler and Lorentz lineshapes can be derived if the correct correlation functions are chosen. These are $\phi(t) = \exp(-\frac{1}{2}\gamma^2 t^2)$ and $\phi(t) = \exp(-\gamma|t|)$ for Gaussian and Lorentz shapes, respectively.

Throughout this study, reference is made to the *near-wings*, *intermediate wings*, and *far-wings* of spectral lines. This is just a qualitative way of referring to different parts of a spectral line: near-wing is the region very close to the line center, far-wing is the region very far from the line center, and intermediate-wing is the region in-between. Standard accepted definitions of these terms do not exist, but near-wing generally means within several half-widths of line center. A more general definition is that the

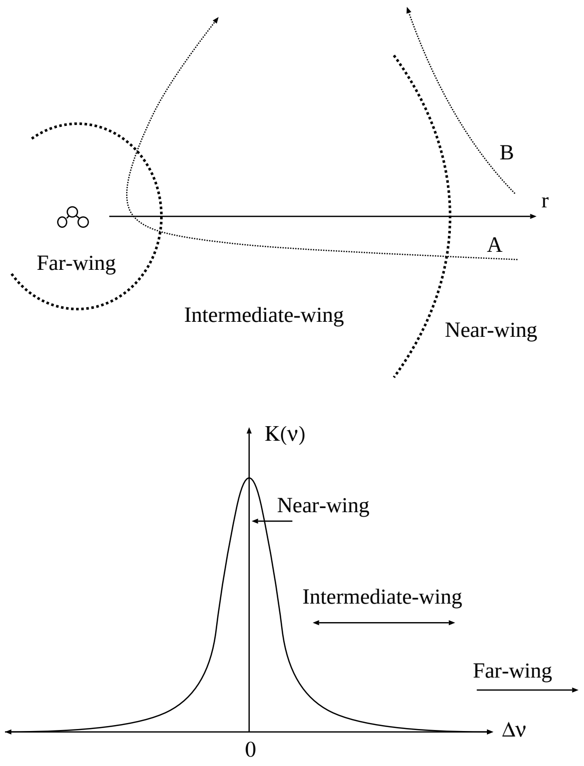

Figure 2.3: Qualitative relation of the distance between the interacting molecules, r, to the distance from the line center, $\Delta\nu$. Absorber-perturber trajectories are also shown for (A) a far-wing, close collision and (B) a near-wing, distant collision.

near-wing region is where the impact approximation is valid. Far-wing can range anywhere from ~10 half-widths to over 1000 cm^{-1} from line center. Using the correlation function/Fourier transform approach to lineshapes, the near-wing is associated with any interactions which occur at large absorber–perturber separation distances while the far-wing is associated with much closer interactions [14]. Thus, in order to obtain a reasonably accurate far-wing lineshape, an equally accurate knowledge of the molecule's behavior during collisions is required. This relation of near- and far-wings of spectral lines to the closeness of the molecular interaction is illustrated in Figure 2.3. Also shown are collision trajectories which result in near and far-wing perturbations. For the near-wing trajectory (B), the time between collisions is long compared to the duration of the collision and the details of the collision can be ignored. For the far-wing trajectory (A), the duration of the collision is not negligible and the details of the collision must be addressed. In general it is difficult to obtain a lineshape which is accurate in both the near- and far-wings. Very often, however, accepted near-wing lineshapes are combined with far-wing lineshapes with an *ad-hoc* interpolation through the intermediate region.

2.3.4.2 Intermolecular Forces and Lineshapes

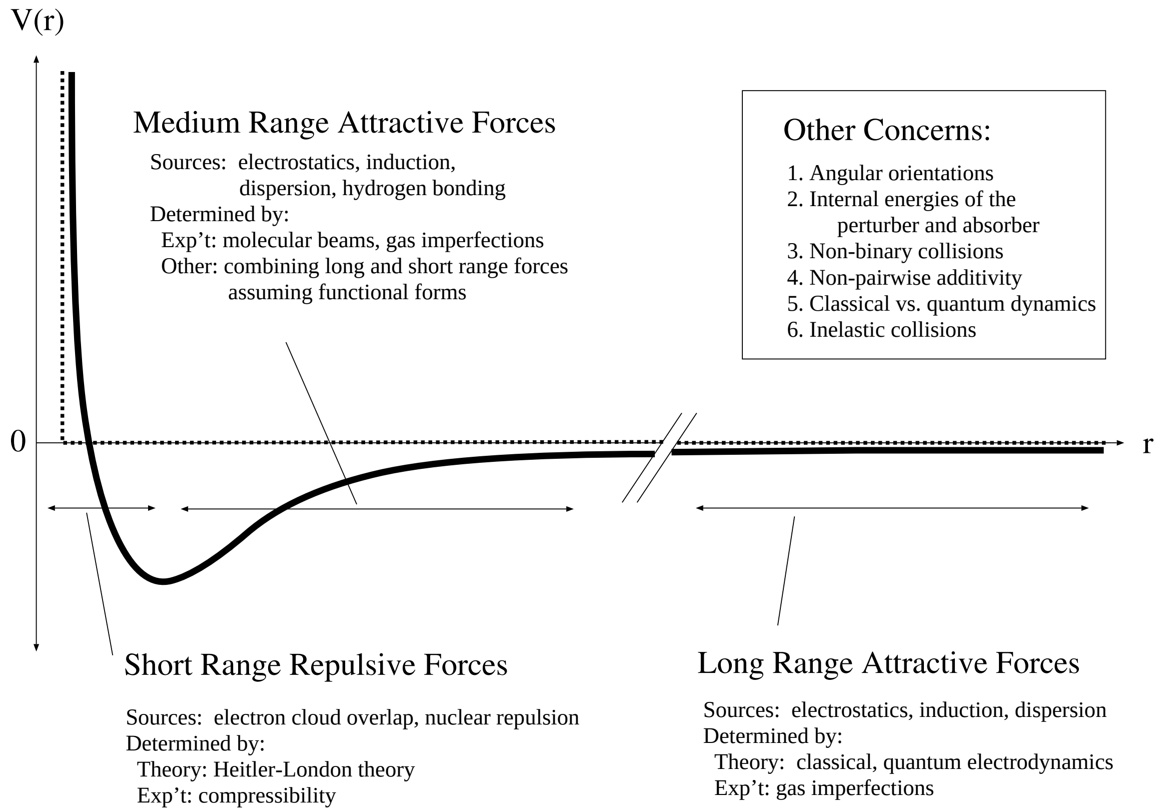

Figure 2.4: A summary of the short, intermediate, and long range intermolecular forces which contribute to collision line broadening. The Lorentz intermolecular potential (thick dotted curve) and a more realistic potential (thick solid curve) are shown.

The contents of this section are summarized in Figure 2.4. An excellent analysis of the intermolecular forces pertinent to molecular collisions is given in Reference [15]. As described in the previous section, if the behavior of the absorber's wavetrain during an optical transition is known, the spectral lineshape can be calculated. For pressure broadening conditions, this is determined by the interaction with perturbing molecules and the intermolecular forces can be divided into three classes: long, intermediate, and short range. Of course, in an experiment, all ranges of interaction are experienced and the resulting lineshape is a composite of all types of collisions. However, using the correlation function approach to lineshapes, whereby the far-wing lineshape is associated with close collisions and the near-wing is associated with distant collisions, the actual forces corresponding to these regions can be investigated by studying different parts of the lineshapes. These forces are reviewed in the following sections. It is important to note that collisions effect the lineshapes not only by accelerating the center of masses of the colloids, but more importantly, by distorting the multipoles of the absorber. The accelerations of the colloids are important, however, because they govern how fast or how slow the interactions take place.

The Lorentz intermolecular potential and a more realistic potential are shown in Figure 2.4. For the Lorentz model, the molecule does not experience any force from the colloid until their separation distance equals the sum of their effective radii. At this point, the molecules experience an infinite repulsive force, leading to an infinite acceleration (instantaneous phase shift) in the wavetrain. As a result, the Lorentz lineshape is too large in the far wing. (i.e. short interaction range $\rightsquigarrow$ far-wing).

In general, the behavior of other lineshapes, if evaluated relative to Lorentz, can provide information on the net intermolecular forces. Additionally, combined with the relation of frequency displacement from line center to interaction distance, judgments about the short, intermediate, and long range forces can be made.

For example, lineshapes are commonly found to less than Lorentz (sub-Lorentz) in the far-wing. This implies that there are fewer high frequency components in the molecule's wavetrain at short separation distances. This, in turn, implies that the molecule does not experience forces in this region which are as large as predicted by the Lorentz model. A more realistic potential is not as repulsive at these short ranges, leading to "softer" close collisions. Likewise, other separation distances correspond to other parts of the lineshape. Super- and sub-Lorentzian lineshape behavior implies that larger or smaller net forces (relative to Lorentz) are observed. For example, molecules generally experience attractive forces at intermediate separations, leading to an acceleration in the wavetrain, and to a super-Lorentz lineshape in the intermediate wing [16]. It should be noted again, however, that there is not a direct relationship between the intermolecular potential and the lineshape; the lineshape is derived from an average over all angular orientations and all internal energies. In fact, the potentials can be derived from the lineshape for only the very simplest of cases – when the potential is isotropic (non angle dependent) and the perturber has few internal energy levels.

2.3.4.2.1 Long Range Forces and Potentials. At large separation distances, species of opposite net electrical charges experience large Coulombic attractive forces. Even if there is no net charge, the symmetry of the positive and negative charge distributions on each molecule can lead to other *electrostatic* interactions. Furthermore, the electric field produced by one molecule can induce small changes in the charge distribution of the other molecule, leading to *induction* interactions. Finally, *dispersion* forces can arise when instantaneous multipoles from one molecule correlate with those of another molecule. For non-polar molecules, these dispersive forces are often the largest long range forces.

Direct electrostatic interactions occur for a pair of uncharged molecules when they have non-spherical charge distributions. This depends strongly on the separation and relative orientation of the molecules. The charge distributions are commonly described by their multipole moments. In general, a molecule may possess a series of multipole moments and there is a tendency to emphasize the lowest non-zero moment although the complete representation requires the inclusion of all non-zero moments. For the polar water vapor molecule, the leading multipole is a dipole. For carbon dioxide, the charge distribution is symmetric about the internuclear axis, leading to a zero dipole moment – however, the the C–O bonds lead to a non-zero quadrupole moment. Dipole and quadrupole moments for some common atmospheric molecules are listed in Table 2.1.

Molecule	Dipole Moment (Debye)	Quadrupole Moment (10^{-40} Cm^2)
H_2	0	+2.1
N_2	0	-4.90
O_2	0	-1.33
CO	0.112	-8.2
CO_2	0	-14.9
H_2O	1.855	+8.7(xx), -8.3(yy), -0.4(zz)
N_2O	0.161	-11.2
NH_3	1.47	-7.7
SO_2	1.59	-16.2(xx), +12.7(yy), +3.4(zz)

Table 2.1: Molecular dipole and quadrupole moments. (1 Debye = 3.3×10^{-30} Cm).

For pairs of molecules, the long range electrostatic interaction is dependent on the separation distance, the relative orientation, and the multipole moments. Averaging over a Boltzmann distribution of orientations, the net long range interaction is attractive and inversely proportional to the separation distance. (i.e. $\propto r^{-3}$ for dipole-dipole, $\propto r^{-4}$ for dipole-quadrupole, and $\propto r^{-5}$ for quadrupole-quadrupole).

Induction interaction occurs when the electric fields produced by a single molecule influence the charge distribution of another. For induced dipole moments, the interaction is attractive for all orientations and falls of as r^{-6}. Other multipoles can also be induced.

The electrostatic and induction interactions are derived completely from classical electrostatics. For molecules with no permanent multipoles, these interactions are zero and the main interaction results from dispersion – even for the polar molecule

HCl, the electrostatics and induction account for only ~20% of the long range interaction. Dispersion arises from the interaction of instantaneous dipoles between a pair of molecules. Even though the average dipole moment of a spherical molecule is zero, temporary moments can occur at any instant. These moments can induce a dipole in a neighboring molecule and, as in induction forces, the overall interaction is attractive. Like the induction forces, the interaction has a r^{-6} dependence. At large separation distances, only the leading dispersive moment makes a substantial contribution to the interaction. At shorter separations, however, higher order moments can become significant.

2.3.4.2.2 Short Range Forces and Potentials. When molecules approach so closely that their electron clouds overlap, the Pauli exclusion principle restricts the overlap and a strong net repulsive force is created. Likewise, the nuclei of the molecules are no longer completely shielded from each other by their electron shells and they also repel. This type of interaction is difficult to treat theoretically but is considered in Heitler-London theory [15]. At very short separations, the interaction varies as $1/r$, due to the nuclear repulsion. At larger separations, the interaction is still repulsive, and varies as e^{-Br}, where B is a constant [15].

2.3.4.2.3 Intermediate Range Forces and Potentials. The intermediate range forces are more difficult to treat than the long and short range forces. The long range forces are expressed in terms of the isolated molecule while the short range forces result from conditions where the isolated molecule properties are meaningless. As a result, the two approaches cannot be combined to obtain the intermediate range interactions – that is, if the long and short range forces are simply added together, the intermediate range forces are very difficult to characterize. This is due partially to the fact that dispersion and induction forces, which are less important in the short and long ranges, are the primary interactions at these ranges. For molecules containing hydrogen atoms, transient hydrogen bonding can also lead to strong attraction in this region. For small molecules with relatively few electrons, the intermediate potential well region can be studied using ab-initio quantum mechanical approaches. This approach, however, is restricted to small molecules and, in general, the characterization of this region must be carried out using experimental techniques. A common approach is to adopt a functional form for the potential and determine its parameters based on the short and long range behavior.

2.3.4.2.4 Representation of the Interactions. Although theoretical investigations of the long and short range forces provide insight into the molecular interactions, it is not possible to produce a potential for all separation distances and angular orientations using quantum mechanics, especially for systems of larger molecules. This is particularly true for the intermediate range forces which produce the potential well. Consequently, the well region has been characterized experimentally using two general approaches: (1) the direct inversion of the potential from various measurements carried out as a function of temperature, and (2) representing the potential with an algebraic form containing several adjustable parameters determined by comparing calculations based on the potential to experimental values of bulk properties of the material. Approach 1 has been carried out for only a small number of systems consisting of monatomic molecules. Additionally, this often requires assumptions about asymptotic behavior of the potential in the short and long ranges. Approach 2 can be successful if it is carried out using a flexible algebraic form and the parameters are optimized using measurements over a wide range of conditions. This approach, however, has two problems associated with it: (1) by assuming a specific algebraic form, the potential is forced to have a certain behavior and (2) the physical properties which are compared to are often not sensitive to the potential well region.

For polyatomic systems, the potential must be represented not only as a function of separation distance, but also for all angular orientations. At a crude level, the short and intermediate range potential is represented with a spherical part, most often similar to a Lennard-Jones “n-6” form, and an anisotropic part consisting of the leading multipole interaction. This, in fact, is the approach taken by the state-of-the-art calculations for the water vapor system, and is discussed in more detail in Chapter 4. Such potentials are very useful for some applications, but are limited because they (1) neglect all multipole interactions other than the leading multipole, (2) neglect totally the anisotropy of the inductive, dispersive, and short-range interactions, and (3) use representations of the potential well region which are potentially very inaccurate.

Common experimental sources of information about the intermolecular potentials include: gas imperfection studies, gas transport properties, molecular beam experiments, van der Waals spectra, and solid and liquid experiments. Of these, gas imperfection and molecular beam studies are the most useful for potentials of gaseous molecules.

Molecular beam experiments are carried out by colliding two beams of molecules and measuring the scattered beam at specific angles relative to the beam geometry. The intensity of the scattered beam is related to the intermolecular potential of the pair. For simple systems, this measurement can be inverted to yield the intermolecular potential, in principle, for all separation distances. Alternatively, calculations performed using a trial potential can be compared to measured results. For polyatomic molecules which can attain many levels of internal energy, inelastic collisions must be addressed, and the inversion of scattering data becomes more difficult. For water vapor, these types of measurements are even more difficult due to problems associated with actually producing a beam of individual H_2O molecules.

Gas imperfection studies provide information about the short and long range forces. This generally involves the study of deviations from the ideal gas law and characterizing viral coefficients. Using the van der Waals equation of state, repulsive interactions raise the pressure above the value for a perfect gas at the same density by excluding small volumes around the molecules. Attractive forces reduce the pressure by slightly reducing the volume. Compressibility measurements are performed by observing these deviations versus pressure and temperature. The main point to be made here is that these measurements probe the short and long range forces, but are relatively insensitive to the intermediate range forces. In other words, a potential can be derived from the data which reproduces the measured quantities very accurately, but does not represent the well region nearly as well. To determine the potential from these types of measurements, second viral coefficients are calculated directly from a trial potential, which is adjusted until agreement is obtained. This approach, however, has the same drawbacks as discussed above. That is, a functional form for the potential is usually assumed, which ultimately corrupts the final result. Inversion methods have also been attempted, but are not very successful for polyatomic systems.

2.3.4.2.5 State-of-the-art Potentials. The most complex systems which have been accurately characterized are those of He_2, $H_2 - He$, and $(H_2)_2$. Other noble gas systems such as $He - Ar$ and $Ar - Kr$ are also well known. Unfortunately, due to the rate at which the calculations and data inversion methods become more complex with more complicated systems, there is little hope of accurate H_2O and CO_2 potentials in the near future. This is particularly true for H_2O. In a recent evaluation of nine CO_2-Ar potentials [17], it was determined that none were capable of accurately reproducing measured line widths.

For more complicated systems, gas imperfection and other experimental sources have resulted in somewhat accurate short and long range potentials. The intermediate region, however, concerned with the potential well has received little attention. In this region, inductive and dispersive interactions are likely to become much stronger, leading to additional attractive forces which are not accounted for in most cases. Spectral lineshape studies, such as the study of water spectra presented here, provide a useful tool for studying the net result of these effects.

2.3.4.3 *Ab-initio* Calculations

It would be nice to calculate a collisional lineshape without any approximations. With quantum mechanics, this involves solving Schrodinger's equation for N interacting molecules and N' photons. N, however, is on the order of 10^{23} which makes the calculations impossible. It is much simpler to use single particle kinetic equations in which the cumulative effects of all molecules are represented by collision cross sections. The assumptions which must be made to solve such equations, even for simple systems such as HF broadened by Ar, often lead to solutions which can be obtained by much simpler means. Truly *ab-initio* calculations have not been performed. In general, the steps needed to carry out these calculations are [18] (1) obtain an accurate representation of the intermolecular forces between the colliding molecules, (2) solve the single particle scattering equations, and (3) use the scattering cross sections in the appropriate kinetic equations to obtain the power spectral response function which leads to the lineshape. Step (1) represents a significant challenge in itself in that accurate potentials are available for only the simplest of molecule-perturber systems. These must be known as a function of the molecule's and perturber's various configurations (i.e. separation distance, angular dependence). The rest of the calculation involves expanding a test wavefunction in terms of all possible states of the unperturbed molecule and a large number of partial waves representing the result of the angular momentum of the molecule-pertuber system. The Schroedinger equation is then solved by imposing boundary conditions by assuming the asymptotic form of the solutions. This is a major task. To date, the molecule-perturber combinations which have been attempted include: D_2-He [18], CO-He, HCl-Ar, HF-Ar, and H_2-Ar [19]. Some simpler systems have also been examined. Recent work on the determination of an accurate interaction potential for the pure rotational H_2O-He system and the more important H_2O-H_2 [20] system is very promising. To make the final lineshape portion of these calculations feasible, however, both the binary collisions and impact approximations must be imposed. As a result, the resulting lineshape is the familiar Lorentzian (although collisional transfer of intensity is allowed so line-mixing is accounted for) and is valid only in the near-wing. Comparisons with measured half-widths and line-shifts, however, are in good agreement and confirm a fundamental correctness of this approach. These calculated widths and shifts prove to be extremely sensitive to small perturbations in the intermolecular potentials, thus showing the need for accurate potentials.

2.3.4.4 Statistical Lineshapes

The basic idea behind most statistical lineshape theories can be described by considering Figure 2.5 which depicts the intermolecular potential curves for two different molecular states (A and B) as a function of the molecule-perturber separation distance r. $E_0 = E' - E''$ is the energy difference between the two states for an unperturbed molecule (i.e. as $r \rightarrow \infty$). A and B, for example, could represent different values of rotational and vibrational energy and E_0 would thus be directly related to the line center of a rotation-vibration spectral transition. Using an interpretation of the Franck-Condon principle, statistical theories assume that molecular transitions take place vertically in the figure and that r, the molecule-perturber separation, does not change during a transition. Another consequence is that the relative velocity between the molecule and perturber remains unchanged during a transition. In other words, transitions take place so quickly that the molecule-perturber interaction (the collision) can be treated as a constant as a function of time for each value of r. In other words, the time between collisions is negligible compared to the duration of a collision. This is essentially the opposite of the impact approximation and is called the *quasi-static* approximation. The details of the close collisions are treated accurately with this approach and the lineshape is most accurate in the far-wing. Because the interaction time is much greater than the time between collisions, the relative motion of the two molecules is neglected

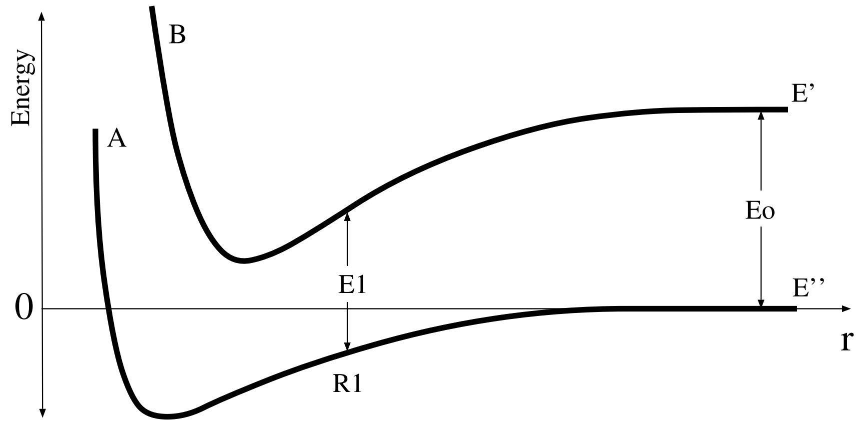

Figure 2.5: Intermolecular potential curves for two different molecular states (A and B) as a function of the molecule-perturber separation distance r. $E_0 = E' - E''$ is the energy difference between the two states for an unperturbed molecule (i.e. as $r \to \infty$).

and the lineshape is therefore least accurate in the near-wing.

The quasi-static approximation is somewhat confusing, or at least not intuitive, for infrared spectra where molecular collisions occur more frequently than transitions. However, proceeding with the statistical treatment, if a transition takes place in Figure 2.5 at $r = \infty$, absorption will occur at the line center $\nu_0 = \frac{E_0}{h}$. If a transition takes place when the molecules are closer together (i.e. $r = R_1$), the transition frequency $\nu_1 = \frac{E_1}{h}$ is slightly shifted from line center. Averaging over all absorber configurations, all broadener configurations, all intermolecular distances, and all intermolecular angles yields the lineshape. Note that this approach inherently assumes binary collisions and that the difference between the shapes of the upper and lower energy interaction curves determines the lineshape.

Statistical calculations therefore begin by assuming a form of the potentials, which is usually of the form $\frac{1}{r^n}$ in the long range limit. In the limit $r \to \infty$ and $n = 3$ (dipole interaction), the resulting lineshape is Lorentzian. In general, for $r \to \infty$, the lineshape has been evaluated for arbitrary n by Margenau and Breene. However, for the statistical treatment to be useful the calculations must avoid taking the infinite separation limit.

Calculations have been performed with this in mind by Rosenkranz [16] and more recently by Ma and Tipping [21] for the water vapor lineshape. These are presented in more detail in Chapter 4. It should be pointed out, however, that even if the statistical method were free of any other approximations, the exact interaction potentials must be known well for all r if accurate results are expected.

2.3.4.5 Formal Constraints on Spectral Lineshapes

Formal lineshapes must satisfy certain conditions. One requirement is that in thermal equilibrium, absorption and emission must balance each other. That is, in a given frequency interval, as much radiation is emitted as absorbed. This is called *detailed balance* and has direct consequences on the behavior of spectral lineshapes. In its simplest form, it relates the Fourier transforms of the correlation function $\phi(t)$ through [13, for example]

$$F(\nu) = \exp(-hc\nu/2kT)F(-\nu) \tag{2.36}$$

with $F(\nu) = \frac{1}{2\pi}\int_{\infty}^{\infty} \mathrm{e}^{-i\nu t}\phi(t)dt$, and $\phi(t) =< \mu(0)\cdot\mu(t) >$ as before. This is sometimes also called the *fluctuation-dissipation* theorem [12, for example]. Combining this principle with the relation between the rate of energy absorption and the absorption coefficient leads to

$$k(\nu) = \frac{8\pi^2\nu}{hc}\tanh(hc\nu/2kT)f(\nu) \tag{2.37}$$

where $f(\nu)$ is Fourier transform of $< \mu(0)\cdot\mu(t) + \mu(t)\cdot\mu(0) >$. This requirement is satisfied, for example, by the Van Vleck-Huber lineshape (Equation 2.32).

Other requirements can also be imposed on lineshapes by making sure that Kramer's Kronig relations are satisfied. This essentially ensures that the radiating molecule does not experience a disturbance before the disturbance actually exists. These will not be discussed here. In general, all of these requirements have their effect in the far-wing. Experimental deviations from these restrictions are therefore usually difficult to detect.

2.3.4.6 χ-functions

A common treatment of lineshapes is to express the true, or measured, lineshape as a ratio to some well-known lineshape. This is often used phenomenologically as a way to express experimental or theoretical results. In this work, for example, the reference lineshape is usually Lorentzian and the χ-function is given by the the ratio of the calculated or measured lineshape to Lorentz:

$$\chi(\nu, \nu_i) = \frac{k(\nu, \nu_i)}{k_L(\nu, \nu_i)}. \tag{2.38}$$

In regions where χ is greater than one, the lineshape is referred to as *super-Lorentzian*, and *sub-Lorentzian* where it is less than one.

Chapter 3

A Spectral Lineshape Model for Carbon Dioxide

3.1 Introduction

The 4.3μm spectral region, which is dominated by the ν_3 vibrational band of CO_2, is particularly useful in retrieving atmospheric temperature profiles. This region and several Q-branches in the 15μm region are useful because the absorption varies strongly with wavenumber, thus allowing many levels of the atmosphere to be probed within a very narrow spectral range. For example, Figure 3.1 shows this behavior with a brightness temperature spectrum measured by the University of Wisconsin's High–Resolution Interferometer Sounder (HIS) [22,23] in the Convection and Moisture Experiment (CAMEX) [24]. The drastic change in the spectrum at the ν_3 R-branch band-head at ~ 2397 cm^{-1} is due in part to the molecular spectroscopy of CO_2, the strong dependence of the Planck function on temperature at this wavelength, and the absence of any strong atmospheric absorbers beyond this region. This behavior is accentuated by the extreme sub-Lorentzian nature of the ν_3 CO_2 lineshape in this spectral region.

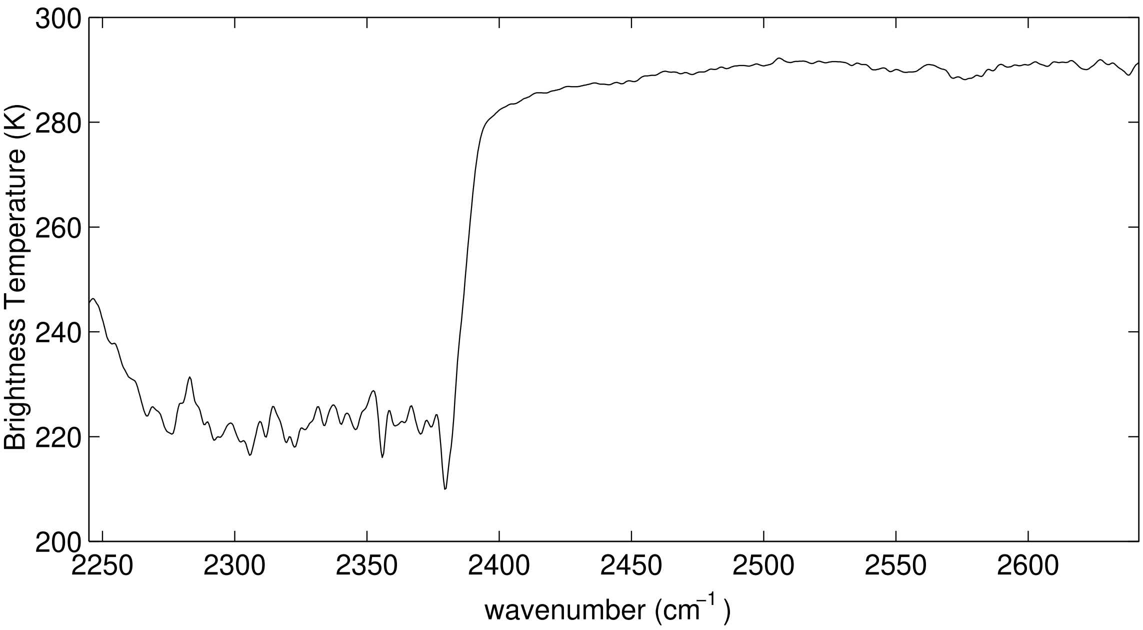

Figure 3.1: A CAMEX validated brightness temperature spectrum measured with HIS in the 4.3μm region. The drastic change in the spectrum at the ν_3 R-branch band-head of CO_2 at $\sim$ 2390 cm^{-1} is accentuated by the extreme sub-Lorentz lineshape behavior in this region. AIRS channels are located continuously from 2170 to 2675 cm^{-1}.

Deviations from Lorentzian lineshape behavior in CO_2 are observed primarily in two cases: (1) when there is significant overlap of adjacent spectral lines and (2) when the spectral region of interest is far from the line center. The Lorentz model fails in these two cases because (1) it neglects the interaction between spectral lines due to inelastic collisions while absorption is occurring and (2) it treats collisions between molecules as if they were instantaneous. These two phenomenon are frequently referred to as line-mixing and the duration-of-collisions effect, respectively. A lineshape which is accurate for the ν_3 band of CO_2 must include both effects.

In this study, this sub-Lorentzian behavior is modeled using CO_2 transmission spectra collected with a Fourier transform spectrometer by John W. C. Johns of NRC, Ottawa. A phenomenological lineshape model is developed by taking into account the effects of line-mixing and the finite duration-of-collisions. The goal here is to develop a simple model which is physically-based that can accurately reproduce the observed spectra.

The lineshape should also be accurate from line center to far-wing over a wide range of atmospheric pressures and temperatures.

Previous studies and the development of the model are discussed in Sections 3.2 and 3.3. This includes (1) the generalization of line-mixing models developed for CO_2 Q-branches [25–32] to P- and R-branches of $\Sigma - \Sigma$ bands and (2) the use of an empirical autocorrelation model to include the effects of non-zero collision times. The molecular spectroscopy necessary to understand the lineshape model is reviewed in Appendix A. The development of the line-mixing model for Q-branches in reviewed in Appendix B [33]. Details concerning calculations and comparisons to measured spectra are presented in Section 3.5. By determining the effects of line-mixing and duration-of-collision effects separately for the ν_3 band, the theory for duration-of-collision is then combined with line-mixing calculations for bands of different symmetry in the 15μm region in Section 3.6. A modified version of the model which is more accurate at the band-head and more useful for line-by-line radiative transfer codes is also proposed.

3.2 Previous Studies of the 4.3μm Lineshape

Previous work for this spectral region has focussed on the regions beyond the band-head and on the microwindows – the small window regions in-between the ν_3 R-branch lines. In the most notable work to date concerning regions beyond the band-head [34, 35], the sub-Lorentzian behavior was modeled with a set of empirical χ-functions in order to obtain the best agreement with data as possible. This work is reviewed briefly in Section 3.2.2. First, however, it is instructive to see how Lorentz calculations compare to measured spectra in this region.

3.2.1 Lorentz Calculations

As discussed in Chapter 2, the Lorentz lineshape models collisions as *instantaneous* phase shifts in the molecules' temporal wave function. These instantaneous phase shifts in temporal space result in the spectral lineshape having large high frequency components. As a result, the Lorentz model is not accurate far from the line center, a requirement which must be satisfied for this study. Figure 3.2 shows a Lorentzian (Voigt) calculation and comparison to a measured spectrum. As expected, the Lorentz model greatly overestimates the absorption beyond the band head. This is caused not only by the far-wing errors of the lines of the fundamental ν_3 band, but also by the errors introduced by all the other "background" lines (all lines other than the $C^{16}O_2$ ν_3 fundamentals, i.e. hot bands, other isotopes, etc...) which add to the absorption. Also shown in the figure is a Lorentz calculation using only the background lines – with the Lorentz model, these lines alone predict too much absorption beyond $\sim$2400 cm^{-1}.

3.2.2 The Cousin *et.al.* χ-functions

Existing line-by-line radiative transfer codes (i.e. FASCODE [36], GENLN2 [37]) generally use the χ-function developed by Cousin *et.al.* [34, 35] to account for the observed

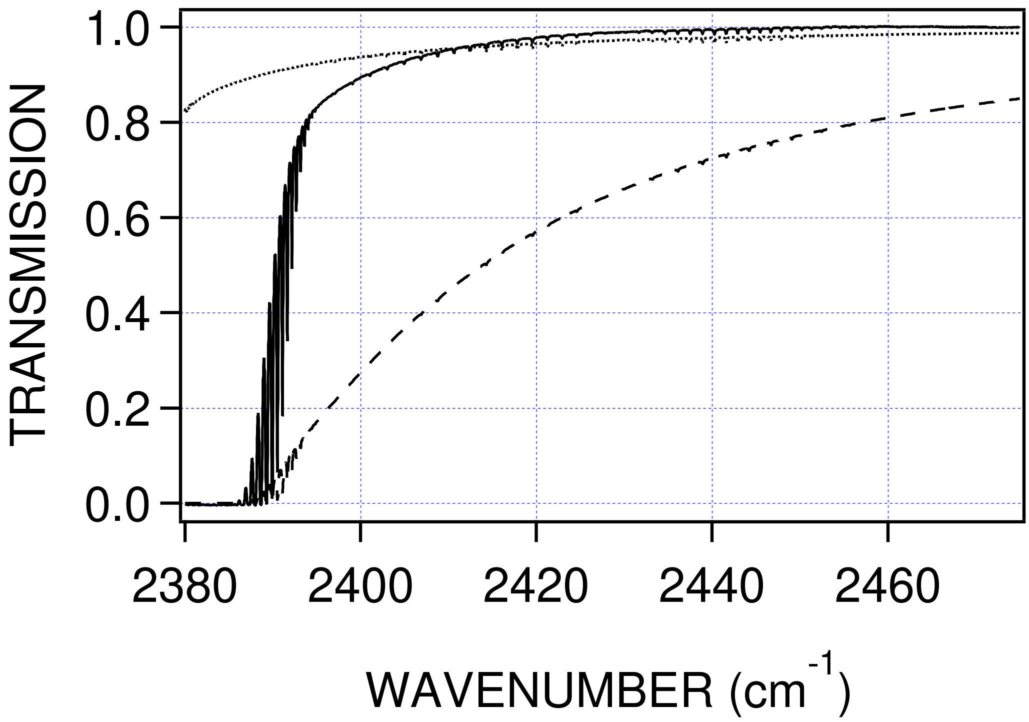

Figure 3.2: Experimental data (solid curve) and a Lorentz calculation (dashed curve) . Temperature=297.0 K, P(CO_2)=38.04 Torr, P(N_2)=723.5 Torr, Path Length=800 cm. The Lorentz model greatly overestimates the absorption far from the ν_3 band center. Weak lines due to a hot band centered at $\sim$2425 cm^{-1} can be seen in the spectra. A Lorentz calculation using only the background lines (dotted curve) is also shown, showing the importance of treating these lines correctly.

sub-Lorentzian behavior in the 4.3μm region. This χ-function was developed by adjusting a Lorentz lineshape to agree with measured laboratory transmission spectra in regions beyond the band-head. The assumption was that the observed sub-Lorentz behavior was due entirely to duration-of-collision effects. Originally, Equation 3.22 was used, effectively fitting for A_m and τ_2 to match their data, but satisfactory agreement was not achieved. Instead, Cousin *et.al.* developed more accurate, but very empirical χ-functions. For nitrogen-broadened CO_2 at 296K, for example, the χ-function was parameterized as:

$$\chi = \begin{cases} 1 & \text{if} \quad 0.00 \le |\nu - \nu_i| \le 0.05 \text{ cm}^{-1} \\ 1.064 \exp(-0.124|\nu - \nu_i|) & \text{if} \quad 0.05 \le |\nu - \nu_i| \le 20.0 \text{ cm}^{-1} \\ 0.125 \exp(-0.164|\nu - \nu_i|) & \text{if} \quad 20.0 \le |\nu - \nu_i| \le 50.0 \text{ cm}^{-1} \\ 0.146 \exp(-0.019|\nu - \nu_i|) & \text{if} \quad |\nu - \nu_i| \ge 50.0 \text{ cm}^{-1} \end{cases} \tag{3.1}$$

The effective lineshape for individual spectral lines is then given by a Lorentzian multiplied by χ. Similar χ-functions were developed for nitrogen broadening at 193K and 238K and for self broadening at 218K and 296K. These are listed in Table 3.1 and shown in Figure 3.3. Together, these χ-functions require 14 adjustable parameters for self-broadened CO_2 and 25 for N_2-broadened CO_2. For other temperatures, a linear interpolation between these reference temperatures is commonly used.

It should be emphasized that these χ-functions were developed for use beyond the band-head, but are commonly used throughout the entire ν_3 band and also in other spectral regions. The accuracy of this approach was analyzed in Reference [38]. While this method is certainly much better than a Lorentz lineshape, the χ-functions lack the functional form required to account for the observed sub-Lorentzian effects within the band. In the intermediate and far-wings, finite collision durations result in a exponentially decaying lineshape, and thus are properly modeled by the Cousin χ-functions. Line-mixing, however, has the overall effect of reducing the Lorentz lineshape by a constant multiplier in the far-wing and the exponential form of the Cousin *et.al.* χ-functions should not be expected to reproduce these effects accurately.

3.2.3 Other 4.3μm Line Mixing Studies

For the R-branch microwindows, only a few studies which have used line-mixing models to account for the observed absorption are noted. A more complete review of studies for this region has been compiled by Rao *et.al.* [39].

To calculate the relaxation processes occurring in line-mixing, the strong collisions

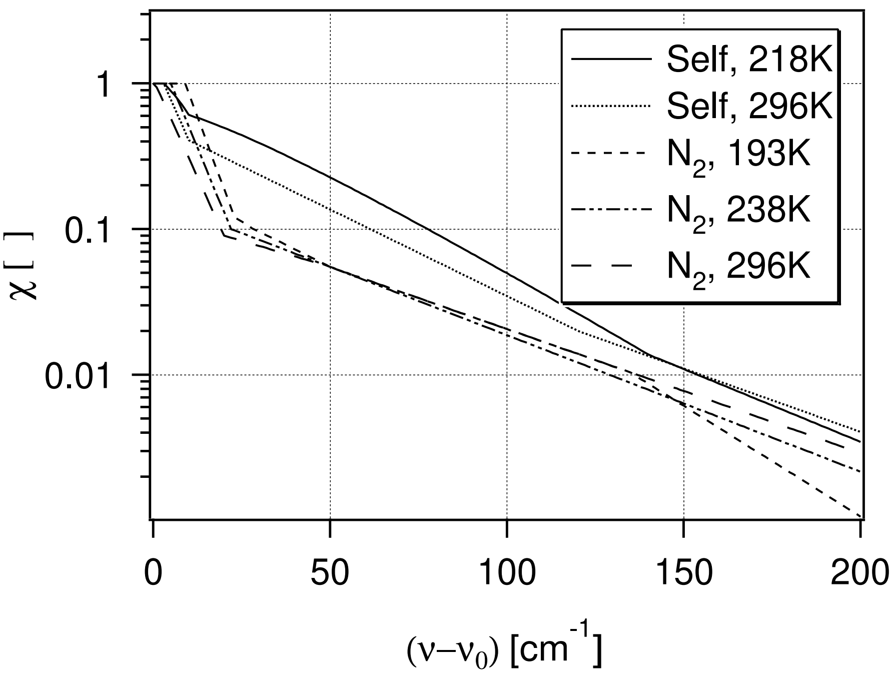

Figure 3.3: Self- and nitrogen-broadened 4.3μm χ-functions of Cousin *et.al.* Functional forms for these χ-functions are given in Table 3.1.

and the EGL models [40] and the ECS model [41, 42] have been implemented with varying success. The basic temperature and frequency dependencies of the absorption coefficients have been achieved. However, the resulting errors due to these models are much too large for remote-sounding applications, especially for low temperature samples which are most important for atmospheric temperature retrievals. The studies [41, 43, 44] conclude that duration-of-collision effects must be taken into account even in the microwindows.

Self-Broadened, 218K, χ =		
1	if	$000 \leq \|\nu - \nu_i\| < 003\mathrm{cm}^{-1}$
$1.169 - 0.0564\|\nu - \nu_i\|$		$003 \leq \|\nu - \nu_i\| < 010$
$0.68\frac{\|\nu-\nu_i\|}{28}\mathrm{K}_1\left(\frac{\|\nu-\nu_i\|}{28}\right)$		$010 \leq \|\nu - \nu_i\| < 140$
$0.345\mathrm{e}^{-\frac{\|\nu-\nu_i\|}{43.448}}$		$140 \leq \|\nu - \nu_i\|$
Self-Broadened, 296K, χ =		
1		$000 \leq \|\nu - \nu_i\| < 003$
$1.470\mathrm{e}^{-\frac{\|\nu-\nu_i\|}{7.782}}$		$003 \leq \|\nu - \nu_i\| < 010$
$0.535\mathrm{e}^{-\frac{\|\nu-\nu_i\|}{36.535}}$		$010 \leq \|\nu - \nu_i\| < 120$
$0.220\mathrm{e}^{-\frac{\|\nu-\nu_i\|}{50.063}}$		$120 \leq \|\nu - \nu_i\|$
N_2-Broadened, 193K, χ =		
1		$000 \leq \|\nu - \nu_i\| < 009$
$3.908\mathrm{e}^{-0.1514\|\nu-\nu_i\|}$		$009 \leq \|\nu - \nu_i\| < 023$
$0.207 - 3.778\mathrm{E} - 3\|\nu - \nu_i\|$		$023 \leq \|\nu - \nu_i\| < 028$
$0.219\mathrm{e}^{-0.0276\|\nu-\nu_i\|}$		$028 \leq \|\nu - \nu_i\| < 050$
$0.146\mathrm{e}^{-0.0196\|\nu-\nu_i\|}$		$050 \leq \|\nu - \nu_i\| < 135$
$1.164\mathrm{e}^{-0.0350\|\nu-\nu_i\|}$		$135 \leq \|\nu - \nu_i\|$
N_2-Broadened, 238K, χ =		
1		$000 \leq \|\nu - \nu_i\| < 005$
$1.968\mathrm{e}^{-0.1354\|\nu-\nu_i\|}$		$005 \leq \|\nu - \nu_i\| < 022$
$0.160\mathrm{e}^{-0.0214\|\nu-\nu_i\|}$		$022 \leq \|\nu - \nu_i\| < 050$
$0.162\mathrm{e}^{-0.0216\|\nu-\nu_i\|}$		$050 \leq \|\nu - \nu_i\|$
N_2-Broadened, 296K, χ =		
1		$000 \leq \|\nu - \nu_i\| < 0.5$
$1.064\mathrm{e}^{-0.1235\|\nu-\nu_i\|}$		$0.5 \leq \|\nu - \nu_i\| < 020$
$0.125\mathrm{e}^{-0.0164\|\nu-\nu_i\|}$		$020 \leq \|\nu - \nu_i\| < 050$
$0.146\mathrm{e}^{-0.0196\|\nu-\nu_i\|}$		$050 \leq \|\nu - \nu_i\|$

Table 3.1: Functional forms of Cousin *et.al.*'s ν_3 CO_2 χ-functions. (K_1 is a modified Bessel function of the first kind.)

3.3 A Lineshape Model for the 4.3μm Region

The lineshape proposed here takes into account the effects of both line-mixing and non-zero collision times. The line-mixing model follows the basic formalism developed by Smith [45] and Rosenkranz [46]. In this work, instead of doing involved calculations of the the relaxation rates as in [40–42], a simple model to approximate the rates is used. Non-zero collision times are modeled with Birnbaum's autocorrelation approach [47]. Least-squares fits to our observed spectra are then performed, varying the magnitude of the rates and the collision time with two parameters until the best agreement with the data is obtained.

The following section reviews the line-mixing formalism, which is (in principle) not specific to any spectral region or molecule. The application to the ν_3 $\Sigma \leftarrow \Sigma$ band of CO_2 is made in Section 3.3.1.2. Much of this is based on a model developed previously for $\Pi \leftarrow \Sigma$ and $\Pi \leftarrow \Delta$ Q-branches [33]; a review of which is given in Appendix B. The main point of this Appendix, with respect to this work, is that we can predict the rotational relaxation rates ($K_{jj'}$) which are responsible for line-mixing in $\Sigma \leftarrow \Sigma$ bands [1]. A way of treating non-zero collision times is then presented in Section 3.3.2. Lastly, in Section 3.3.3, the two effects, line-mixing and collision durations, are combined.

3.3.1 Line-Mixing Lineshape

Section 3.3.1.1 reviews the development of the basic line-mixing theory for infrared spectra. Section 3.3.1.2 then describes its application to the ν_3 band of CO_2.

3.3.1.1 General Theory

Deviations from the Lorentz lineshape in regions of overlapping spectral lines have been observed in many cases [48–52] . In particular, large deviations are found in infrared Q-branches, where the spectral lines are very closely spaced. Most attempts

[1]Using the notation presented later, this means we expect $\zeta = 1$.

[48, 50, 51, 53] to account for line-mixing have used the impact approximation. This simply means that the theory treats the collisions between molecules as instantaneous and will therefore be accurate only in spectral regions close to the line centers.

Within an ensemble of colliding molecules, a single molecule is not a conservative system. Through interactions with the other molecules, its internal energy can be transformed into other forms of energy throughout the ensemble. For this reason, if the system is defined as a single molecule, the energy of the system does not have to be conserved. Quantum mechanically, this means that the Hamiltonian of the system does not have to be Hermitian and the system can have imaginary energies. The total Hamiltonian of the molecule is given by $H(t) = H_0(t) + \mathcal{H}(t)$. In this expression, $H_0(t)$ is the Hamiltonian of the molecule without any interaction with its perturbers. $H_0(t)$ therefore has real eigenvalues and its eigenvectors are the stationary states of the molecule. $\mathcal{H}(t)$ is the Hamiltonian representing the interaction of the molecule with its perturbers. It could, for example, represent the effect of inelastic collisions. $\mathcal{H}(t)$ has energies which are partially imaginary.

Collision broadening is determined by the behavior of a molecule when making a transition between two known states. This implies that transitions should not be described by two independent functions which model each state separately, but by a wavefunction which represents the evolution from one state to another. This evolution is described by the evolution operator, $T(t)$. According to the Schroedinger equation, $T(t)$ is given by $e^{-\imath(H_0+\mathcal{H})\frac{t}{\hbar}}$. Let the initial and final states of a transition be given by Φ_i and Φ_f. Since both of these are stationary states of the molecule, they are solutions to $H_0\Phi = E_0\Phi$ and have totally real energies. For a transition of duration τ_t, which begins at time $t = 0$, the total wavefunction of the system at various times is:

$$\Psi(t = 0) = T(0)\Psi(0) \equiv \Phi_i \tag{3.2}$$

$$\Psi(0 \le t \le \tau_t) = T(t)\Phi_i = \Phi_i e^{-\imath(H_0+\mathcal{H})\frac{t}{\hbar}} \tag{3.3}$$

$$\Psi(t = \tau_t) = T(\tau_t)\Phi_i = \Phi_i e^{-\imath(H_0+\mathcal{H})\frac{\tau_t}{\hbar}} \equiv \Phi_f \tag{3.4}$$

Since $\mathcal{H}(t)$ has imaginary eigenvalues, $\Psi(t)$ is subject to a damping term which drains energy from the system, therefore allowing for absorption. To calculate the absorption coefficient from this model, the autocorrelation function of the electric dipole moment $\mu(t)$ is used. The autocorrelation of $\mu(t)$ is given by $\phi(t) =< \mu(0) \cdot \mu(t) >$, where $<>$ denotes a statistical average over the entire system. Because $\mu(t)$ has contributions from many different elements of the system, $\phi(t)$ will, in general, involve a complicated sum. The absorption coefficient is then calculated by taking the Fourier Transform of $\phi(t)$ [47]. An expression for the correlation of the electric dipole moment of this system over the duration of a transition is written as [53]

$$\phi(t) =< \mu(0) \cdot \mu(t) >= \sum_{if} \rho_i [< \Phi_i(0)|\mathbf{d}|\Phi_f(0) > \cdot < \Phi_f(t)|\mathbf{d}|\Phi_i(t) >] \tag{3.5}$$

where the sum is taken over all possible states. $\mathbf{d}$ is the dipole moment operator of the system and ρ is the density matrix, which is related to the relative population of states and is assumed to be constant during a transition. Substituting the evolution operator into this expression, the time dependence of the correlation function is obtained. It is here that the impact approximation must be made. This allows the interaction Hamiltonian, $\mathcal{H}(t)$, which is generally a fluctuating, time-dependent interaction, to be represented by an effective constant interaction [53]. Since $\mathcal{H}$ is taken to be a constant in time, its effect on the correlation function is greatly simplified. If this assumption were not made, the time dependence of $\mathcal{H}$ would be required. Instead, only the "time-averaged" interaction is needed and the details of its time dependence are ignored. With this approximation, the lineshape is then calculated by taking the Fourier transform of $\phi(t)$. Baranger [53] calculated the lineshape to be

$$k_{mix}(\nu) = \frac{\rho}{\pi} \mathbf{IM} \left(\sum_i < \Phi_i|[D(\nu - H_0 - \mathcal{H})^{-1}]|\Phi_i > \right) \tag{3.6}$$

where the sum is over all initial states and $D = \sum_f \mathbf{d}|\Phi_f >< \Phi_f|\mathbf{d}$. If $\mathcal{H}$ is diagonal, with diagonal elements of $\imath\gamma_j$, where γ_j are the Lorentz widths of the spectral lines, the resulting lineshape is the sum of many Lorentzians:

$$k(\nu) = \sum_j \frac{d_j^2 \rho_j \, \gamma_j}{(\nu - \nu_0)^2 + \gamma_j^2} \tag{3.7}$$

where $d_j^2 \rho_j$ is essentially the line strength. This Lorentzian result shows that the model obeys the impact approximation. It also demonstrates the role of the off-diagonal elements of the interaction potential – they are the cause of interaction between spectral transitions. If the off-diagonal elements of $\mathcal{H}$ are non-zero, intensity can be transferred from one line to another, with the “amount” of line-mixing determined by the magnitude of the corresponding off-diagonal element of $\mathcal{H}$. This is why the phenomenon is often called line-mixing. Thus, a vibration-rotation band cannot be regarded as the simple sum of individual transitions, but must be treated as a complex interacting system. The interaction, which is discussed later, is provided by a bath of inelastic collisions. Inelastic collisions between an absorbing molecule and a perturber can cause the the absorber to gain or lose rotational energy. If this process occurs while a transition is occurring, it is possible that intensity is transferred from one spectral line to another.

The line-mixing absorption coefficient was re-written in doubled-state form better suited for computation of infrared spectra by E. W. Smith [45]. If the eigenvalues of H_0 are the line center frequencies (energy and frequency are used interchangeably here) and the interaction, $\mathcal{H}$, is linearly proportional to the pressure P (binary collisions), $k_{mix}(\nu)$ can be re-written as [25, 45, 54]

$$k_{mix}(\nu) = \frac{N}{\pi} \mathbf{IM} \left(\sum_{j,k} d_j \ll j \mid [(\nu - \nu_0) - \imath P\mathbf{W}]^{-1} \mid k \gg d_k \rho_k \right) \tag{3.8}$$

where N is the molecular density of absorbers, d_j and d_k are the dipole moment matrix elements corresponding to the radiative transitions $|j \gg$ and $|k \gg$, ν is a diagonal matrix with $\ll j|\nu|k \gg = \nu\delta_{jk}$, ρ_k is a density matrix element that represents the population difference between the upper and lower levels of the transition $|k \gg$, and P is the gas pressure. **W** is the relaxation, or interaction, matrix with off-diagonal elements, $W_{j,k}(j \neq k)$, representing the rate, or magnitude, at which collisions transfer intensity from line k to j and its diagonal elements, $W_{j,j}$, representing the line widths of line $|j>>$.

Calculating an absorption coefficient for many transitions over a large spectral range using Equation 3.8 involves the inversion of a large matrix for each desired frequency. For this reason, $k_{mix}(\nu)$ was re-written as [55]

$$k_{mix}(\nu) = \frac{N}{\pi}\mathbf{IM}\left(\mathbf{d}\cdot\mathbf{G}(\nu)^{-1}\cdot\rho\cdot\mathbf{d}\right) \tag{3.9}$$

where $\mathbf{G} = \nu - \mathbf{H}$ and $\mathbf{H} = \nu_0 + \imath P\mathbf{W}$. $\mathbf{H}$ is diagonalized with a complex matrix $\mathbf{A}$ to get the diagonal matrix $\mathbf{L} = \mathbf{A}^{-1}\cdot\mathbf{H}\cdot\mathbf{A}$. $\mathbf{G}$ is also diagonalized by $\mathbf{A}$ and $k_{mix}(\nu)$ is written as

$$k_{mix}(\nu) = \frac{N}{\pi}\mathbf{IM}\left(\sum_i \frac{(\mathbf{d}\cdot\mathbf{A})_i(\mathbf{A}^{-1}\cdot\rho\cdot\mathbf{d})_i}{\nu - l_i}\right) \tag{3.10}$$

where l_i are the diagonal elements of $\mathbf{L}$. In this form, the calculation of the absorption coefficient requires only one matrix inversion.

Using time-independent perturbation theory, the second order energy correction for an interaction potential, H_1, is given by $\sum_{m\neq k}\frac{|(\Phi_k,H_1\Phi_m)|^2}{E_k-E_m}$. Following this approach, and assuming that $PW_{jk}/(\nu_j-\nu_k)$ is small for all lines, Rosenkranz found the first-order approximation for $k_{mix}(\nu)$ to be [46, 56]

$$k_{1st}(\nu) = \frac{N}{\pi}\sum_j S_j\left(\frac{P\gamma_j + (\nu-\nu_j)PY_j}{(\nu-\nu_j)^2 + (P\gamma_j)^2}\right) \quad \text{with} \quad Y_j = 2\sum_{k\neq j}\frac{d_k}{d_j}\frac{W_{kj}}{\nu_j-\nu_k} \tag{3.11}$$

where Y_j are first-order mixing coefficients. For a single transition, this lineshape is the sum of a Lorentzian and an asymmetric term. Far from the line centers, the asymmetric terms become proportional to ν^{-1}. In order for $k_{1st}(\nu)$ to go to zero in these regions, the sum of the coefficients must vanish. That is, detailed balance must be obeyed. In this context, Strow and Reuter [28] showed that detailed balance is obeyed if

$$\sum_j S_j Y_j = 0. \tag{3.12}$$

They also used this result to show that, in the far-wing limit, the ratio of mixing and

Lorentz absorption coefficients is a constant [28]:[2]

$$\frac{k_{1st}}{k_L} = 1 + \frac{\sum_j S_j Y_j \nu_j}{\sum_j S_j \gamma_j} \tag{3.13}$$

This is a useful result because it allows the mixing lineshape to be calculated by simply multiplying the Lorentz lineshape by a constant in the far wing. $k_{1st}(\nu)$ is also useful because it provides a compact form for expressing the effects of line mixing. The amount of line mixing for a single line can be represented by the magnitude of the first-order mixing coefficients. Thus, lines which experience a large amount of mixing will have Y's of large magnitude and those which are Lorentzian will have Y's which are zero. The accuracy of the first order mixing absorption coefficient decreases with pressure. The largest errors in first-order mixing occur in spectral regions where lines overlap significantly. As long as this overlap is not too great or as long as the spectral region of interest is in the far-wing, however, the first-order approximation is accurate.

The only point left to be addressed is the determination of the off-diagonal, or mixing, terms of **W**. Direct calculations of these terms are very complex, involving a detailed knowledge of the intermolecular potentials and energy transfer during a collision. More often, empirical scaling laws based on energy changes caused by inelastic collisions are used to model the interactions. Several of these laws have been developed to model collisions for rotational-vibrational transitions, one of which is the exponential power energy-gap, or PEG scaling law. The PEG law models the energetically upward state-to-state inelastic collisional rates as a function of the rotational energy difference, $\Delta E_{j'j}$. An upward rate going from the state j to state j' is modeled as

$$K_{j'j} = a_1 \left(\frac{\mid \Delta E_{j'j} \mid}{B_0} \right)^{-a_2} \exp\left(\frac{-a_3 \mid \Delta E_{j'j} \mid}{kT} \right) \tag{3.14}$$

where B_0 is the rotational constant and a_1, a_2, and a_3 are adjustable parameters which are discussed below. Other similar scaling laws are also employed. They include the modified exponential energy-gap, or MEG scaling law and the ECSL law [57, 58]. All of

[2]The ratio of k_{mix} to Lorentz is also a constant in the far-wing.

these methods have shown to give similar results as the PEG law [59]. A more realistic model would not only depend on the energy difference between two levels, but would include rotational and vibrational factors as well.

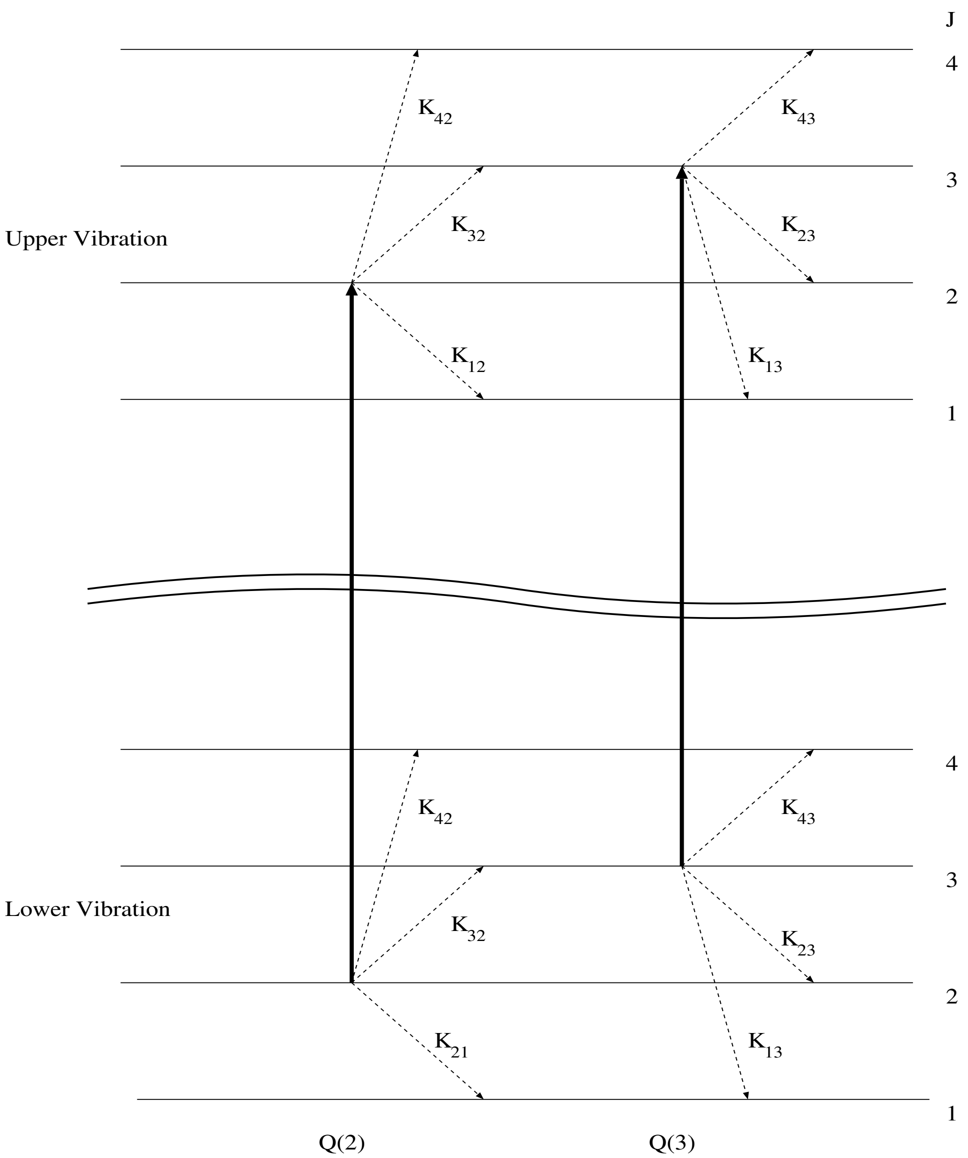

Figure 3.4: Inelastic collisional rates for the J=2 and J=3 Q-branch lines of a $\Pi^- \leftarrow \Pi^+$ band. For line-mixing to occur between Q_2 and Q_3, K_{32} (or K_{23}) must occur in both upper and lower vibrations.

Detailed balance is obeyed if

$$K_{jj'}(2j'+1)e^{-\frac{E_{j'}}{kT}} = K_{j'j}(2j+1)e^{-\frac{E_j}{kT}} \tag{3.15}$$

This relation essentially ensures that energy is conserved and gives the downward rates, $K_{jj'}$:

$$K_{jj'} = \frac{2j+1}{2j'+1}e^{\frac{\Delta E}{kT}} \tag{3.16}$$

a_1, a_2, and a_3 of Equation 3.14 are determined by equating the width of a spectral line to the sum of all of the rates which limit the lifetime of that transition via a least-square fit to the known linewidths [33]. This is based simply on the fact that any rates which shorten the molecule's lifetime in a specific energy state broadens the spectral line. These rates include all of those which occur in either the lower or upper state of the transition. Since vibrational energies are much greater than rotational energies, only collisions between states within the same vibrational level are considered. Therefore, using line widths extracted from experimental data, a_1, a_2, and a_3 are determined by requiring

$$\gamma_j \equiv \mathbf{W_{jj}} = \sum_{j' \neq j} \text{All } K_{j'j} \text{ which limit the transition lifetime.} \tag{3.17}$$

This is obviously not the exact expression used in calculations; its details depend on the type of transition which is occurring. This is detailed later when specific symmetries are investigated. Equation 3.17 is valid only if elastic reorientation collisions and vibrational relaxations do not contribute significantly to the widths, which appears to be valid for CO_2-X systems.

The off-diagonal elements of **W** are then taken to be proportional to the corresponding collisional rates of **K**. These are the mixing terms. For two rotational levels which are energetically close, the collisional rate between them is relatively large and they experience mixing. On the other hand, if two levels are energetically far from each other, the corresponding **K** rates are negligible and no mixing occurs.

In order for line-mixing to occur, collisions which connect two spectral lines must

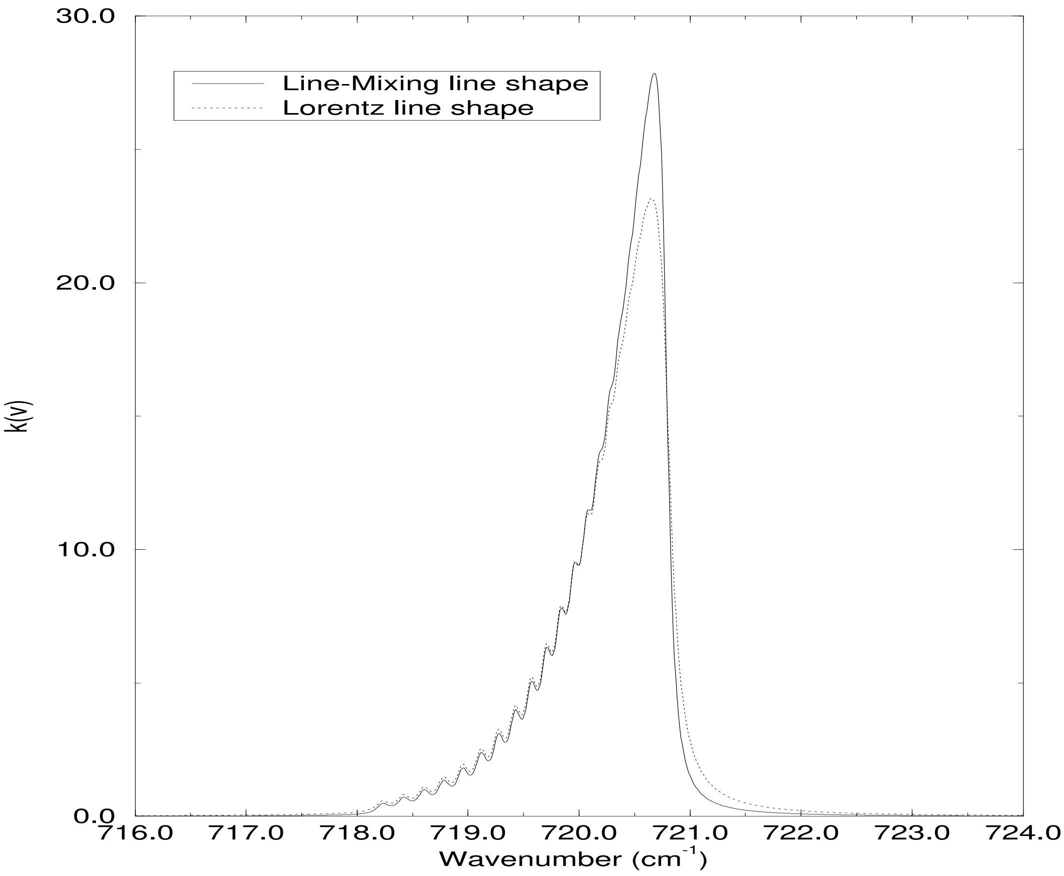

Figure 3.5: A Lorentz calculation and a line mixing calculation for a $\Sigma \leftarrow \Pi$ Q-branch at atmospheric pressures. Line mixing has an overall effect of "narrowing" the observed transmission. That is, increased absorption at the center of the Q-branch and decreased absorption in the wings. P(CO_2)=20 Torr, P(N_2)=740 Torr, T=296 K.

occur in both the upper and lower vibrational states. If, for example, inelastic collisions occurred in only the upper vibrational state, the only effect would be to limit the transition lifetime, and therefore increase the line width. This point is significant for cases in which the collision rates in the upper and lower vibrational states are not equal.

Summarizing the calculational procedures, the relaxation rates, $K_{jj'}$, are first determined by adjusting a_1, a_2, and a_3 so that the sum of all relaxation rates which limit the lifetime of a transition equals the known line width. This is done using an equation similar to Equation 3.17. The off-diagonal elements of **W** are then taken to be proportional to the corresponding off-diagonal elements of **K**. The details of this step depend on the symmetry of the band and is discussed in Section 3.3.1.2. The diagonal elements of **W** are equated to the line widths. The absorption coefficients are then calculated using full- (k_{mix}, Equation 3.10) or first- (k_{1st}, Equation 3.11) order mixing. This procedure is incorporated into a least-squares fitting algorithm in which an adjustable parameter that controls the magnitude of the off-diagonal mixing terms of **W** is adjusted to obtain optimum agreement with measured spectra. This process is described in more detail in Section 3.5.

3.3.1.2 Application to the ν_3 fundamental

Application of the general line-mixing theory to the ν_3 band of CO_2 is presented here. The development of **W** for the ν_3 $\Sigma \leftarrow \Sigma$ band follows our earlier work for several types of CO_2 Q-branches. By studying Q-branches of different symmetries, we gained useful insight into how an accurate **W** is developed. For this reason, a review of the line-mixing theory for CO_2 Q-branches is presented in Appendix B.

As in Sections B.1 and B.2, the details of **W** depend on the type of transition which is occurring. For $\Pi - \Sigma$ and $\Pi - \Delta$ Q-branches, a generalized model was developed [33,60–62] to treat the rotational relaxation in a consistent manner. This model differentiates the relaxation rates which connect energy levels of similar rotational symmetry from those which connect levels of opposite symmetry by introduction of the "β" factor. For example, we find β=0.5 for self-broadened CO_2, implying that when two CO_2 molecules collide, they are equally likely to keep their original rotational symmetry or switch to the opposite rotational symmetry. For N_2-broadened CO_2, we find β=0.61 in Π vibrations and β=0.89 in Δ vibrations, implying that when a CO_2 molecule collides with N_2, it is more likely to retain its original rotational symmetry. Adopting these values greatly improves the agreement with measured spectra.

For the P and R- branches of $\Sigma - \Sigma$ bands, however, the situation is less complicated.

Figure 3.6 depicts the energy levels and relaxation rates for a $\Sigma \leftarrow \Sigma$ band. Due to symmetry requirements, only even J rotational levels exist in the lower state and only odd J levels in the upper state of the fundamental ν_3 band. As a result, there are no relaxation rates between energy levels of opposite rotational symmetry in either upper or lower vibrational state. In other words, following the approach used for the Q-branches, we expect $\beta = 1$ in Σ vibrations. In this case, the sum rule equating the sum of all relaxations which limit the lifetime of a transition to its line width is given by

$$\mathrm{W}_{jj} = \gamma_{RJ} = \frac{1}{2}\left(\sum_{j' \neq j}^{\text{even}} K_{j'j}^{\Sigma^+(e \leftarrow e)} + \sum_{j' \neq j+1}^{\text{odd}} K_{j'j+1}^{\Sigma^-(f \leftarrow f)}\right) \tag{3.18}$$

for R-branch lines and

$$\mathrm{W}_{jj} = \gamma_{PJ} = \frac{1}{2}\left(\sum_{j' \neq j}^{\text{even}} \mathrm{K}_{j'j}^{\Sigma^+(e \leftarrow e)} + \sum_{j' \neq j-1}^{\text{odd}} \mathrm{K}_{j'j-1}^{\Sigma^-(f \leftarrow f)}\right) \tag{3.19}$$

for P-Branch lines. $K_{j'j}$ are again given by the PEG scaling law (Equation 3.14). Superscripts on K have been included to denote the vibrational state and rotational symmetry (e for even, f for odd) of the involved energy levels. The off-diagonal elements of **W** are taken to be

$$\mathrm{W}_{j'j} = -\zeta \mathrm{K}_{j'j} \tag{3.20}$$

where ζ is introduced as a single adjustable parameter to control the magnitude of line-mixing. Based on the model used for $\Pi - \Sigma$ and $\Pi - \Delta$ Q-branches, ζ should be approximately 1 if $K_{j'j}$ are well represented by the scaling law [33, 60, 61]. For line-mixing calculations, mixing is included for inter-P-branch and inter-R-branch mixing, but not for mixing between the P and R-branches, which are well separated in frequency.

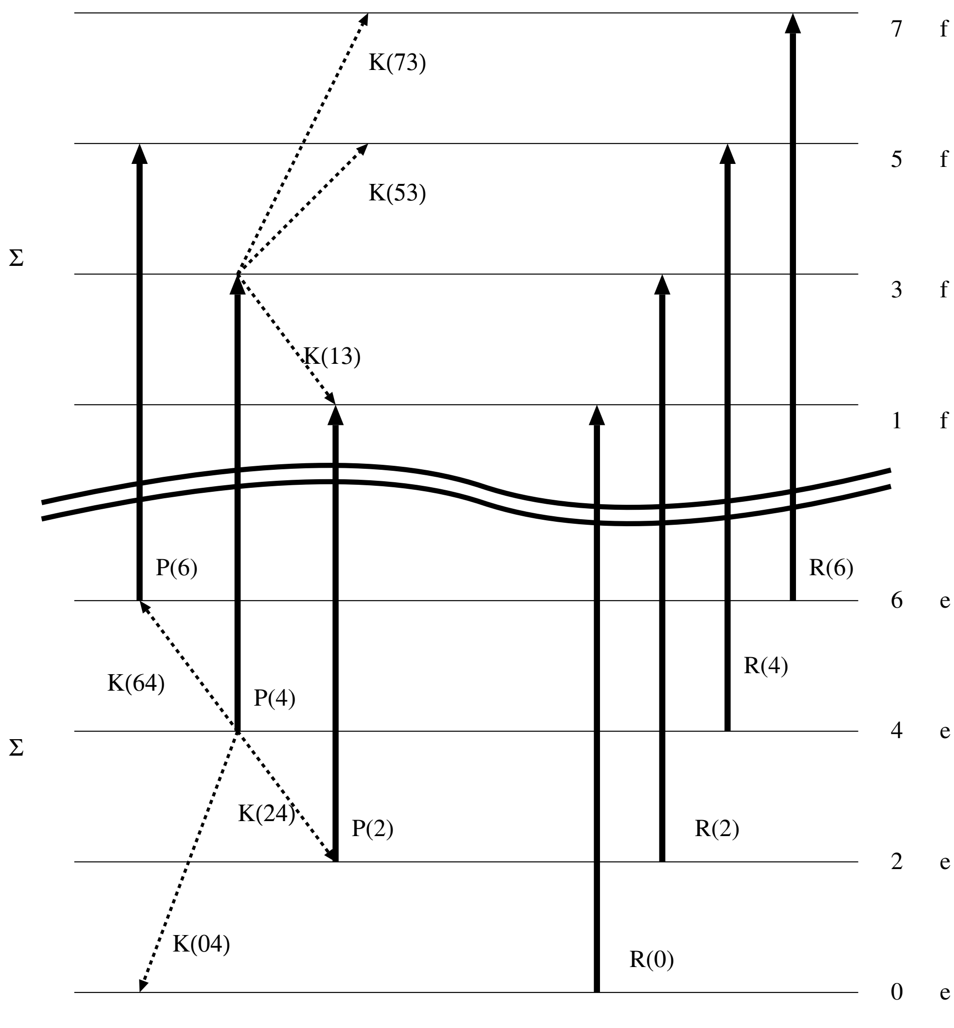

Figure 3.6: Energy level structure and rotational relaxation rates, $K_{j'j}$, for a $\Sigma \leftarrow \Sigma$ transition. Because Σ vibrations (ℓ=0) consist of rotational levels of like symmetry, the effective β factor is 1. i.e. there can be no relaxations to energy levels of opposite symmetry because they do not exist.

3.3.2 Duration-of-Collision Effects

In addition to ignoring the effects of line mixing, the Lorentz model is inaccurate because it is based on the impact approximation. That is, the duration of the interaction between two colliding molecules is assumed to be negligible. Therefore, the Lorentz lineshape is too large at frequencies far from the line centers. A more accurate model treats the molecules as softer charge distributions with collisions therefore having finite durations. Just how long the collisions last is difficult to determine, but depends on how the molecular potentials interact during a collision. Assuming that the collisions have a finite duration eliminates the need for instantaneous derivatives in the temporal wave function and therefore decreases the high frequency components of the spectral distribution. This effect is shown in Figure 3.7.

This problem is approached by determining the behavior of the dipole moment during the collision. Birnbaum developed a theory using a versatile empirical correlation function [63, 64] with known short and long time behavior and derived expressions for the absorption coefficient as a function of frequency for spectral transitions whose levels are perturbed by collisions. A flexible model was used:

$$\phi(t) =< \mu(0) \cdot \mu(t) >= \exp\left(\frac{\tau_{dur} - (\tau_{dur}^2 + y^2)^{\frac{1}{2}}}{\tau_{col}}\right) \tag{3.21}$$

with $y = (t^2 - \imath 2\tau_0 t)^{1/2}$ and $\tau_0 = \frac{\hbar}{2kT}$. τ_{dur} represents the mean duration of collisions and τ_{col} is the mean time between collisions. The lineshape function is then determined by Fourier analysis of $\phi(t)$. At long times, Equation 3.21 reduces to $\exp\left([\tau_{dur} \pm \imath\tau_0 - |t|]\tau_{col}^{-1}\right)$ and the resulting line shape is Lorentzian with a width of τ_{col}^{-1}. In terms of the Lorentz shape ($k_L(\nu)$), a lineshape representing an average collision duration of τ_2 is given by [29]

$$k_B(\nu) = k_L(\nu)\chi_B(\nu) = k_L(\nu)A_m z K_1(z)\exp\left(\tau_2\gamma_j + \tau_0\Delta\nu\right) \tag{3.22}$$

with

$$z = \sqrt{(\gamma_j^2 + \Delta\nu^2)(\tau_0^2 + \tau_2^2)} \text{ and } \Delta\nu = \nu - \nu_j \tag{3.23}$$

where $K_1(z)$ is a modified Bessel function of the second kind, $\tau_0 = \frac{0.72}{T}$ [3], and A$_m$ is a constant representing the effect of line-mixing far from band center. χ_B is independent of vibrational band except for the mixing factor A_m. Although τ_2 is expected to decrease with increasing temperature [64], no explicit temperature dependence is included in this application.

This "corrective" factor, $\chi_B(\nu)$, for the Lorentz line shape removes much of the far-wing absorption due inherently to the impact approximation. Since we are essentially multiplying two line shapes, this can be seen as taking the convolution of the Lorentzian wave train with the correlation function.

3.3.3 Combined Line-Mixing and Duration-of-Collision Lineshape

Both line-mixing and the duration-of-collision effect have shown to reduce the amount of absorption in the far-wing limit. Since the line-mixing theory is valid only under the impact approximation, the combined effects of line-mixing and duration-of-collision are approximated as if each effect were independent. In order to include the effects of line-mixing over the entire frequency range, $k_L(\nu)A_m$ in Equation (3.22) is replaced by the first order mixing absorption coefficient:

$$k(\nu) = \sum_i k_{1st}(\nu_i, \nu)\chi_B(\nu_i, \nu). \tag{3.24}$$

This represents the proposed lineshape model. The full line-mixing lineshape $k_{mix}(\nu)$ can also be implemented by using $k(\nu) = \frac{k_{mix}(\nu)}{\sum_i k_{Lor}(\nu_i,\nu)} \sum_i k_{Lor}(\nu_i, \nu)\chi_B(\nu_i, \nu)$ if the first-order approximation is too inaccurate (which is seldom true for atmospheric applications).

To show the sub-Lorentzian nature of this lineshape, ratios to the Lorentz profile are shown in Figure 3.8. Far from the ν_3 band center, line-mixing has the overall effect of scaling the Lorentzian profile by a constant, approximately 0.10. Also in the far-wing, χ_B is well approximated by a decaying exponential. One obvious result of these

[3] τ_0 and τ_2 have been converted to units of cm by multiplication by 2πc.

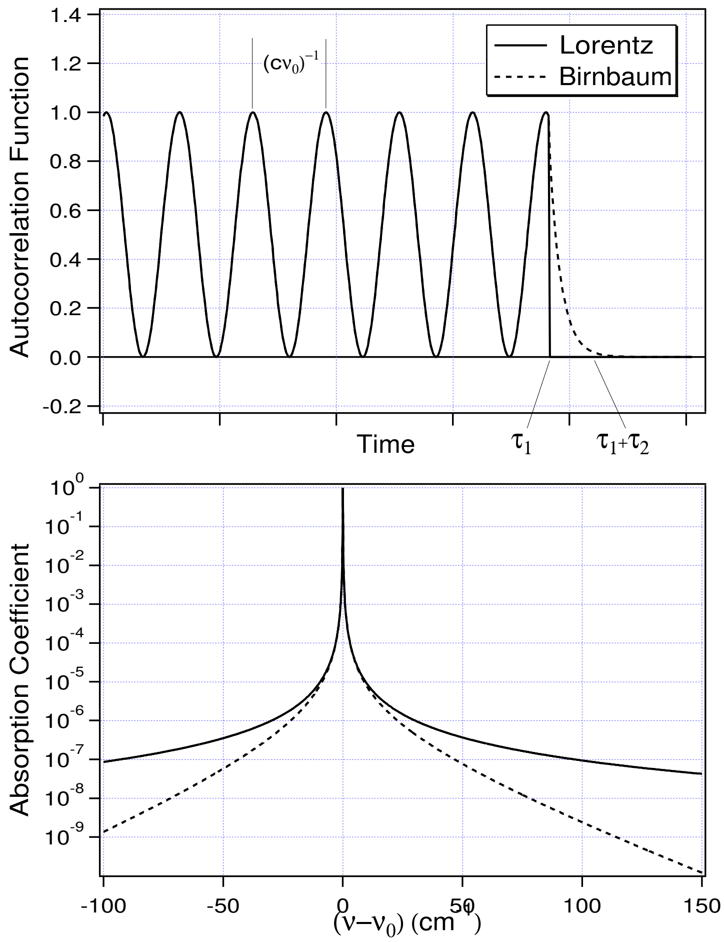

Figure 3.7: A cartoon (top panel) illustrating the Lorentz (solid curve) and finite duration-of-collision (dashed curve) models of the time development of the dipole moment autocorrelation function when a collision occurs. τ_1 is the time between collisions and τ_2 is the collision duration. The bottom panel shows the resulting lineshapes with the durations-of-collisions model computed with τ_2/τ_1=0.015.

calculations is that line-mixing is responsible for the majority of the observed sub-Lorentz behavior directly beyond the band-head.

Summarizing, Equation 3.24 represents the proposed lineshape model. It includes both line-mixing and duration-of-collision effects – the two phenomenon responsible for nearly all deviations from Lorentz lineshape behavior in CO_2. Because the variables

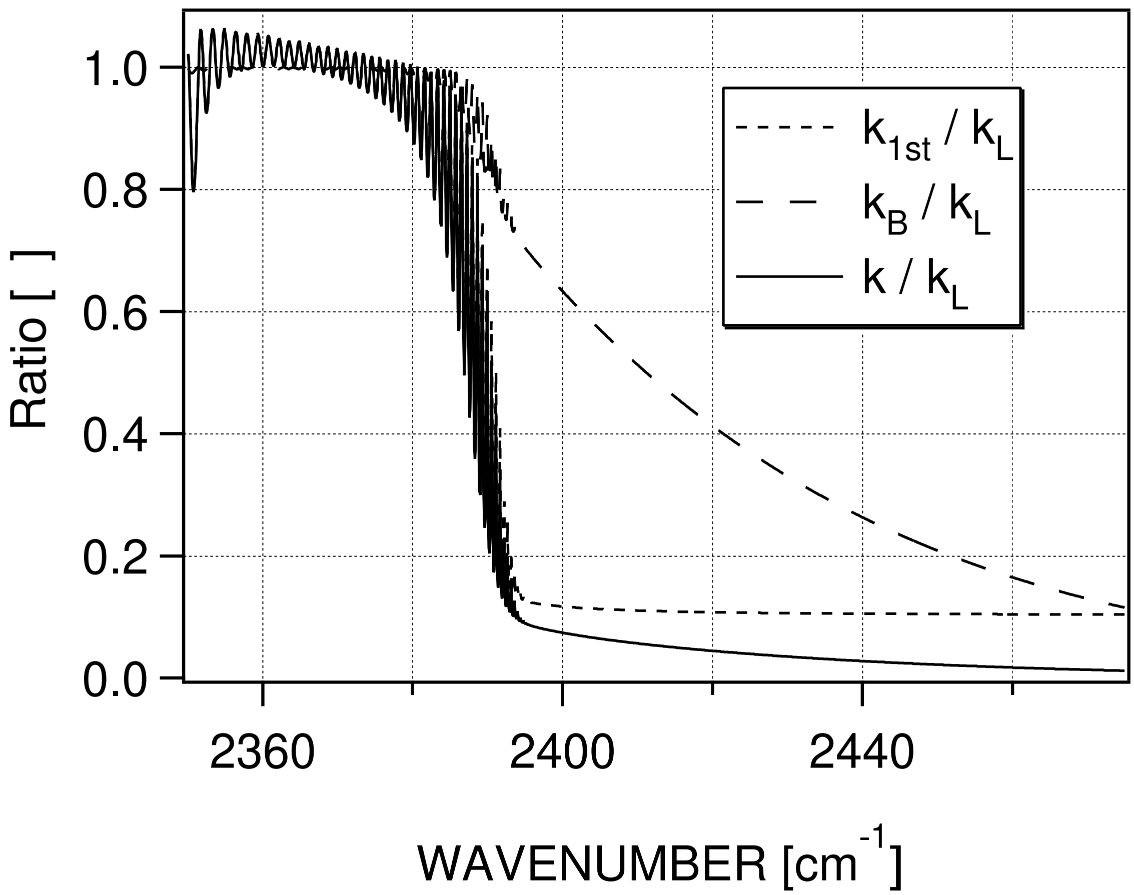

Figure 3.8: Ratios of the line-mixing (Equation 3.11), duration-of-collision (Equation 3.22), and combined (Equation 3.24) absorption coefficients to Lorentz for the fundamental ν_3 R-branch computed using ζ=1 and τ_2=0.0275. In the far wing, the ratios of line-mixing to Lorentz is a constant while the finite duration-of-collision effect leads to a decaying exponential.

ζ and τ_2 are built into the model, it is capable of producing a wide range of lineshape behavior. If, for example, ζ and τ_2 are set equal to zero, the resulting lineshapes are Lorentzian, while if $\zeta = 1$ and $\tau_2 \gg 0$, the resulting lineshape is extremely sub-Lorentzian in the far-wing. The goal then is to use this model to (1) obtain optimum agreement with measured transmission spectra by adjusting ζ (amount of line-mixing) and τ_2 (mean collision duration) and (2) infer information about the mechanisms responsible for the observed lineshapes from the fitted values of ζ and τ_2. The experimental spectra used for this are described in the next section. Details concerning the calculations and least squares fitting technique are presented in Section 3.5.

3.4 Measured Spectra

Spectra were provided by J. W. C. Johns of the Herzberg Institute of Astrophysics at the National Research Institute of Canada. Self- and nitrogen-broadened transmission spectra were recorded using a modified BOMEM Fourier transform spectrometer and a long path gas cell [65]. All spectra were recorded at an unapodized resolution of $\sim$0.01 cm^{-1}. This resolution is high enough that all of the lines are fully resolved for the experimental conditions used here. An instrument function was therefore not necessary to introduce into the data analysis. Experimental parameters for the available spectra are shown in Table 3.4. Most runs extend beyond $\sim$2450 cm^{-1} in order to obtain background runs in regions were there is relatively low absorption, resulting in more accurate 0% and 100% baselines. All data were used as they were recorded with the interferometer and have not been massaged in any way.

P_{CO_2}	P_{N_2}	L.(m)	T(K)	T_{fitted}(K)†	Region (cm^{-1})
00.77	751.8	8.00	297.0	296.61	2350–2400
38.04	723.5	24.00	297.0	297.91	2350–2500
38.04	723.5	72.00	297.0	297.79	2350–2550
38.04	723.5	8.00	297.0	297.40	2350–2475
1.90	378.5	16.00	219.6	219.57	2350–2450
1.07	101.0	16.00	219.2	215.26	2350–2450
760.60	0.0	8.00	295.0	No Fit	2350–2600
741.00	0.0	0.15	300.0	299.52	2385–2420
370.00	0.0	0.15	300.0	299.19	2380–2410
100.00	0.0	0.15	300.0	299.57	2370–2390

Table 3.2: Measured transmission spectra. All pressures given in torr. †:Determined by least-squares fits to unsaturated lines at the R-branch band-head.

The quoted temperatures near 296K have errors of about $\pm$1K. At lower temperatures, the errors are slightly larger, perhaps $\pm$2K. Due to the sensitivity of these spectra to varying temperature, the temperatures were determined directly from the spectra using several unsaturated lines at the R-branch band head. This was carried out using a non-linear least squares fit of these local lines to Lorentzian profiles, letting the temperature float as an adjustable parameter. In addition, a second order polynomial (as a function of wavenumber) was used as the background absorption and was also allowed to float. Note that these fits only cover a narrow wavenumber range, nominally $\sim 0.75\ \text{cm}^{-1}$. The lines were fit to the noise level of the data. Fitted temperatures are listed in Table 3.4.

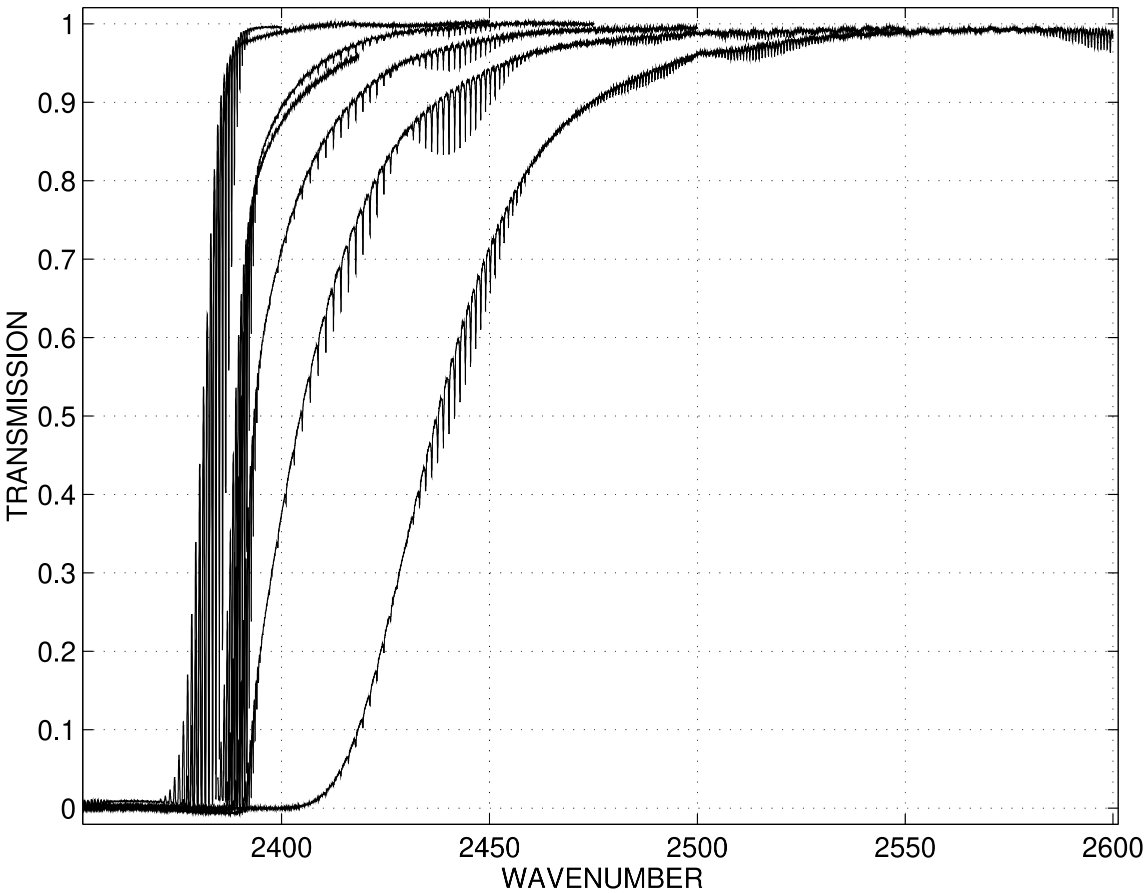

Figure 3.9: Several of the measured transmission spectra listed in Table 3.4.

3.5 Calculations and Least-Squares Fits for the 4.3μm Region

This section describes the calculations and least squares fits which have been performed for the proposed lineshape model. It discusses the details of how the calculations were performed and also the accuracy and limitations of the results. A "global" model in which all of the spectra are treated consistently is also presented.

3.5.1 General Considerations

Calculations have been performed using the lineshape models described in Sections 3.2.2 and 3.3 for the data listed in Table 3.4. All calculations have been performed by summing over the various lineshape profiles using all CO_2 lines between 2200 and 2500 cm^{-1} in the 1992 HITRAN database. While this amounts to approximately 13,000 individual spectral lines, over 90% of the total intensity is due to only ~100 main isotope lines of the fundamental ν_3 band. Nevertheless, the absorption due to the other 10% of the lines, if not treated consistently, can cause problem in the data analysis for the required accuracies. This was illustrated in Figure 3.2. To reduce computing time and to avoid an ill-posed problem, line-mixing and duration-of-collision effects have been included for only the strongest bands. Table 3.5.1 lists these bands and their percent contribution to the total intensity in this region. Together, these bands account for ~99.50% of the total intensity of all lines considered. For bands not listed in the table, a Voigt profile is used. Line-mixing in $\Pi \leftarrow \Pi$ and $\Delta \leftarrow \Delta$ bands is treated the same as for $\Sigma \leftarrow \Sigma$ bands, except considerations are taken to account for the missing lowest J rotational levels.

The spectral lines of this region are shown in Figure 3.10. In addition, the half-widths and pressure-induced frequency shifts of the ν_3 fundamental are shown in Figure 3.11. The HITRAN strengths are primarily based on the work of L. S. Rothman, R. L. Hawkins, and R. B. Wattson [66]. The errors in these strengths are probably somewhere between 1–3%. The widths are also from HITRAN and are based on the work R.

Band	Symmetry	Species	% Absorption †
00011← 00001	$\Sigma \leftarrow \Sigma$	$C^{16}O_2$	90.99
00011← 00001	$\Sigma \leftarrow \Sigma$	$C^{18}O_2$	0.93
01111← 01101	$\Pi \leftarrow \Pi$	$C^{16}O_2$	6.51
01111← 01101	$\Pi \leftarrow \Pi$	$C^{18}O_2$	0.53
02211← 02201	$\Delta \leftarrow \Delta$	$C^{16}O_2$	0.26
10012← 10002	$\Sigma \leftarrow \Sigma$	$C^{16}O_2$	0.17
10011← 10001	$\Sigma \leftarrow \Sigma$	$C^{16}O_2$	0.10

Table 3.3: The bands for which line-mixing and duration-of-collision effects are included in the calculations. †: These values represent the total band strength divided by the total intensity for all lines from 2200 to 2500 cm^{-1}.

R. Gamache, L. Rosenmann, and J. -M. Hartmann [67]. Errors in the widths are on the order of 5% or slightly smaller.

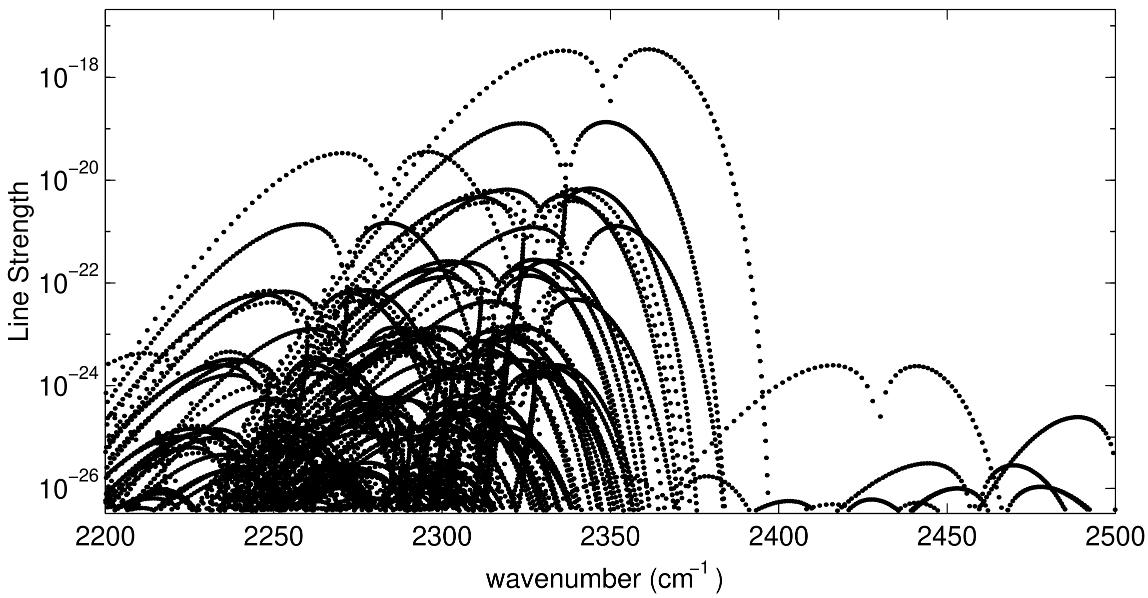

Figure 3.10: The spectral lines of CO_2 in the 4μm region. Along with the ν_3 fundamental centered at 2350 cm^{-1} are many other hot bands, combination bands, as well as many bands of $C^{18}O_2$ and $C^{17}O_2$.

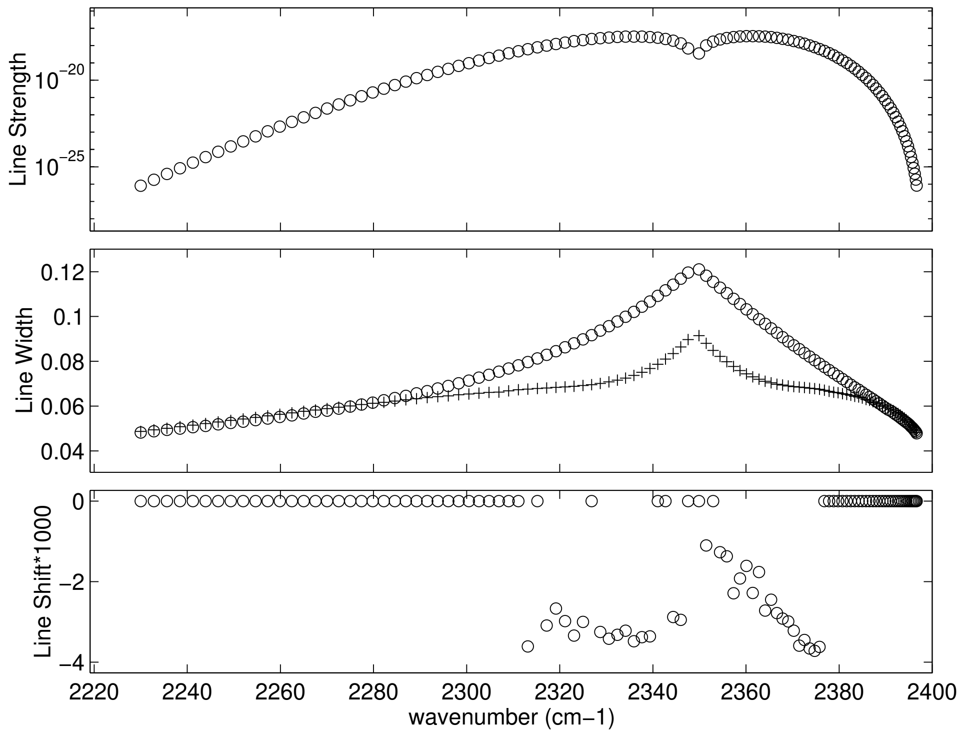

Figure 3.11: Spectral line parameters of the ν_3 fundamental. The top panel shows the line strengths and line positions. The middle panel shows the self- (circles) and nitrogen- (x's) broadened halfwidths, given in (cm^{-1}/atm) and the bottom panel displays the pressure induced line center shifts also in (cm^{-1}/atm).

3.5.2 Least-squares Fits for ζ and τ_2

As described in section 3.3, ζ is used as a multiplier of the mixing terms of the relaxation matrix **W** and τ_2 represents the average collision duration. After determining the relaxation rates, $K_{j'j}$, by adjusting a_1, a_2, and a_3 via non-linear least squares to satisfy Equations 3.18 and 3.19, absorption coefficients are calculated using the proposed lineshape (Equation 3.24) for desired values of ζ and τ_2. Calculated spectra show high sensitivity to ζ and τ_2. This is illustrated by the fact that if these parameters are set to zero, the resulting lineshape is Lorentzian, which clearly overestimates the absorption. To obtain the best obtainable agreement with the observed spectra and to fine-tune our models, non-linear least-squares fits to the data were performed, letting ζ and τ_2 float as adjustable parameters. This required an iterative approach where a fit for the parameters was performed by varying them only for the ν_3 fundamental P- and R-branches of $C^{16}O_2$, and then recalculating the contributions for the weaker bands with these new estimated parameters, and iterating again until the calculations converged. Convergence typically requires 3 or 4 iterations. Initial values of ζ and τ_2 are 1 (based on the Q-branch studies) and 0.0275 (based on Birnbaum's single line fit [64]), respectively. This method was followed for each measured spectrum using a Levenberg-Marquardt fitting algorithm. Results of these fits are listed in Table 3.5.2 and sample calculations are shown in Figures 3.12 through 3.14. For a nitrogen-broadened spectrum, the effective parameters scale as a function of the partial pressures; i.e. $\zeta = \frac{P_{CO_2}\zeta_{CO_2}+P_{N_2}\zeta_{N_2}}{P_{Total}}$.

File #	P(CO_2)	P(N_2)	P.L.(m)	T(K)	ζ	τ_2 (cm)
1	00.77	751.8	8	292.42	8.84e-01	6.49e-03
2	38.04	723.5	24	295.75	9.71e-01	4.33e-03
3	38.04	723.5	72	296.15	1.00e+00	3.59e-03
4	38.04	723.5	8	297.43	9.44e-01	5.33e-03
5	1.90	378.5	16	217.51	9.14e-01	7.32e-03
6	1.07	101.0	16	214.42	1.16e+00	7.87e-05
7	760.60	0.0	8	297.01	6.98e-01	2.60e-02
8	741.00	0.0	0.15	296.79	7.40e-01	9.08e-03
9	370.00	0.0	0.15	296.41	7.47e-01	9.83e-03
10	100.00	0.0	0.15	298.02	7.56e-01	9.54e-03

Table 3.4: Individual fitted values of ζ and τ_c. Pressures are given in torr.

Least squares fits for ζ and τ_2 were also performed using a variety of slight modifications to the standard method. These include (1) minimizing the difference in the absorption coefficient rather than transmission, (2) minimizing the percent difference in the transmission, and (3) minimizing the percent difference in the absorption coefficient. All of these were implemented to improve the resulting calculation errors. However, no significant improvements over the standard method were achieved.

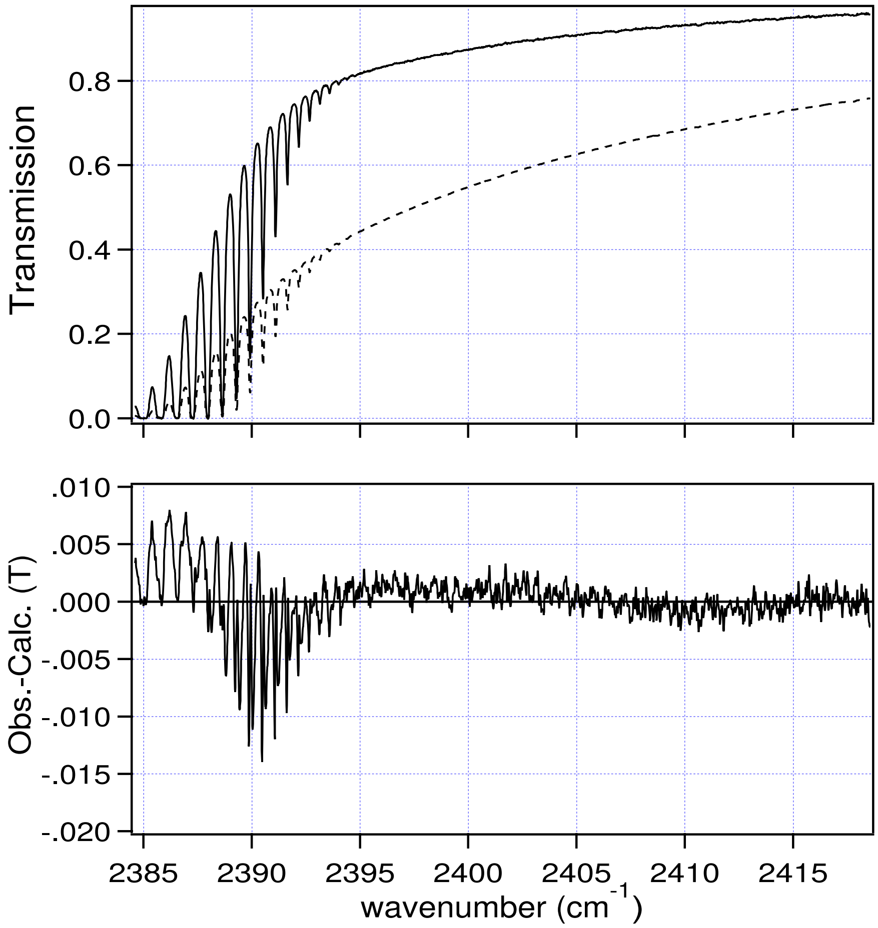

Figure 3.12: A measured pure spectrum and a Lorentz calculation (top panel) and the error incurred (bottom panel) due to the line-mixing/duration-of-collision lineshape (ζ=0.74,τ_2=9.1E-03). Experimental conditions are 741Torr CO_2, 15cm path length, 299.5K.

Because spectra of various optical depths and varying spectral ranges have different sensitivity to both the line-mixing and duration-of-collision effects, the individual fitted values of ζ and τ_2 vary. Therefore, in order to make a final determination of the parameters, least squares fits were also performed by fitting all spectra simultaneously, resulting in two sets of parameters, one for self-broadened and one for nitrogen-broadened, which yield the best overall agreement with the data. These are listed in

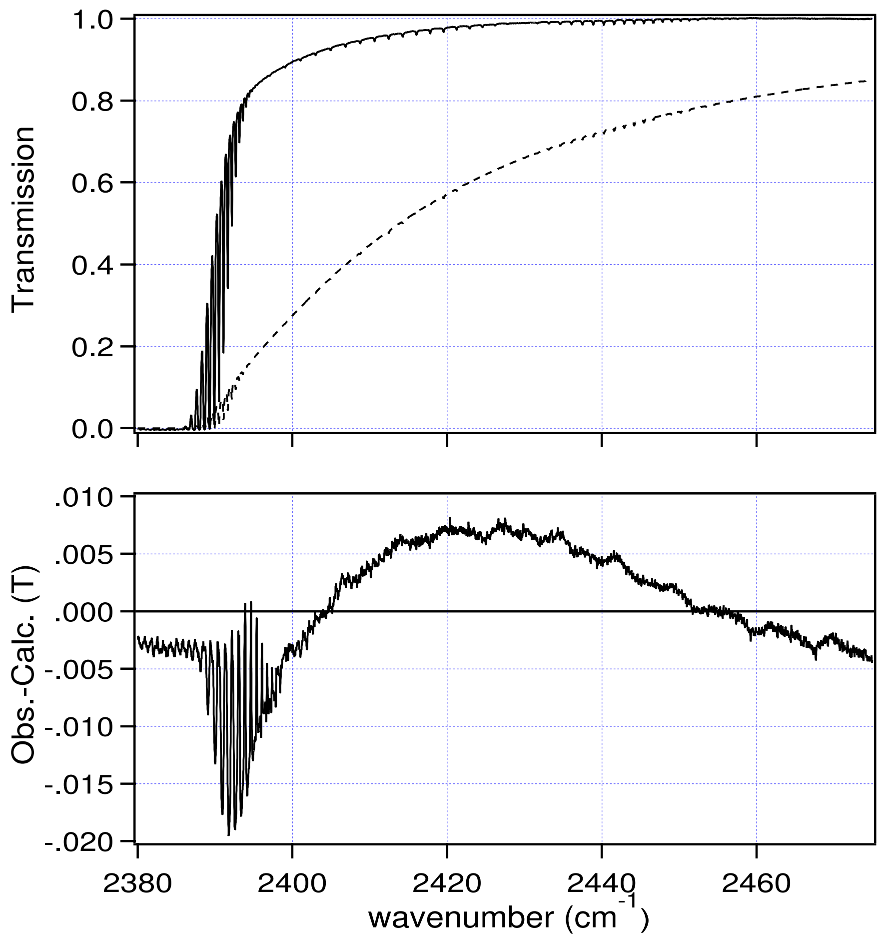

Figure 3.13: A measured room temperature nitrogen-broadened spectrum and a Lorentz calculation (top panel) and the error incurred (bottom panel) due to the line-mixing/duration-of-collision lineshape (ζ=0.94,τ_2=5.3E-03). Experimental conditions are 38.04Torr CO_2, 723.5Torr N_2, 800cm path length, 297.4K.

Table 3.5.2, and are referred to as “global” fits hereafter.

	ζ ( )	τ_2 (cm)
Self-broadened	0.698	0.0100
N_2-broadened	0.995	0.0038

Table 3.5: Global fitted values of ζ and τ_2.

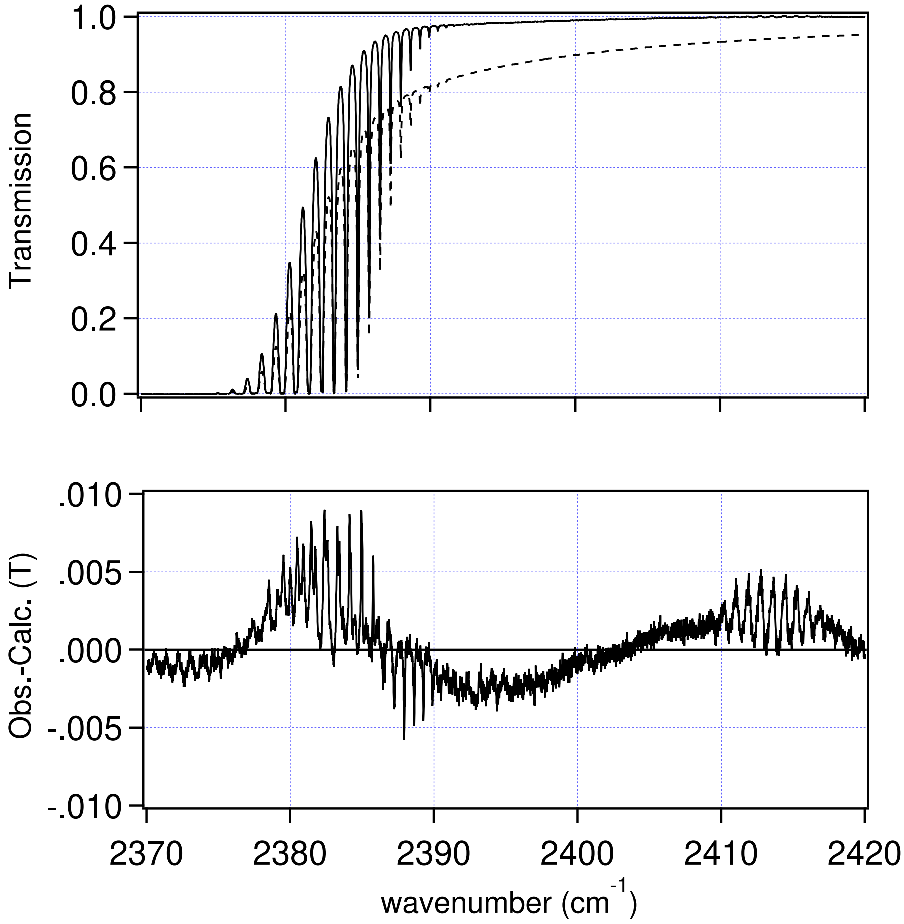

Figure 3.14: A low temperature measured nitrogen-broadened spectrum (top panel) and the error incurred (bottom panel) due to the line-mixing/duration-of-collision lineshape (ζ=0.91,τ_2=7.3E-03). Experimental conditions are 1.90Torr CO_2, 378.5Torr N_2, 1600cm path length, 219.6K.

Going from the individual fits to the global fits, the model loses a factor of $\sim$2 in terms of accuracy in exchange for one set of parameters which yields the best overall agreement with all of the spectra. Sample calculations using the globally fitted parameters are shown in Figure 3.15 for a pure spectrum and in Figures 3.16 and 3.17 for two nitrogen-broadened spectra. The accuracy shown here is typical of the other results, with all spectra reproduced to better than $\sim$0.03 in transmission. Obviously, the spectra have not been reproduced to within the noise level of the data. Unfortunately, there are, no doubt, errors in the measured spectra other than random noise (i.e baseline errors), which makes it difficult to distinguish between actual model errors and experimental errors. Systematic residual errors remain for the unsaturated lines at the band-head – this is attributed to small errors in the background absorption coefficient. For example, if only narrow regions spanning the unsaturated lines at the band-head are considered, the spectra can be reproduced almost to within the noise level of the data using a sum of Lorentzians plus a fitted second order polynomial to represent the background absorption. In other words, unless the far-wing lineshape of the background lines is modeled almost perfectly, the unsaturated lines at the band-head show residual errors. The errors could also be due in part to small systematic errors in the experimental data. Additionally, this residual could also be due to the inaccuracy of our PEG model for collisional rates at high J. While the PEG law is believed to be fairly accurate for low values of J ($J \leq 30$), its accuracy has not been verified for higher values. In this work, we use the PEG law for all the lines of the ν_3 band, including up to J ~100 at the R-branch band-head, where the lines overlap significantly. This is done in part so that our calculations can be used in totality with the lines listed on the 1992 HITRAN database.

In terms of accuracy, the only very obvious advantage of this model over Cousin's is for self-broadening. Beyond ~2410 cm^{-1}, both models yield comparable results for N_2-broadening both at room temperature and 220K. Within the band, our model is ~ 50 % better due to our treatment of line-mixing. However, it should be noted again that Cousin's model was originally developed for use only beyond the band-head, but is frequently used throughout the band in line-by-line codes. Furthermore, our model requires only two adjustable parameters which have direct physical meanings in the model, as opposed to the 39 empirical parameters in the Cousin model.

Due to the inaccuracies of this model, a modified model has been developed and optimized for use within the R-branch band head. This model is described in Section

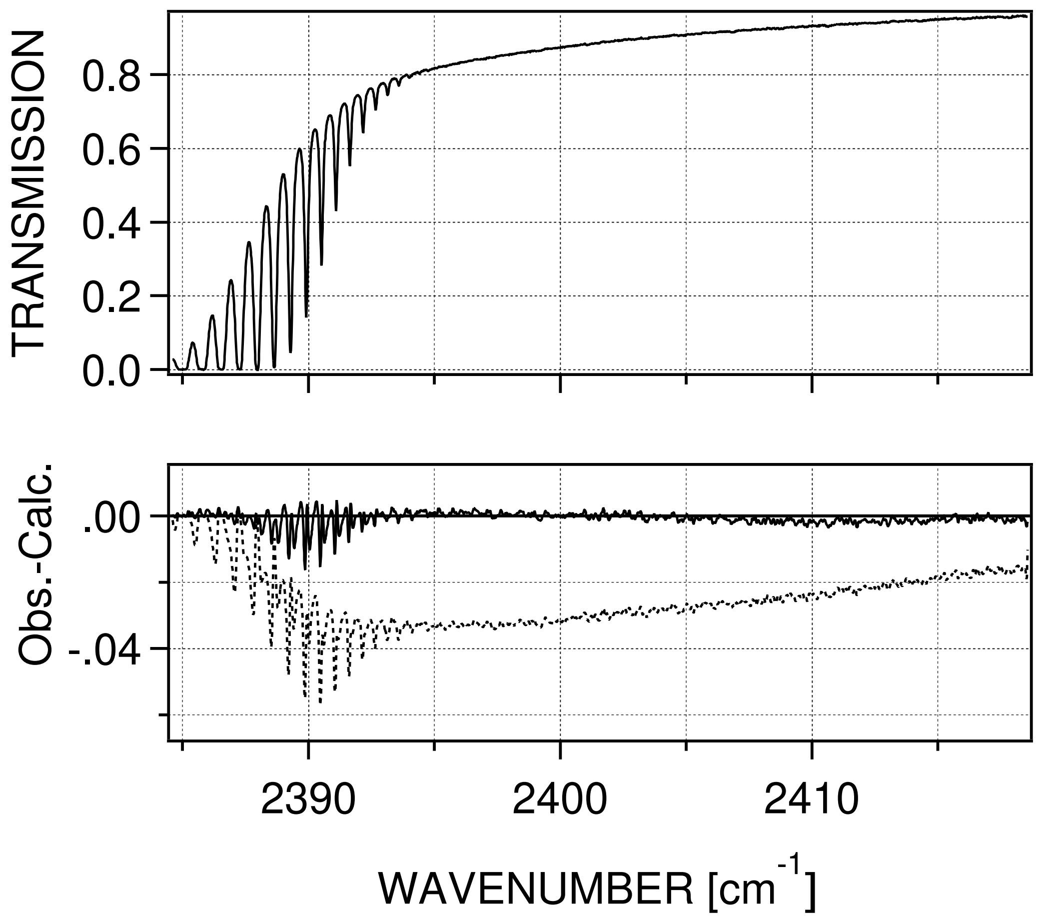

Figure 3.15: A measured pure spectrum and a Lorentz calculation (top panel) and errors incurred (bottom panel) due to the line-mixing/duration-of-collision lineshape using the globally fitted parameters (solid curve) and the Cousin lineshape (dashed curve). Experimental conditions are 741Torr CO_2, 15cm path length, 299.5K.

3.7.

The least-squares fits for ζ and τ_2 were complicated by the fact that both line-mixing and duration-of-collision effects have roughly the same effect on the observed spectrum. That is, they both reduce the absorption in the far-wing. For this reason, unique solutions for these parameters were difficult to determine. The total residual

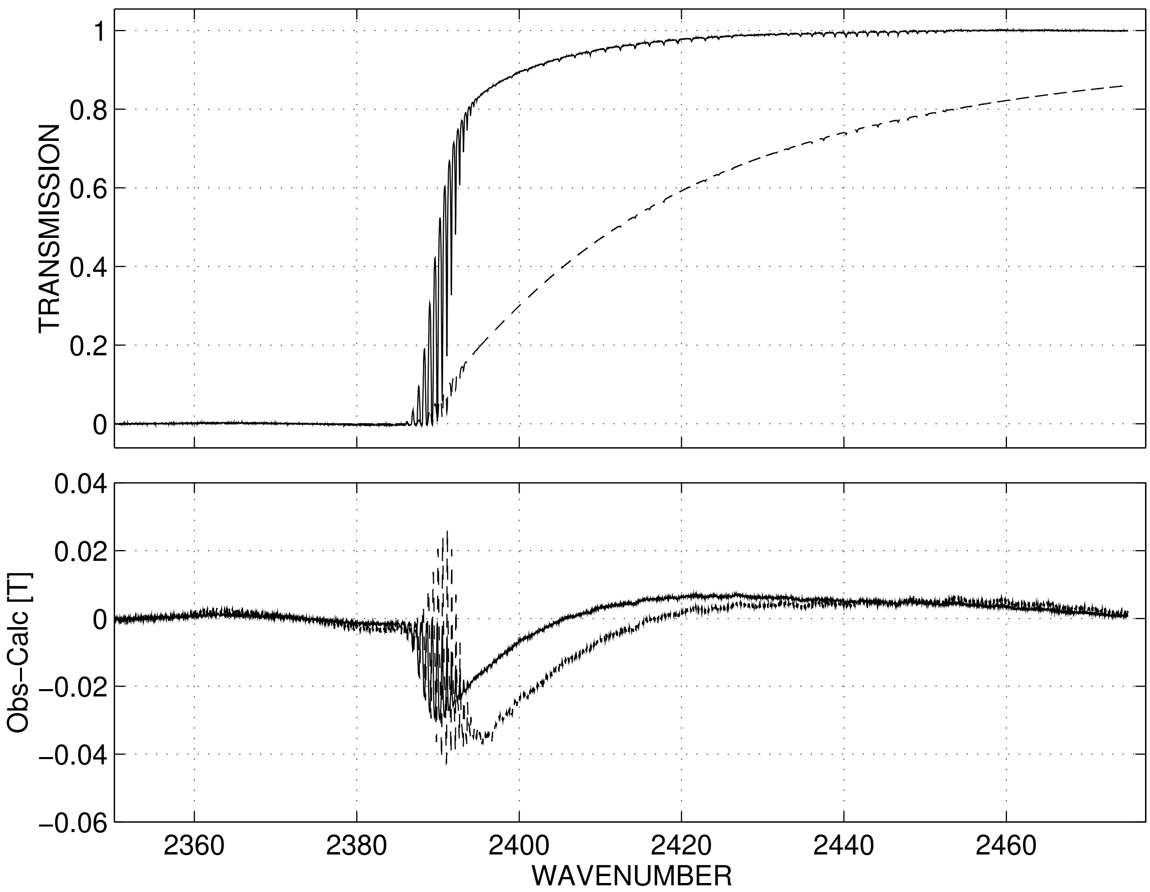

Figure 3.16: A measured room temperature nitrogen-broadened spectrum and a Lorentz calculation (top panel) and errors incurred (bottom panel) due to the line-mixing/duration-of-collision lineshape using the globally fitted parameters (solid curve) and the Cousin lineshape (dashed curve). Experimental conditions are 38.04Torr CO_2, 723.5Torr N_2, 800cm path length, 297.4K.

or contour of the residuals (square of standard residuals summed over wavenumber space) as a function of both ζ and τ_2 is shown in grey-scale in Figure 3.18 for room temperature nitrogen broadening. Darker regions represent lower residual. The global minimum is located at (ζ, τ_2)=~(0.99,0.004) but other minima are located throughout the parameter space. Because we expect ζ to be close to 1 from previous studies, we have confidence that we are converging on their proper values. In other words,

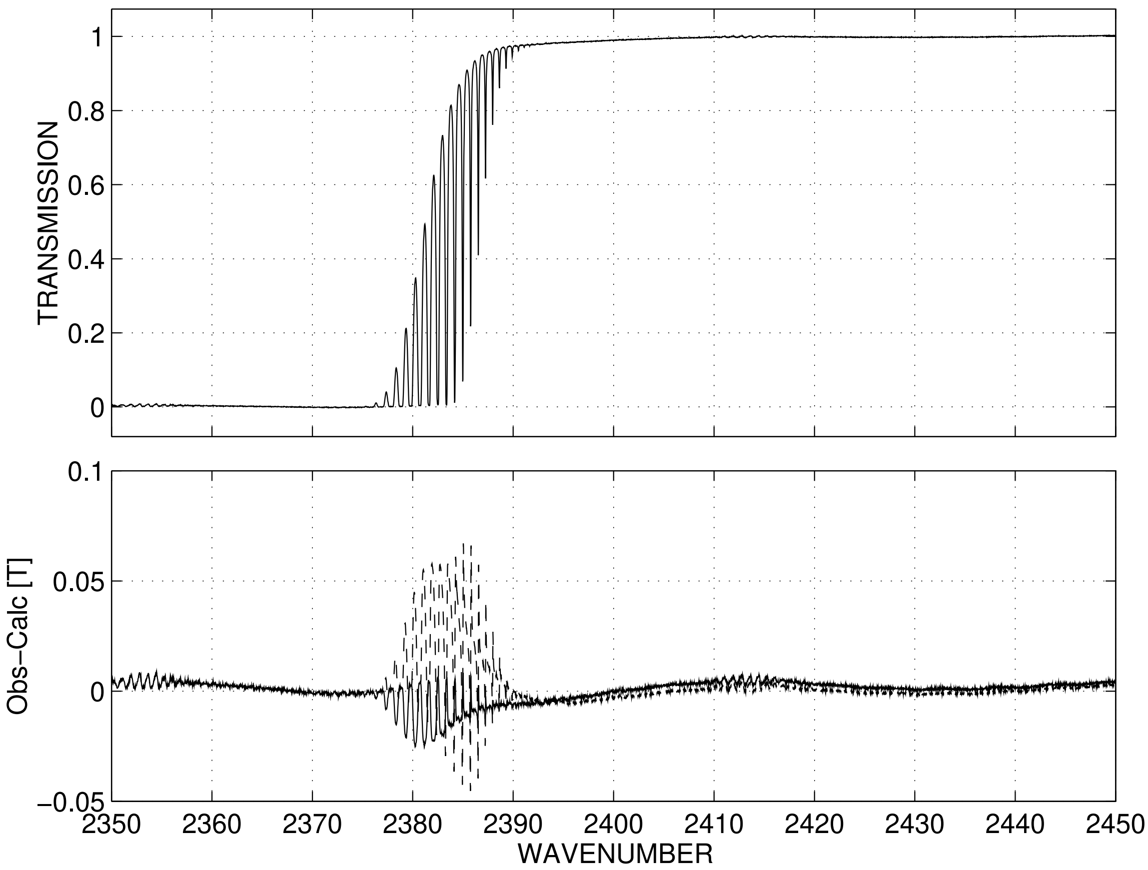

Figure 3.17: A low temperature measured nitrogen-broadened spectrum (top panel) and errors incurred (bottom panel) due to the line-mixing/duration-of-collision lineshape using the globally fitted parameters (solid curve) and the Cousin lineshape (dashed curve). Experimental conditions are 1.90Torr CO_2, 378.5Torr N_2, 1600cm path length, 219.6K.

the solutions for $\zeta < 0.5$ and $\tau_2 > 0.05$ are totally incompatible with our relaxation model developed for Q-branches. Accepting these solutions would have led to the conclusion that the observed sub-Lorentz behavior is due mainly to the duration-of-collision effect, with line-mixing having little effect (smaller ζ) on the spectra. On the other hand, accepting the solution at (0.99,0.004) allowed the application of the duration-of-collision effect, with τ_2 determined more accurately from this study, to be applied to other spectral regions. This is addressed further in Section 3.6.

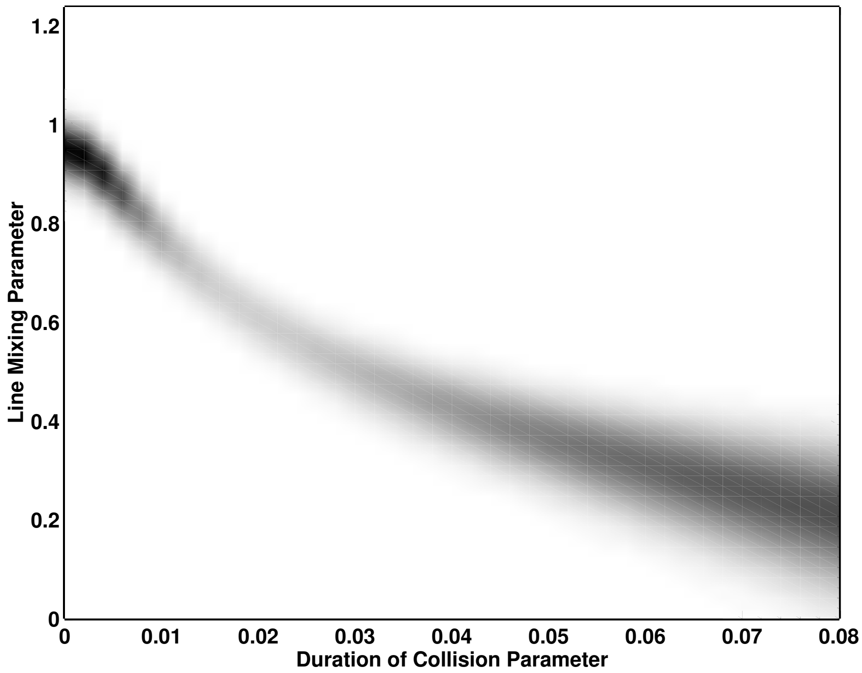

Figure 3.18: Contour of the residuals as a function of ζ and τ_2 for multiple N_2-broadened spectra. Darker regions represent regions of low residual. See the text for details.

Our fitted ζ is very close to its predicted value of 1 (~0.99) for N_2-broadened CO_2. However, for self-broadened CO_2, ζ is significantly lower than 1 (~0.70), implying that our method for representing the rotational relaxation rates is inaccurate for CO_2-CO_2 collisions. Using these values of ζ, the ratio of line-mixing to Lorentz absorption coefficients far from the band center at 296K is calculated to be ~0.34 for self-broadening and ~0.07 for N_2-broadening.

The fitted value of τ_2 for nitrogen-broadening is more than two times smaller than for self-broadening, implying that the interaction time for CO_2-N_2 collisions is much shorter than for CO_2-CO_2 collisions. This is reasonable given that the quadrupole moment of CO_2 is nearly three times stronger than that of N_2. For self-broadening, τ_2 is almost three times smaller than Birnbaum's value of 0.0275 cm obtained by a single line model fitted to raw data [64]. However, to correctly compare τ_2 values, our least-squares fits should be performed using only regions beyond the band-head as he did. It should also be noted that the values of these collision times are model dependent and direct comparisons to values obtained by other means should be done with this in mind. Also, these values are of course subject to any errors in the data analysis. In particular, for nitrogen-broadening, τ_2 could be slightly contaminated by minor pressure-induced N_2 continuum absorption.

3.6 Application to the 15μm Region

Existing radiative transfer codes generally use the Cousin *et.al.* χ-functions (determined totally from 4.3μm spectra) at 15μm as well, which is dominated by perpendicular bands rather than $\Sigma \leftarrow \Sigma$ bands. This is theoretically an inappropriate use of χ-functions developed using far–wing spectra of the ν_3 band of CO_2 at 4.3 μm. Cousin *et.al.* assumed that the sub-Lorentz behavior beyond the 4.3μm R-branch band-head was due entirely to duration-of-collision effects. Because duration of collision effects do not vary with vibration, others have applied their model to other spectral regions dominated by bands of different symmetry. While the duration-of-collision parameter is expected to vary very little between vibrational bands, line-mixing is much weaker in a $\Pi - \Sigma$ band than in a $\Sigma - \Sigma$ band. With our models, this is simply because one-half of the rotational levels in the Π state do not participate in radiative transitions. Consequently, collisions that place the CO_2 molecule into these states effectively stop any further line-mixing during the absorption process. Since all rotational states in a Σ state contribute to spectral lines, all collisions can potentially contribute to further line-mixing.

The end result is that for $\Sigma \leftarrow \Sigma$ bands, the ratio of the line-mixing absorption coefficient to Lorentz is about 0.10 in regions far from the band center, compared to a value of $\sim$ 0.50 for $\Pi \leftarrow \Sigma$ bands. Applying the Cousin χ-function, which was derived from $\Sigma \leftarrow \Sigma$ bands, to the 15μm region therefore essentially over-estimates the amount of line-mixing and ultimately results in absorption coefficients which are too small in-between the lines. These concerns were also addressed in Reference [29]. With our model, because the line-mixing and collision duration effects are represented in a separable and (somewhat) clear manner, this confusion is avoided. Furthermore, because the collision duration effect has been determined from the 4.3μm study, it can be incorporated into line-mixing calculations for the 15μm region.

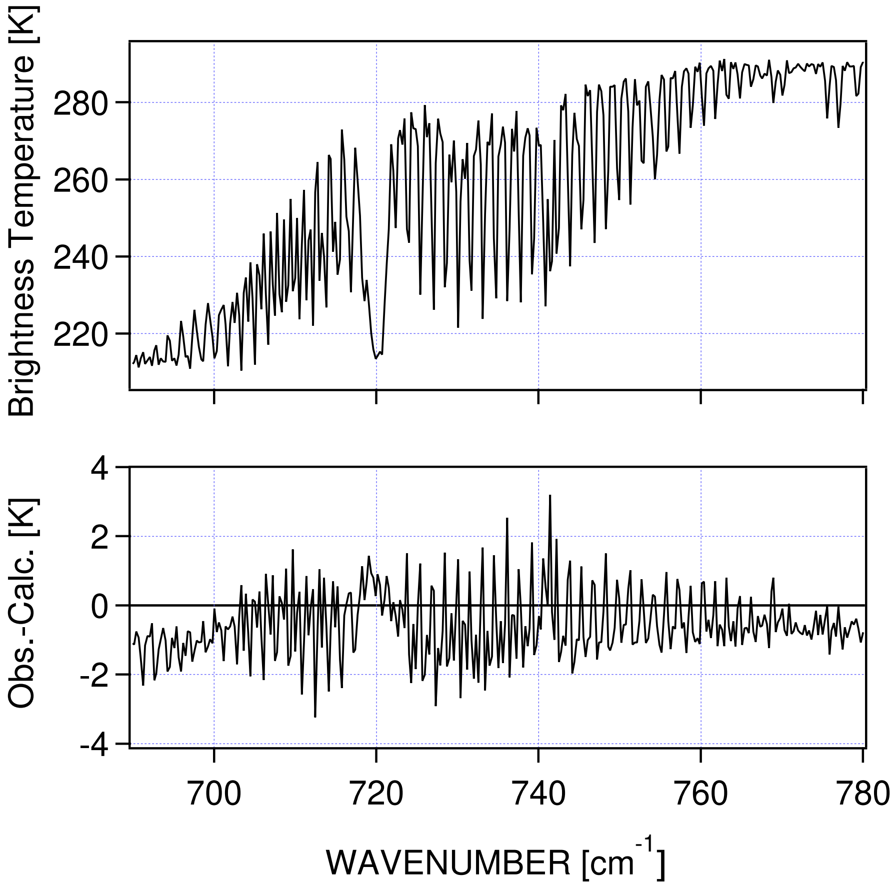

Figure 3.19: A brightness temperature spectrum (top panel) measured with HIS during the CAMEX1 campaign in the 15μm region. The bottom panel shows the errors incurred when using the Cousin lineshape model discussed in the text.

The fact that the Cousin *et.al.* model predicts slightly too little absorption in-between spectral in the 15μm region can be observed in well characterized atmospheric measurements. In particular, it was observed in down-welling radiance measurements performed with the HIS [23] while flying on a high-altitude ER-2 aircraft during NASA's CAMEX1 [24] campaign. A validated HIS spectrum is shown in Figure 3.19 for the 690 – 780 cm^{-1} range. In-between the P and R-branch lines of the 720 cm^{-1} $\Pi \leftarrow \Sigma$ band, the Cousin model used in a FASCODE calculation predicts too little absorption, resulting in ~-1.5K systematic errors in-between the lines. The ability to predict this type of behavior perhaps shows an advantage of our simple line-mixing models over more complex approaches.

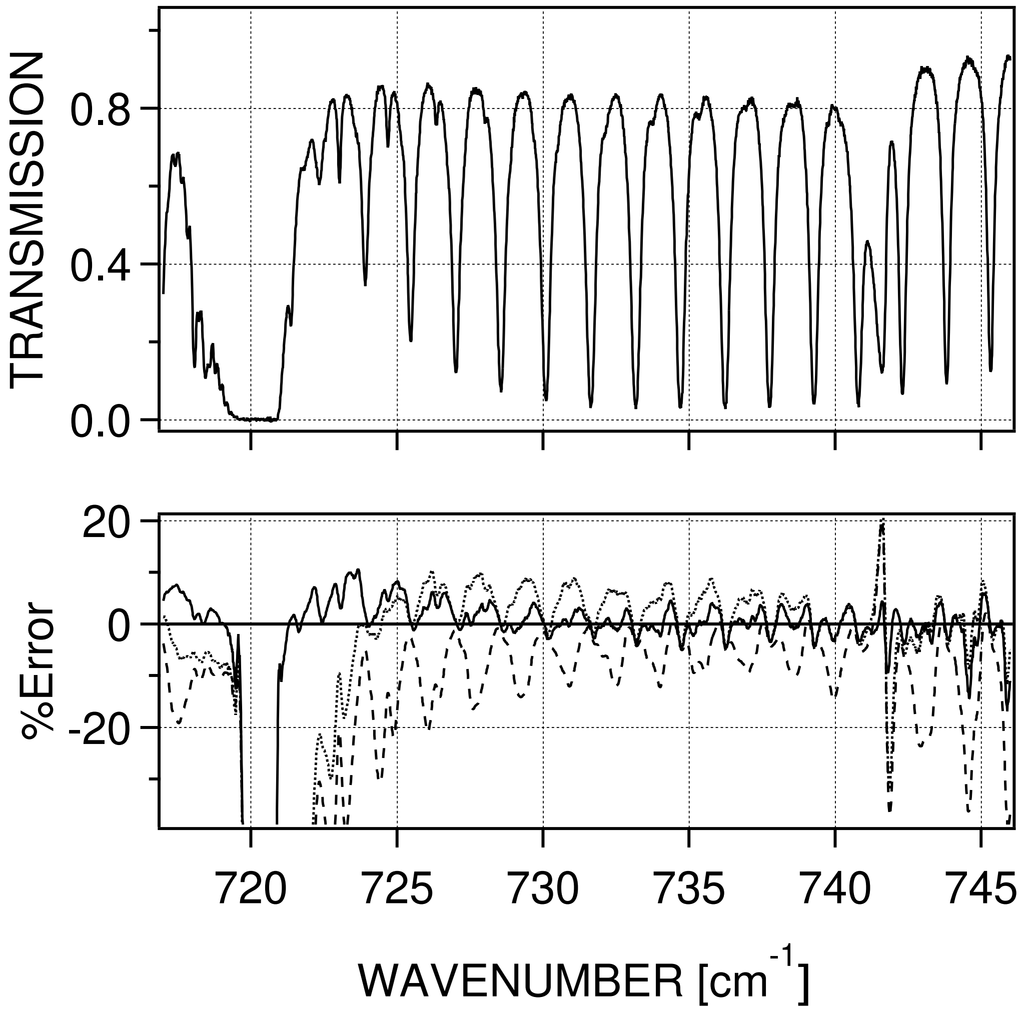

Figure 3.20: A measured CO_2 transmission spectrum in the 15μm region and percent errors in the calculated absorption coefficients ($100\frac{k_{exp't}-k_{calc}}{k_{calc}}$)for the Lorentz (dashed curve), Cousin (dotted curve), and line-mixing/duration-of-collision (solid curve) lineshapes. Experimental conditions are 766 torr CO_2, 0Torr N_2, 15cm path length, 296.7K.

To test the accuracy and applicability of our model in the 15μm region, calculations were performed for a measured transmission spectrum for the 15μm region. Again, this spectrum was provided by John W. C. Johns of NRC, Ottawa. This is a pure CO_2 spectrum (766 torr) recorded at a path length of 15 cm and temperature of 296.7K. It is shown in Figure 3.20 along with percent errors in the calculated absorption coefficients using several different lineshapes. As expected, the Cousin χ-functions underestimate the absorption coefficients by ~10% in-between the 720 cm^{-1} band R-branch lines. As usual, the Lorentz calculation predicts too much absorption in-between the lines. The line-mixing/duration-of-collision calculation greatly improves the agreement with the spectrum over both Lorentz and Cousin. The details of these calculations are described in the following paragraphs.

The Lorentz and Cousin calculations were performed by summing the contributions (using the appropriate lineshapes) of the lines shown in Figure 3.21. This includes all $C^{16}O_2$, $C^{18}O_2$, $C^{17}O_2$ transitions which contribute a significant amount of absorption to the 710–750 cm^{-1} region.

The line-mixing/duration-of-collision calculation is rather involved, taking into account line-mixing and duration-of-collision effects for all bands in the region. Line-mixing is included for the $\Pi \leftrightarrow \Sigma$ Q-branches centered at 618, 648, 662, 667, 720, and 791 cm^{-1} and for the $\Pi \leftrightarrow \Delta$ Q-branches at 668 and 741 cm^{-1} using the methods described in [33, 60, 61]. With exception of the 720 cm^{-1} band, the far-wing line-mixing lineshape for the P- and R-branches of the same bands are approximated as 0.5 times the corresponding Lorentz lineshape. For the 720 cm^{-1} band P- and R-branches, the full line-mixing absorption coefficient is calculated using the same relaxation rules as for $\Pi \leftrightarrow \Sigma$ Q-branches. Line-mixing is included separately for the P-branch and for the R-branch, with no interaction between the two. In the band wing, at approximately 820 cm^{-1}, this results in the ratio of mixing to Lorentz to be constant, with a value of ~ 0.48. Using Birnbaum's full expression for χ_B with a value of τ_2 of 0.010 cm determined in Section 3.5, duration-of-collision effects are included for all transitions. **These calculations were performed with no adjustable parameters**. The spectral lines used in this calculation are shown in Figure 3.21. As expected, this lineshape predicts sub-Lorentzian behavior in-between the 720 cm^{-1} band R-branch lines, but not as much as predicted by Cousin *et.al.* Some residual errors remain on either side of the 720 cm−1 band Q-branch at ~718 and ~723.5 cm^{-1}, which could be due to the lack of inter-branch mixing in the calculations.

In Figure 3.22, we show the individual effects of line-mixing and duration-of-collision by plotting ratios to Lorentz. In-between the 720 cm^{-1} band R-branch lines, line-mixing is responsible for most of the sub-Lorentzian behavior and therefore the lineshape is not extremely sensitive to the duration-of-collision effect in this region. However, it is still more accurate than the other approaches. At most, this shows that our 4.3μm τ_2 value is compatible with observations in this spectral region. A more definitive conclusion about the optimum value of τ_2 for this region could be made using higher optical depth spectra in the 800 cm^{-1} region. Such an experiment would be more sensitive to the duration-of-collision effect from the fundamental ν_2 band (667 cm^{-1}).

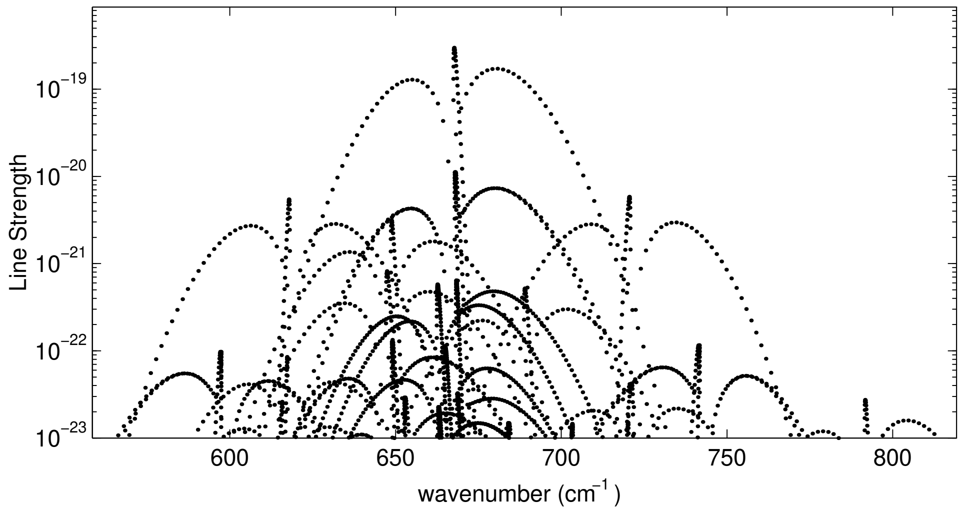

Figure 3.21: Spectral lines of CO_2 included in the calculation for the transmission spectrum discussed in section 3.6.

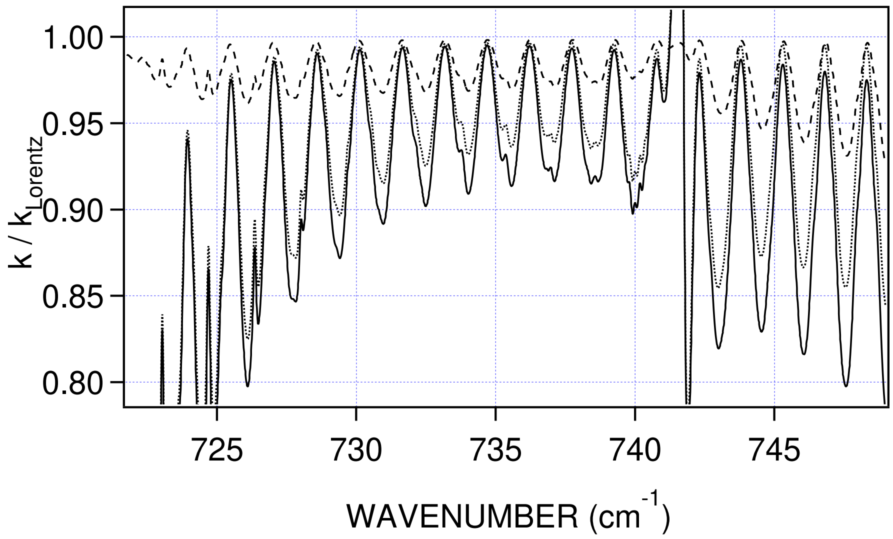

Figure 3.22: Absorption coefficient ratios to Lorentz to show the separate effects of line-mixing (dotted curve) and duration-of-collision(dashed curve). The combined effects (solid curve) are also shown. Experimental conditions are the same as for Figure 3.20.

3.7 Application to Line-by-Line Codes: A Modified Model

The model discussed so far for the 4.3μm region yields fairly accurate results throughout and beyond the ν_3 band-head. However, the residuals at the R-branch band-head are still a factor of 2 or so too large for atmospheric temperature retrievals. The micro-windows within the band-head are especially important for colder, higher altitude temperature retrievals and therefore, this spectral region needs to be modeled as accurately as possible. Furthermore, because of our formulation, when $k_{1st}(\nu)$ and $\chi_B(\nu)$ are combined, we are effectively multiplying many linear wavenumber terms (i.e. $(\nu - \nu_j)\mathrm{Y}_j)$ by $\chi_B(\nu)$. Since Y_j can be negative, this leads to a model which has poor computational stability. Specifically, if detailed balance is not met to a very high degree, this method can produce negative absorption coefficients if the calculations are extended too far beyond the band-head.

We therefore suggest that when implementing these methods in line-by-line codes, the Cousin χ-functions be used beyond ~2410 cm^{-1} and a modified version of our model (presented below) be used throughout the band-head and up to ~2410 cm^{-1}. Beyond ~2410 cm^{-1}, Cousin χ-functions are nearly as accurate as our proposed model, and are also very robust computationally.

Our modified model is the same as discussed in Section 3.3 except that it is optimized using only spectral regions below ~2400 cm^{-1} and a simpler expression for the duration-of-collision χ-function is used. The computation of χ_B is slow because of the Bessel function. Setting τ_0 and γ_j to zero in Equation 3.22 yields $\chi_B = \tau_2|\Delta\nu|K_1(\tau_2|\Delta\nu|)$. A function which has similar behavior is

$$\chi(\nu) = \exp(-\tau_c|\Delta\nu|^{\frac{3}{2}}) \tag{3.25}$$

Although this function was chosen somewhat arbitrarily, the important point is that over the important range of values for τ_c, Equation 3.25 is able to mimic the behavior of $\tau_2|\Delta\nu|K_1(\tau_2|\Delta\nu|)$.

Once again, as in Section 3.5, global fits for ζ and τ_c were performed. The fitted values are given in Table 3.7. Sample calculations for the band-head region are shown in Figures 3.23 through 3.25. These figures show the measured absorption coefficients and the percent error in the calculated absorption coefficients ($100\frac{k_{exp't}-k_{calc}}{k_{exp't}}$) for our modified method and the Cousin *et.al.* χ-functions [34,35]. In transmission, the residual errors at the band-head for our method are now on the order of 0.01–0.015 for all spectra. In the microwindows, percent errors in the calculated absorption coefficients are less than 5%. When comparing the results of this work and Cousin *et.al.*, it is important to note that the differences can arise from both model errors and errors in the data used to produce them.

	ζ	τ_c
Self-broadened	0.655	4.68E-4
N_2-broadened	0.876	2.08E-4

Table 3.6: Global fitted values of ζ and τ_c determined from our modified lineshape model using only the band-head spectral region and Equation 3.25.

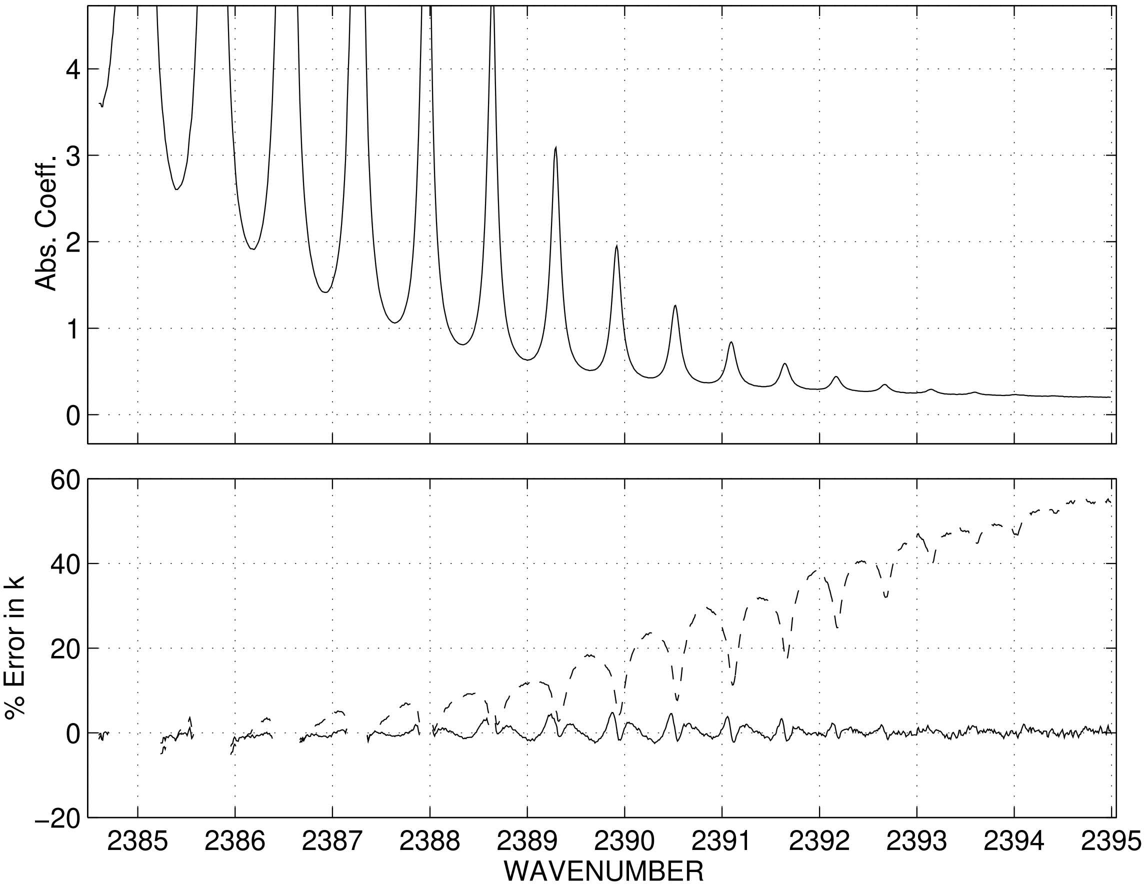

Figure 3.23: Measured absorption coefficient for a pure CO_2 sample at room temperature is shown in the top panel. In the bottom panel are percent errors in the calculated absorption coefficient for our modified method (solid line) and the Cousin χ-functions (dashed line). Experimental conditions are 741Torr CO_2, 15cm path length, 299.5K.

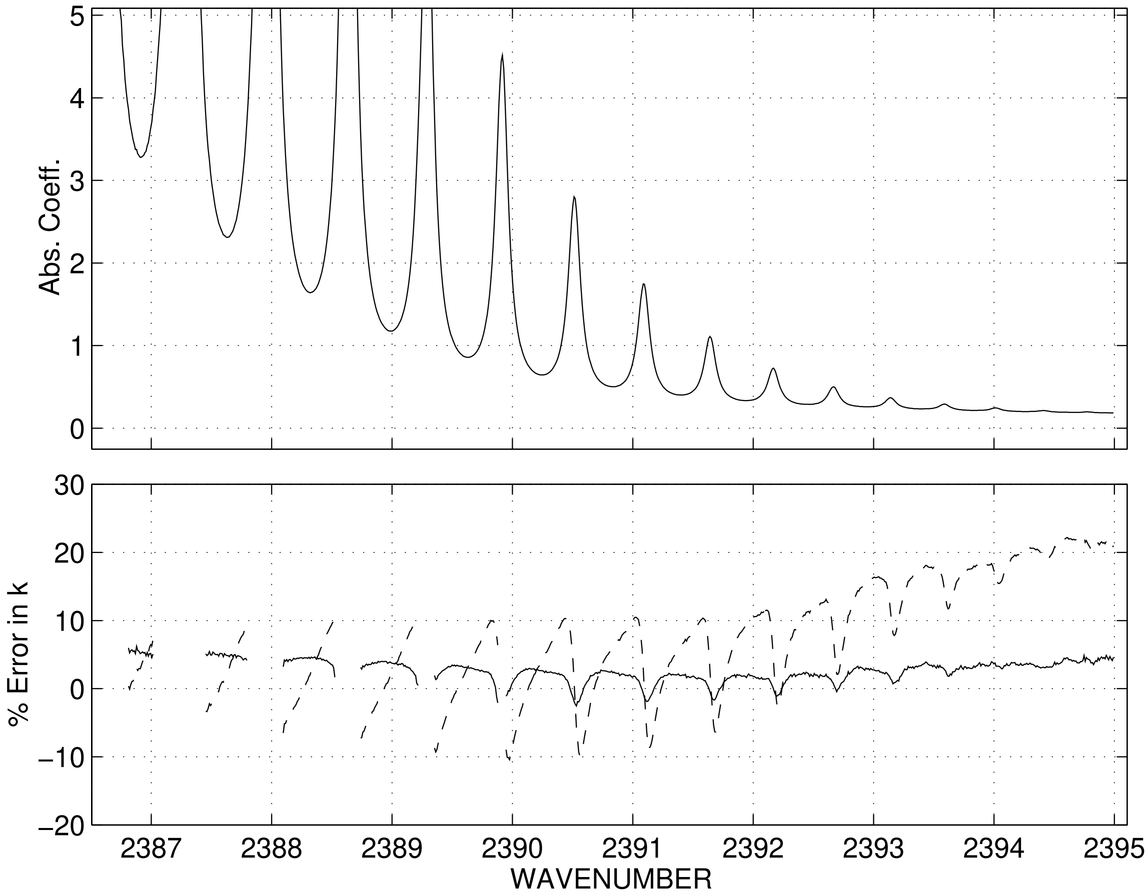

Figure 3.24: Measured absorption coefficient for a N_2-broadened sample at room temperature is shown in the top panel. In the bottom panel are percent errors in the calculated absorption coefficient for our modified method (solid line) and the Cousin χ-functions (dashed line). Experimental conditions are 38.04Torr CO_2, 723.5Torr N_2, 800cm path length, 297.4K.

For ease of computation, the first-order mixing coefficients used in this method have been least-squares fit to a simple polynomial for each line. Temperature dependent coefficients for these coefficients of the fundamental ν_3 P- and R-branches are listed in Tables C.1 through C.4 in Appendix C. Using A, B, C, and D from these tables, the mixing coefficients are calculated at temperature T [K] with:

$$Y_j(T) = (\frac{200}{T})^{\frac{3}{4}} \left(A_j + B_j(T-200) + C_j(T-200)^2 + D_j(T-200)^3\right) \tag{3.26}$$

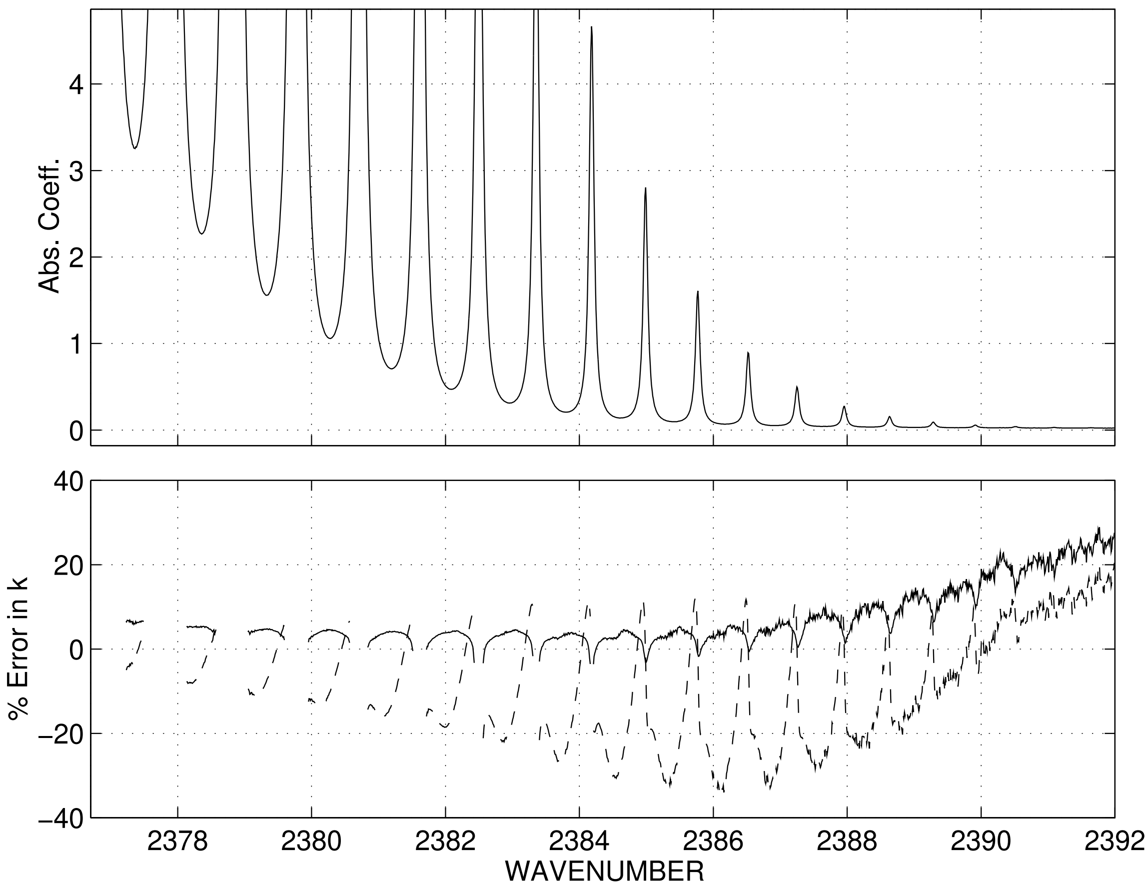

Figure 3.25: Measured absorption coefficient for a N_2-broadened sample at 220K is shown in the top panel. In the bottom panel are percent errors in the calculated absorption coefficient for our modified method (solid line) and the Cousin χ-functions (dashed line). Experimental conditions are 1.90Torr CO_2, 378.5Torr N_2, 1600cm path length, 219.6K.

All of the cautions prescribed in [60] about using the mixing coefficients also apply here. Specifically, these coefficients should be used in totality and only in conjunction with the 1992 HITRAN line parameters.

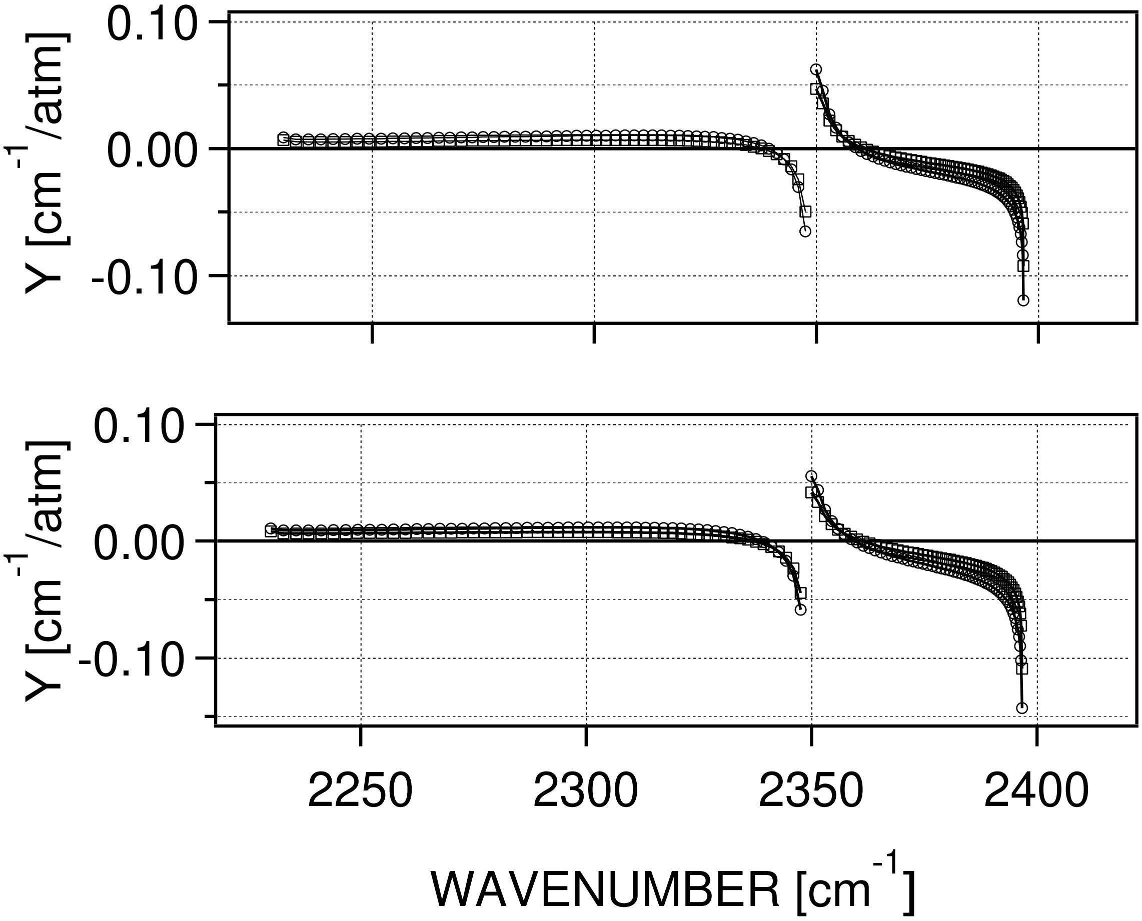

Figure 3.26: First order mixing coefficients calculated using Tables C.1 through C.4. The top panel is for self-broadening and the bottom panel for N_2-broadening; circles: 220K, squares: 296K.

3.7.1 Parameterization

The proposed lineshape model is easily parameterized for use in radiative transfer codes. The form this parameterization may take is somewhat arbitrary. Outside of the the ν_3 band-head, Birnbaum's χ-function can be modified to include line-mixing by including the appropriate multiplicative constant. The calculation inside the band-head, where the important temperature sounding channels are located, requires an explicit calculation of first–order line-mixing plus a duration-of-collision χ-function term. This should be fairly easy to implement since most codes already use a temperature dependent first-order parameterization for the 15μm Q-branches. Alternatively, a look–up table for the CO_2 wing absorption may be sufficient and easier to implement.

3.8 Summary

A physically-based CO_2 lineshape model for the 4.3μm region which accounts for line-mixing and non-zero collision times has been developed. The model was fine-tuned by adjusting two parameters, ζ and τ_2, by non-linear least-squares fits to measured transmission spectra. Reasonably good agreement with the data is obtained for all pressures, temperatures, and broadening species considered. While almost all existing atmospheric transmission algorithms use Cousin's empirical χ-function in this spectral region, our model is physically based and requires only 2 adjustable parameters.

To a large degree, the duration-of-collision effects at 4.3μm have been determined separately from the line-mixing effects. Assuming the collision time to be independent of vibration, the results at 4.3μm were applied to one pure spectrum at 15μm. For both the 4.3 and 15μm regions, line-mixing is responsible for the majority of the observed sub-Lorentzian behavior in our observed spectra.

A modified version of our model which has a simpler form for the duration-of-collision χ-function has been optimized for use directly at the R-branch band-head. Combined with the use of the Cousin χ-functions beyond ~2400 cm^{-1}, this model is more accurate than present methods and should be fairly easy to incorporate into line-by-line codes.

3.9 Future Work

Suggested future work includes:

- Test the proposed lineshape models with other laboratory. Conduct double-blind studies which test the overall accuracy of this model as compared to others (Cousin *et.al.*).
- Incorporate the 4.3μm and 15μm lineshape models into a line-by-line radiative transfer code and test them with well characterized atmospheric measurements.

See if they improve temperature profile retrievals.

- Determine the 15μm collision duration parameter τ_2 more accurately with high optical depth spectra in the 800 cm^{-1} region. By comparing results from such an experiment to the 4.3μm τ_2 value, the effect of vibration on collision duration (if any) can be studied.

- Fit directly for the first order mixing coefficients. Use multiple spectra to ensure the model works for all pressures. This has potential to provide the most accurate parameterization.

Chapter 4

Experimental Investigation of the Water Vapor Continuum

4.1 Introduction

The absorption of radiation by water vapor has been studied extensively for the atmospheric windows (in-between the strong H_2O and CO_2 absorption bands) at 4 and 10 μm. Due to a lack of many strong absorption lines, these windows are extremely transparent to infrared radiation and are therefore useful in characterizing the Earth's surface from satellite observations. The small amount of infrared radiation that is absorbed, however, is primarily absorbed by the far-wings of water vapor lines from the pure rotational and vibrational bands. In 1991 it was concluded [68] that the largest discrepancy between calculations of longwave fluxes (for clear sky conditions) from different climate models was due to the many different ways in which this absorption is treated. Due to a number of laboratory and field measurements, as well as advances in far-wing lineshape theories, this absorption is reasonably well characterized and understood in principle.

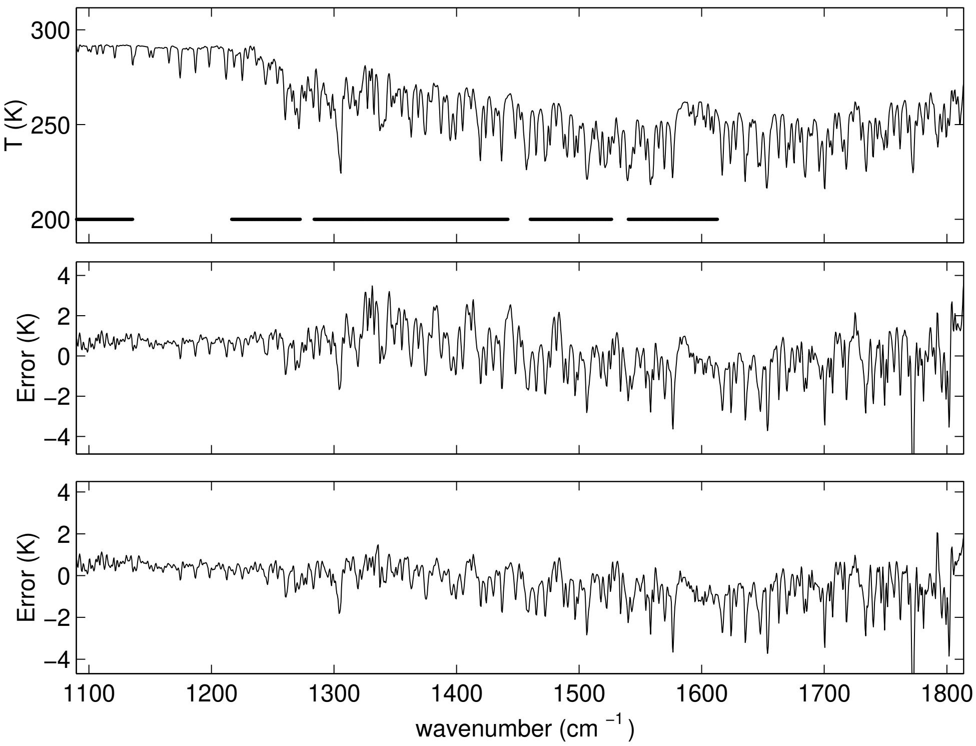

Figure 4.1: A validated atmospheric brightness temperature spectrum in the H_2O ν_2 region measured with the HIS during CAMEX 1. The measured spectrum and the centers of the AIRS retrieval channels are shown in the top panel. The middle and bottom panels show errors due to calculations using two commonly used continuum models (CKDv0 and CKDv2.1), which are presented in Section 4.2.5.

Although much less studied, non-Lorentz H_2O lineshapes also have a significant impact *within* the strong pure rotational and vibrational bands. This *in-band* continuum is particularly important for satellite infrared remote sensing of atmospheric H_2O profiles. For example, AIRS has H_2O channels located continuously throughout the ν_2 P-branch. An accurate retrieval of the H_2O profile from the channel radiances requires a detailed knowledge of atmospheric water vapor transmittances inside the band, especially between lines where the radiative transfer weighting functions vary most sharply with altitude. Unfortunately, these optimum humidity sounding channels, being located in-between the ν_2 spectral lines, are subject to rather large water transmittance errors because of uncertainties in the lineshape. An atmospheric brightness temperature spectrum measured by the HIS for this spectral region is shown in Figure 4.1. The measured spectrum and the positions of the AIRS retrieval channels are shown in the top panel. The middle and bottom panels show differences between observation and calculations using two common continuum models (CKDv0 and CKDv2.1). In principle, if the atmosphere were characterized perfectly and if our knowledge of H_2O transmittances was perfect, these errors would fall within the noise level of the instrument. It is likely that most of the errors in-between the lines are due to spectroscopic uncertainties and not uncertainties in the H_2O profile. The AIRS sounder will have noise levels below 0.2K in this region, far below the existing accuracy of the H_2O continuum.

For well isolated pressure-broadened water vapor lines in the infrared, the Lorentz lineshape is very accurate near line center. However, calculations based on the impact approximation generally overestimate the observed absorption in the far-wing atmospheric window regions and underestimate the absorption within the rotational and vibrational bands. If all lines have the same lineshape, these factors lead to the conclusion that the actual water vapor lineshape is extremely sub-Lorentzian in the far-wing and at least somewhat super-Lorentzian in the intermediate and near-wing. Since most experimental studies have focussed on the window regions, the far-wing lineshape has received most of the attention and its behavior has been characterized more accurately than the near-wing (roughly within 5 to 25 cm^{-1} of line center).

This study involves the collection and analysis of a large number of laboratory spectra of high optical depth H_2O to improve our knowledge of the ν_2 in-band H_2O continuum and near-wing lineshape. Measurements of the H_2O continuum in the 1200-2200 cm^{-1} region have been performed with a high resolution Fourier transform spectrometer.

Several factors combine to make this a timely study: (1) AIRS needs accurate H_2O continuum spectroscopy in this spectral region for successful remote sensing of daily, global humidity profiles, (2) Atmospheric (HIS) measurements have shown significant errors in the existing continuum models which can be ascribed to both model deficiencies and errors in the laboratory measurements on which these models are based, (3) Recent work by Theriault *et.al.* examined the low wavenumber edge of this region and found very large differences with the existing continuum model. (4) R. Toth of NASA/JPL has recently done some prerequisite measurements of the H_2O line strengths in the ν_2 band that will allow a more definitive study of the in–band line shape and continuum, (5) Recent theoretical work by Ma and Tipping provides a possible theoretical foundation for analysis of new data, and (6) The Molecular Physics Division of NIST/Gaithersburg (Walter Lafferty, Bruce Olson) have developed a long–path cell coupled to a high–resolution BOMEM FTS that was available for this research.

Background information and relevant experimental and theoretical studies, as well as an actual definition (an empirical, somewhat arbitrary definition) of the continuum, are presented in Section 4.2, followed by a more detailed description of the problem under investigation in this work. Section 4.3 describes the experimental set-up and procedures used to collect the transmission spectra. The remainder of the study is concerned with the analysis of these spectra. A brief overview of the molecular spectroscopy of water vapor in Appendix D. Section 4.4 describes some general analysis issues such as the accuracy of the spectral line parameters used to reduce the spectra and the determination the amount of water vapor in the cell. In Section 4.7, the analysis of the spectra for regions chosen to be in-between the strong absorption lines and comparisons to existing measurements and models is presented. The spectra are then analyzed closer to the lines in Section 4.10 to characterize the near-wing lineshape. Finally, self- and nitrogen-broadened χ-functions are determined from the spectra and compared to present lineshape theories. Some of these results have been incorporated into a line-by-line radiative transfer code and compared to validated HIS atmospheric radiances.

4.2 Previous Studies and Background Information

Deviations of H_2O spectral lineshapes from Lorentz have been studied extensively for the atmospheric windows at 4 and 10 μm. In general, these deviations are observed to vary slowly with wavenumber and the anomalous absorption has become known as the water vapor continuum. Due to the lack of an accepted reference lineshape to express these deviations, inconsistent treatments of distant absorption lines, and the lack of a theoretical basis for this absorption, conclusions about the magnitude of these deviations and whether they represent a surplus or deficit of absorption as compared to impact theory varied widely in the past.

Several characteristics were found to be common to all window region continuum studies. In general, the continuum absorption [69,70, for example]: (1) does not change rapidly with wavenumber, (2) decreases rapidly with increasing temperature for pure water vapor, (3) is greater for self-broadening than for foreign broadening, (4) is more significant in regions of weak absorption than in regions of strong absorption, and (5) displays the pressure dependencies associated with gaseous absorption.

For some studies showing an excess of absorption over impact theory, the possibility of absorption by the water vapor dimer or even larger clusters of H_2O monomers was raised as a possible explanation. Dimer populations are known to decrease rapidly with increasing temperature, and thus they were targeted as a possible source of the continuum absorption. Studies show, however, that under atmospheric conditions, dimers lack the large populations needed to account for the observed deviations.

A more accepted conclusion is that the deviations from the impact theory calculations in window regions are due to the non-Lorentz behavior of the far-wings of pure rotational and vibration-rotation water vapor absorption lines. Based on the consistent analysis of several sources of experimental data and on recent theoretical advances in the water vapor far-wing lineshape, this conclusion, in fact, appears to be the logical cause of the water vapor continuum.

In the following sections, a review of previous studies of this continuum absorption is presented. These can be separated into two generally different approaches. The first, which is most often adopted in experimental studies, is to express the observed deviations from Lorentzian behavior through the use of *continuum coefficients*. With this method, the cumulative effects of all lines are characterized in a convenient form. The second approach, which provides more information about the shape of individual spectral lines, is used in most theoretical studies. χ-functions are often the end result of this approach.

4.2.1 A Definition of the Continuum

In order to discuss the nature of the continuum absorption and to compare experimental and theoretical results, the continuum must first be defined. In this work, the definition proposed by Clough is used. This definition is widely used in atmospheric spectroscopy and radiative transfer, particularly in line-by-line codes such as FASCODE [36], GENLN2 [37], LINEPAK [71], and LBLRTM [21]. The "local" absorption for a single transition is defined as a Lorentz lineshape out to $\pm 25\text{cm}^{-1}$ from the line center, minus the Lorentz value at 25cm^{-1}. For several lines, the local absorption is expressed as [72]

$$k_{local}(\nu) = \nu \tanh\left(\beta\nu/2\right) \rho_{ref} \frac{T_{ref}}{T} P_{H_2O} L \sum_i \frac{S_i}{\pi} \begin{cases} \frac{\gamma_i}{\Delta\nu^2+\gamma_i^2} - \frac{\gamma_i}{25^2+\gamma_i^2} & \text{if } |\Delta\nu| \leq 25\text{cm}^{-1} \\ 0 & \text{if } |\Delta\nu| > 25\text{cm}^{-1} \end{cases} \tag{4.1}$$

where $T_{ref} = 273.15K$, ρ_{ref} is the absorber number density per atmosphere at T_{ref}, $\beta = hc/kT$, and $\Delta\nu = \nu - \nu_i$. All of the continuum measurements presented in this work are consistent with Equation 4.1. This is actually a slight modification of Clough's definition[1], which also includes the negative resonance terms ($\frac{\gamma_i}{(\nu+\nu_i)^2+\gamma_i^2}$). In the infrared region (actually for $\nu > 25$ cm^{-1}), the two definitions are equal. *The continuum*

[1] Equations 6 through 8 of Reference [72] do not reflect the local lineshape definition used in FASCODE. They actually lead to a χ dependent local lineshape, which is not used in the line-by-line codes.

is then simply defined to be any observed absorption not attributable to the local absorption. The continuum therefore includes far-wing absorption (beyond 25cm^{-1} from line center), absorption due to any near-wing (within 25cm^{-1}) non-Lorentz behavior, and the Lorentzian value at 25cm^{-1} within $\pm$25cm^{-1} of line center (this is often called the "basement" term). This is illustrated in Figure 4.2 for a single absorption line. The "basement" term is a relatively minor part of the continuum and is introduced to ensure a smooth continuum for computational reasons. If the basement term were not included, the continuum would have discontinuities at $\pm$25 cm^{-1} from line centers and the resulting total continuum could not be smoothly interpolated across regions which contain many strong absorption lines. This definition of the continuum is not the most physically intuitive definition, but the main point here is that in order to compare independent measurements and calculations, a consistent definition must be used.

It should be noted that with this definition of the local absorption, the continuum is always a positive quantity. The basement and far-wing components are certainly always positive. The near-wing component, which represents the difference between the actual lineshape and Lorentz within 25 cm^{-1}, is also positive because water vapor has a super-Lorentzian lineshape in this region. It should also be noted that with this definition, a non-zero continuum exists even for the Lorentz lineshape. A calculation of the total absorption coefficient and the continuum absorption (total minus local) using the Lorentz lineshape for the 0-4000 cm^{-1} region is shown in Figure 4.3. All of the high frequency components of the absorption are contained in k_{local} and the continuum is therefore a smoothly varying function. Using this formalism in a line-by-line code, the effects of all lines beyond 25 cm^{-1} of the frequency of interest can be stored as the continuum in a look-up table, saving the need to include these lines in the local calculation and greatly reducing calculation times.

In the line-wings, the displacement $\Delta\nu$ is much greater than the halfwidth γ and the Lorentz terms can be approximated as $\frac{\gamma_i}{\Delta\nu^2}$. This leads to a quadratic pressure

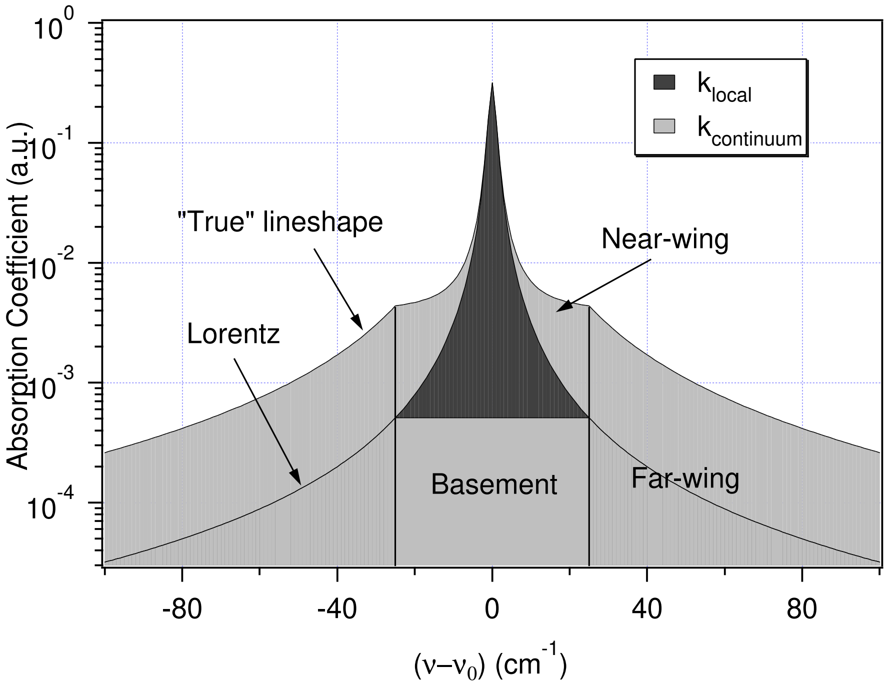

Figure 4.2: The local lineshape definition used in this work. The far-wing (beyond 25 cm^{-1}), near-wing (within 25 cm^{-1}), and basement components of the continuum are labeled.

dependence in the absorption coefficient on P_{H_2O} for self-broadened water vapor and a linear dependence on both P_{H_2O} and the broadening pressure, P_f, for foreign broadened water vapor. Since the continuum is mainly due to line wings, the total continuum absorption coefficient for all lines is formulated as [69, 72]

$$k_{con}(\nu) = \nu \tanh(\beta\nu/2)\, \rho_{ref} \frac{T_{ref}}{T} P_{H_2O} L \frac{296}{T} \left(P_{H_2O} C_s^0(\nu, T) + P_f C_f^0(\nu, T) \right) \tag{4.2}$$

where C_s^0 and C_f^0 are the self- and foreign-broadened continuum coefficients at 296K and 1 atmosphere. To express experimental and theoretical results, the quantities C_f^0 and C_s^0 are often used.

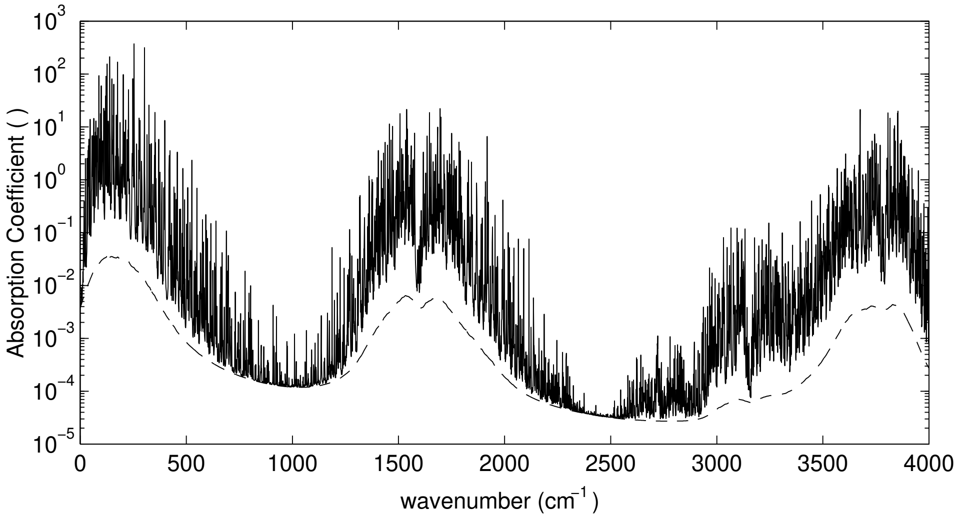

Figure 4.3: Absorption coefficient calculations using the Lorentz lineshape for 0-4000 cm^{-1} at ~2 cm^{-1} resolution. The total (solid curve) and continuum (dashed curve, as defined by Equation 4.1) absorption coefficients are shown. The calculations include the effects of all lines between 0 and 5000 cm^{-1}. Conditions are: 1 torr H_2O, 760 torr N_2, 12 m path length, 296K.

4.2.2 Window Regions Measurements

A large number of measurements, done both in the laboratory and in the field [73–76, for example] have been performed to characterize the window region continuum. Measurements techniques include: ground, aircraft, and ship-based atmospheric radiance measurements with interferometers, grating spectrometers, and radiometers, long path atmospheric absorption using broad band sources and filters, spectrophones and White-cells with CO_2 lasers, White-cells with spectrometers and tunable diode lasers, and several others. Several thorough reviews of these works exist [70, 77, for example], and will not be repeated here. Because absorption in the windows is very weak, all of these techniques require very long path lengths. The laboratory studies have focussed primarily on self- and nitrogen broadening at room temperature or above, while most atmospheric measurements have naturally looked at air-broadening at room temperature or below. Most of the results from these measurements are in accord with those of Burch *et.al.*, which are discussed below.

4.2.3 Laboratory Measurements of Burch *et.al.*

The most notable experimental studies of the water vapor continuum are those of Burch and co-workers [69, 78–81]. In fact, they are the only investigators known to this author who have performed laboratory measurements of the continuum within the fundamental ν_2 band. Their work was carried out a number of years ago at relatively low spectral resolution (~0.5 cm^{-1} at 1500 cm^{-1}) using a grating spectrometer coupled to a White cell. Self and nitrogen broadened spectra were collected for a range of temperatures and pressures. Within the ν_2 band, the wavenumber regions for these studies were chosen to be at the center of the so-called microwindows such that the absorption due to lines within ~1cm^{-1} could be ignored and so the low instrument resolution would not distort the spectra. As a result, the number of continuum measurements within the ν_2 band was relatively small (13 points between 1400 and 1850 cm^{-1}). A compilation of these measurements is shown in Figure 4.4 for self-broadened water vapor and in Figure 4.5 for nitrogen-broadened water vapor. The continuum coefficients shown in these figures have been modified [2] from their published values to be consistent with Equation 4.1. Van Vleck-Weisskopf continuum coefficients are also shown for comparison. Obvious conclusions from these measurements is that the impact theory predicts too much absorption in the window regions at 4 and 10μm and not enough within the rotation-vibration bands. Due to a lack of other laboratory measurements and because these in-band regions are dominated by near-wing lineshapes, Burch's measurements have led to most of our present understanding of near-wing lineshapes and have formed the benchmark for theoretical comparisons within the ν_2 band. Furthermore, they have been used to produce empirical lineshapes which are used in operational radiative transfer codes and band models which in turn are used

[2]Thanks to S. A. Clough for providing these data.

in Global Climate Models. The accuracy of these measurements is therefore crucial for several applications and is deserving of investigation.

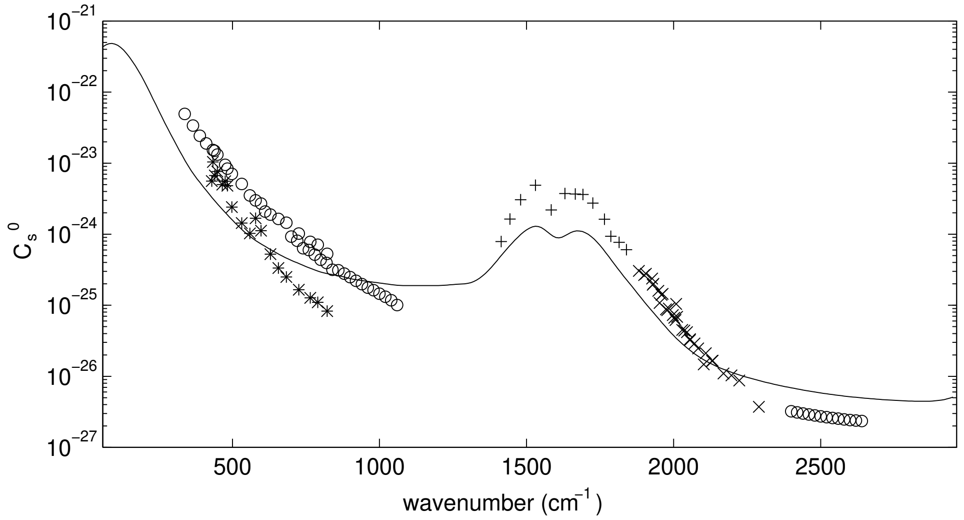

Figure 4.4: Burch's measurements of C_s^0 and impact theory calculations (solid curve) from 0 to 3000 cm^{-1}. Measurements are shown for temperatures of 296K (circles), 308K (+'s), and 322K (x's), and 430K (asterisks).

4.2.4 Theoretical Studies

A recent article by Tipping and Ma [21] contains a useful summary of the history of theoretical work on water vapor lineshapes and will not be repeated in detail here. Only the works of Clough, Davies, Rosenkranz, and Ma and Tipping will be outlined.

Considerable progress in the last 15 years was initiated by Clough *et.al.* [82] with the development of a rigorous foundation for an autocorrelation function approach that takes finite duration of collisions into account. Following the approach of Anderson and Weiss [83], the impact approximation was modified by eliminating discontinuities in the derivative of the autocorrelation function at the time of a collision, resulting in a Gaussian shape in the far-wing. This resulted in an improvement over the impact approximation, yet was still unable to explain the continuum measurements. For pure

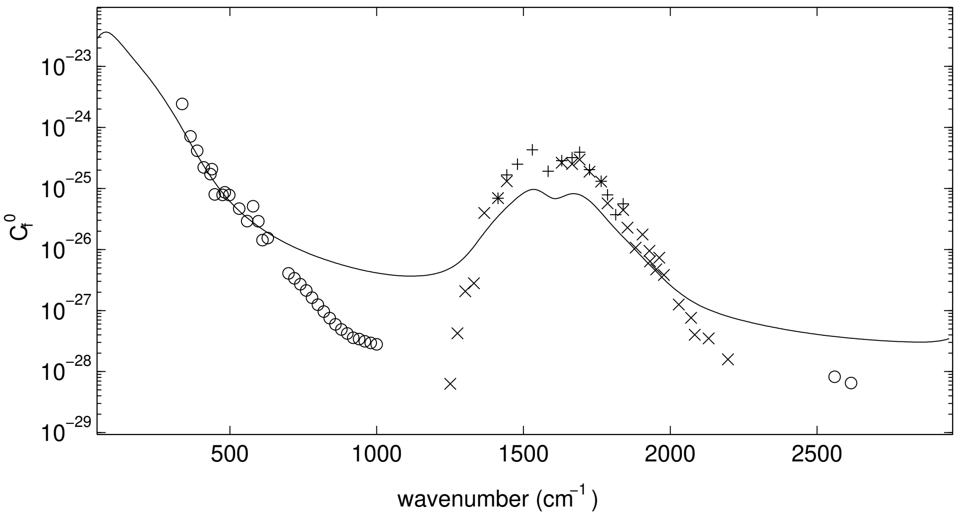

Figure 4.5: Burch's measurements of C_f^0 and impact theory calculations (solid curve) from 0 to 3000 cm^{-1}. Measurements are shown for temperatures of 296K (circles), 308K (+'s), and 353K (x's).

water vapor, the theory was parameterized by introducing an empirical expression for the continuum. This included several adjustable parameters which were determined by fitting the model to data at 0 cm^{-1} and 300–1200 cm^{-1}. This greatly improved the agreement between theory and experiment over impact theory and provided a realistic physical framework for future parameterizations [72, 84], which are discussed in section 4.2.5.

The foundation for further theoretical advances was developed by Davies *et.al.* [85]. Rather than develop a model of the autocorrelation function, an explicit microscopic description of the short-time behavior (during a collision) of the autocorrelation function and the transition to the long-time impact result was developed. The resulting lineshape, which is not specific to water vapor, displayed the usual Lorentz behavior in the near-wing and also decayed exponentially in the far-wing.

Following the basic formalism of Davies, Rosenkranz [16,86] developed a lineshape based on the quasi-static approximation for the high frequency wing of the pure rotational band of water vapor (300-1100 cm^{-1}) for self- and nitrogen-broadening. An absorber-perturber potential of Lennard-Jones form was used. Parameters in the potential were adjusted to match Burch's continuum measurements at 764.6 and 900.0 cm^{-1} at 296K. These calculations reproduced the magnitude and the negative temperature dependence of the observed continuum absorption remarkably well. Aside from the quasi-static approximation, the approximations which this theory makes are (1) the far-wing, high-frequency approximation that the observation frequency is much greater than the resonant frequencies ($\nu \gg \nu_i$) and (2) the narrow band approximation that the observation frequency is much greater than the differences in the resonant frequencies ($\nu \gg \nu_i - \nu_j$). As a result, this theory ignores the detailed effects of in-band line-mixing and is suitable only in the far-wing.

Ma and Tipping [87] extended Rosenkranz's approach to include more allowable rotational states in the calculations (up to J=4) and applied the results to the high wavenumber wing of the ν_2 band. Using the same approach, but proceeding in a completely different way mathematically, the high-frequency approximation was avoided and a theory applicable to the low frequency wing of the pure rotational band was also developed [88]. In all cases, reasonably good agreement between the calculations and measured continuum was found.

Ma and Tipping [21, 89] have also developed a quasi-static theory which has been generalized for use within vibration-rotation bands [90] and for foreign broadening [91]. A Lennard-Jones potential is used, with the various constants determined from compressibility measurements and thus contains no adjustable parameters. Their extensive work can reproduce many of the existing window region measurements to an accuracy that validates their approach in the far wings of lines, but is not sufficiently accurate for some applications due to inaccuracies in the near-wing [84].

The calculations by Rosenkranz and by Ma and Tipping can be expressed with χ-functions. Given these χ-functions, the absorption coefficients are calculated using [21]

$$k(\nu) = n_a \sum_i \frac{S_i}{\pi} \frac{\nu \sinh(\beta\nu/T)}{\nu_i \sinh(\beta\nu_i/T)} \left(\frac{1}{(\nu - \nu_i)^2} \chi_+(\nu - \nu_i) + \frac{1}{(\nu + \nu_i)^2} \chi_-(\nu + \nu_i) \right) \quad (4.3)$$

where n_a represents the absorber amount. Notice that the width terms are missing from the $\frac{1}{(\nu \pm \nu_i)^2}$ displacement terms due the far-wing nature of these theories. Thus, all of the broadening information has come from the potentials and is contained in the χ-functions. The only other inputs are the line centers and strengths. The same χ-function is used for all lines. In light of the fact that water vapor half-widths vary widely from line to line, these are potentially the most significant and limiting approximations for calculations performed within the ν_2 band.

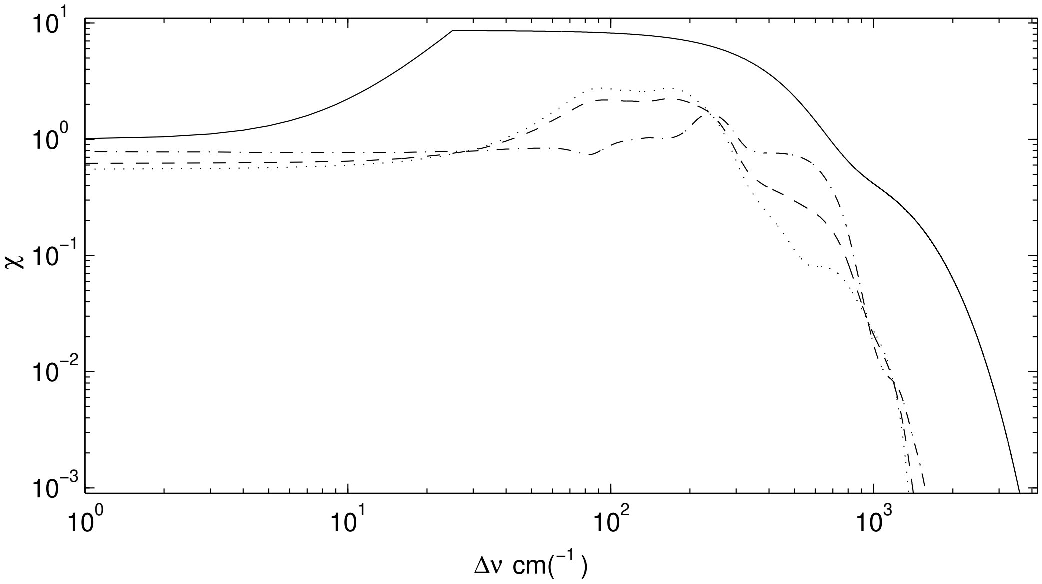

Figure 4.6: Self-broadened χ-functions of Rosenkranz, Ma and Tipping, and Clough at 296K. The dashed curve is from Rosenkranz's calculations ($\chi_+ = \chi_-$). Ma and Tipping's χ_+ and χ_- are the dotted and dash-dot curves, respectively. These functions have all been set to 1 at line center. The solid curve is Clough's CKDv0 χ-function.

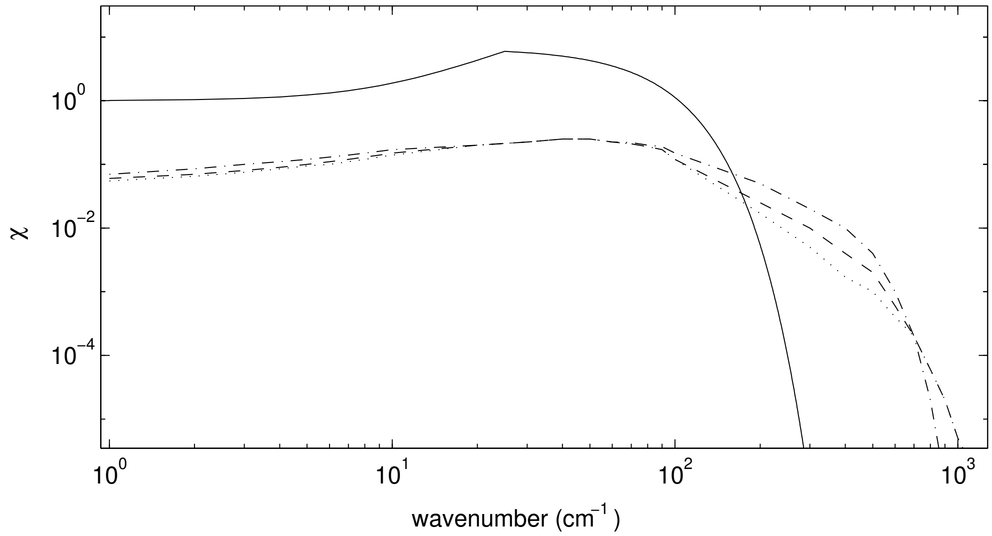

Figure 4.7: N_2-broadened χ-functions of Rosenkranz, Ma and Tipping, and Clough at 296K. The dashed curve is from Rosenkranz's calculations ($\chi_+ = \chi_-$). Ma and Tipping's χ_+ and χ_- are the dotted and dash-dot curves, respectively. These functions have all been set to 1 at line center. The solid curve is Clough's CKDv0 χ-function.

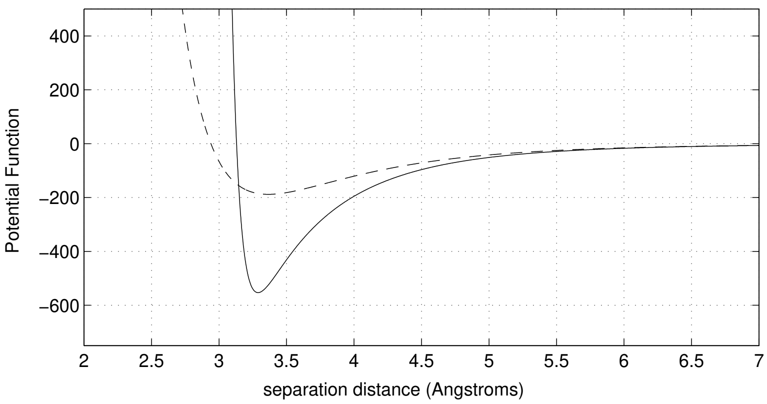

Figure 4.8: Scalar part of the H_2O-H_2O (solid curve) and H_2O-N_2 (dashed curve) intermolecular potentials used in Rosenkranz's calculations.

The χ-functions of Equation 4.3 are shown in Figures 4.6 and 4.7 for self- and nitrogen-broadened water vapor at 296K. Due to their far-wing nature and inaccuracies in the near wing, these χ-functions do not necessarily become Lorentz at line center. Also shown in the figures are empirical χ-functions of Clough *et.al.* which are presented in the next section. The self-broadened χ-functions of Rosenkranz and Ma and Tipping remain essentially constant for $\Delta\nu < 10$ cm^{-1}, become extremely super-Lorentzian near 100 cm^{-1}, and then fall off rapidly near 1000 cm^{-1}. For nitrogen-broadening, the χ-functions increase gradually to about $\sim$300 cm^{-1} from line center, and fall off rapidly near 1000 cm^{-1}.

Qualitatively, the behavior of the χ-functions can be described by the considering the shape of the intermolecular potentials, which are shown in Figure 4.8. The potentials in this figure are actually only the scalar part of the intermolecular potentials; the complete potential includes these terms and the electrostatic interaction which is given by Gr^{-m}, where G contains all of the dependence on the rotational states of the absorber and perturber, m=3 for dipole-dipole interaction, and m=4 for dipole-quadrupole interaction. This approach of representing the intermolecular potential as the sum of a spherical part and an anisotropic part consisting of the leading multipole term was reviewed in Section 2.3. The rapid fall-off of χ in the far-wings is due to the repulsive parts of the potentials which limit the closeness of the interacting molecules and therefore also the perturbation of transition frequencies during a collision. The super-Lorentzian nature of the χ-functions in the intermediate wing is due in part to the attractive terms in the potentials. The attractive potential increases the relative velocity of the colliding molecules, leading to higher frequency components in the line-shape for this region. The self-broadening χ-functions also have more structure than the nitrogen-broadened χ-functions, which is partially due to the narrow and deeper potential well of the H_2O-H_2O potential.

The isotropic potentials shown in Figure 4.8 are Lennard-Jones type of the form

$$V(r) = C\sigma^{-6}\left((\frac{\sigma}{r})^{s} - (\frac{\sigma}{r})^{6}\right) \tag{4.4}$$

where C, σ, and s are constants which have been determined from compressibility

Reference	Source	s	$\sigma(A)$	$C(10^5 A^6 K)$	perturber
[]	compressibility	12	2.65	5.3	H_2O
[]	compressibility	18	2.71	5.2	H_2O
[]	compressibility	24	2.76	5.1	H_2O
[]	compressibility	∞	3.16	8.0	H_2O
[16]	IR absorption	48	3.13	8.0	H_2O
[]	compressibility	12	3.14	8.2	N_2
[16]	IR absorption	9	2.94	8.2	N_2

Table 4.1: C, σ and s of the scalar part of the water vapor intermolecular potential.

measurements and by Rosenkranz by adjusting their values to agree with Burch's data in the 500–1100 cm^{-1} region. These values are listed in Table 4.1. At large separations, the potential falls off as r^{-6}, as suggested by theoretical investigation of the dispersive forces. The short range varies as r^{-s} in contrast to the e^{-Br} and $1/r$ forms suggested by theory. Intermediate range forces leading to the potential wells are determined by adopting the $s-6$ functional form.

These χ-functions are inherently least accurate near line center. For self-broadening, Ma and Tipping have provided a near-wing correction term for their χ-functions [92], but still within the quasi-static framework. However, within 10 cm^{-1} of line center, the approximations used to derive this correction term, and the quasistatic approximation itself, are not valid [92].

In summary, despite many efforts an accurate near-wing lineshape does not exist. This is due in part to (1) the inaccuracy of quasi-static calculations in the near-wing, (2) the lack of accurate intermediate-range intermolecular potentials, and (3) the of a lack of adequate laboratory data for testing of theory. These considerations have prompted the measurements presented in this work.

4.2.5 Clough's CKD Continuum Models

All of the theoretical approaches discussed above have been oriented toward modeling far-wing non-Lorentz behavior in order to predict radiative transfer in the atmospheric windows and consequently are least accurate in the near-wing of the line, which is also more difficult to handle theoretically. The very near-wing lineshape is determined primarily by the long range interaction and the number of collisions per second experienced by the absorber. The far-wing is determined by the durations of the very fast, close collisions which are governed by the strong repulsive potential at small separation distances. The near/intermediate-wing lineshape, however, requires an accurate description of the absorber-perturber interaction for all intermediate time scales, as well as for all separation distances and angular orientations. This becomes a complicated two-body problem involving not only the long range interaction, but also other short-lived electrostatic interactions which arise at shorter separation distances.

Lacking an accurate intermediate-wing lineshape model, Clough *et.al.* [72, 84] have developed empirical models of the continuum to obtain the best overall agreement with measurements in both the window regions and within the bands. These models are widely used in a variety of atmospheric applications. Clough's model expresses the absorption coefficient as

$$k(\nu) = \nu \tanh(\beta\nu/2) \sum_i \frac{S_i}{\pi} \left(\frac{\gamma_i}{(\nu-\nu_i)^2+\gamma^2} \chi(\nu-\nu_i) + \frac{\gamma_i}{(\nu+\nu_i)^2+\gamma^2} \chi(\nu+\nu_i) \right) \quad (4.5)$$

χ is an empirical function used to include non-Lorentz behavior and is given by

$$\chi = \left(\begin{array}{ll} 1-(1-\chi')\frac{(\nu\pm\nu_i)}{25^2} & \text{for } |\nu\pm\nu_i| \le 25\text{cm}^{-1} \\ \chi' & \text{for } |\nu\pm\nu_i| \ge 25\text{cm}^{-1} \end{array} \right. \quad (4.6)$$

where χ' is determined empirically. These models, which are known as the CKD (Clough, Kneizys, Davies) continuum models, are shown in Figures 4.6 and 4.7, along with the results of Rosenkranz and Ma and Tipping.

The original CKD model (CKDv0) was developed by fitting Equation 4.5 (with the use of line parameters from the 1986 HITRAN database) to match the laboratory continuum measurements of Burch, which are shown in Figures 4.4 and 4.5. The values of χ' were determined to be:

$$\chi' = 8.63 \exp(-z_1^2) + (0.83 z_2^2 + 0.033 z_2^4) \exp(-|z_2|) \tag{4.7}$$

with $z_1 = \frac{\nu \pm \nu_i}{400}$ and $z_2 = \frac{\nu \pm \nu_i}{250}$ for self-broadened H_2O, and

$$\chi' = 6.65 \exp(-z_1^2) \tag{4.8}$$

with $z_1 = \frac{\nu \pm \nu_i}{75}$ for nitrogen broadened H_2O.

The functional form of Equation 4.6 was chosen because of the known near and far-wing behavior. The χ-functions were held fixed at 1 at line center, adjusted to some value in the intermediate wing, and then forced to decay exponentially in the far-wing. Because Burch's measurements included in-band as well as window region measurements, Clough's χ-functions were forced to assume the correct overall behavior in the near, intermediate, and far-wing. It should be noted that the form of the χ-functions between 0 and 25 cm^{-1} has no direct physical justification, but was adopted simply to interpolate between the line center and fitted region.

Burch's measurements and continuum coefficients computed with CKDv0 and by Ma and Tipping are shown in Figures 4.9 and 4.10. Also shown are two subsequent CKD models: CKDv1 and CKDv2.1. These newer models represent modifications to CKDv0 made to maintain agreement with measurements. For instance, C_s^0 of the CKDv1 model is given by

$$C_s^0 = C_s^0(\text{version0}) \left(1 - 0.2333 \frac{200^2}{(\nu - 1050)^2 + 200^2}\right) \tag{4.9}$$

which results in a 23 percent reduction at 1050 cm^{-1}, yielding better agreement with HIS field measurements, yet remaining compatible with Burch's laboratory results. Thus, there are no χ-functions associated with the later CKD versions. Measurements which have led to CKDv2.1 are discussed in the next section.

The data shown in Figures 4.9 and 4.10 for Ma and Tipping's calculations were provided by Q. Ma. For these calculations, a Lorentz lineshape was used within 25

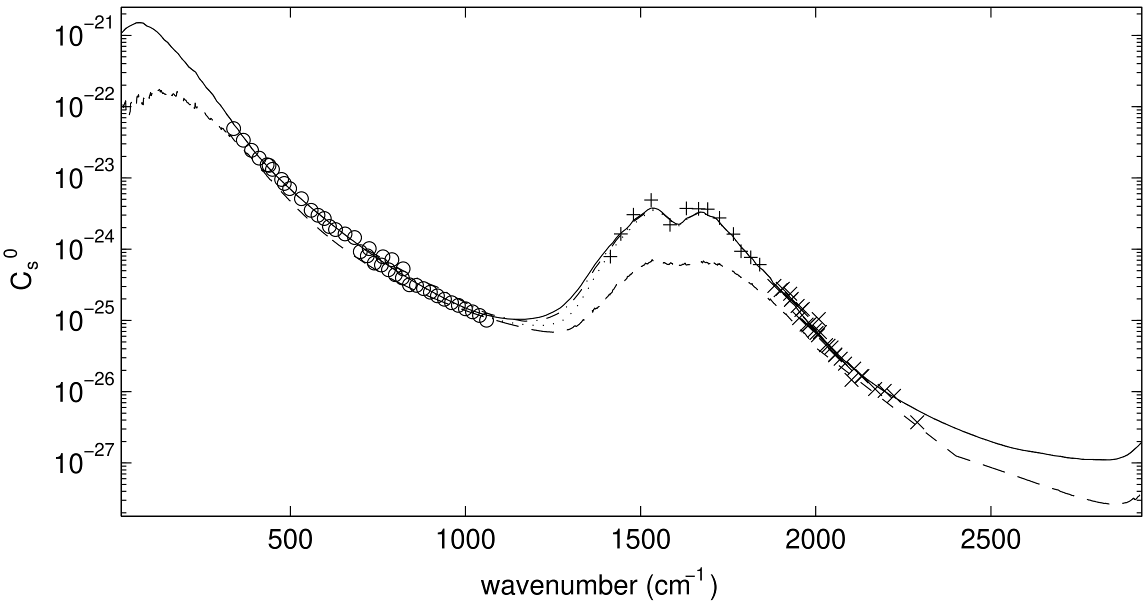

Figure 4.9: Self-broadened continuum coefficients of Ma and Tipping (dashed curve), Burch (circles, 296K; pluses, 308K; x's, 322K), CKDv0(solid curve), CKDv1(dotted curve), CKDv2.1(dash-dot curve).

cm^{-1} of line centers due the inaccuracy of their χ-functions in the near wing. Thus, their coefficients do not include any non-Lorentz behavior within 25 cm^{-1}. Their coefficients have also been modified from their original form by this author to include the basement terms to achieve consistency with the continuum definition.

With an accurate description of the χ-function responsible for the in-band water vapor continuum, its relation to the observed absorption can be presented. In window regions, C_s^0 and C_f^0 vary smoothly with wavenumber since there are relatively few strong local absorption lines. Within strong absorption bands, however, the continuum may be influenced more by high frequency near-wing non-Lorentz behavior and these continuum coefficients may not vary as smoothly with wavenumber. Figure 4.11 shows the individual contributions of the far-wing, near-wing, and basement components to the total continuum (as described in Figure 4.2) in the ν_2 region based on the CKDv0

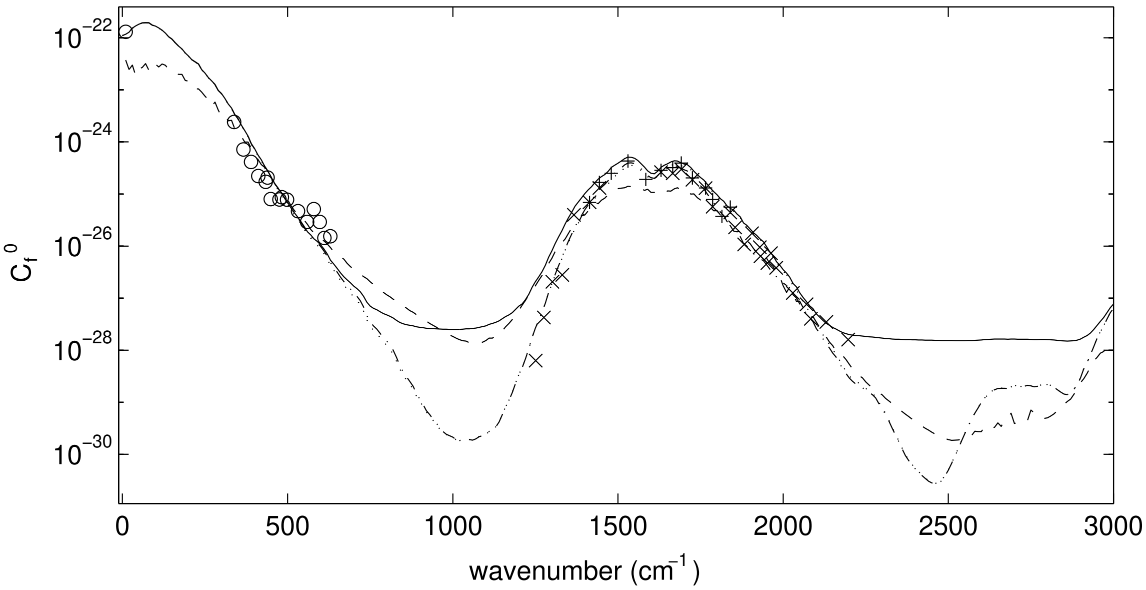

Figure 4.10: Nitrogen-broadened continuum coefficients of Ma and Tipping (dashed curve), Burch (circles, 296K; pluses, 308K; x's, 322K), CKDv0(solid curve), CKDv1(dotted curve), CKDv2.1(dash-dot curve).

χ-function. Although the continuum is dominated by far-wing effects in the wings of the ν_2 band, the near-wing contributions dominate the continuum at the peaks of the P- and R-branches. By studying the continuum in this region, information about the near and intermediate wing lineshape can be determined.

4.2.6 Recent Field Measurements

Recent field measurements have led to modifications in the CKD models. Theriault *et.al.* [93] recently recorded atmospheric transmission spectra over a horizontal path of 5.7 km. These spectra were utilized to test the accuracy of the existing H_2O continuum. Their results suggest that, in the wings of the ν_2 band, the foreign component of the CKDv0 continuum had to be decreased by approximately a factor of 2 to recover good model-measurement agreement. The accuracy of these findings, however, is limited

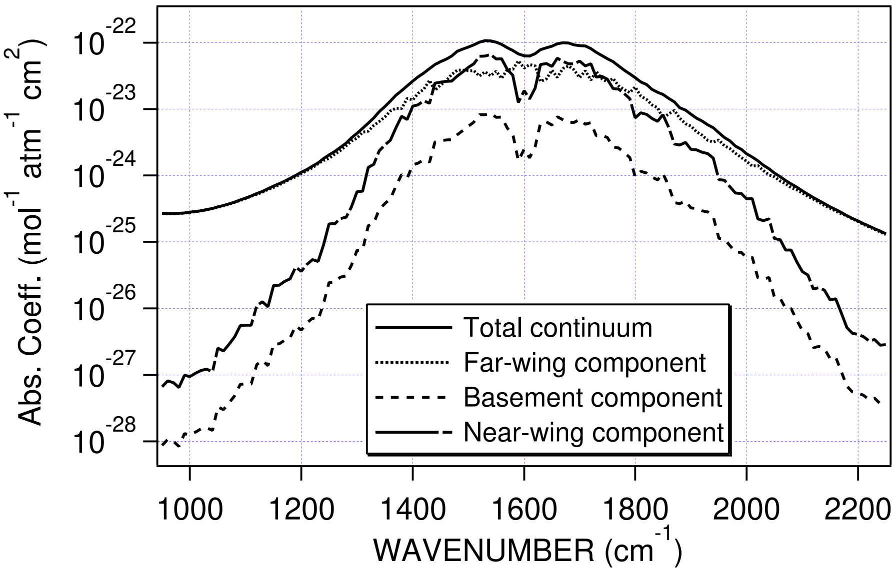

Figure 4.11: The individual contributions of the far-wing (beyond 25 cm^{-1}), near wing (within 25 cm^{-1}), and "basement" components to the total continuum absorption based on the CKDv0 χ-function.

by the nature of the experiment and the difficulties in characterizing the optical path. These measurements are shown in Figure 4.12.

Atmospheric emission spectra from the University of Wisconsin's High Resolution Interferometer (HIS) [23, 93, 94] also show that large errors remain in CKDv0. These spectra are very sensitive to the continuum and provide an excellent test of the models when the atmospheric state is well characterized. Differences between observed and calculated high-resolution atmospheric radiances can be as large as 4K in brightness temperature in-between lines inside the ν_2 band when using CKDv0 [93, 95, 96].

Clough recently modified his continuum model to obtain better agreement with several types of atmospheric observations [84, 93, 94]. In particular, the atmospheric studies suggested that the nitrogen-broadened continuum near $\sim$1200 cm^{-1} was approximately a factor of 2 smaller than predicted by CKDv0. This improved model (CKDv2.1) reduces the maximum errors in HIS calculated radiances to $\sim$2K in-between

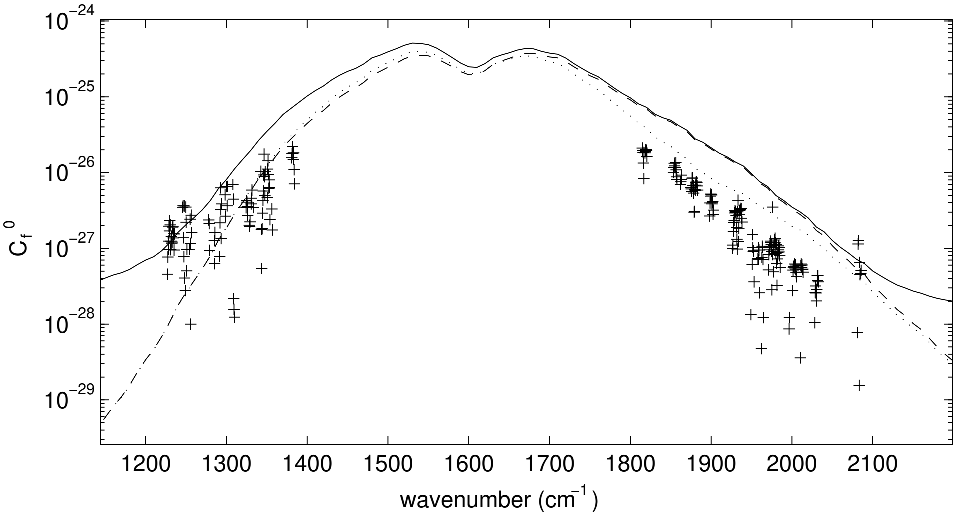

Figure 4.12: Nitrogen broadened continuum coefficients reported by Theriault. The CKD models are also shown: solid, CKDv0; dashed, CKDv1; dotted, CKDv2.1.

spectral lines in the 1200 cm^{-1} region [97]. However, these errors are highly dependent on wavenumber and the newer model also appears to have produced slightly worse results (as compared to CKDv0) further into the band, near the band center. Errors due to CKDv0 and CKDv2.1 for these measurements have been shown in Figure 4.1.

4.2.7 This Research

Despite the considerable progress in theoretical and empirical water vapor lineshapes, large errors remain in the continuum within the ν_2 band. This is partially due to the lack of high resolution laboratory measurements in this region and to the difficulty in determining information about the continuum from atmospheric measurements.

A large series of laboratory spectra of high optical depth H_2O have been recorded to improve our knowledge of the ν_2 in-band H_2O continuum. A main goal is to verify the accuracy of Burch's measurements in this region and to obtain a more dense wavenumber coverage of the continuum for satellite remote sensing applications. These laboratory spectra provide a good test for new theoretical and model calculations, which have been limited by the sparsity of Burch's measurements. We were also prompted to do these measurements because the HIS observations indicated the need for wavenumber dependent changes to the continuum that are initially best studied with laboratory data.

Measurements of the H_2O continuum in the 1350-2100 cm^{-1} region recorded with a high resolution Fourier transform spectrometer are reported. We will first make a direct comparison to the work of Burch in the sense that we first report the continuum at the same wavenumbers as Burch, as well as in other wide microwindows. The main difference between Burch and our work is that our measurements were made at relatively high spectral resolution, generally 0.04 cm^{-1}. Since the wavenumbers chosen by Burch are in microwindows that are largely unaffected by his lower spectral resolution, we should be able to compare our data directly to his. Since existing H_2O continuum models are in large part based on the work of Burch, we felt it was worthwhile to initially examine our data in a form that is directly comparable to his work, and that can be easily used by others for atmospheric calculations in these microwindows. The analysis of continuum measurements made at a much denser wavenumber scale throughout the ν_2 band and the implications for atmospheric H_2O continuum models is presented later in Section 4.8.

Self, nitrogen, and oxygen broadened spectra were recorded. Laboratory measurements of the self-broadened water vapor continuum are very important because it is difficult to measure C_s^0 within the ν_2 band with atmospheric measurements. Given a sea level atmosphere at 310K and 85% relative humidity, the continuum within the ν_2 band is dominated by the foreign broadened component, as seen in Figure 4.13, and the measured continuum has little sensitivity to C_s^0. In the laboratory, however, pure water vapor samples can be studied. Note that the opposite can also be true; that is, C_f^0

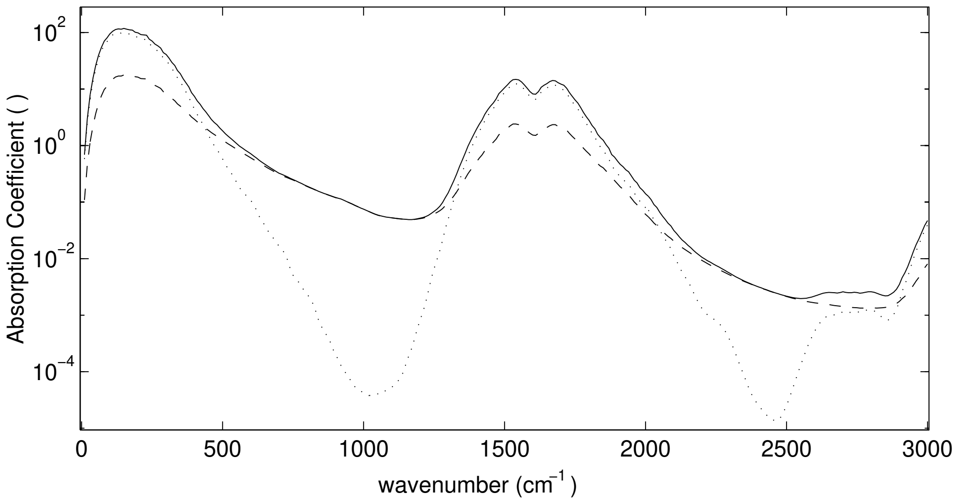

Figure 4.13: Total (solid curve), self-broadened (dashed curve), and foreign-broadened (dotted curve) continuum absorption coefficients calculated with CKDv2.1 for 16 torr H_2O, 760 torr N_2, 310K, and unit path length.

cannot be measured accurately in the window regions with atmospheric measurements.

Nitrogen broadening was investigated due to its obvious importance for atmospheric applications and because most theoretical studies have dealt with the H_2O-N_2 system. Also, most line width studies have been done for nitrogen broadening. Oxygen broadened spectra were also recorded due to its abundance in air. Knowing the effects of both nitrogen and oxygen, the effects for air can be calculated using, *i.e.* $C^0_{air} \simeq 0.80C^0_{N_2} + 0.20C^0_{O_2}$.

Low temperature (260K) spectra were collected for their importance to upper troposphere studies, although we had instrument problems that ultimately corrupted much of these data. Low temperature continuum absorption has not been studied in the laboratory previously, partially due to the inability to introduce large amounts of water vapor into an absorption cell at these temperatures and to the lack of long path length coolable cells. Most studies have used higher temperatures and then extrapolated to lower temperatures.

High pressure nitrogen broadening (up to 9 atmospheres) was also studied due to theoretical interest and simply because an absorption cell capable of these pressures was available. These spectra may prove quite useful for examining the near-wing line-shape, but may be inapplicable to atmospheric studies and present theoretical work because they may be in a regime where the binary collision assumption is invalid.

Most of the above studies were conducted at an unapodized instrument resolution of 0.040 cm^{-1}. This resolution was used for several reasons which are discussed in the following section. Some spectra were also collected at 0.011 cm^{-1} resolution and very low optical depths to test the accuracy of the line widths used in the data analysis.

4.3 Experimental Set-up and Data Collection

This section describes the experimental set-up and data collection process used to collect the transmission spectra. Spectra were collected using the facilities at the National Institute of Standards and Technology (NIST), Molecular Physics Division. Spectra were collected using a Fourier transform spectrometer (FTS) coupled to a long-path absorption cell. This combination is well suited for water vapor continuum measurements for several reasons. FTS can provide the wide spectral coverage needed to cover the entire ν_2 band (over 1000 cm^{-1}). With this large spectra range, using an FTS simplifies the lineshape analysis because its spectral response is largely independent of wavenumber. Long-path absorption cells provide the large optical depths which are needed to measure the absorption *in-between* the spectral lines where the absorption is weakest and where the continuum has its largest effect. Due to condensation above the saturation pressure, only small amounts of water vapor are possible in a cell at room temperature, and thus the large optical depths must be achieved with long path lengths. The spectrometer at NIST has a maximum resolution of 0.002 cm^{-1} and the absorption cell is capable of optical path lengths up to 84 meters.

The measurement concept is simple. Radiation from a broad band source passes through the FTS. This modulated radiation then passes through the absorption cell and onto the detector. The radiation is recorded as a function of the optical path difference of the FTS and an interferogram is produced. Radiances are obtained by simply taking the Fourier transform of the interferogram. If the absorption cell is empty, the recorded spectrum characterizes only the effects of the spectrometer (source, beam splitter, apertures, etc...), the various windows and filters, the absorption cell, and the detector. When an absorbing gas is in the cell, some of the input radiation is absorbed. The ratio of the sample radiances to the empty cell radiances is the transmission spectrum.

The FTS used in this work was manufactured by BOMEM, Inc. This spectrometer can be operated under complete computer control. The movable mirror is adjusted with scanning motors and the optical path difference monitored with the interference fringes of a reference HeNe laser. The FTS can be configured to run for a defined number of scans to reach a desired signal-to-noise ratio. Outputs, including the raw interferograms and other data, are converted to binary and saved to disk.

4.3.1 Spectra Collected at NIST

The experimental data presented in this section were collected at the Molecular Physics Division of the National Institute of Standards and Technology in the summer and fall of 1994. The instrument and the cell performed remarkably well throughout this time and a large set of high quality spectra were collected. This is due to several factors including (1) the optical and mechanical stability of the absorption cell and transfer optics, (2) the stability of the absorption cell as an inert container for the gas mixtures, and (3) the choice to collect data at a moderate resolution. The one drawback with this system was the lack of a port for a relative humidity probe.[3] The addition of a probe would have required the drilling of a rather large hole through the body of the cell.

Self, nitrogen, and oxygen broadened spectra were recorded at room temperature for path lengths of 12, 44, and 84 meters. Water vapor pressures ranging from 0.1 to 15 torr and total pressures up to 9 atmospheres were used.

4.3.1.1 Experimental Set-up

Spectra were collected using an FTS (BOMEM, Inc.,Model DA3.002) connected to a VAX mini computer and a custom White-type long path absorption cell. Figure 4.14 shows a schematic diagram of the experimental setup.

Spectra were recorded using a broad band Globar (heated ceramic) source, a KBr beam-splitter, CaF_2 windows on the input and output ports of the absorption cell, and a narrow range MgCdTe detector. The beam splitter and window materials were chosen

[3]The cell was originally designed to study the molecular spectroscopy of more exotic species and it was never imagined that it would be intentionally exposed to water vapor.

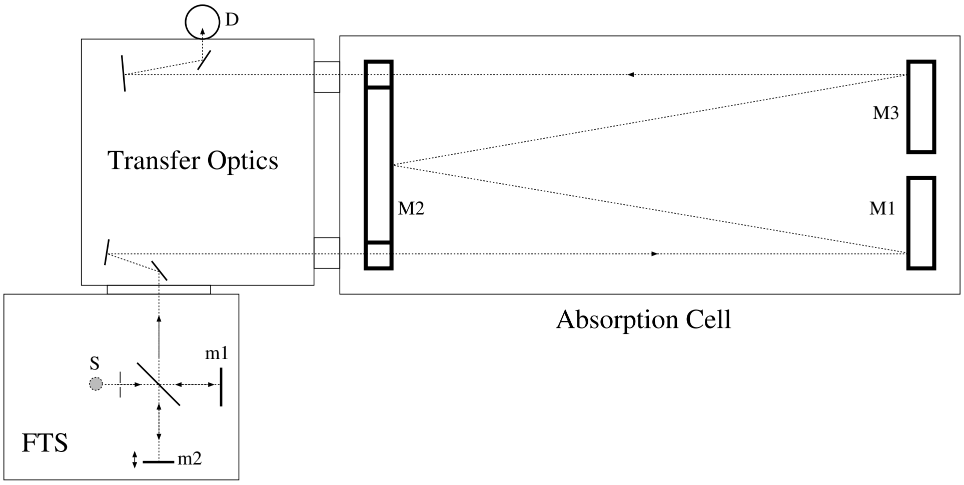

Figure 4.14: Experimental set-up at NIST. Labeled are the: source (S), fixed (m1) and movable mirrors (m2), field mirror (M2), back mirrors (M1, M3), and detector (D). Not drawn to scale. (The optical layout of the FTS in the figure is a simplification; the details of the design are available from BOMEM.)

for their transparency within the ν_2 region.[4] We did consider using KBr windows, but these are highly hydroscopic and would have limited the H_2O cell pressure to less than ~5 torr.

Source aperture diameters of 3.5mm (84 meter path length) and 5mm (12 and 44 meter path lengths) were used for most spectra. These choices were compromises between getting the highest signal through to the detector and also fitting all of the source images onto the field mirror of the multi-pass cell without overlapping the images.

4.3.1.1.1 Multiple Reflection Absorption Cell. The cell has a base path length of 2 meters and possible optical path lengths of 4, 12, 20, 28m, etc. The front and two back mirrors are made of Zerodur and are mounted on a frame connected rigidly only

[4]Originally, because CaF_2 begins to cut out light below ~1200 cm^{-1}, we had hoped to use BaF_2, IRTRANS (ZnSe), or Thallium Bromoiodide (KRS-5) windows but these were unavailable during our time on the instrument. Due to the high pressure design of the cell, these windows must be rather thick (6 mm) and are therefore expensive and hard to find.

to the front end of the enclosing tank. The separation of the mirrors is maintained by four rods of superinvar for temperature independence of the optical system. The rest of the system is fabricated of stainless steel, and is sealed with fluorosilicone O-rings.

The path length is adjusted by changing the inclination of the field mirrors at the back end of the cell so that the desired number of passes is achieved and the exiting beam passes through the exit port and onto the detector. The volume of the cell is approximately 3×10^6 cc. The entire optical path from the FTS to the detector can be evacuated. Two vacuum pumps, a diffusion pump capable of pumping the cell to well below 0.001 torr, and a mechanical pump are configured to the cell. Additionally, the FTS has its own mechanical vacuum pump. Three capacitance pressure gauges are located on a port at the center of the cell with full-scale pressure ranges of 10, 100, and 1000 torr and accuracies better than 1% of the full scale reading. A manifold for inputting various gases is attached at the back end of the cell. The cell can be pressurized up to 12 atmospheres. For these higher pressures, a Heise pressure gauge is used. The cell can be cooled to ~230K with an accuracy of ±0.5K over the entire cell volume by circulating methanol cooled with liquid nitrogen through a coil of copper wrapped around the cell and end-plates. A feedback control system using a thermocouple mounted in the methanol stream just outside the cell is used to regulate the coolant flow. The temperature of the cell is monitored with three thermocouples mounted on the Invar optical frame in the cell. Once thermal equilibrium is reached at low temperature, these agree to better than ±0.5K. The cell is also wrapped with insulation to minimize heat transfer.

The BOMEM DA3.002 FTS has, for the largest aperture a diameter of 1 cm, a beamsplitter radius of 3.81 cm, and a focal length of 45.72 cm. Thus the square root of the etendue divided by π is 1/24 cm for this aperture. The evacuated transfer optics puts an image of the FTS magnified by a factor of 3.175, radius R_a = 1.587cm, at the entrance of the White cell, and simultaneously, without use of a field lens, puts an image of the beamsplitter of radius 5.2493 cm on the top back mirror of the White cell, thus matching the etendue of the White cell to that of the FTS. The height of the front mirror is large enough to permit 22 transits for a 44 meter path length with this maximum image size. For other FTS apertures: 7mm allows 30 transits, 5 mm allows 42 transits, and 3.5 mm allows 58 transits. Some adjustment of the transfer optics is required when changing aperture size, since the bottom of the circular input image must be tangent to the upper edge of the front mirror for close packing of the images in columns. Details of the optical design of the cell are given by Tobin *et.al.* [98].

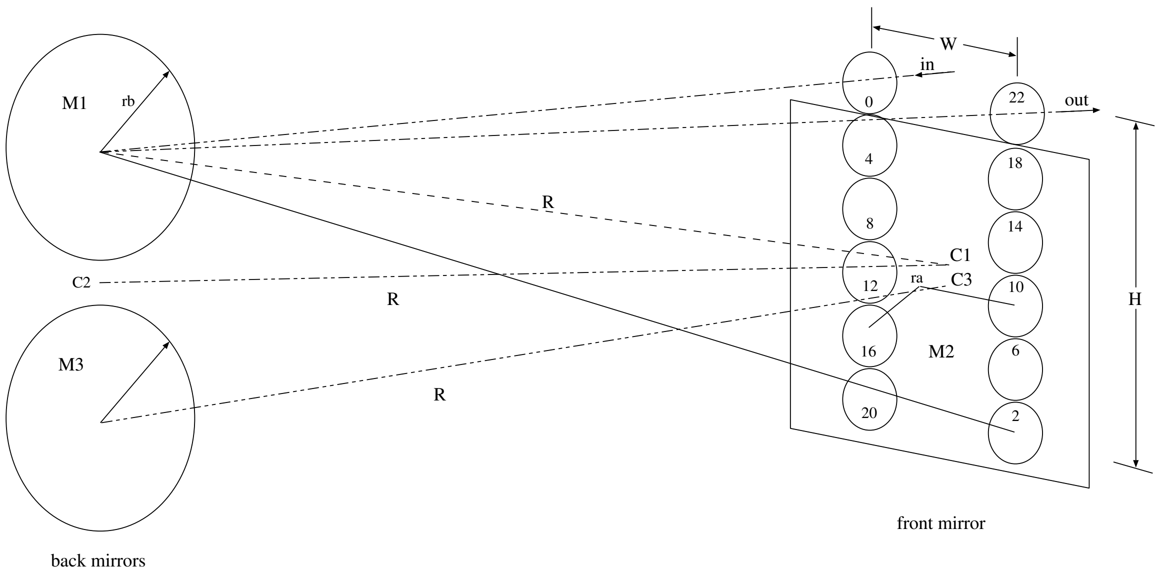

Figure 4.15: Modified White Cell design. C_1, C_2, and C_3 are centers of curvature of M_1, M_2, and M_3, respectively. The cell is configured for 22 transits corresponding to a path length of ~44 meters.

4.3.1.1.2 Cell Alignment. The cell must be aligned for each change in path length. This is accomplished using a visible source (Quartz) and a CaF_2 beamsplitter to actually see the images on the field mirror through a window at the back of the cell. For example, the cell in Figure 4.15 is aligned for 22 transits of the cell, yielding a total path length of 44 meters. (Actually, due to the thickness of the field mirror and the spacing between the mirror and the front of the cell, the initial and final transits are slightly longer, resulting in a path length of 44.05 meters.) The alignment is achieved by adjusting the input beam with the initial stages of the transfer optics so that it passes just over the field mirror and is incident on the top of the first back mirror (M1). The next step is to adjust the vertical and horizontal inclinations of the back mirrors so that a vertical structure of images similar to those in Figure 4.15 is achieved. The final transit must pass over the field mirror onto the transfer optics. The visible source and beam splitter are then replaced with the infrared components and as a final adjustment, the last stage of the transfer optics is tweaked with the aid of the FTS read-out or an oscilloscope so that the light focuses directly on the detector element.

4.3.1.2 Data Collection

The first step in the data collection process is to turn on the source and cool down the detector so that they reach equilibrium before the data collection begins. Typically, this takes about 30 to 60 minutes. The next step is to evacuate the cell, transfer optics, FTS, and manifold lines with the mechanical pumps. The cell is evacuated further with the diffusion pump to roughly 10^{-3} torr. In some cases, the cell was pumped, purged with N_2, pumped again, and the procedure repeated several times to rid the cell and cell walls of unwanted molecules. At this point, the pressure gauge readings are recorded for calibration purposes. An evacuated background scan is then recorded. The cell is then exposed to a container of distilled water through the manifold lines and the desired amount of water vapor is evaporated into the cell. The relative humidity in the cell is kept under $\sim$75% to avoid any possible condensation on surfaces within the cell. Although this was not monitored directly, no unexpected effects such as decreased reflectivity of the mirrors due to condensation were observed. The pressure is monitored for several minutes and then recorded. In general, the pure water vapor samples stabilized almost immediately after adding the vapor. This stabilization was also monitored with the temperature gauges. A pure sample spectrum is then recorded. This can take up to 3 hours depending on the resolution, path length, and the desired signal to noise ratio. Thus, the stability of the cell, for maintaining the optical alignment and for maintaining the conditions within the cell, is crucial. The stability of the source and the detector over this time are also extremely important. The pressure and temperature gauges, as well as the throughput of the cell, are monitored continually throughout this time. The throughput is monitored with the "centerburst" of the interferogram, which measures the integrated intensity at the detector for each mirror scan. If the centerburst varied more than several percent from scan to scan or if it slowly decreased or increased over the course of a run, the data collection was aborted. After the desired number of scans, the interferogram is down-loaded and an FT performed to obtain radiances. The manifold is then purged with pure nitrogen to remove any residual water vapor from the lines and a broadening gas (nitrogen or oxygen) is then added into the cell. Typically, about 200 torr of gas is introduced at this time. The pressure and temperature gauges are monitored until they reach equilibrium, which can take up to ~5 minutes. The first foreign broadened spectrum is then recorded. Again, this can take a considerable amount of time and the conditions of the cell and spectrometer are monitored continuously. This last step is then repeated for several more (3 or 4) broadening pressures, up to a total pressure of ~1 atmosphere. Finally, the cell is evacuated and another background run recorded. A typical "set" of spectra therefore consists of one pure spectrum and 3 or 4 foreign-broadened spectra with roughly the same water vapor amount. Several sets of these spectra were recorded with variable H_2O partial pressures and pathlengths.

Sample background and sample radiances are shown in Figure 4.16 for a 84 meter path length, 10 torr of H_2O, and 800 torr N_2.

For each run, three files were saved: (1) the actual spectrum (*.SPC), (2) a housekeeping file including information such as wavenumber range, resolution, the spectrometer's configuration, etc... (*.HSK), and (3) a file noting the pressure, temperature,

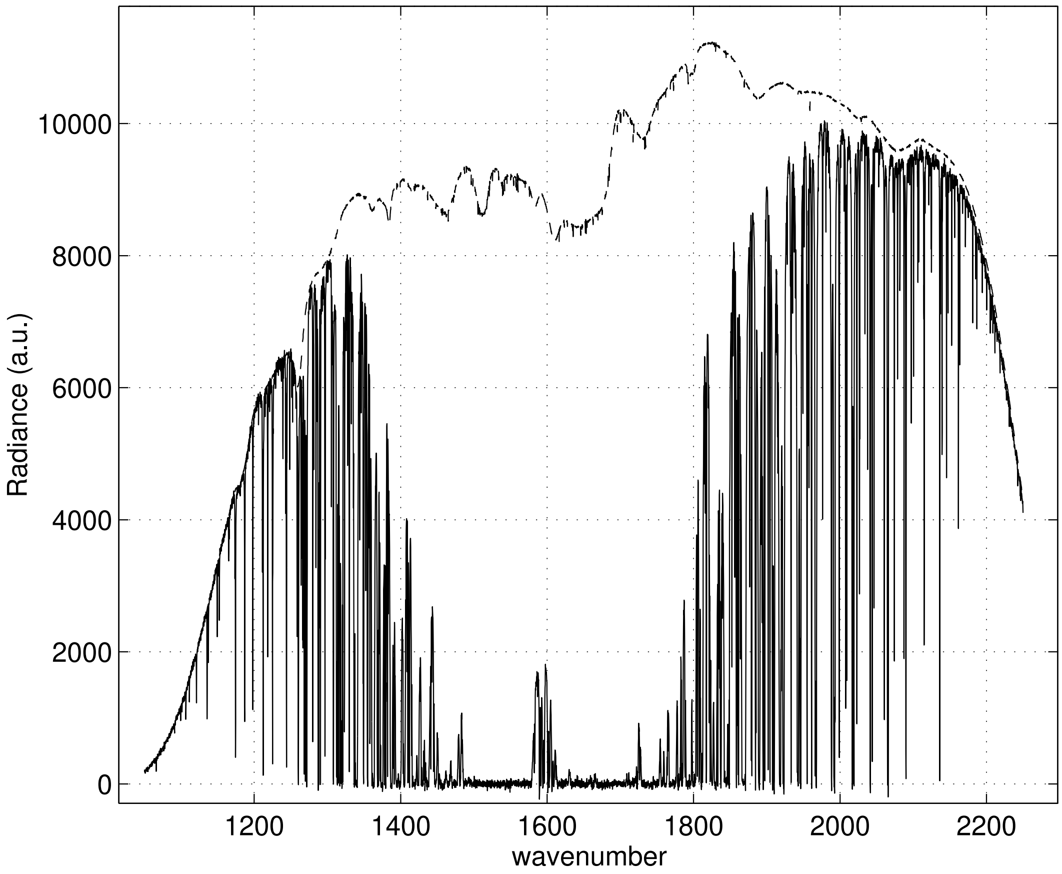

Figure 4.16: Sample measured radiances for an evacuated cell (dashed curve, file number 49) and a sample run (solid curve, file number 52).

and centerburst readings as a function of time (*.PAR). The calibrated pressure readings and the temperatures can then be plotted as a function of time. A sample of the gauge readings is shown in Figure 4.17. In general, for room temperature samples, the temperature in the cell remained constant to within $\sim \pm 0.1$K for a single run, although a gradual temperature increase was observed over the course of a day ($\sim$+1K over $\sim$10 hours). This is most likely due to the heating of the room throughout the day and to the increasing pressures in the cell. The three thermocouples all agreed to within 0.1K. In general, the pressure gauge readings remained constant to within $\sim \pm 0.1$ torr for a single run. The importance of monitoring the conditions within the cell cannot be

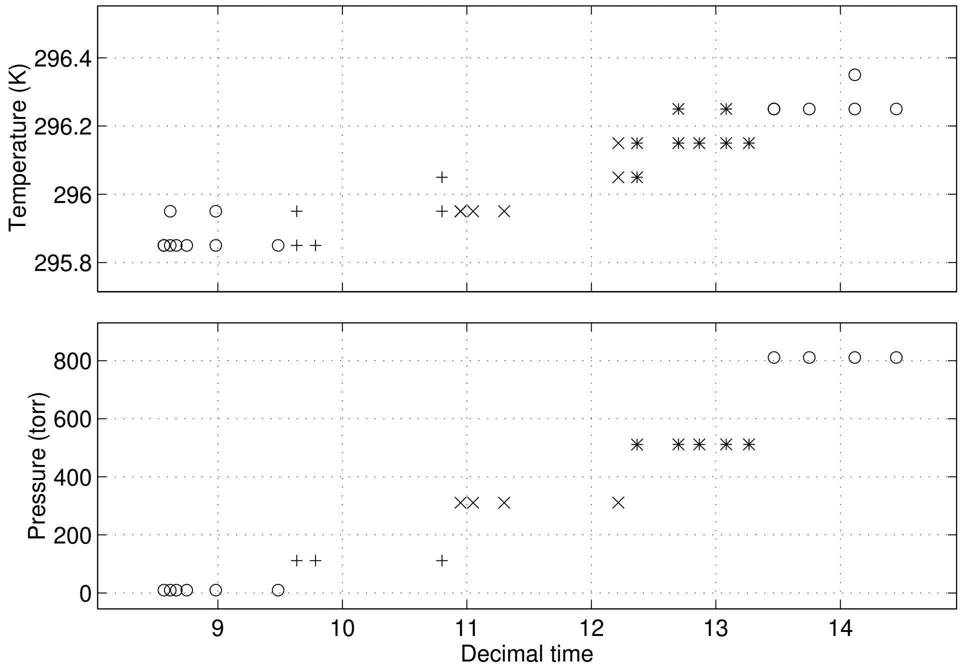

Figure 4.17: Temperature and total cell pressure gauge readings as a function of time (in hours) for files 150 through 154 (~10 torr H_2O (o's) plus 100(+'s), 300(x's), 500(*'s), 800(o's) torr N_2).

overstated.

To see if the addition of gas into the cell distorted the background scans in any way, background scans were also recorded with one atmosphere of pure nitrogen in the cell. We found inconsequential differences between these scans and empty cell scans, so we subsequently just used empty cell scans for the background runs.

For the nitrogen broadened spectra, Scott "Ultra Zero Ambient Monitoring Zero" grade nitrogen was used. We found that it contained no detectable amounts of CO gas and about 2ppm CO_2 whose bands fortunately do not fall in the spectral region studied in this work.

The majority of the spectra were recorded at an unapodized resolution of 0.040 cm^{-1}. This resolution allows sufficient resolution of important spectral features while limiting the data collection time, minimizing any long term drifts in the spectrometer, the detector, and the conditions within the cell. Average run times ranging from 45 minutes (12m path length) to over 3 hours (84m path length) were required to achieve adequate signal-to-noise ratios. An added benefit of our relatively low spectral resolution was the ability of the BOMEM processing unit to cover a large enough wavenumber range (1150 – 2250 cm^{-1}) so near 100% transmission baselines could be recorded on both sides of the ν_2 band. Furthermore, using this resolution helped to avoid any possible problems associated with the tilting of the FTS movable mirror at large path differences.

Res.	Range	P_{H_2O}	P_{total}	Broadeners	T	L
0.04	1050–2250	3,5,10,15	100,400,800	Self,N_2	296	12, 44, 84
2.00	1050–7000	3,5,10,15	100,400,800	Self,N_2	296	84
0.04	1050–2250	1	100,400,800	Self,N_2	260	12, 84
0.04	1050–2250	8	100,400,800	Self,O_2	296	84
0.04	1050–2250	5	1,3,5,7,9atm	Self,N_2	296	12
2.00	1050–7000	5	1,3,5,7,9atm	Self,N_2	296	84
0.01	1050–2250	0.1,7	100,400,800	N_2,O_2	296	12

Table 4.2: Summary of the experimental parameters for spectra collected at NIST. Temperatures are given in K, pressures in torr (unless noted otherwise), resolutions and ranges in cm^{-1}, and L in meters. Parameters are approximate. (760 torr = 1 atm = 1.01325×10^5 Pascals)

To further reduce the time for recording a set of spectra and to minimize any further contributions to noise, evacuated background scans were recorded at a resolution of 0.50 cm^{-1}. These were then linearly interpolated in wavenumber to match the sample runs' resolution, with no loss in accuracy over the standard method.

For all but the low temperature spectra, the data collection went very well. For the low temperature spectra, most of the interferograms were corrupted. We attribute this to mechanical vibrations caused by the thermocouple switch controlling the feedback loop of the cooling system. As the switch activated the liquid nitrogen flow, a small jolt could be felt, possibly disturbing the fringe counting and causing the FTS to lose track of the zero path difference position. As a result, individual scans were recorded, saving the interferograms to disk after each non-corrupt scan. This, however, greatly slowed the process and the signal-to-noise ratios suffered.

Table 4.3.1.2 summarizes the collected spectra and Table 4.3 details the experimental parameters. Spectra were recorded for a range of path lengths and partial pressures to obtain optimum optical depths throughout the band.

Table 4.3: Parameters for the spectra collected at NIST. Dates are in Month/Day/Year, $\nu_{\max}$ and resolution are in cm^{-1}, # S is the number of scans, L is the path length in m, T is in K, C is a code (1 for evacuated, 2 for pure H_2O, 3 for N_2-broadened, 4 for O_2-broadened), pressures are in torr. P_{H_2O} is the water vapor pressure determined from the gauges and P'_{H_2O} is the water vapor pressure determined from analyzing the spectra.

File	Date	$\nu_{\max}$	Res.	# S	L	T	C	P_{TOT}	P_{H_2O}	P'_{H_2O}
21	70694	2250	0.500	300	84.05	296.00	1			
22	70694	2250	0.040	192	84.05	296.00	2	5.021	5.021	
23	70694	2250	0.040	192	84.05	296.10	3	105.700		4.866 ± 0.130
24	70694	2250	0.040	192	84.05	296.30	3	395.400		4.866 ± 0.130
25	70694	2250	0.040	192	84.05	296.40	3	808.700		4.866 ± 0.130
26	70794	2250	0.500	300	84.05	296.00	1			
27	70794	2250	0.040	192	84.05	295.90	2	14.932	14.932	
28	70794	2250	0.040	192	84.05	296.08	3	121.760		14.520 ± 0.490
29	70794	2250	0.040	192	84.05	296.20	3	403.300		14.520 ± 0.490
30	70794	2250	0.040	43	84.05	296.40	3	811.300		14.520 ± 0.490
31	70794	2250	0.500	300	84.05	296.30	1			
32	70894	2250	0.500	300	84.05	296.10	1			
33	70894	2250	0.040	192	84.05	296.10	2	3.042	3.042	
34	70894	2250	0.040	192	84.05	296.20	3	55.060		3.074 ± 0.340
35	70894	2250	0.040	192	84.05	296.40	3	159.800		3.074 ± 0.340
36	70894	2250	0.500	300	84.05	296.20	1			
37	71194	2250	0.500	300	84.05	295.40	1			
38	71194	2250	0.040	192	84.05	295.40	1			
39	71194	2250	0.500	300	84.05	295.40	1			

continued on next page

continued from previous page

File	Date	ν_{max}	Res.	# S	L	T	C	P_{TOT}	P_{H_2O}	P'_{H_2O}
40	71194	2250	0.040	192	84.05	295.50	2	3.151	3.151	
41	71194	2250	0.040	192	84.05	295.80	3	537.700		3.074 ± 0.340
42	71194	2250	0.500	300	84.05	295.70	1			
43	71294	2250	0.500	300	84.05	295.70	1			
44	71294	2250	0.040	192	84.05	295.70	2	10.025	10.025	
45	71294	2250	0.040	192	84.05	295.90	3	112.700		9.334 ± 0.280
46	71294	2250	0.040	192	84.05	296.10	3	311.300		9.334 ± 0.280
47	71294	2250	0.500	300	84.05	296.10	1			
48	71394	2250	0.500	300	84.05	295.80	1			
49	71394	2250	0.500	300	84.05	295.80	1			
50	71394	2250	0.040	192	84.05	295.90	2	9.998	9.998	
51	71394	2250	0.040	192	84.05	296.20	3	511.300		9.334 ± 0.280
52	71394	2250	0.040	192	84.05	296.30	3	814.400		9.334 ± 0.280
53	71394	2250	0.500	300	84.05	296.30	1			
54	71494	2250	0.500	300	84.05	296.05	1			
55	71494	7000	2.000	300	84.05	296.05	1			
56	71494	7000	2.000	300	84.05	296.05	2	5.003	5.003	
57	71494	7000	2.000	300	84.05	296.15	3	106.300		
58	71494	7000	2.000	300	84.05	296.15	3	405.800		
59	71494	7000	2.000	300	84.05	296.25	3	800.050		
60	71494	7000	2.000	300	84.05	296.25	1			
61	71494	7000	2.000	300	84.05	296.55	1			
62	71494	7000	2.000	300	84.05	296.65	2	9.998	9.998	
63	71494	7000	2.000	300	84.05	296.75	3	111.750		
64	71494	7000	2.000	300	84.05	296.75	3	409.420		
65	71494	7000	2.000	300	84.05	296.85	3	805.650		
66	71494	7000	2.000	300	84.05	296.59	1			
67	71494	7000	2.000	300	84.05	296.85	1			
68	71494	7000	2.000	300	84.05	296.95	2	14.982	14.982	
69	71494	7000	2.000	300	84.05	296.95	3	120.180		

continued on next page

continued from previous page

File	Date	$\nu_{\max}$	Res.	# S	L	T	C	P_{TOT}	P_{H_2O}	P'_{H_2O}
70	71494	7000	2.000	300	84.05	297.05	3	414.410		
71	71494	7000	2.000	300	84.05	297.15	3	811.310		
72	71494	7000	2.000	32	84.05	297.15	1			
73	71494	7000	2.000	300	84.05	297.15	1			
74	71994	2250	0.500	100	84.05	295.80	1			
75	71994	2250	0.500	300	84.05	263.60	1			
76	71994	2250	0.040	192	84.05	263.30	2	0.866	0.866	
77	71994	2250	0.040	10	84.05		2	0.866	0.866	
78	71994	2250	0.040	35	84.05	263.00	2	0.865	0.865	
79	71994	2250	0.040	32	84.05	262.90	2	0.865	0.865	
80	71994	2250	0.040	32	84.05	262.80	2	0.865	0.865	
81	71994	2250	0.040	32	84.05	262.80	3	401.400		0.827 ± 0.083
82	71994	2250	0.040	64	84.05	262.70	3	401.400		0.827 ± 0.083
83	71994	2250	0.040	96	84.05	262.70	3	402.000		0.827 ± 0.083
89	72094	7000	2.000	600	84.05	295.60	1			
90	72094	7000	2.000	600	84.05	295.70	2	1.444	1.444	
91	72094	7000	2.000	600	84.05	296.20	3	1560.500		
92	72094	7000	2.000	600	84.05	296.40	3	2321.800		
93	72094	7000	2.000	600	84.05	296.10	1			
94	72094	7000	2.000	600	84.05	296.40	5	752.000	0.000	
95	72194	2250	0.500	100	84.05	296.00	1			
96	72194	2250	0.500	100	84.05	296.00	1			
97	72194	2250	0.500	300	84.05	296.10	1			
98	72194	2250	0.040	192	84.05	296.20	2	7.987	7.987	
100	72194	2250	0.040	192	84.05	296.30	4	392.870		
102	72294	2250	0.500	300	84.05	296.20	1			
103	72294	2250	0.040	192	84.05	296.20	2	8.014	8.014	
104	72294	2250	0.040	192	84.05	296.30	4	101.570		7.309 ± 0.340
105	72294	2250	0.040	192	84.05	296.40	4	400.170		7.309 ± 0.340
106	72294	2250	0.040	192	84.05	296.60	4	798.570		7.309 ± 0.340

continued on next page

continued from previous page

File	Date	ν_{max}	Res.	# S	L	T	C	P_{TOT}	P_{H_2O}	P'_{H_2O}
107	72294	2250	0.040	10	84.05	296.30	1			
108	72294	2250	0.500	300	84.05	296.30	1			
109	72594	2250	0.500	300	44.05		1			
110	72694	2250	0.500	300	44.05	296.60	1			
111	72694	2250	0.040	192	44.05	296.60	2	5.046	5.046	
112	72694	2250	0.040	192	44.05	296.70	3	105.290		4.816 ± 0.130
113	72694	2250	0.040	192	44.05	296.70	3	198.290		4.816 ± 0.130
114	72694	2250	0.500	300	44.05	296.90	1			
115	72794	2250	0.500	300	44.05	296.80	1			
116	72794	2250	0.040	192	44.05	296.80	2	5.054	5.054	
117	72794	2250	0.040	192	44.05	296.80	3	405.600		4.816 ± 0.130
118	72794	2250	0.040	192	44.05	297.10	3	804.660		4.816 ± 0.130
119	72794	2250	0.500	300	44.05	296.90	1			
120	72894	2250	0.500	300	44.05	296.90	1			
121	72894	2250	0.040	192	44.05	296.90	2	15.133	15.133	
122	72894	2250	0.040	192	44.05	296.90	3	116.290		14.340 ± 0.550
123	72894	2250	0.040	193	44.05	297.10	3	413.960		14.340 ± 0.550
124	72894	2250	0.040	192	44.05	297.20	3	813.460		14.340 ± 0.550
125	72894	2250	0.500	300	44.05	297.00	1			
126	80194	2250	0.500	300	44.05	296.00	1			
127	80194	2250	0.040	192	44.05	296.10	2	3.057	3.057	
128	80194	2250	0.040	192	44.05	296.20	3	54.400		2.894 ± 0.160
129	80194	2250	0.040	192	44.05	296.30	3	156.700		2.894 ± 0.160
130	80194	2250	0.040	192	44.05	296.60	3	533.100		2.894 ± 0.160
131	80194	2250	0.500	300	44.05	296.50	1			
132	80294	2250	0.500	300	44.05	296.40	1			
133	80294	2250	0.040	192	44.05	296.40	2	10.139	10.139	
134	80294	2250	0.040	192	44.05	296.50	3	110.970		9.726 ± 0.220
135	80294	2250	0.040	192	44.05	296.70	3	310.970		9.726 ± 0.220
136	80294	2250	0.500	300	44.05	296.70	1			

continued on next page

continued from previous page

File	Date	ν_{max}	Res.	# S	L	T	C	P_{TOT}	P_{H_2O}	P'_{H_2O}
137	80394	2250	0.500	300	44.05	296.40	1			
138	80394	2250	0.040	192	44.05	296.40	2	10.130	10.130	
139	80394	2250	0.040	192	44.05	296.50	3	512.140		9.726 ± 0.220
140	80394	2250	0.040	192	44.05	296.70	3	808.140		9.726 ± 0.220
141	80394	2250	0.500	300	44.05	296.60	1			
142	80594	2250	0.500	200	12.05	296.30	1			
143	80594	2250	0.040	96	12.05	296.30	2	4.988	4.988	
144	80594	2250	0.040	96	12.05	296.40	3	105.950		4.817 ± 0.160
145	80594	2250	0.040	96	12.05	296.50	3	207.950		4.817 ± 0.160
146	80594	2250	0.040	96	12.05	296.60	3	406.050		4.817 ± 0.160
147	80594	2250	0.040	96	12.05	296.80	3	806.450		4.817 ± 0.160
148	80594	2250	0.500	200	12.05	296.60	1			
149	80894	2250	0.500	200	12.05	295.80	1			
150	80894	2250	0.040	96	12.05	295.90	2	9.974	9.974	
151	80894	2250	0.040	96	12.05	295.90	3	111.270		9.506 ± 0.250
152	80894	2250	0.040	96	12.05	296.00	3	310.970		9.506 ± 0.250
153	80894	2250	0.040	96	12.05	296.20	3	511.370		9.506 ± 0.250
154	80894	2250	0.040	96	12.05	296.30	3	811.070		9.506 ± 0.250
155	80894	2250	0.500	200	12.05	296.20	1			
156	80994	2250	0.500	200	12.05	296.20	1			
157	80994	2250	0.040	96	12.05	296.20	2	3.011	3.011	
158	80994	2250	0.040	96	12.05	296.30	3	152.970		2.859 ± 0.100
159	80994	2250	0.040	96	12.05	296.30	3	532.870		2.859 ± 0.100
160	80994	2250	0.040	96	12.05	296.60	3	803.970		2.859 ± 0.100
161	80994	2250	0.500	200	12.05	297.60	1			
162	81094	2250	0.500	200	12.05	296.40	1			
163	81094	2250	0.040	96	12.05	296.40	2	15.365	15.365	
164	81094	2250	0.040	96	12.05	296.40	3	118.750		14.500 ± 0.530
165	81094	2250	0.040	96	12.05	296.50	3	419.650		14.500 ± 0.530
166	81094	2250	0.040	96	12.05	296.60	3	818.550		14.500 ± 0.530

continued on next page

continued from previous page

File	Date	ν_{max}	Res.	# S	L	T	C	P_{TOT}	P_{H_2O}	P'_{H_2O}
167	81094	2250	0.500	200	12.05	296.50	1			
168	81194	2250	0.500	200	12.05	296.30	1			
169	81194	2250	0.040	96	12.05	296.40	2	2.989	2.989	
170	81194	2250	0.040	96	12.05	295.60	3	802.610		2.874 ± 0.047
171	81194	2250	0.040	96	12.05	296.80	3	2298.880		2.874 ± 0.047
172	81194	2250	0.040	96	12.05	297.10	3	3875.480		2.874 ± 0.047
173	81194	2250	0.040	96	12.05	297.30	3	5326.180		2.874 ± 0.047
174	81194	2250	0.500	200	12.05	296.20	1			
175	81594	2250	0.011	64	12.05	296.10	1			
176	81594	2250	0.011	64	12.05	296.20	3	203.505	0.100	
177	81594	2250	0.011	64	12.05	296.30	3	203.505		
178	81594	2250	0.011	128	12.05	296.40	3	402.105		0.042 ± 0.002
179	81694	2250	0.011	128	12.05	296.30	3	790.705		0.030 ± 0.002
180	81694	2250	0.011	128	12.05	296.30	1			
181	81794	2250	0.011	128	12.05	296.40	4	202.005		
182	81794	2250	0.011	128	12.05	296.70	4	401.805		
183	81894	2250	0.011	128	12.05	296.50	4	601.315		
184	81894	2250	0.011	128	12.05	296.60	2	7.028	7.028	
185	81994	2250	0.011	128	12.05	297.10	4	611.005		
186	82294	2250	0.500	200	12.05	296.00	1			
187	82394	2250	0.500	100	12.05	295.50	1			
188	82394	2250	0.011	96	12.05	295.50	4	207.250		
189	82394	2250	0.011	96	12.05	295.50	4	407.423		
190	82394	2250	0.011	128	12.05	295.30	3	208.233		
191	82494	2250	0.011	96	12.05	295.30	3	408.283		
192	82494	2250	0.011	128	12.05	295.40	3	608.483		
193	90194	2250	0.500	100	84.05	295.40	1			
194	90194	2250	0.500	300	84.05	295.70	1			
195	90194	2250	0.500	200	84.05	296.30	5	804.660		
196	90194	2250	0.500	200	84.05	262.90	1			

continued on next page

continued from previous page

File	Date	$\nu_{\max}$	Res.	# S	L	T	C	P_{TOT}	P_{H_2O}	P'_{H_2O}
197	90194	2250	0.040	60	84.05	262.90	2	0.964	0.964	
198	90194	2250	0.040	60	84.05	262.90	2	0.954	0.954	
199	90194	2250	0.040	60	84.05	262.90	2	0.955	0.955	
200	90194	2250	0.040	60	84.05	263.00	3	400.460		
201	90194	2250	0.040	60	84.05	263.00	3	400.460		
202	90194	2250	0.040	60	84.05	263.00	3	400.360		
203	90194	2250	0.040	120	84.05	263.10	3	801.060		
204	90194	2250	0.040	60	84.05	263.00	3	800.960		
205	90194	2250	0.040	60	84.05	263.00	3	1194.760		
206	90194	2250	0.040	60	84.05	263.00	3	1194.760		
207	90194	2250	0.040	60	84.05	262.90	3	1194.760		
208	90194	2250	0.040	100	84.05	262.60	1			

4.4 Data Analysis: General Considerations

This section describes various factors which are addressed in the data analysis. These include: (1) the ratioing of sample to background scans to obtain transmission spectra, (2) the adjustment of 100% transmission baselines, (3) fringes in the spectra, and (4) the effect of the instrument function on the spectra. Two other concerns, the determination of the H_2O partial pressures and an analysis of the spectral line parameters, are addressed separately in Sections 4.5 and 4.6. Sample transmission spectra are shown in Figure 4.18 and in more detail in Figures 4.19 through 4.29.

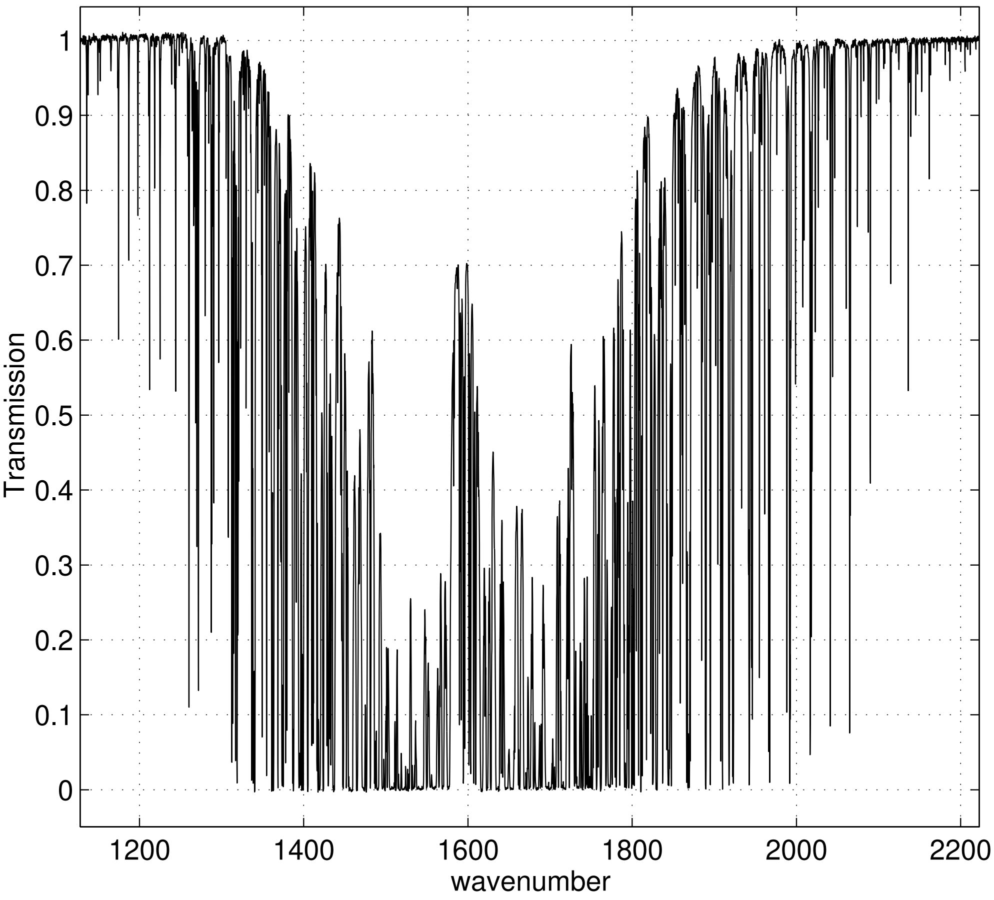

Figure 4.18: A sample spectrum collected at 0.040 cm^{-1} resolution. Experimental parameters are: 14.5 torr H_2O, 804.5 torr N_2, 1205 cm path length, 296.6K.

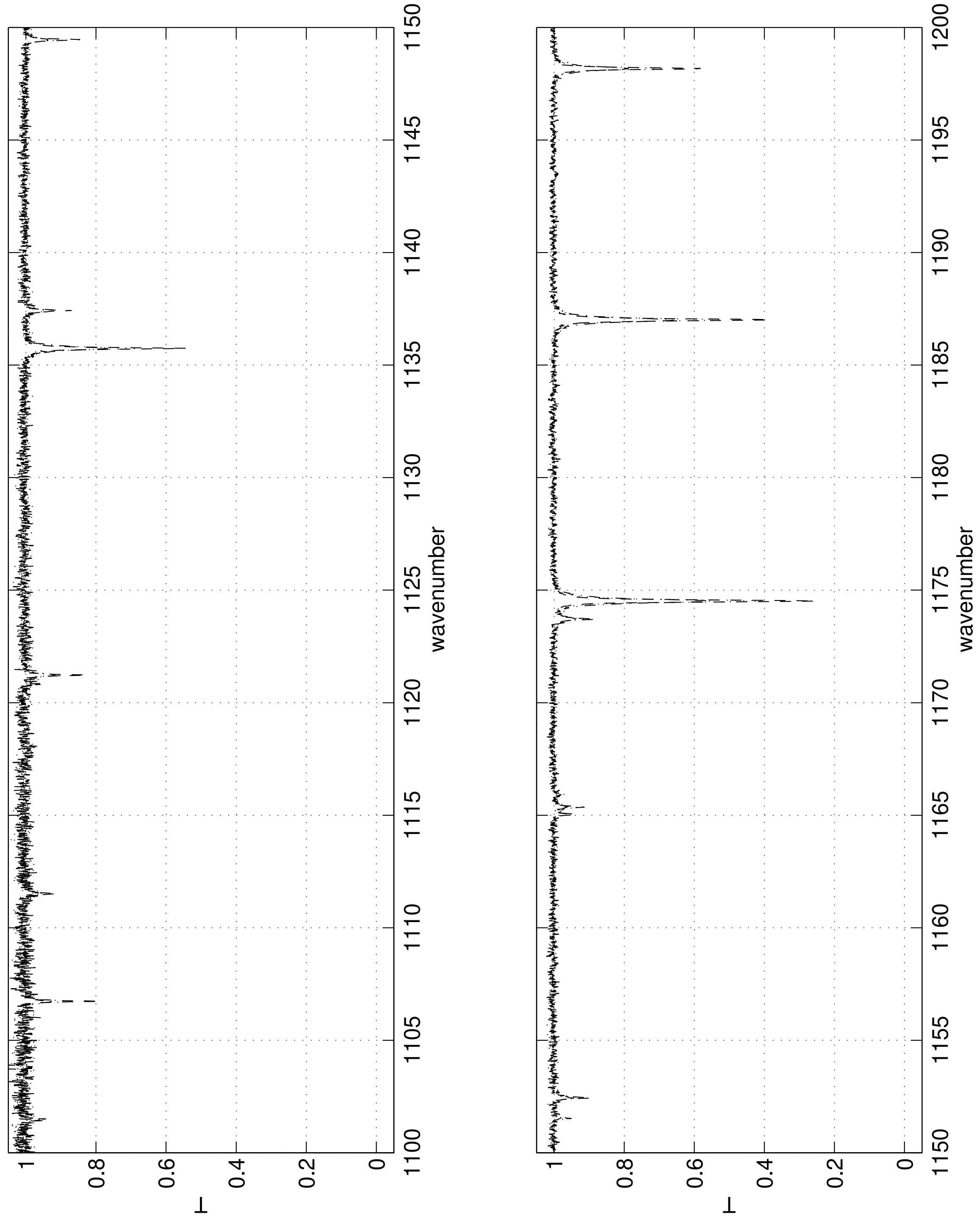

Figure 4.19: Sample spectra between 1100 and 1200 cm^{-1}. Experimental parameters are: 0.03 torr H_2O (solid curve); 9.5 torr H_2O, 300 torr N_2 (dashed curve), 500 torr N_2 (dotted curve), and 800 torr N_2 (dash-dot curve), 1205 cm path length, 296.5K.

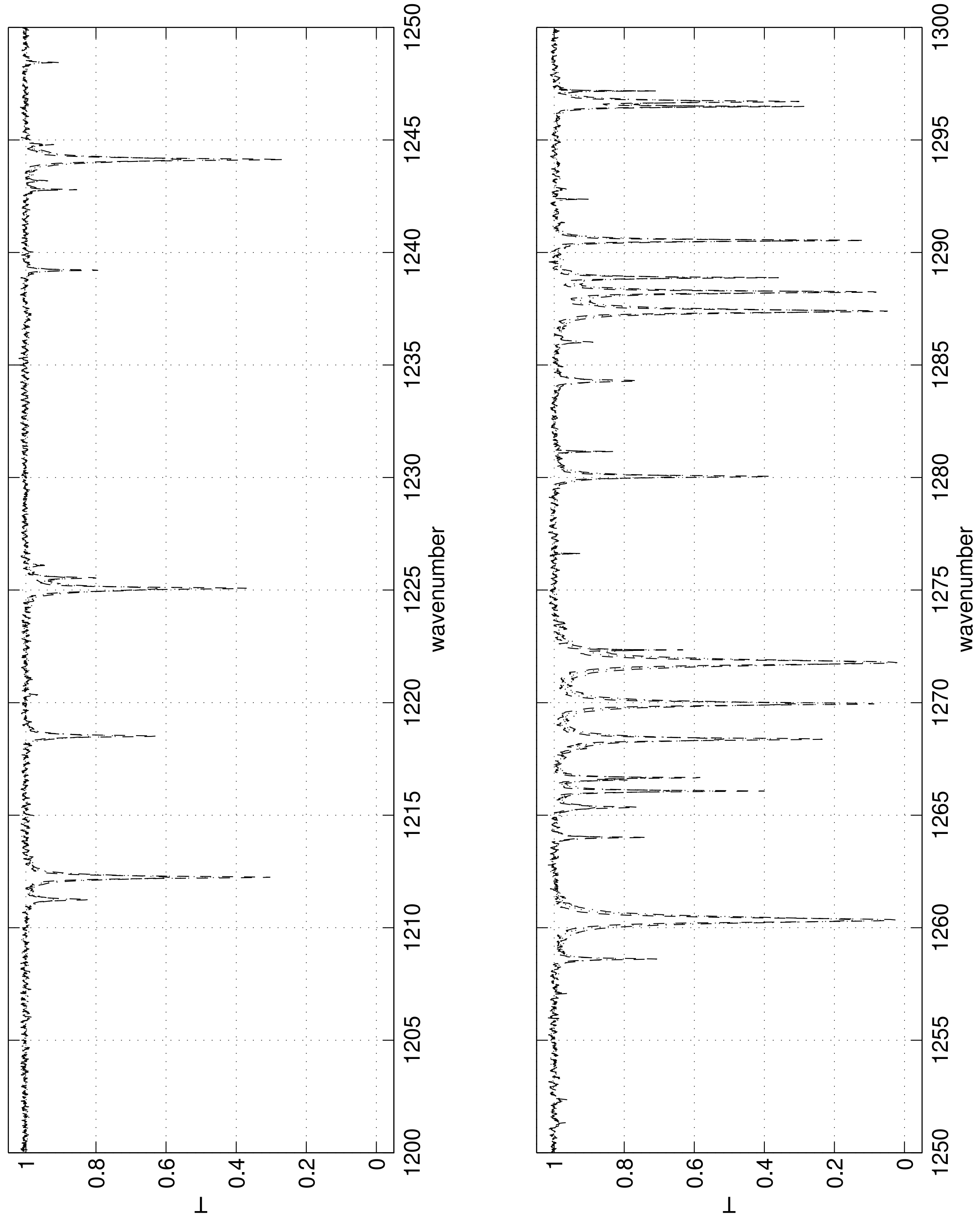

Figure 4.20: Sample spectra between 1200 and 1300 cm^{-1}. Experimental parameters and curve labels are the same as for Figure 4.19.

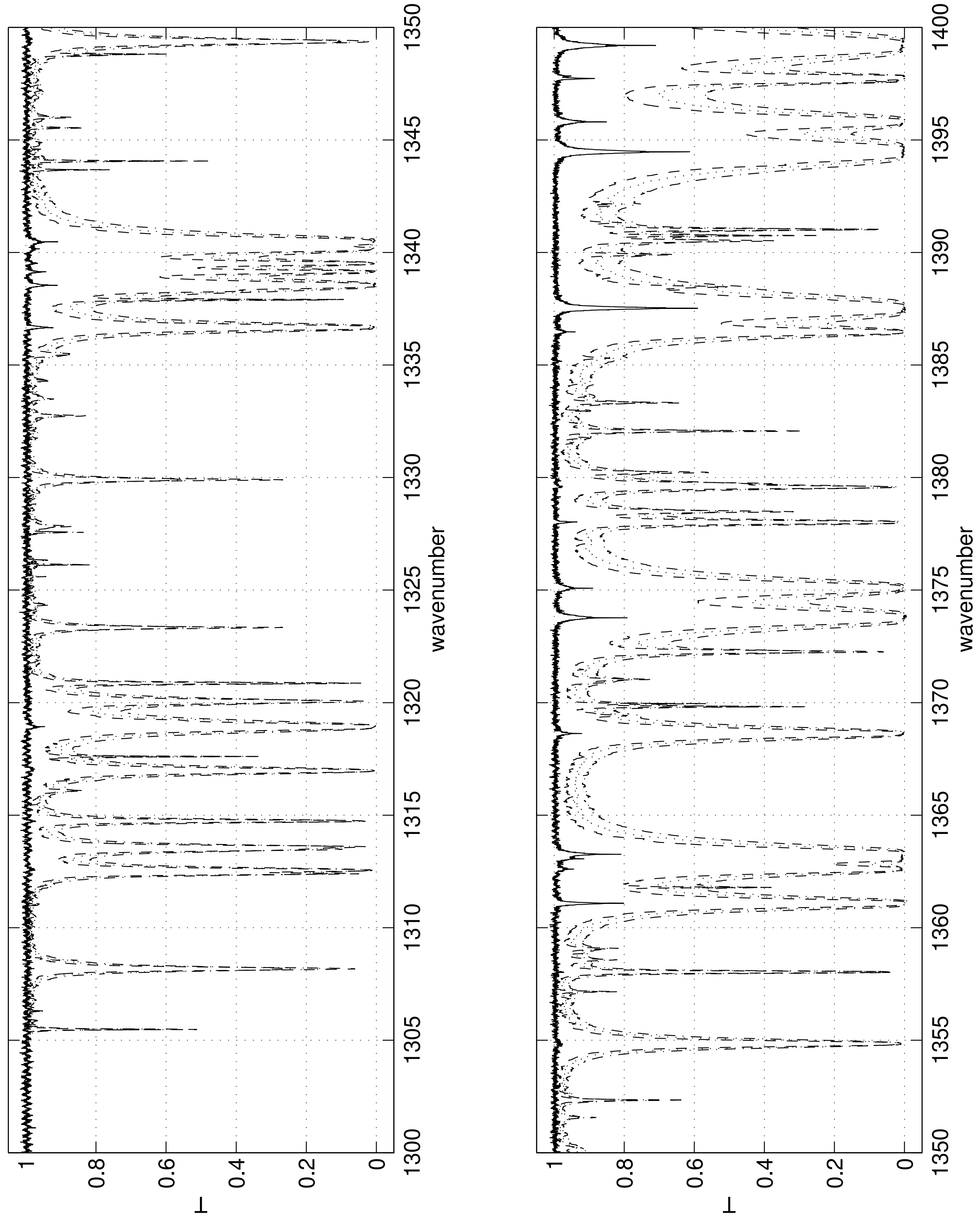

Figure 4.21: Sample spectra between 1300 and 1400 cm^{-1}. Experimental parameters and curve labels are the same as for Figure 4.19.

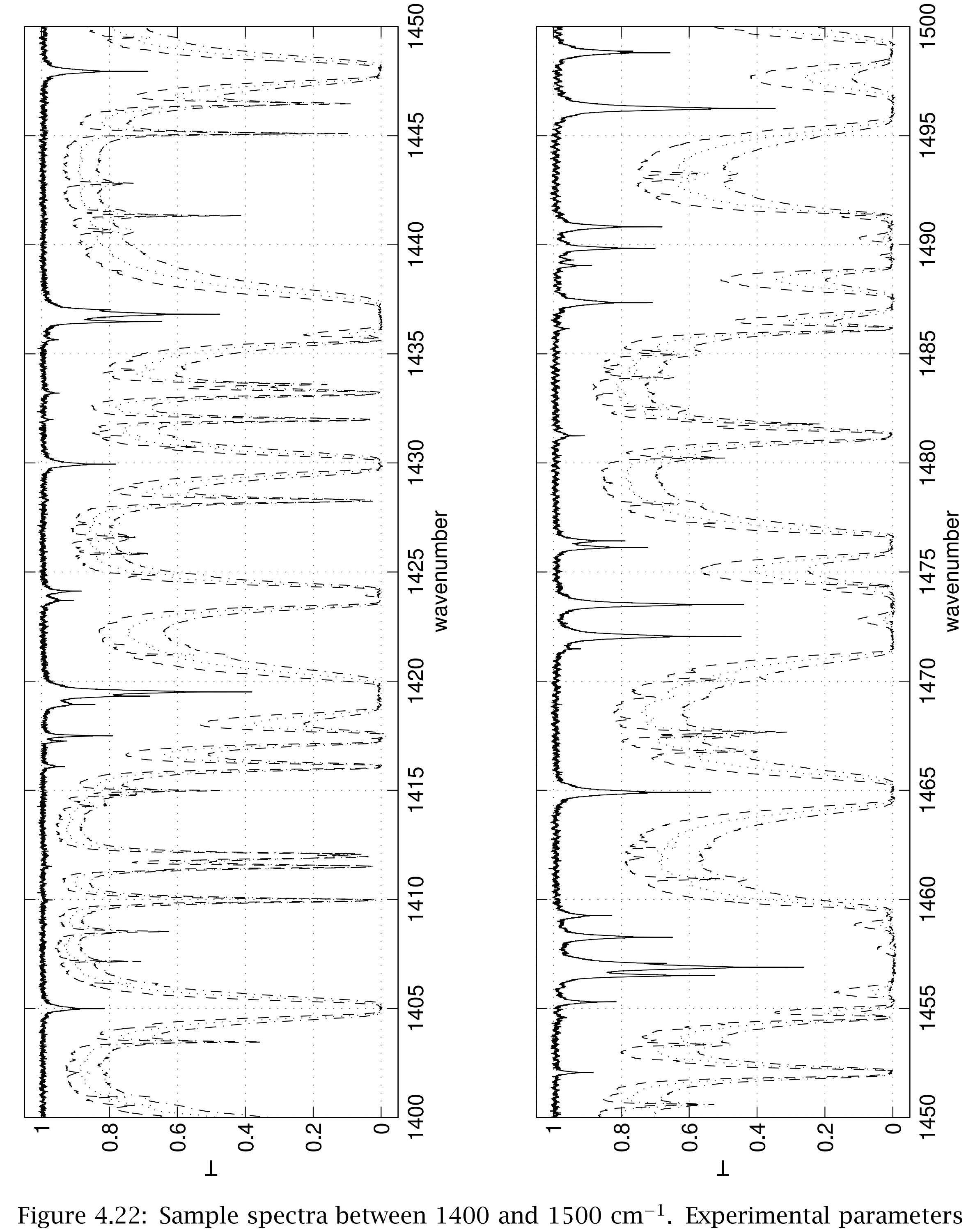

Figure 4.22: Sample spectra between 1400 and 1500 cm^{-1}. Experimental parameters and curve labels are the same as for Figure 4.19.

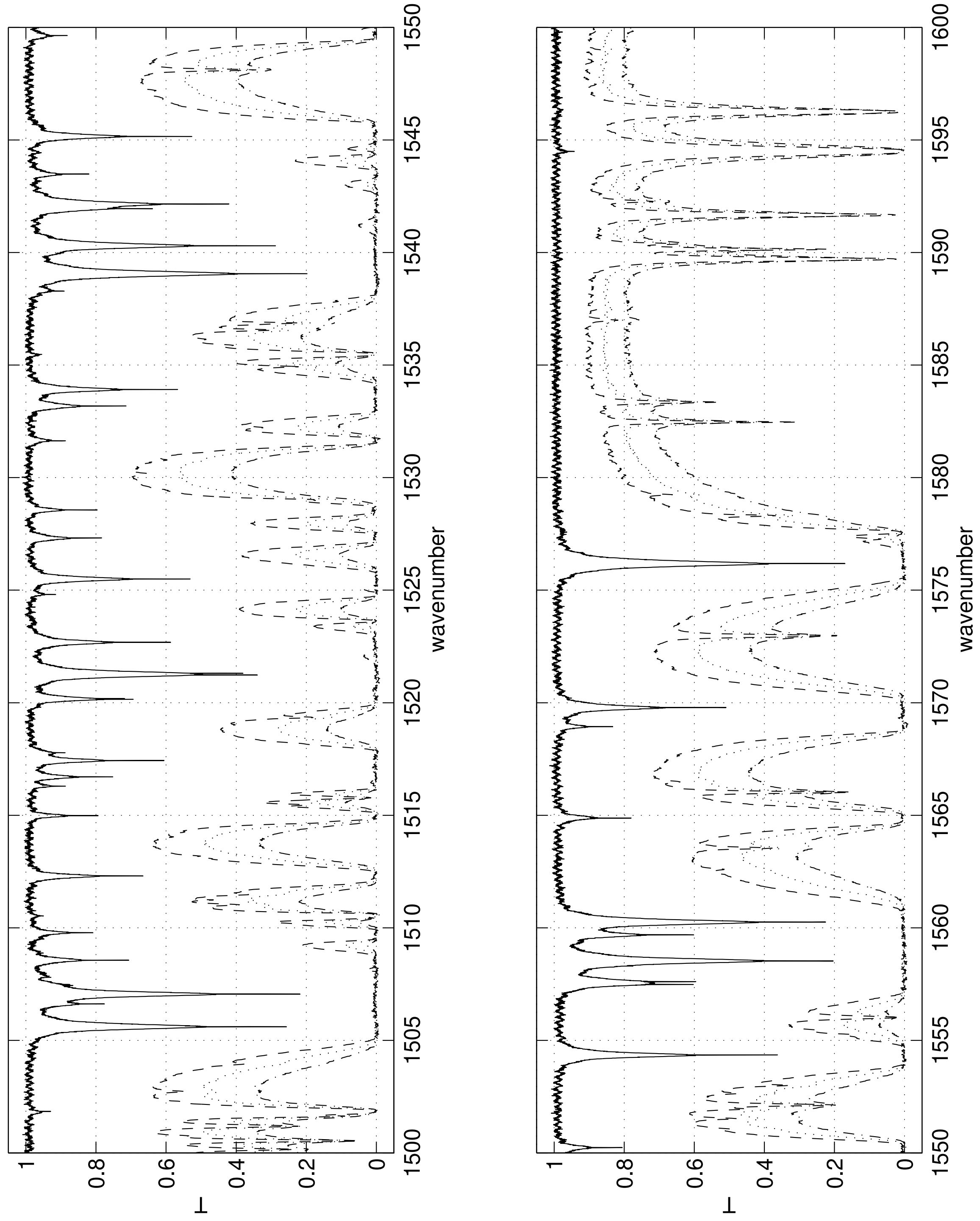

Figure 4.23: Sample spectra between 1500 and 1600 cm^{-1}. Experimental parameters and curve labels are the same as for Figure 4.19.

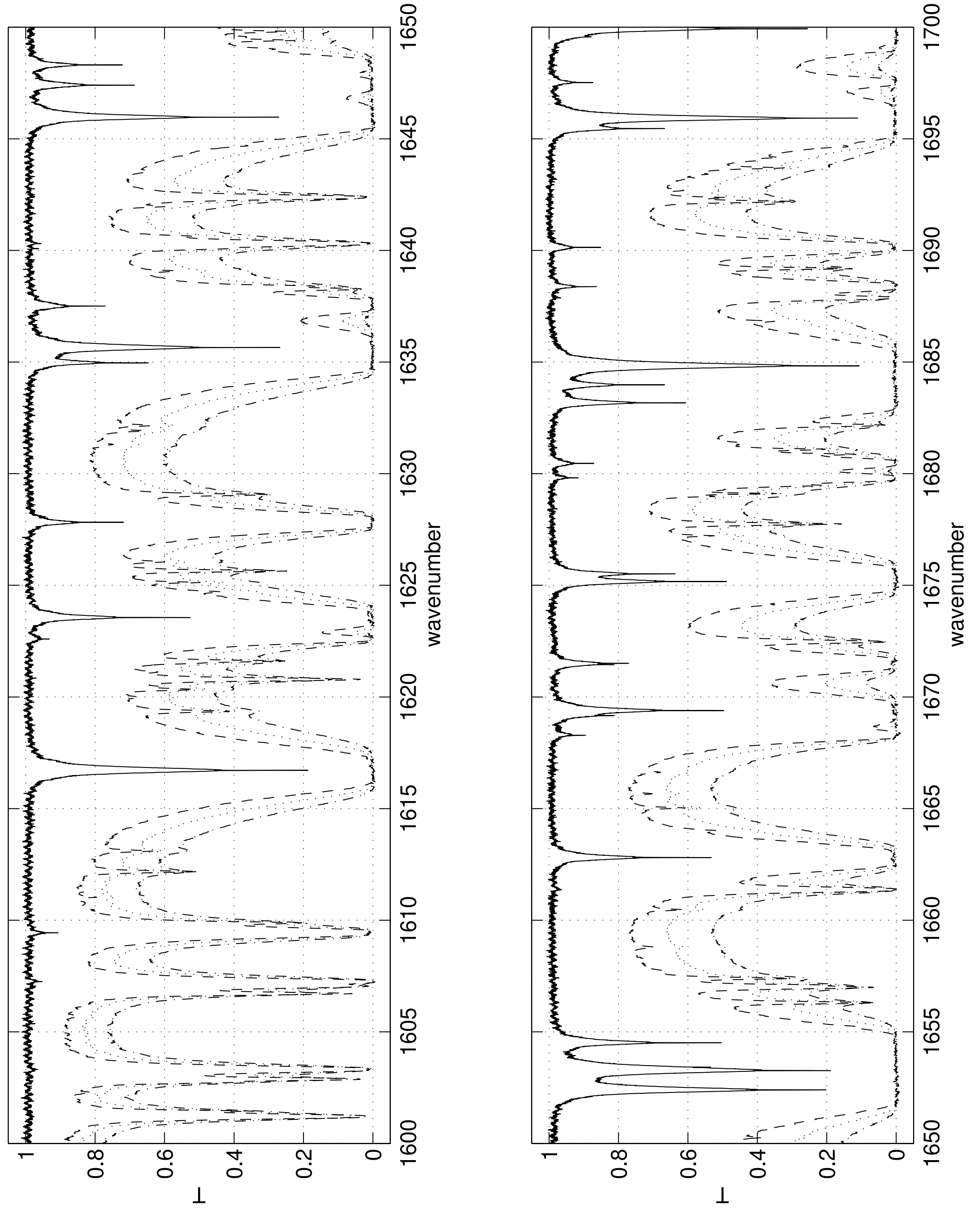

Figure 4.24: Sample spectra between 1600 and 1700 cm^{-1}. Experimental parameters and curve labels are the same as for Figure 4.19.

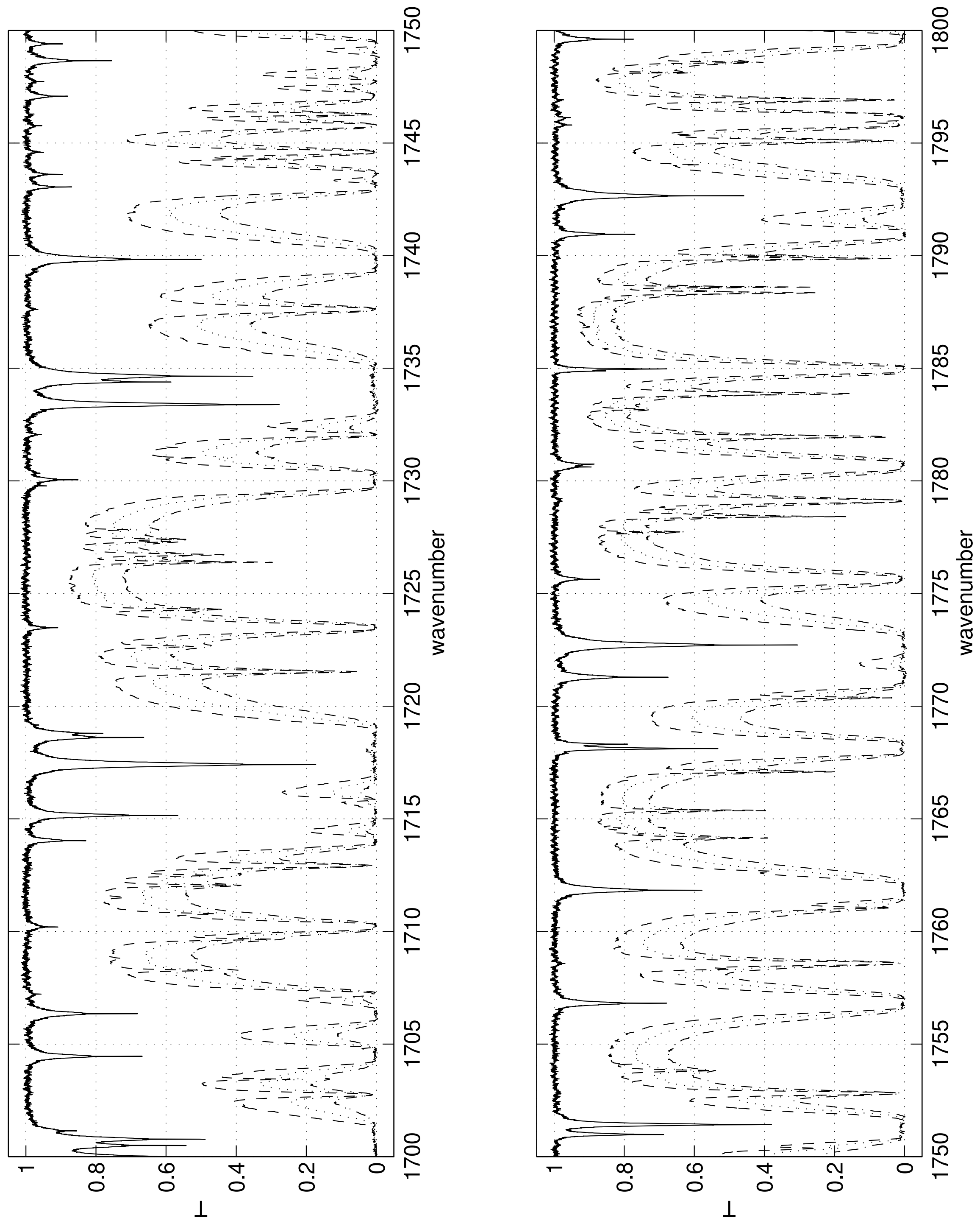

Figure 4.25: Sample spectra between 1700 and 1800 cm^{-1}. Experimental parameters and curve labels are the same as for Figure 4.19.

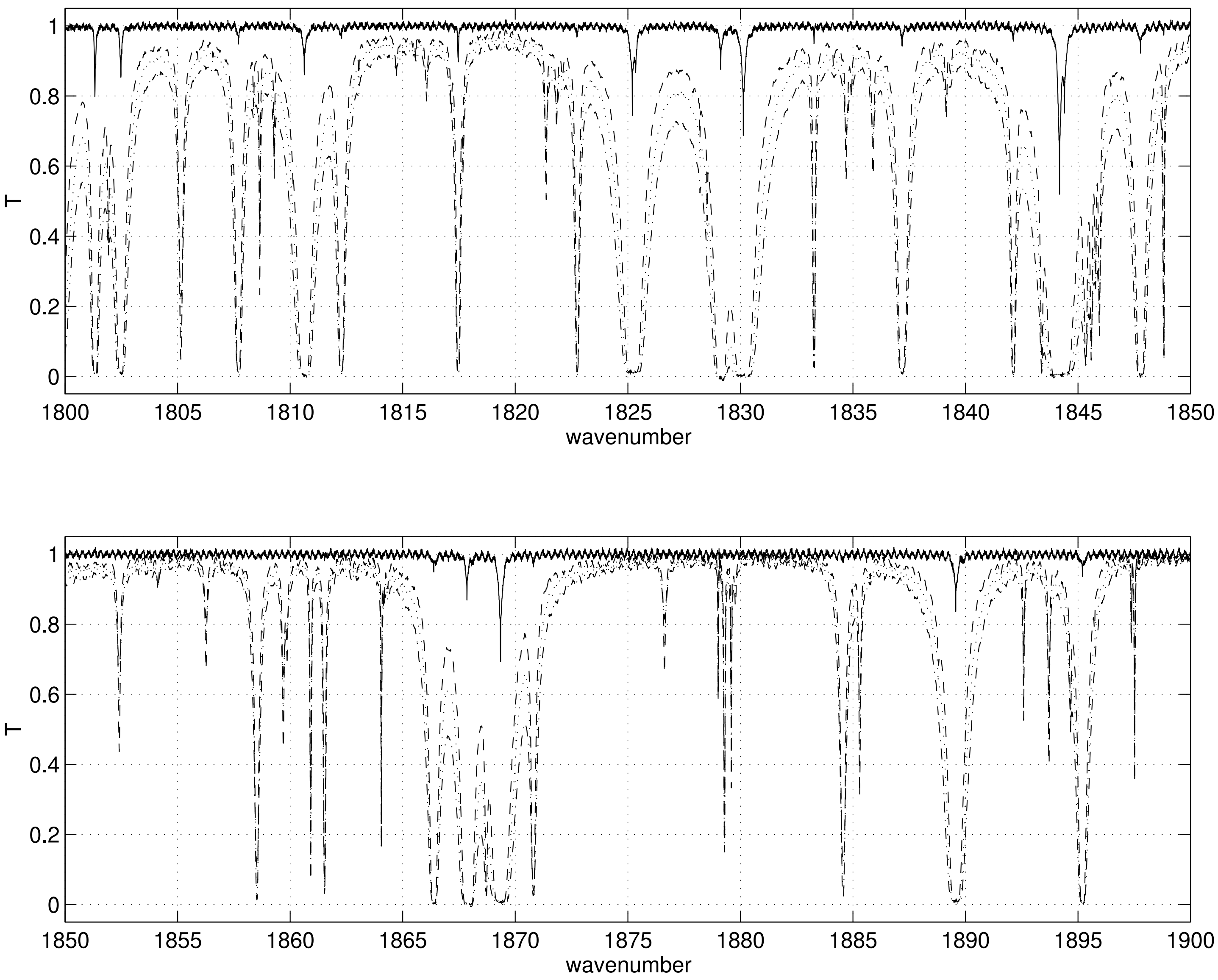

Figure 4.26: Sample spectra between 1800 and 1900 cm^{-1}. Experimental parameters and curve labels are the same as for Figure 4.19.

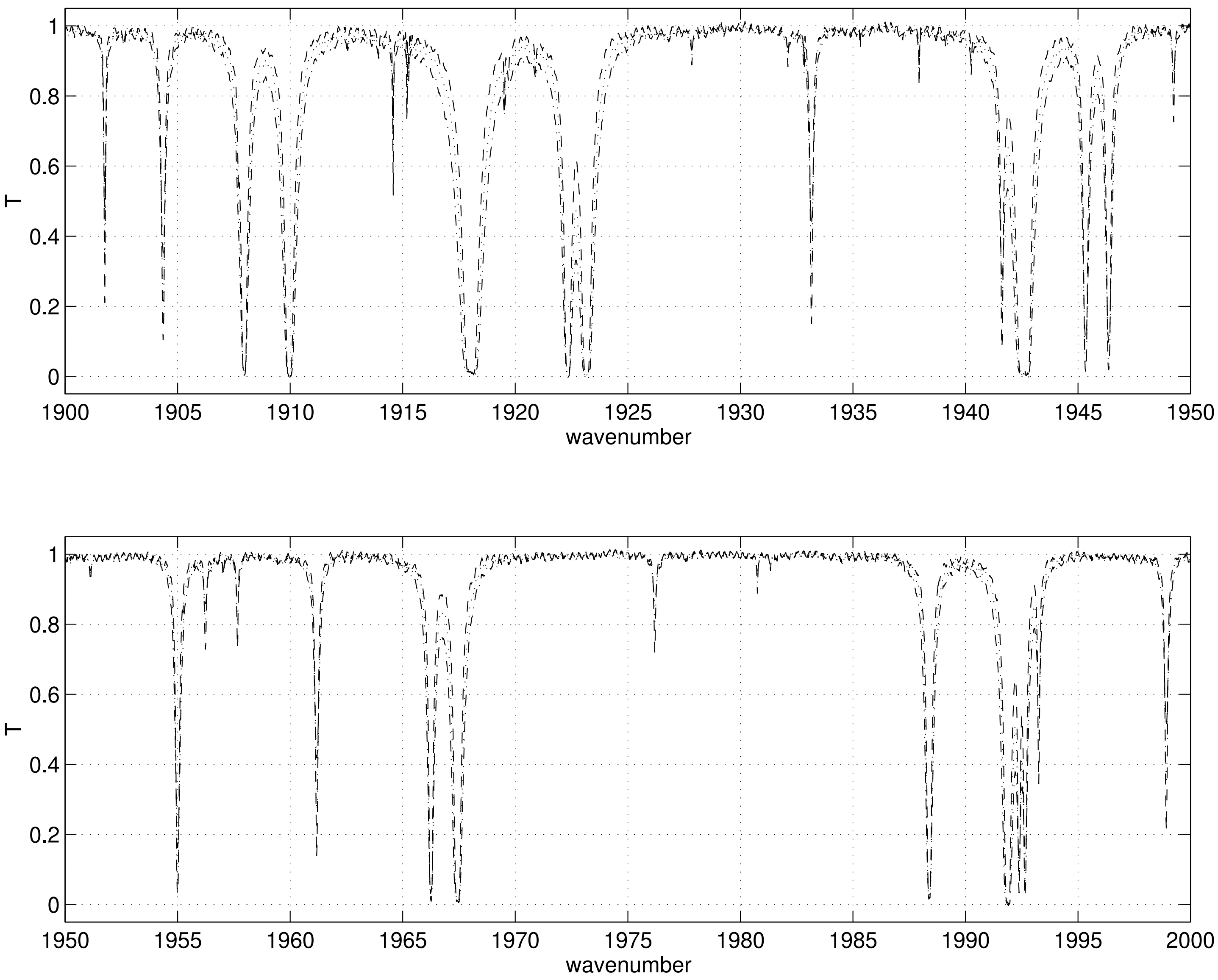

Figure 4.27: Sample spectra between 1900 and 2000 cm^{-1}. Experimental parameters and curve labels are the same as for Figure 4.19.

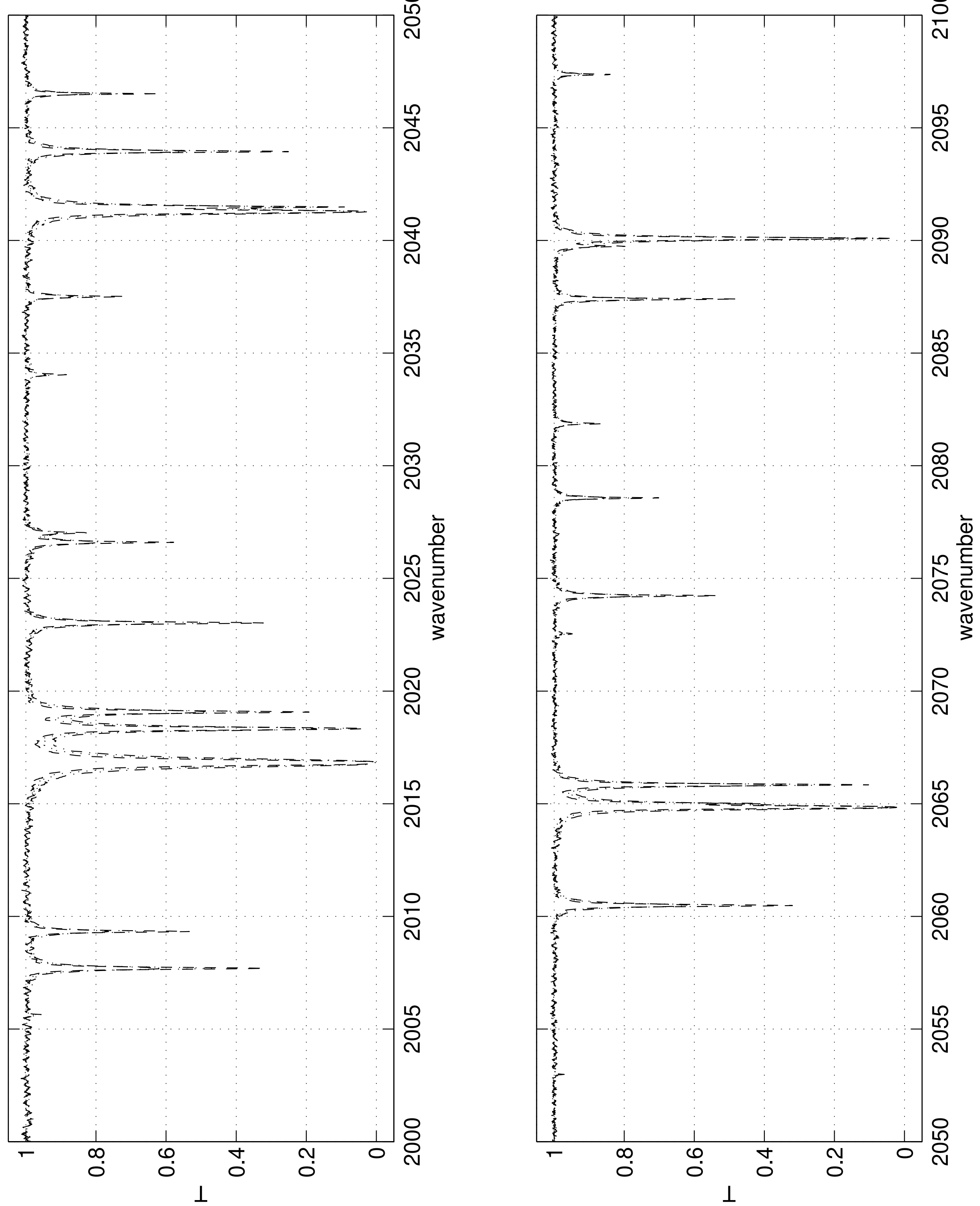

Figure 4.28: Sample spectra between 2000 and 2100 cm^{-1}. Experimental parameters and curve labels are the same as for Figure 4.19.

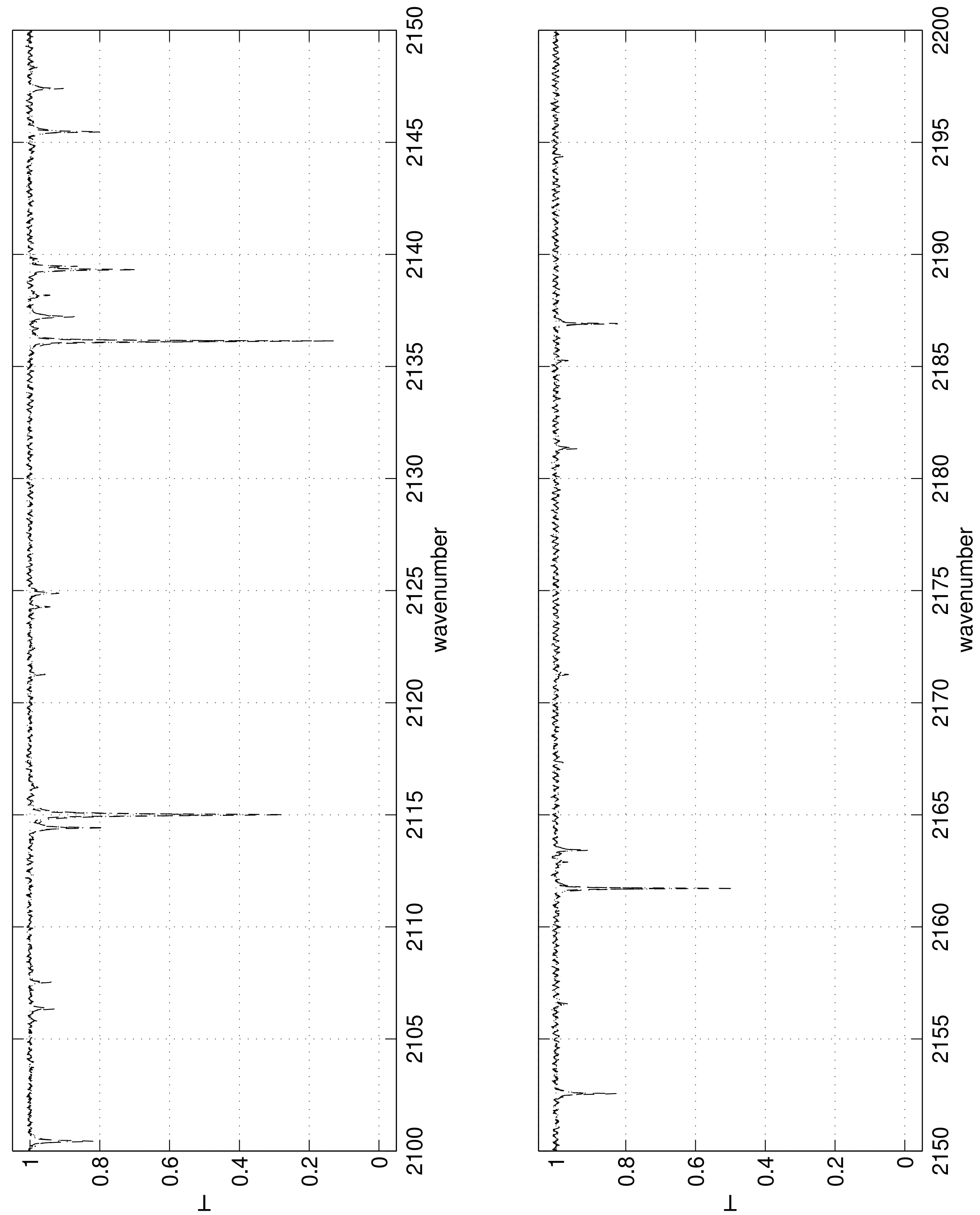

Figure 4.29: Sample spectra between 2100 and 2200 cm^{-1}. Experimental parameters and curve labels are the same as for Figure 4.19.

4.4.1 100% Transmission Baselines

Transmission spectra are obtained by ratioing the absorption scans to the background scan. In the wings of the band, where the transmission is constant as a function of wavenumber in-between the lines (i.e. where there is virtually no observable absorption), the transmission is set equal to one. This is done to account for any small long term drifts in the detector, source, or other effects and is accomplished by using a scalar multiplication to the sample radiances. Generally, this results in less than a $\sim$1% modification. The 0% transmission baselines were observed to be very flat (with wavenumber) when the true transmission was known to be zero so no attempt to modify them was made.

A 1-2% discontinuity in the ratio of consecutive (evening to morning) background scans was observed for a large number of spectra. This is illustrated in Figure 4.30. For this reason, the method for setting the the transmission spectra to 1 is performed separately for wavenumber regions less than and greater than $\sim$1700 cm^{-1}, using the low and high frequency band wings as reference. Specifically, the 1140–1200 cm^{-1} region is used to adjust below 1700 cm^{-1} and the 2150–2220 cm^{-1} region is adjust above 1700 cm^{-1}. The source of the discontinuities is unknown, but is speculated to be due to a non-linear response in the detector as the room heated up slightly. To avoid this problem, the detector was wrapped in foam to provide better thermal insulation, but the discontinuity was still observed. In any event, because the ratio is constant on either side of 1700 cm^{-1}, and because this effect was consistent, we feel that we are justified in ratioing these two wavenumber region separately.

Also evident in Figure 4.30 are some relatively high frequency components in the background scans. These are attributed to the response of the detector and were found consistently throughout the data collection. Their presence does not corrupt the spectra in any way.

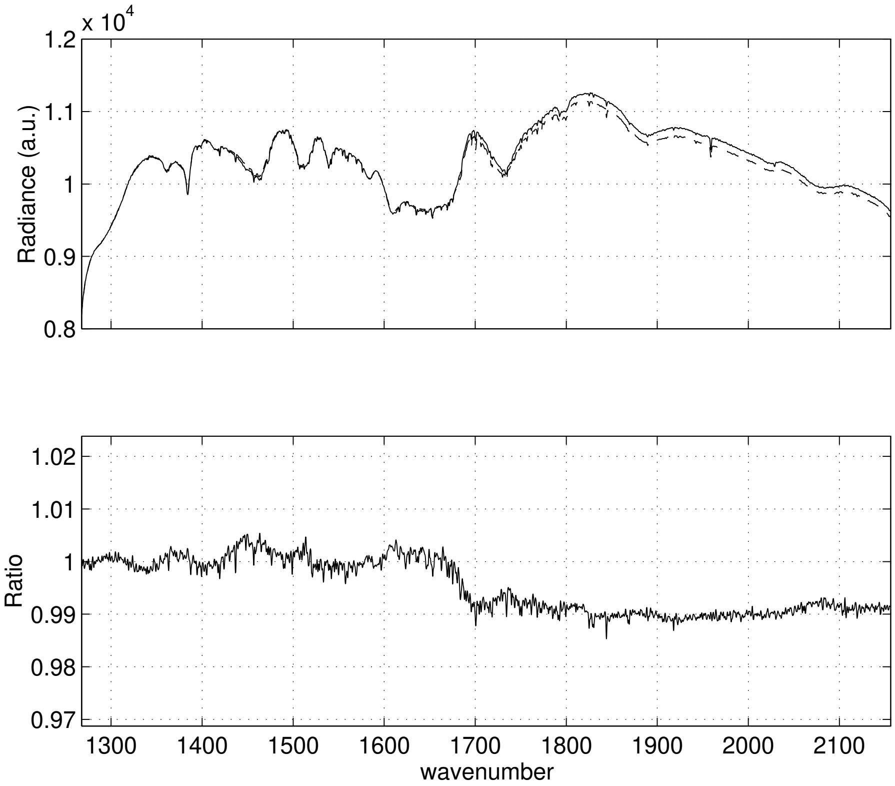

Figure 4.30: Two consecutive evacuated background scans (top panel) recorded before (solid curve) and after (dashed curve) the sample runs and their ratio (bottom panel). Elapsed time ~ 10 hours.

The 100% transmission baselines were fine-tuned further by adjusting the transmission in the two regions of low absorption on each side of the ν_2 band to agree with calculations based on CKDv2.1. For the highest N_2-broadened optical depth spectrum (file number 30: 84m, 15 torr H_2O, 800 torr N_2), this results in adjusting the transmissions to 0.9946 and 0.9976 in the 1140–1200 cm^{-1} and 2150-2220 cm^{-1} regions, respectively. These adjustments fall well within the noise level of the data in these regions. Thus, even for the highest optical depth studied here, the baseline adjustments are very small and have little effect on the measured absorption coefficients *within* the band. For example, a 0.997 adjustment to a spectrum has a ~1% effect on the absorption coefficient for regions of 15% absorption and a ~0.25% effect for regions of 70% absorption. (The continuum coefficients presented in Section 4.7 were analyzed with and without this final baseline adjustment – the differences in the resulting coefficients are negligible.)

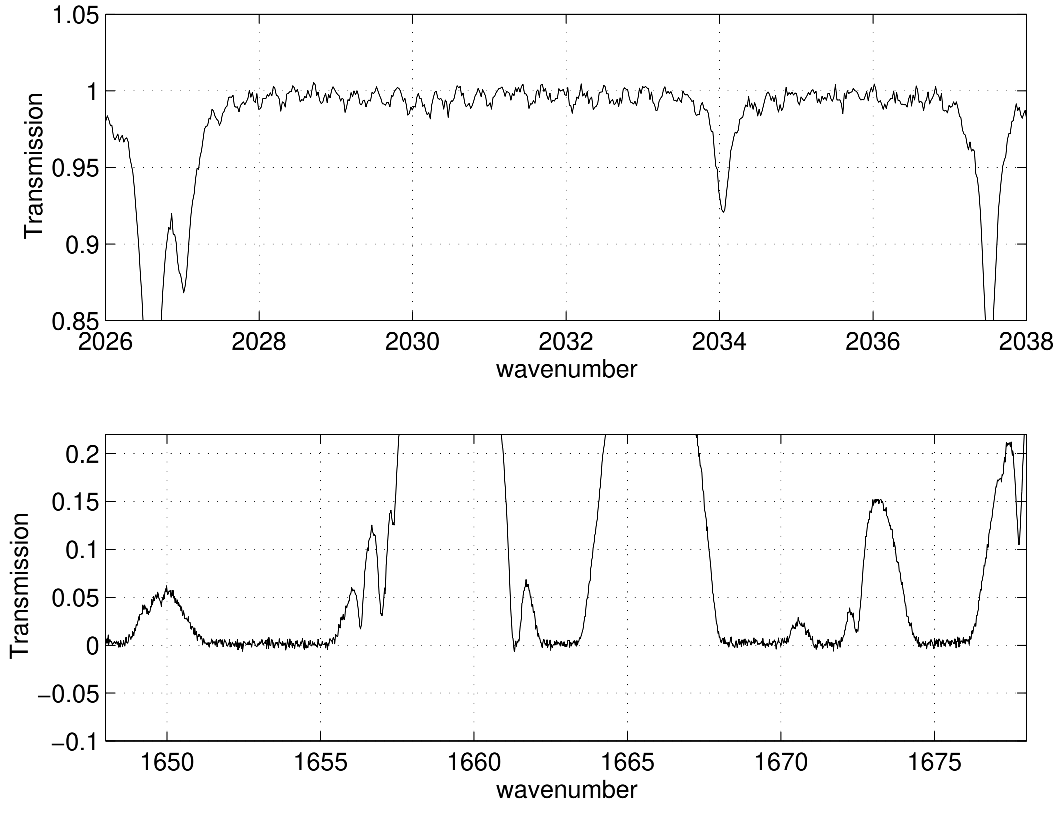

Figure 4.31: Sample 100% transmission baseline and fringes (top panel) and 0% transmission baseline (bottom panel).

Figure 4.31 illustrates typical 100% and 0% transmission baselines. Fringes are evident in the top panel – these are addressed below.

4.4.2 Fringes

Fringes similar to those in the top panel of Figure 4.31 were observed in a large number of spectra. They are due to some sort of standing wave in the optical path, although their exact source is unknown. In general, they have a cosine form with a period of $\sim$0.25 cm^{-1}. No known features in the optical path (i.e. distance between windows, etc...) have this characteristic length. The period of the fringes vary slightly with wavenumber and thus they are not true standing waves. Furthermore, they vary in period and amplitude from one spectrum to another and thus are not easily removed. Several attempts to remove them from the spectra have been made. The most effective include: (1) smoothing in wavenumber space, (2) smoothing in Fourier space, and (3) Wavelets smoothing. In general, these attempts were marginally successful in regions where there are relatively few spectral lines. However, because there are frequency components in the spectra which are very close in amplitude and frequency to the fringes, their removal is difficult. Thus, for the analysis presented here, due to the possibility of also corrupting other information in the spectra, the fringes have not been removed. For the majority of this research, this is not a problem because the wavenumber regions under investigation (the “microwindows”) are much wider than a typical fringe and thus the fringes can simply be averaged out.

4.4.3 Instrument Function

The instrument function is developed by mimicking the behavior of the FTS. Starting with a calculated monochromatic transmission spectrum, the spectrum is taken smoothly to zero outside the spectral region of interest. The Fourier transform of the spectrum is then taken. The interferogram is set equal to zero beyond the maximum optical path difference corresponding to the instrument’s resolution (i.e. 26.39 cm for 0.040 cm^{-1} resolution, 92.30 cm for 0.011 cm^{-1} resolution.) The inverse Fourier transform of the interferogram is then taken, but with a reduced number of points consistent with the point spacing of the raw data, yielding a spectrum of the desired resolution.

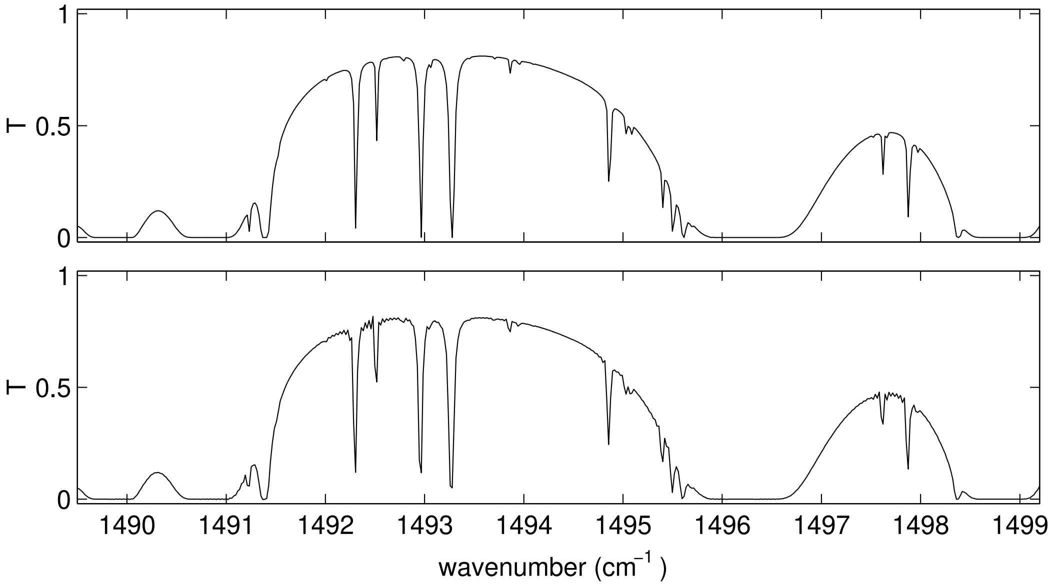

Figure 4.32: Monochromatic (top panel) and 0.040 cm^{-1} resolution (bottom panel) pure spectra calculated for 10 torr H_2O, 84 m path length, and 296K.

H_2O self-broadened halfwidths range from 0.1 cm^{-1}/atm for the weaker lines up to 0.55 cm^{-1}/atm for the strongest lines. Assuming a pure sample of $\sim$ 10 torr H_2O, the widest lines have widths of $\sim$0.014 cm^{-1}. Therefore, with a resolution of 0.040 cm^{-1} (and even 0.011 cm^{-1}), the unsaturated, self-broadened lines are not resolved with these measurements. For this reason, and because the self-broadened widths have been measured by other investigators, an analysis of these parameters is not attempted in this work. However, within the band where lines are extremely saturated, the spectra are fully resolved, even for pure spectra. This is illustrated in Figure 4.32 with a calculated monochromatic pure spectrum and a calculated spectrum degraded to 0.040 cm^{-1} resolution. (Actual calculations, not measured spectra, are compared here to avoid any errors in spectral line parameters which could appear as instrumental broadening.) While the weaker, narrow lines in the figure between $\sim$1492 and 1493.5

cm^{-1} are not resolved, the wings of the strong lines centered at ~ 1490.7, 1496.2, and 1498.7 cm^{-1} are fully resolved.

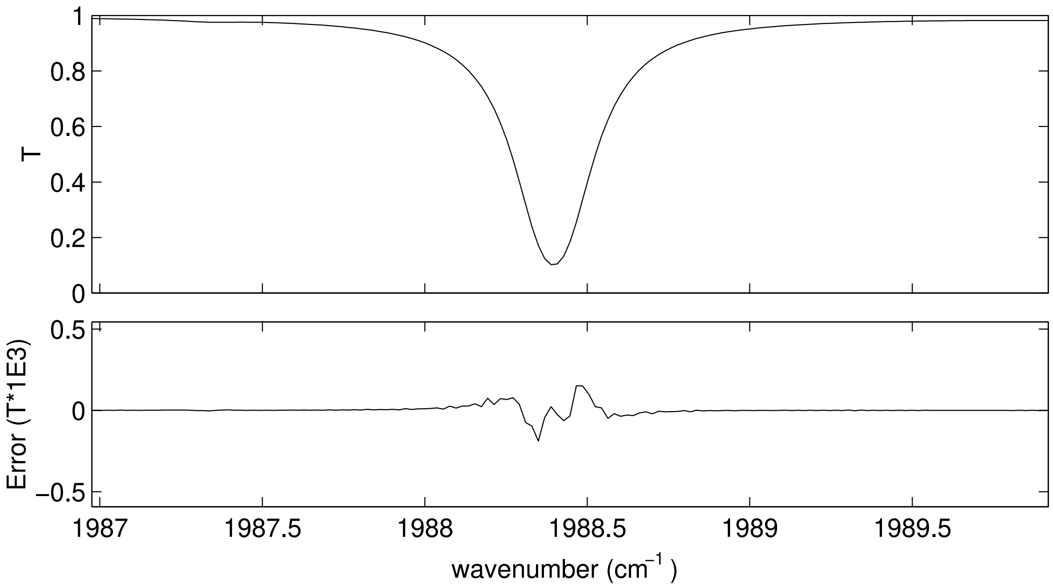

Figure 4.33: Monochromatic (solid curve) and 0.040 cm^{-1} resolution (dashed curve) calculations for an isolated nitrogen broadened line are shown in the top panel. The difference (multiplied by 1000) is shown in the bottom panel. Parameters are 5 torr H_2O, 500 torr N_2, 12 m path length, and 296K.

For foreign broadened spectra, the saturated low J lines within the band are fully resolved at 0.040 cm^{-1} resolution. Furthermore, most of the stronger, high J band wing lines are also fully resolved at 0.040 cm^{-1} resolution as long as the broadening pressure is high enough. The nitrogen-broadened halfwidths of the stronger H_2O lines are on the order of 0.12 cm^{-1}/atm. Therefore, assuming a self pressure of ~10 torr, most of the lines are fully resolved as long as the nitrogen pressure is greater than ~150 torr. This is fortunate, and allows for examination of the nitrogen broadened halfwidths when warranted. However, some nitrogen broadened widths are much smaller, on the order of 0.04 cm^{-1}/atm, and are not resolved unless the broadening pressure is well above 1 atmosphere. These narrower lines must be avoided when determining lineshape

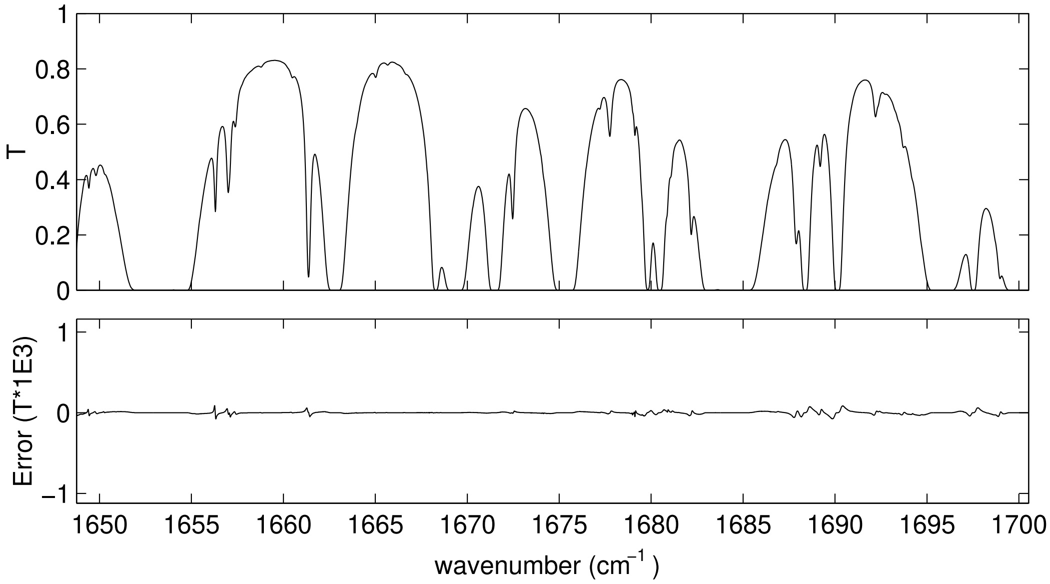

Figure 4.34: Monochromatic (solid curve) and 0.040 cm^{-1} resolution (dashed curve) calculations between 1650 and 1700 cm^{-1} for nitrogen broadening are shown in the top panel. The difference (multiplied by 1000) is shown in the bottom panel. Parameters are 5 torr H_2O, 500 torr N_2, 12 m path length, and 296K.

behavior from the spectra. Monochromatic and 0.040 cm^{-1} resolution calculations and their difference (magnified by 1000) for an isolated line at 1988.4 cm^{-1} broadened with 500 torr of nitrogen are shown in Figure 4.33. Similar calculations within the band are shown in Figure 4.34.

4.5 H_2O Partial Pressures

When analyzing the spectra, a very simple and yet extremely important factor is knowing the water vapor pressure in the cell as the spectrum is recorded. For pure water vapor samples, the water vapor pressure can be measured directly with the capacitance pressure gauges. However, due to the observed tendency [78, 99] of water vapor to adsorb onto even relatively smooth surfaces, combined with the relatively long times required to perform a measurement, makes it non-trivial to be certain of the water vapor pressure when the cell contains a mixture of gases. As a result, for foreign broadened spectra, water vapor amounts have been determined directly from the spectra rather than simply using the (total) pressure gauge readings.

For these determinations, Lorentzian profiles were fit to unsaturated, well-isolated, well-resolved nitrogen-broadened lines. Since the spectral resolution (0.04 cm^{-1}) is sufficient to resolve N_2-broadened lines in the band wings, H_2O partial pressures can be monitored using these lines if the line strengths have been determined independently. These fits were performed in a way such that the water vapor pressures were determined independently from the line-widths, with the main source of error due to the uncertainties in the line strengths. Summarizing the results of this analysis, the main conclusions are: (1) By comparing pressure gauge readings for pure samples to the fitted water amounts for nitrogen-broadened samples, roughly 3 to 5 % of the water vapor appears to adsorb onto the cell walls, (2) Within experimental error, the water vapor partial pressures remain stable after addition of the first ~150 torr of nitrogen into the cell, and (3) Averaging over 30 to 40 spectral lines, the water amounts are determined with accuracies of 3 to 4 %, which is due primarily to the accuracy of the line strengths [100].

The fact that the isolated, unsaturated lines used for this analysis show Lorentzian behavior is an important observation in itself. First of all, it implies that there is no significant instrumental broadening of these lines, which would probably lead to more of a Gaussian lineshape. More importantly, the Lorentzian behavior shows that the impact approximation is valid within the 1–2 halfwidths of line center which are probed with these optical depths.

For each nitrogen broadened spectrum recorded at 0.040 cm^{-1}, lines in the band wings (~1090–1375 cm^{-1}, 1800–2240 cm^{-1}) were chosen for the fits. Lines which (1) do not overlap significantly with other lines, (2) have the correct optical depth ($0.2 \le T \le 0.8$), and (3) are fully resolved, were selected. For each spectrum, 30–40 spectral lines were selected. For each line, the H_2O partial pressure is determined by fitting the data to:

$$k(\nu) = P_{H_2O} L \frac{S}{\pi} \frac{\gamma_{obs}}{\left(\gamma_{obs}^2 + (\nu - \nu_0 - \delta\nu)^2\right)} + b \tag{4.10}$$

where the water vapor pressure, P_{H_2O}, the observed halfwidth, γ_{obs}, a possible lineshift, $\delta\nu$, and b are allowed to float. b is generally very close to zero and is included to account for far-wing absorption by other lines and/or inaccurate baselines. Allowing the line width to float effectively decouples the fit from uncertainties in the width and any residual instrument broadening. Note that the width term does not explicitly include P_{H_2O}, effectively decoupling the dependency of the fitted H_2O partial pressure from the observed line width. This is a rather important point since most of these widths are not known very accurately – this will be addressed further in Section 4.6. The quality of these fits was very high, with residuals due only to noise in the data. Thus, the optical depth, $P_{H_2O}LS$, of each line is determined to the accuracy of the data. The accuracy of P_{H_2O} is then limited mainly by the accuracy of the independently measured line strengths.

Sample fits are shown in Figures 4.35, 4.36, 4.37 for file numbers 152, 153, and 154 (~10 torr H_2O plus 300, 500, 800 torr N_2, 296K, 12m path length). The fits were complicated by the presence of fringes in some spectral regions. To account for these, a cosine function was also included in the fit, fitting for its amplitude and frequency. This was marginally successful for only for a small number of lines. For example, in the top rows of Figures 4.35 through 4.37, the fits did not successfully account for the fringes. However, because the residuals are centered around zero, the fitted water vapor pressures are not distorted by the presence of the fringes. In general, the fits were also more conclusive in the high wavenumber band wing due to the increased signal-to-noise in this region over the lower wavenumber wing.

Averaging over all of the selected spectral lines, the statistical error in the fitted water amounts is 3 to 4%. This error is probably a combination of uncertainties in the line strengths and measurement errors. Figure 4.38 shows the fitted water vapor pressures for several lines in the high wavenumber wing for four sets of N_2-broadened spectra. After a close examination of all lines, the fitted partial pressures versus line center show similar trends for different sets of spectra, leading to the conclusion that the pressure determinations are limited by the accuracy of the line strengths. The strengths used for this analysis are from HITRAN and are based on measurements by Toth [100], with quoted accuracies of 2–4 %. It is likely that the relative strengths of isolated lines in HITRAN are quite accurate, so it is not surprising that the statistical error in the H_2O partial pressure is so low. Systematic errors in the line strengths will of course affect the determination of the H_2O partial pressure. However, since a strength/pressure product which is derived from the spectra is used to compute the local absorption, systematic errors in the line strengths will partially cancel in the continuum determinations.

The water vapor pressures determined here will be used to analyze the continuum and lineshape behavior further into the band. To be certain that the derived pressures are accurate for this application, an assumption that the line strengths have no significant systematic offsets between the regions used for this analysis (the band wings) and within the band must be made. Since the strengths used for this analysis are the product of one investigator and one instrument (Kitt Peak FTS), this assumption is most likely valid. This concern will be addressed further in Section 4.6.

The derived H_2O partial pressures indicate that roughly 5% of the water vapor was adsorbed onto the cell walls with the addition of the first ~100 torr of N_2 (or O_2). However, no evidence that the H_2O partial pressure changed thereafter was found, allowing the use of an average H_2O partial pressure derived from spectra at all pressures in each data set. This is illustrated in Figure 4.39 for a line at ~2060.5 cm^{-1}, where the slope of the fitted water vapor pressure versus increasing total cell pressure is essentially zero.

Fits were also performed for a given line by fitting for a single water vapor pressure using all of the nitrogen broadened spectra simultaneously. For example, the spectra for files 152, 153, and 154 would be fit simultaneously for each selected line. In contrast to the method described above, this method assumes that the water vapor pressure is constant with increasing nitrogen pressures. Sample fits are shown in Figure 4.40. The resulting fitted water vapor pressures fall within the accuracy of the previous results and the residuals are also comparable to those described above. Thus, the conclusion that the water vapor pressure is unchanged after the first addition of nitrogen appears to be correct.

Fitted water vapor pressures and their uncertainties, which are used in the rest of the analysis, are listed in the last column of Table 4.3. These values were determined by fitting for the water amounts for each spectrum and for each line. For each line, a mean partial pressure is determined for every set of spectra (one value for all nitrogen pressures). These values and their uncertainties are then combined by averaging over all selected lines to arrive at a final partial pressure and uncertainty.

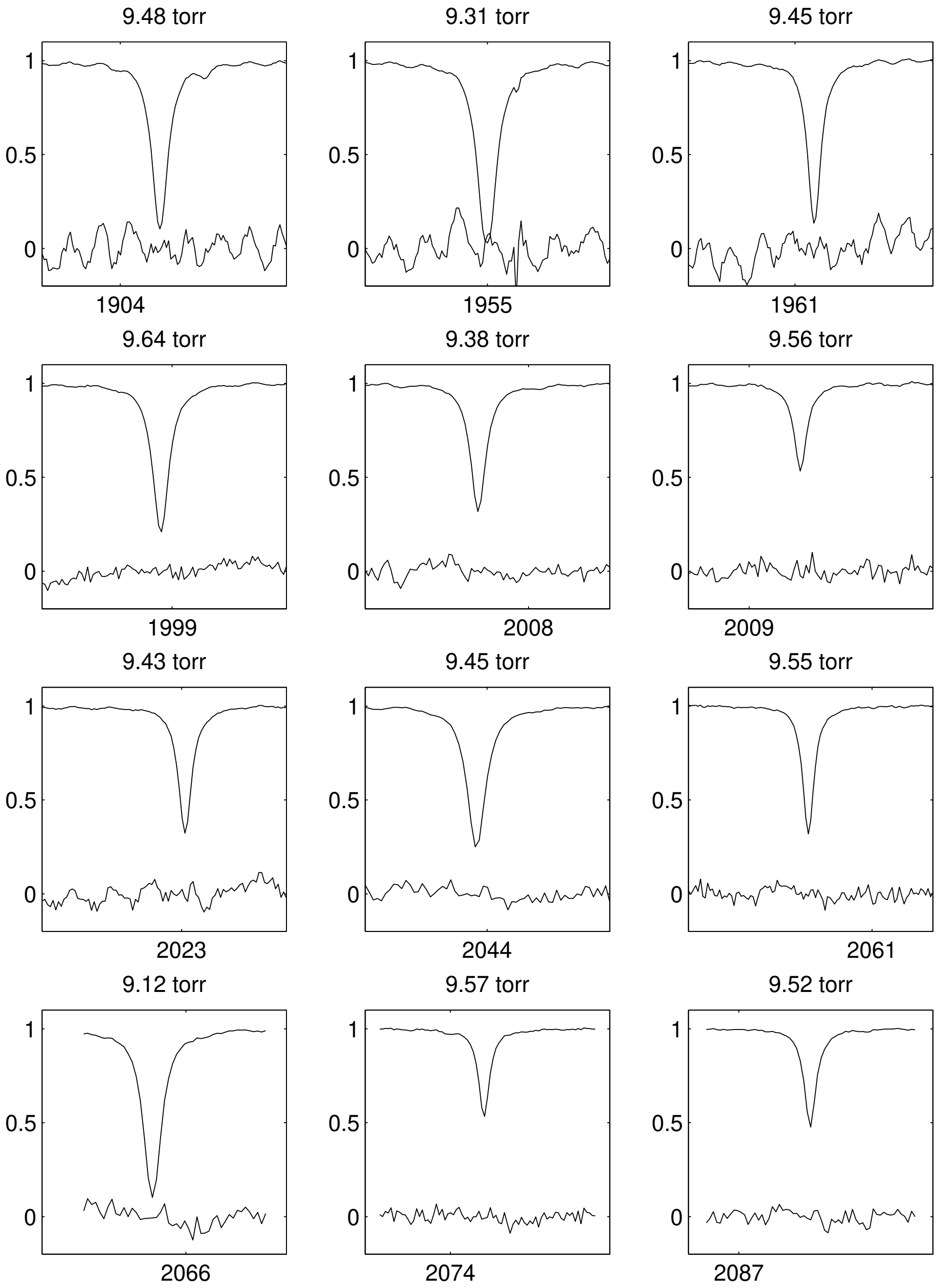

Figure 4.35: Fits for water vapor pressures for file number 152 (~9.5 torr H_2O, 300 torr N_2, 12 m path length, 296K) for 12 lines in the high wavenumber band wing. The figures show measured transmission and residuals (multiplied by 10) versus wavenumber. The fitted water vapor pressures are also noted.

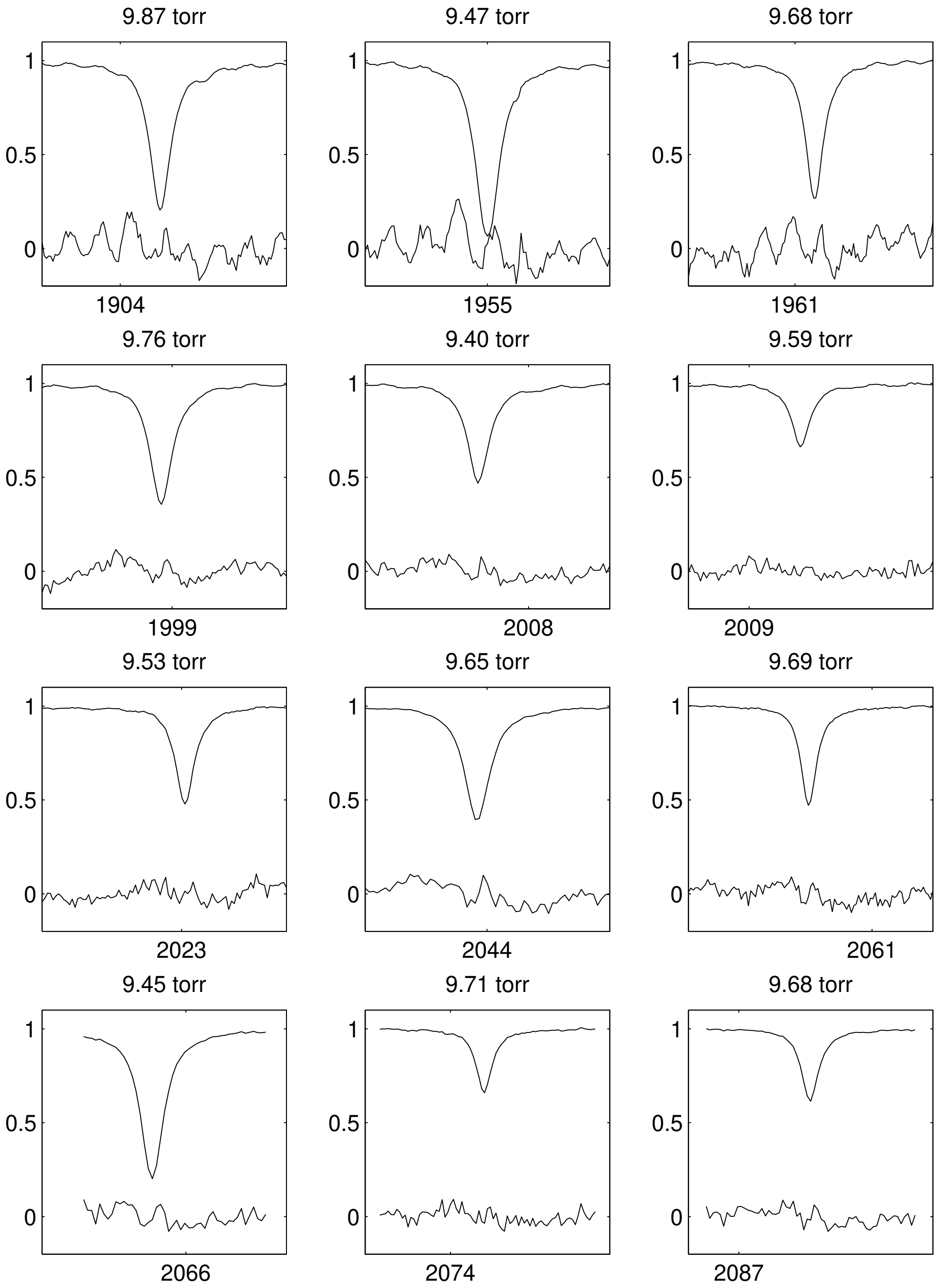

Figure 4.36: Fits for water vapor pressures for file number 153 (~9.5 torr H_2O, 500 torr N_2, 12 m path length, 296K) for 12 lines in the high wavenumber band wing. The figures show measured transmission and residuals (multiplied by 10) versus wavenumber. The fitted water vapor pressures are also noted.

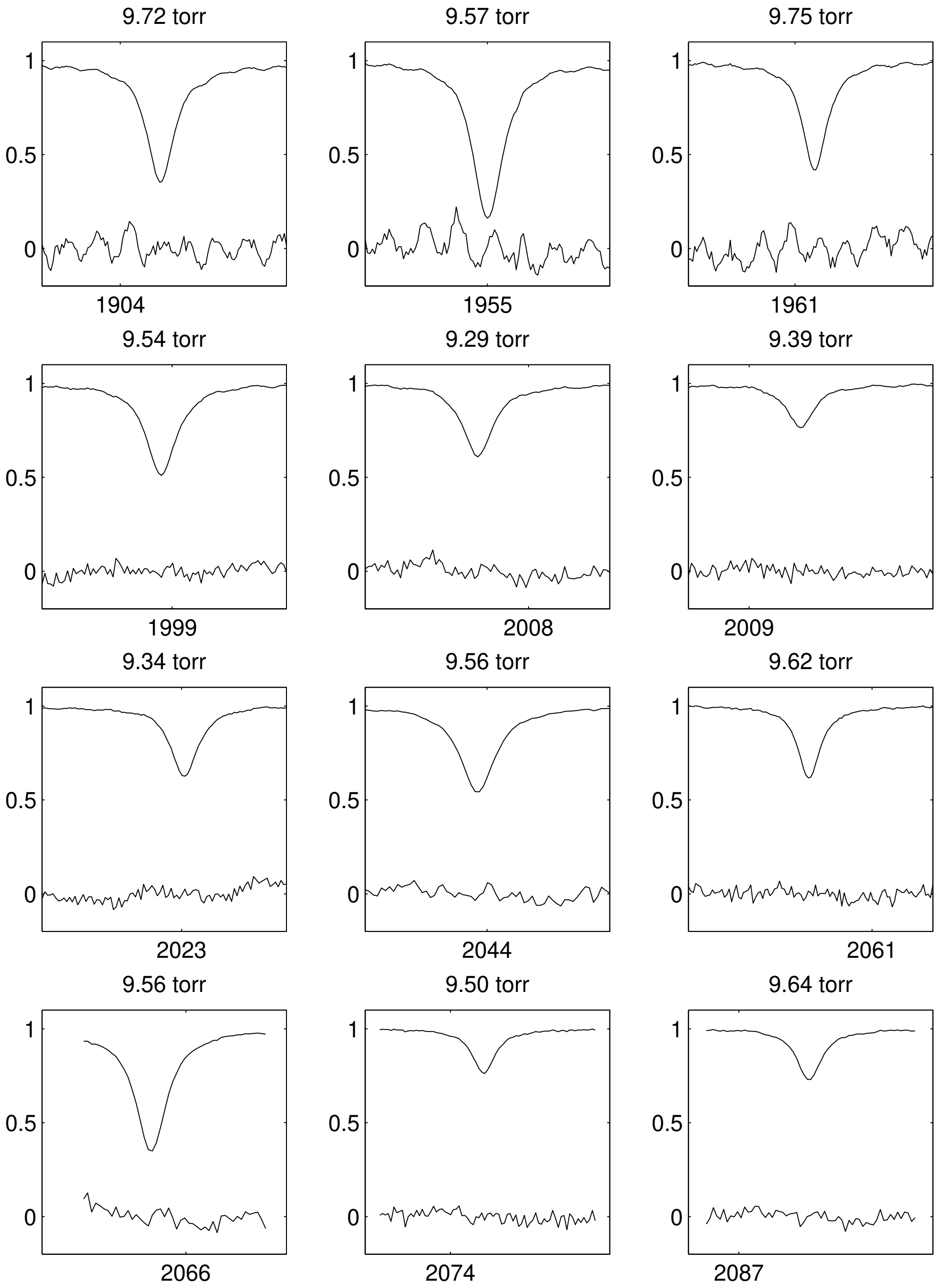

Figure 4.37: Fits for water vapor pressures for file number 154 (~9.5 torr H_2O, 800 torr N_2, 12 m path length, 296K) for 12 lines in the high wavenumber band wing. The figures show measured transmission and residuals (multiplied by 10) versus wavenumber. The fitted water vapor pressures are also noted.

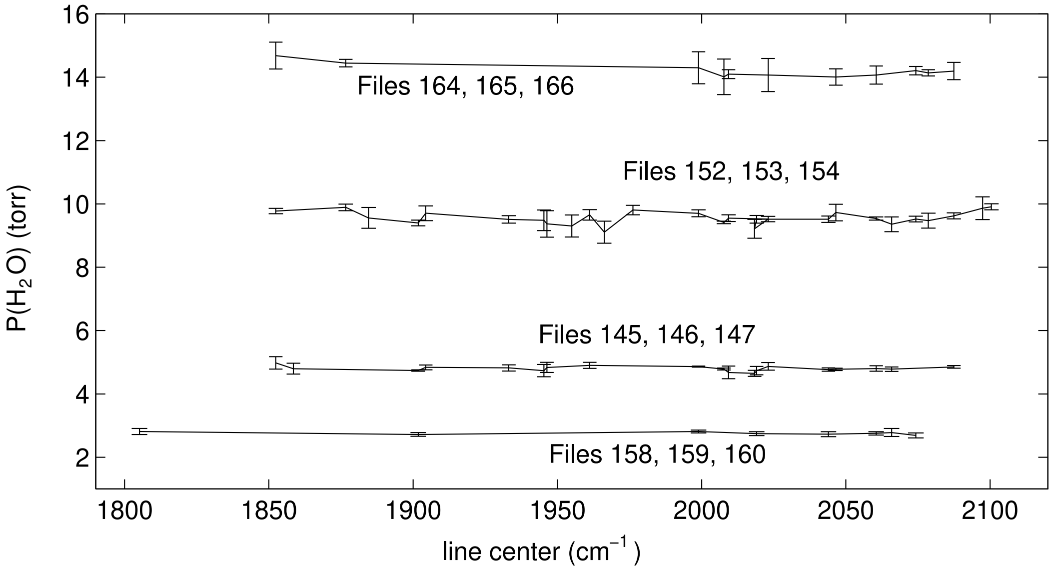

Figure 4.38: Water vapor partial pressures determined for four sets of N_2-broadened spectra in the high wavenumber band wing. Error-bars are determined by averaging over results obtained from spectra of various N_2 pressures.

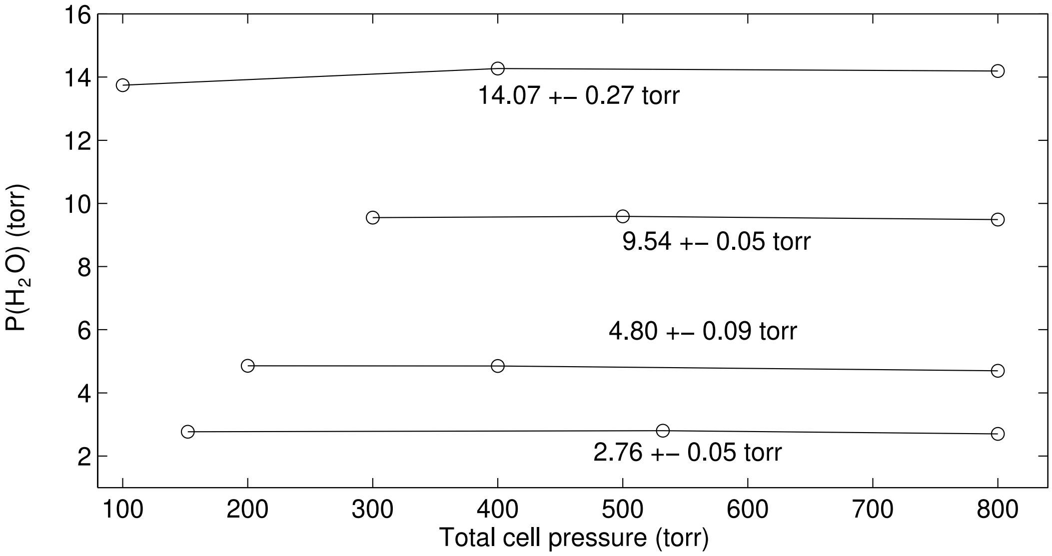

Figure 4.39: Water vapor partial pressures determined for spectra at various N_2 pressures from a line at $\sim$2060.5 cm^{-1}.

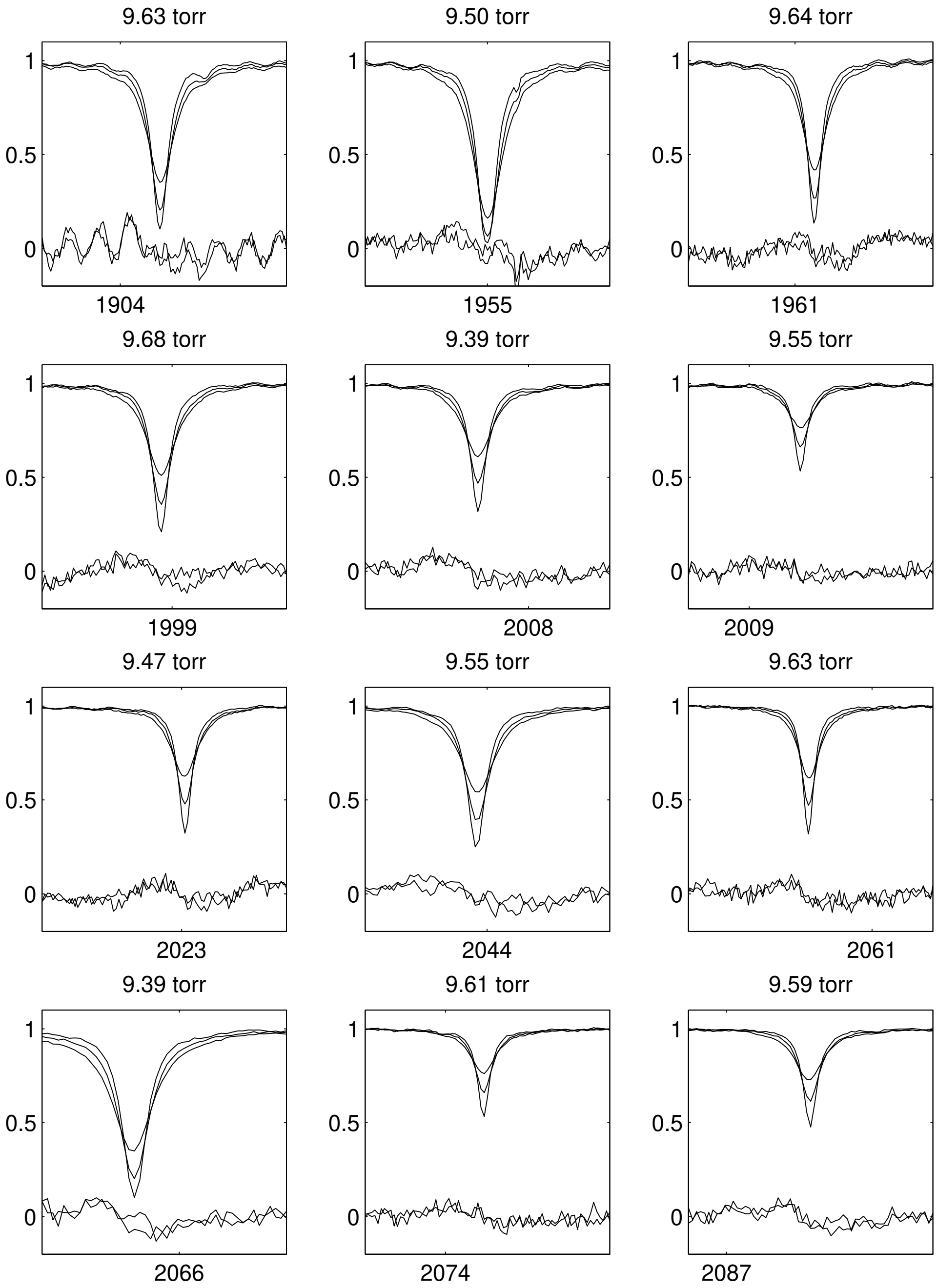

Figure 4.40: Fits for water vapor pressures for file numbers 152, 153, and 154 (~9.5 torr H_2O, 300, 500, and 800 torr N_2, 12 m path length, 296K) for 12 lines in the high wavenumber band wing. The figures show measured transmission and residuals (multiplied by 10) versus wavenumber. The fitted water vapor pressures are also noted.

4.6 Line Parameters

This section discusses the spectral line parameters used to calculate the local absorption coefficients (Equation 4.1). Unlike the window regions at 4 and 10μm, there are many strong spectral lines within the ν_2 band (approximately 7,500 transitions between 1000 and 2500 cm^{-1}). To determine the continuum absorption (and simply to calculate the local absorption), these lines must be characterized as accurately as possible. Because of the direct relationship between the local and continuum absorptions, any errors in the line parameters for lines within 25 cm^{-1} of the observation frequency will lead to errors in the retrieved continuum coefficients. This is particularly true when examining deviations from Lorentzian behavior very close to line center – in this case, any uncertainty in the line strengths and/or widths translates directly to the ability (or inability) to determine the actual lineshape. Determining the continuum in the microwindows (more than $\sim$1 cm^{-1} from any strong lines) does not require such strict constraints, but is also sensitive to the line parameters.

A review and analysis of the parameters are given in the following sections. However, a summary of the choice of line parameters is given here. Line positions and strengths are taken from the 1992 HITRAN database [3], which consists primarily of measurements by R. Toth [100] for the ν_2 band of $H_2^{16}O$. Self broadened widths were provided by R. Toth [101]. Nitrogen broadened halfwidths are taken from the 1992 HITRAN database, from recent measurements by R. Toth [101], and from measurements by J. J. Remedios [102]. For the strong lines at the center of the $H_2^{16}O$ ν_2 fundamental, the self- and nitrogen broadened halfwidth measurements of Remedios are used. His corresponding air-broadened widths are currently on the HITRAN database. Toth's measured values of nitrogen broadened halfwidths are used for the $H_2^{18}O$ and $H_2^{17}O$ lines. For all remaining lines, the HITRAN air-broadened values are used, divided by a factor or 0.9 to convert them to nitrogen broadening. Independent nitrogen broadened halfwidth measurements have also been performed using the spectra collected at 0.011

cm^{-1} resolution and good agreement is found with the values of Remedios for the $H_2^{16}O$ lines. For lines which have optimum measurement conditions, we find agreement to within 2 to 3 percent, which is considered very good agreement in the field.

The line centers, shifts, strengths, and widths used in this work are presented below. For the case of self, nitrogen-, and air-broadened line widths, measurements have been performed by R. Toth of JPL specifically for use in this analysis and for AIRS. Previously, analysis of the in-band water vapor continuum was not attempted, due in part to the inaccuracies of these parameters. For each individual parameter, the obvious questions are (1) How well is this parameter known? and (2) How does its uncertainty impact the analysis of the continuum absorption? Answering these questions for each and every H_2O transition is far too time consuming and tedious. In this analysis, the works of several investigators are combined and used as inputs into this data analysis. To some degree, the accuracy of these values are accepted on faith. When warranted, however, independent studies to test their accuracy have been performed.

4.6.1 Line Centers and Strengths

Zero pressure line centers and line strengths are taken from the 1992 HITRAN database. These values are the result of measurements by R. Toth [100] of JPL performed with a high resolution (0.0052 cm^{-1}) FTS at the McMath solar telescope facility at Kitt Peak National Observatory. Spectra were collected with path lengths ranging from 0.08 to 433 meters and H_2O pressures of 0.018 to 13.1 torr at room temperature. In all, over 4500 measurements of line strengths and centers were made for over 900 $H_2^{16}O$ transitions. These measurements are regarded in the community as the most accurate set of line centers and strengths available. Some measurements of $H_2^{18}O$ and $H_2^{17}O$ were also performed – when measurements are not available, these strengths are determined from the corresponding $H_2^{16}O$ values adjusted for the natural atmospheric abundance. The line strengths and positions between 1100 and 2200 cm^{-1} are shown in Figure 4.41 for reference.

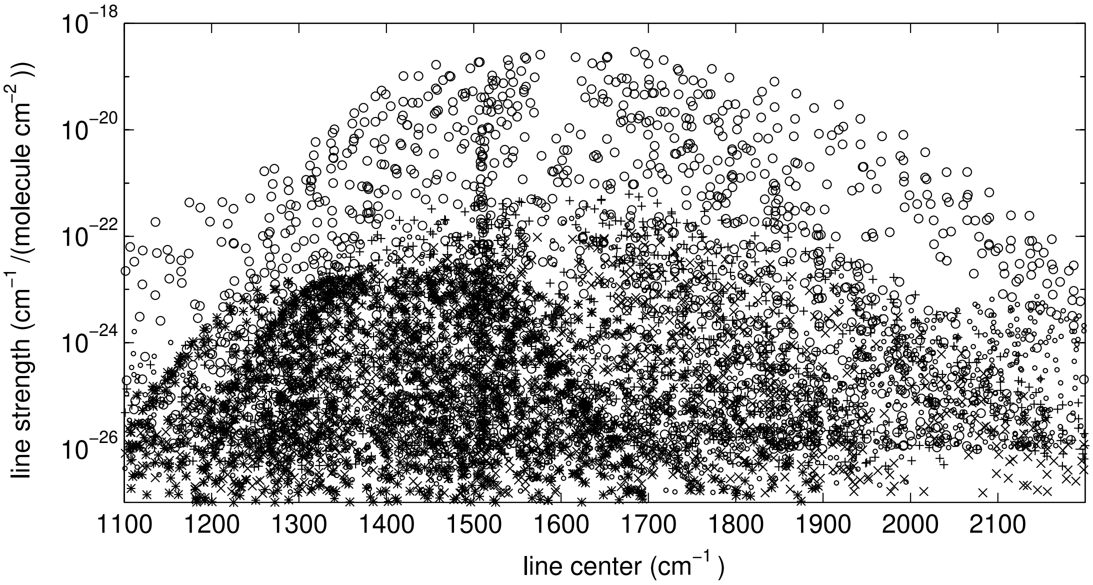

Figure 4.41: 1992 HITRAN water vapor transitions between 1100 and 2200 cm^{-1}: (o) $H_2^{16}O$ ν_2 band; (+) $H_2^{18}O$ ν_2 band; (x) $H_2^{17}O$ ν_2 band; (*) $HD^{16}O$ ν_2 band; (∘) other hot bands.

For the majority of the stronger lines, the transition frequencies are given to 5 places past the decimal and have absolute uncertainties of 6×10^{-5} cm^{-1}. For the weaker lines in the band wings, the uncertainties are slightly higher, but do not exceed 1×10^{-4} cm^{-1}. Thus, for this work, the line centers can be considered to be known perfectly, and do not introduce any noticeable errors into the data analysis.

In general, it is difficult to make blanket statements about the accuracy of a set of 900 independent measurements. This is particularly true for the line strengths which contain values ranging over 7 orders of magnitude. However, for the stronger lines near band center (i.e. $J \leq 4$), the strengths have quoted uncertainties that are generally less than 2%. For the higher J lines in the band wings, the uncertainties range from 2 to 4 %. These uncertainties are important for several reasons in this work: (1) the strengths of the band wing lines are used to determine the water vapor partial pressures (Section

4.5), and (2) the strengths of the strong low J lines and the partial pressures are used to determine the continuum. Any systematic errors in the strengths are also important since the water vapor partial pressures determined with band wing lines are used for analyzing the data further into the band. For these reasons, an analysis of the strengths has been performed with the 0.040 and 0.011 cm^{-1} resolution spectra collected in this work.

The accuracy of the band wing lines has already been presented, although in a different form, in Section 4.5 when the water vapor partial pressures were analyzed. Averaging over many lines, the partial pressures were determined to an accuracy of ~3-4 % using the high optical depth 0.04 cm^{-1} resolution spectra. Due to the manner in which the least squares fits were performed, these uncertainties are also the measured uncertainties in the line strengths. Thus, for the band wing lines, it appears that the quoted line strength accuracies of 2–4 % are consistent with our spectra.

The strengths of the stronger low J lines were also examined. This was accomplished using high resolution (0.011 cm^{-1}) to resolve the lines and very low optical depths so that the lines at band center are not saturated (i.e. file number 179). The high optical depth spectra that are used to determine the water vapor partial pressures cannot be used for this analysis because these stronger lines are totally saturated under high optical depth conditions. For the low optical depth spectra, only ~0.1 torr of water vapor was added to the cell. The lines were then broadened with nitrogen and spectra were collected at total cell pressures of 200, 400, and 800 torr. Due to the uncertainty in the water vapor partial pressures, the absolute values of the line strengths can not be determined with these spectra. However, the optical depth of each line (i.e. $P_{H_2O}LS_i$) can be examined and therefore, since P_{H_2O} and L are constants, systematic errors in the strengths can be monitored.

An analysis of file number 179 is shown in Figure 4.42. The fitted water vapor pressures are plotted versus line strength and line center. These values represent the spectral regions where optimum agreement was obtained – details of how these fits

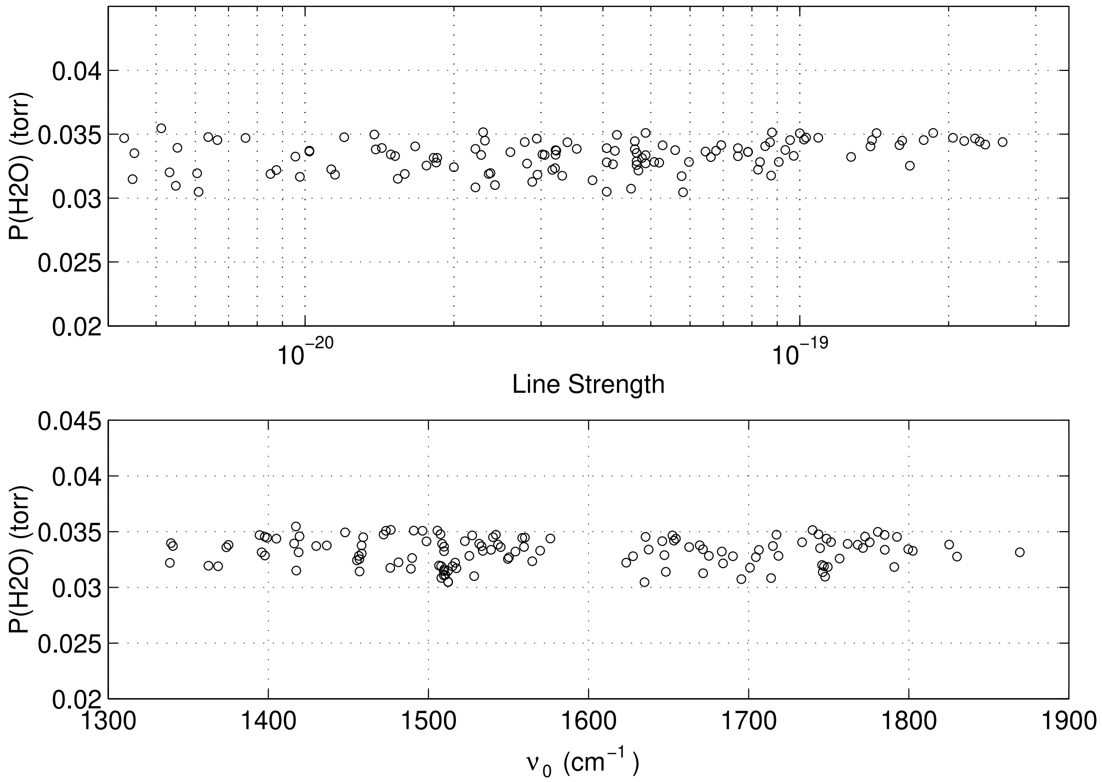

Figure 4.42: Fitted water vapor pressures versus line strength (top panel) and line center (bottom panel) for file number 179. (~0.034 torr H_2O, 790 torr N_2, 12m, 296K.)

were performed are presented in the line width analysis. Determining strengths from spectra is typically much easier than extracting broadening information – the only concern is that the integrated intensity of the line is well represented. In general, the best fits were obtained for the strongest, well-isolated lines and therefore, values for stronger lines have more confidence than for weaker lines. Note that there is smaller spread in the fitted water amounts in Figure 4.42 for the stronger lines. Lines below ~1300 cm^{-1} and above ~1850 cm^{-1} were not measured due to insufficient optical depth. Averaging over all measured lines, the partial pressure is 0.033(2) ± 0.001(3) torr (~4% uncertainty).

The main conclusion is that there are no obvious systematic errors in the fitted water amounts as a function of line center or line strength. The spread in fitted pressures for the weaker lines is due primarily to the quality of the fits and to the larger uncertainties in the strengths of the weaker lines. If there are systematic errors in the strengths over the ν_2 band, they appear to be on the order of 5% or less. To a certain degree, this validates the extension of the band wing analysis of the water vapor partial pressures for use further into the band.

4.6.2 Pressure Induced Line Center Shifts

Line center shift measurements were also provided by R. Toth of JPL. These came from the same data sets collected at the Kitt Peak facilities. This constitutes the most complete investigation of H_2O line shifts to date – all of the HITRAN values are zero.

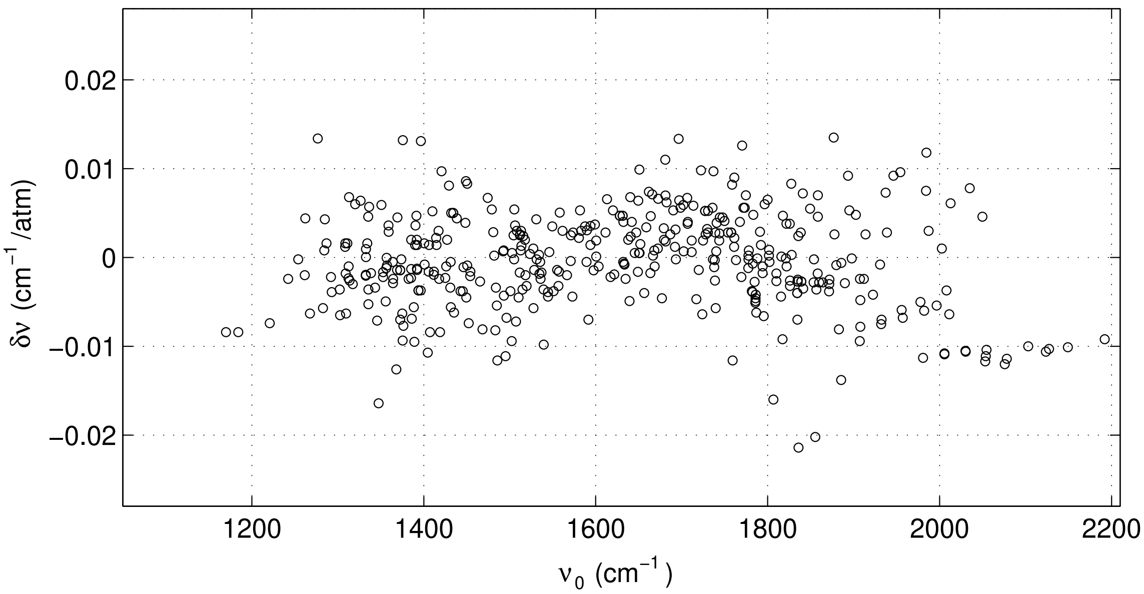

Figure 4.43: N_2 pressure-induced frequency shifts measured by R. Toth.

The shifts for broadening by nitrogen and by air are shown in Figures 4.43 and 4.44. These are “smoothed” values, obtained (by Toth) in the following way. For each line, several measurements were made and average values were obtained by using a

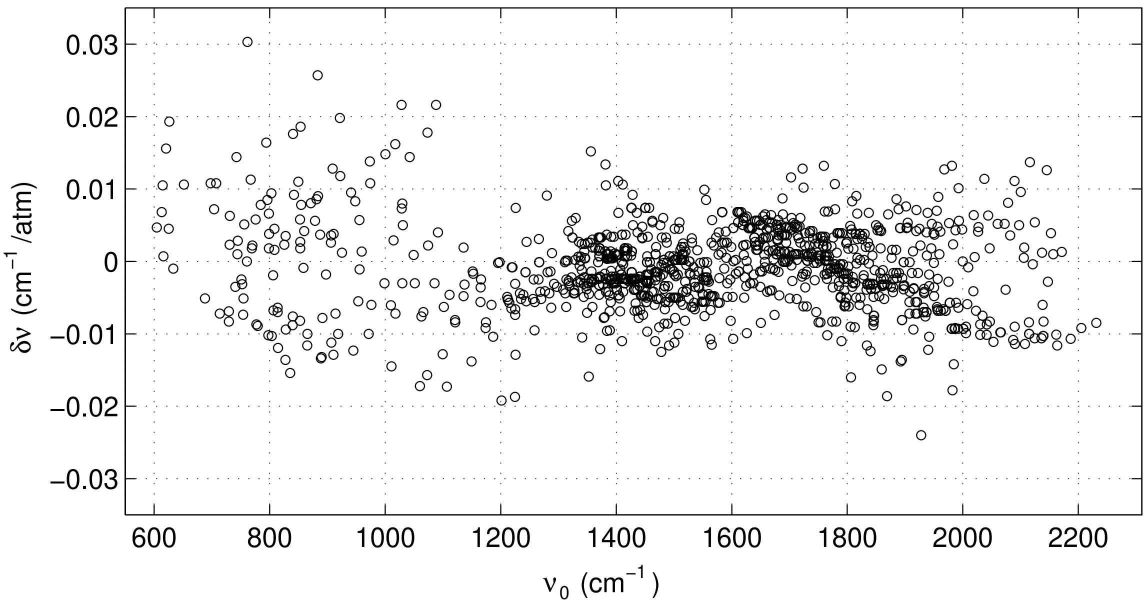

Figure 4.44: Air pressure-induced frequency shifts measured by R. Toth.

weighted mean. The smoothed values were then derived from plots of J versus the average values with each plot representing a family of transitions. For example, one series of transitions in rotational quantum numbers is: 111←000, 212←101, 313←202, 414←303, etc. ($JK_aK_c \leftarrow J'K_a'K_c'$).

Difference were noted between the R and Q^R transitions and the P and Q^P transitions, and therefore their values were not averaged as is sometimes done for line widths. Furthermore, due to the lack of an accepted way to extrapolate these measurements to other unmeasured lines [103], only the lines which were actually included in Toth's measurements are assigned shift values. All other lines receive shift values of zero.

For both air and nitrogen broadening, the uncertainty in the shifts range from 1 to 80 %, but are typically on the order of 20-40 %. Fortunately, the continuum analysis is not very sensitive to the line shifts. Furthermore, when individual lines are analyzed in this work, the shifts are usually determined independently.

4.6.3 Line Widths

The difficulties in characterizing the collision broadened line widths of H_2O have been discussed by Gamache *et.al.* [9]. They conducted an exhaustive review of H_2O line width measurements and calculations. Despite the quoted uncertainties of $\sim$1% in width measurements from many different investigators using modern high resolution spectrometers, the overall agreement between independent measurements for identical lines remains on the order of 10–15 percent, even for the most studied lines. These errors are clearly too large – the 1990 Atmospheric Spectroscopy Applications workshop [104] concluded that the widths should be known to 5% for most industrial/remote sounding applications. For spectroscopic studies such as this work, the uncertainties should be even lower. The large disagreement between individual measurements is attributed to larger systematic errors which are neglected in the data collection and analysis. These include: the inconsistent treatment of background lines, inaccurate baselines, poorly characterized optical depths, electronic non-linearities, not including an instrument function when needed, etc ... H_2O widths are also difficult to characterize because, unlike molecules such as CO_2, they vary over a wide range and follow no *simple* trends as a function of rotational quantum numbers. Thus, the choice of which widths to use is difficult. The sources and uncertainties in the self, nitrogen, air, and oxygen broadened widths used in this work are reviewed in the following sections. While all of the widths are important, the accuracies of the nitrogen broadened widths are crucial – due to the fact that in the lower troposphere, the total line widths are dominated by the nitrogen component. Likewise, the nitrogen component of the continuum is dominant within the ν_2 band.

4.6.3.1 Self-broadened Line Widths

Self-broadened line widths were provided by R. Toth of JPL. This is fortunate because many of the current values on HITRAN are zero and also because the self-broadened widths are not measurable with the resolutions used in this work. As with the line positions, shifts, and strengths, these measurements were performed with the Kitt Peak facilities.

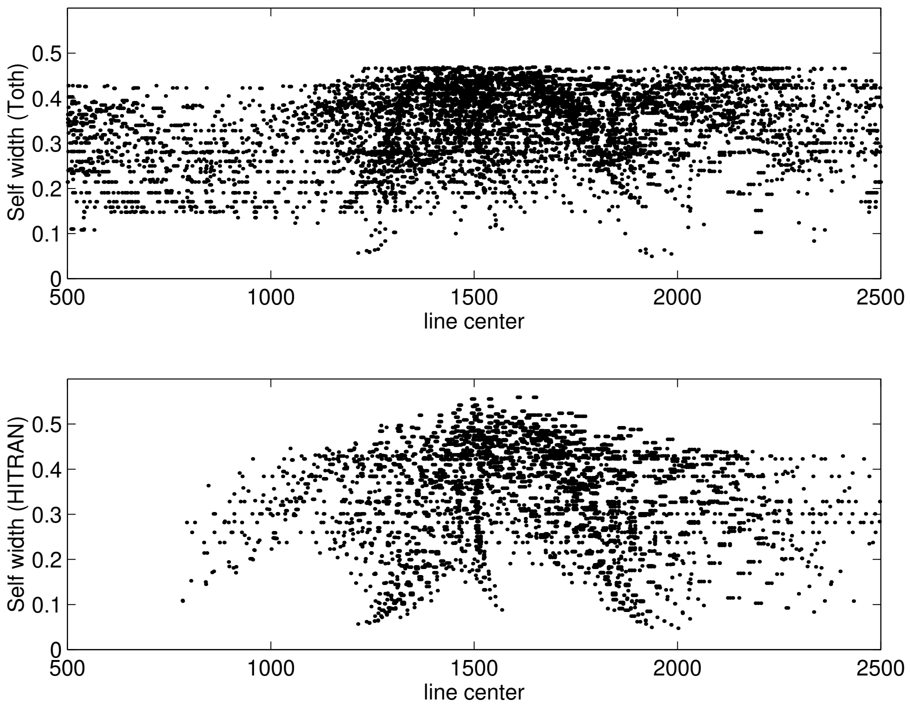

Figure 4.45: Self-broadened H_2O line widths of R. Toth (top panel) and HITRAN (bottom panel).

Toth's values were derived from the measurements of over 4000 lines of $H_2^{16}O$, $H_2^{17}O$, and $H_2^{18}O$ observed in the 010←000, 020←010, 020←000, 100←000, 110←000, 040←000, 120←000, 200←000, and 002←000 vibrational bands ($\nu_1\nu_2\nu_3 \leftarrow \nu_1'\nu_2'\nu_3'$). No statistically significant differences were found between R and Q^R transitions and P and Q^P transitions and their values were combined in the averaging process. Furthermore, vibrational and/or isotopic effects could not be determined and therefore average values were determined for all measurements relating to the same rotational transition. As with the line shifts, smoothed values were derived from plots of J versus the averaged values for each family of rotational transitions.

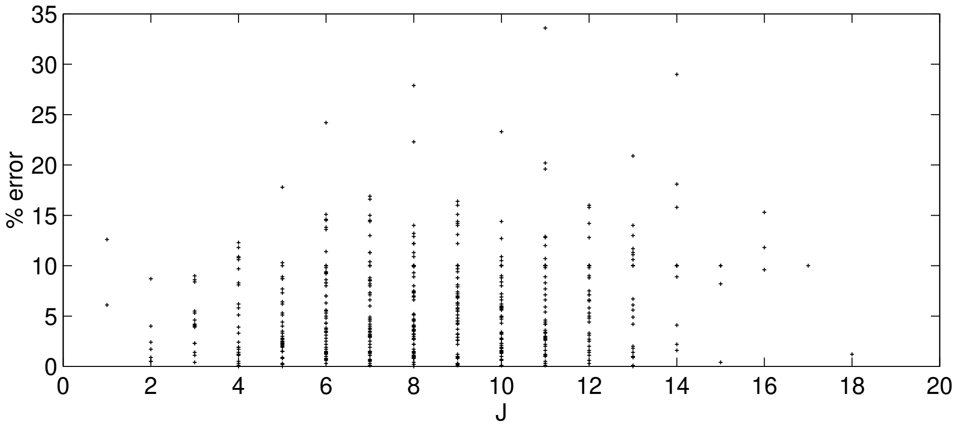

Figure 4.46: Measurement errors in Toth's self-broadened widths as a function of J.

The self-broadened widths of Toth and HITRAN are shown in Figure 4.45. The percent error in Toth's measurements are generally less than ~10%, although they are somewhat larger for $J \geq 6$. These are shown in Figure 4.46 as a function of J. For the strongest lines near band center (low J), the HITRAN widths are roughly 10% greater than those reported by Toth. Despite the fact that self widths are roughly 5 times greater than the nitrogen broadened widths, a ~10 percent error in the self widths fortunately has almost no effect on the total widths for a nitrogen broadened sample. For example, the percent error in the total widths computed for 10 torr of H_2O and 760 torr of N_2 using the HITRAN self widths versus using Toth's self widths is shown in Figure 4.47 as a function of line strength and line center. The errors for the strong lines are ~1%. For pure samples, however, the ~10-15 percent uncertainty in the widths must be accepted and factored into the analysis of the self-broadened near-wing lineshape.

4.6.3.2 N_2-broadened Line Widths

Nitrogen broadened halfwidths are taken from the 1992 HITRAN database, from recent measurements by R. Toth [101], from measurements by J. J. Remedios [102], and from

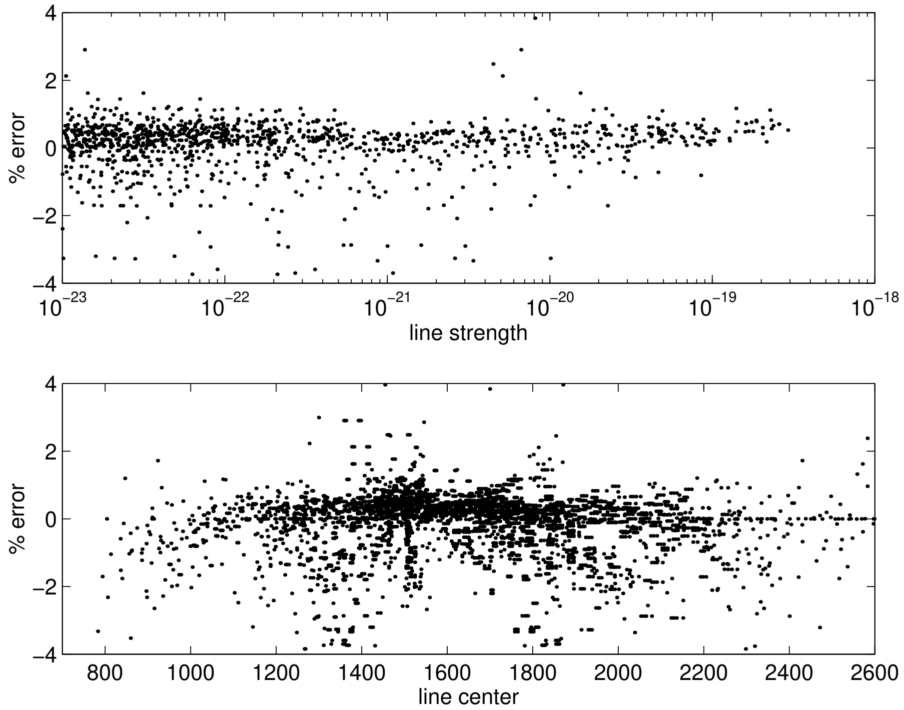

Figure 4.47: Percent errors in the total widths using HITRAN self widths versus Toth's self widths for 10 torr H_2O and 760 torr N_2 versus line strength (top panel) and line center (bottom panel).

independent measurements. The positions of these lines are shown in Figure 4.48.

4.6.3.2.1 Toth's measurement – $H_2^{18}O$ and $H_2^{17}O$ lines.

Toth's measured values of nitrogen broadened halfwidths are used for the $H_2^{18}O$ and $H_2^{17}O$ lines. Measurements were to be performed by Toth for the strong lines of the ν_2 band. However, due to a short air path in the optical path used when specific absorption cells are utilized, the strong lines were not measured – the data was collected at high N_2 optical depth to overcome the small air path and thus, the strong $H_2^{16}O$ lines were saturated. Instead, the fundamental lines of $H_2^{18}O$ and $H_2^{17}O$ were measured. These are shown as the $\oplus$ symbols in Figure 4.48.

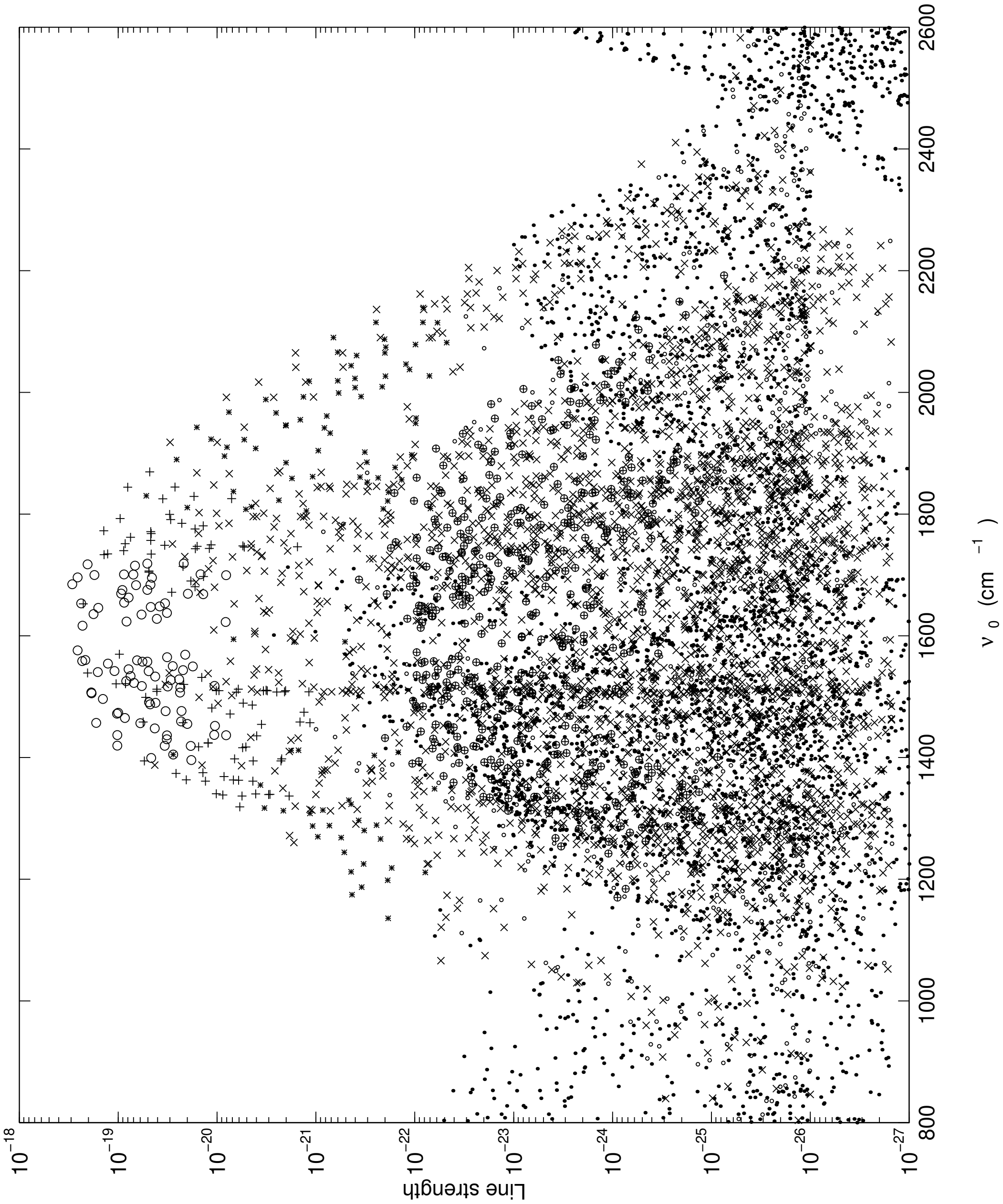

Figure 4.48: Sources of N_2-broadened widths: o, Remedios; +, this work (LOD); *, this work (HOD); x, Gamache QFT calculations; ₒ, Gamache scaled, average values; ⊕, Toth; ·, other.

Toth did not observe any significant differences between the R and Q^R transitions and the P and Q^P transitions, nor any isotopic or vibrational dependence. All values for similar rotational transitions were combined in the averaging process and smoothed values were obtained from plots of widths versus J for families of transitions, just as was done for the self-broadened widths.

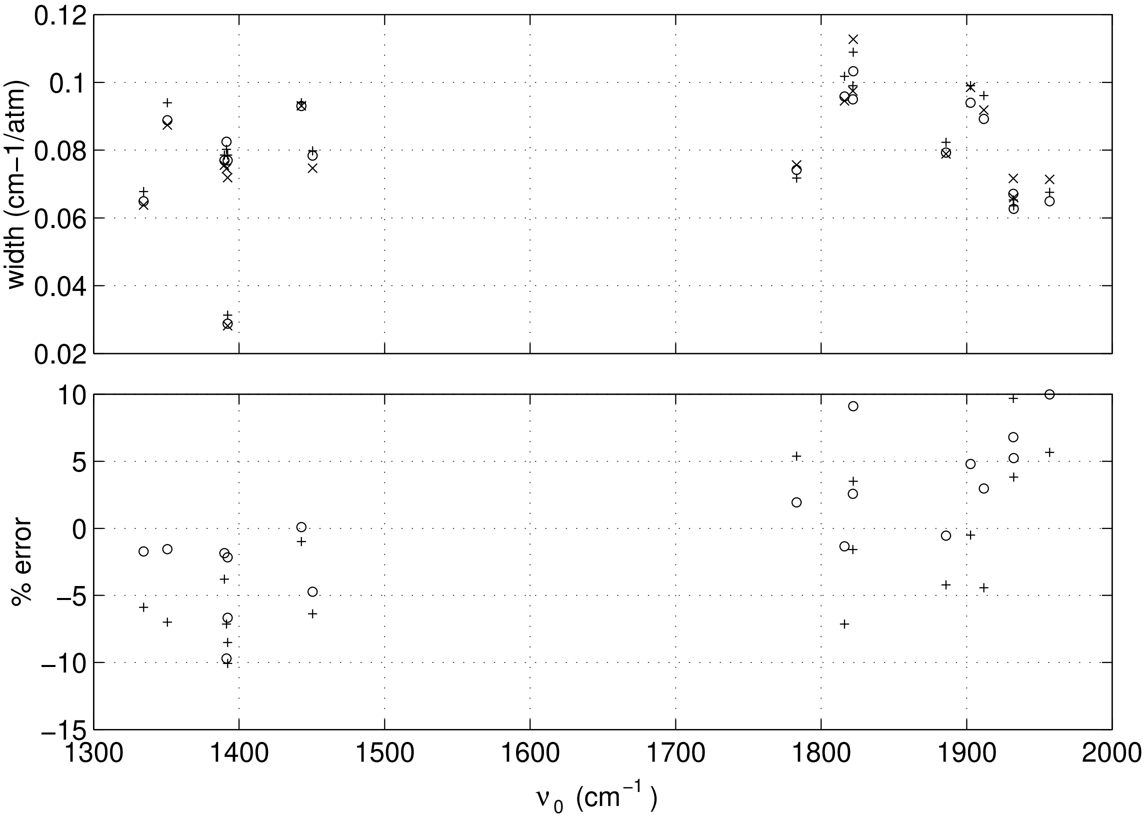

Figure 4.49: N_2 broadened widths for $H_2^{18}O$ lines measured with the HOD spectra: +, HITRAN; o, Toth; x, HOD measurements. The bottom panel shows the percent errors (relative to the HOD measurements) of Toth's and HITRAN's values.

Some of these lines were also measured with the high optical depth spectra (HOD) of this work. For the few lines where a good measurement was possible, ~5% agreement with Toth was found for most lines. These are shown in Figure 4.49. Because Toth has actually measured these lines, as opposed to the HITRAN values which are based on calculations by Gamache, Toth's values are used in the data analysis.

4.6.3.2.2 Remedios' measurements – low J $H_2^{16}O$ lines. For the strong lines of $H_2^{16}O$ at the band center, Remedios' values are used. This is due primarily to the fact that his measurements agree very well with ours. His corresponding air-broadened widths are currently on the HITRAN database. These measurements were performed with a high resolution BOMEM FTS and were the basis of his Ph.D. thesis research.

4.6.3.2.3 Our LOD measurements – low J $H_2^{16}O$ lines. Measurements were also performed for the strong low J lines with the low optical depth (LOD) spectra (i.e. file number 179) of this work. These are the + symbols in Figure 4.48. Measurements were also performed for all of the lines measured by Remedios – good agreement is found between these measurements and those of Remedios. A comparison is shown in Figure 4.50. For the strongest (and best measured) lines, the agreement is within 2 to 3 percent. Based on this, Remedios' values are the used in the continuum analysis.

Toth's measurements of the corresponding rotational transitions for $H_2^{18}O$ are also shown in Figure 4.50. Due to larger errors, the isotopic dependence of H_2O widths is ignored in most cases. For example, the 1992 HITRAN values have no isotopic dependence (i.e. $\gamma_{H_2^{16}O-N_2} = \gamma_{H_2^{18}O-N_2}$). In this study, however, we observe what appears to be a clear isotopic dependence. Toth's values for $H_2^{18}O$ are about 10 percent lower than the $H_2^{16}O$ values we measure for the strongest lines (which also agree with Remdios). Based purely on mass differences and neglecting differences in the scattering cross sections, the $H_2^{16}O$ line widths should be roughly 3 to 4 percent larger than the $H_2^{18}O$ values. Due to the difference between Toth's values and the values of Remedios and this work, Toth's $H_2^{18}O$ values are not used for the $H_2^{16}O$ lines.

Roughly 150 widths were measured with the LOD spectra. Samples are shown in Figures 4.51 through 4.54. Residuals from calculations using the HITRAN widths, Toth's

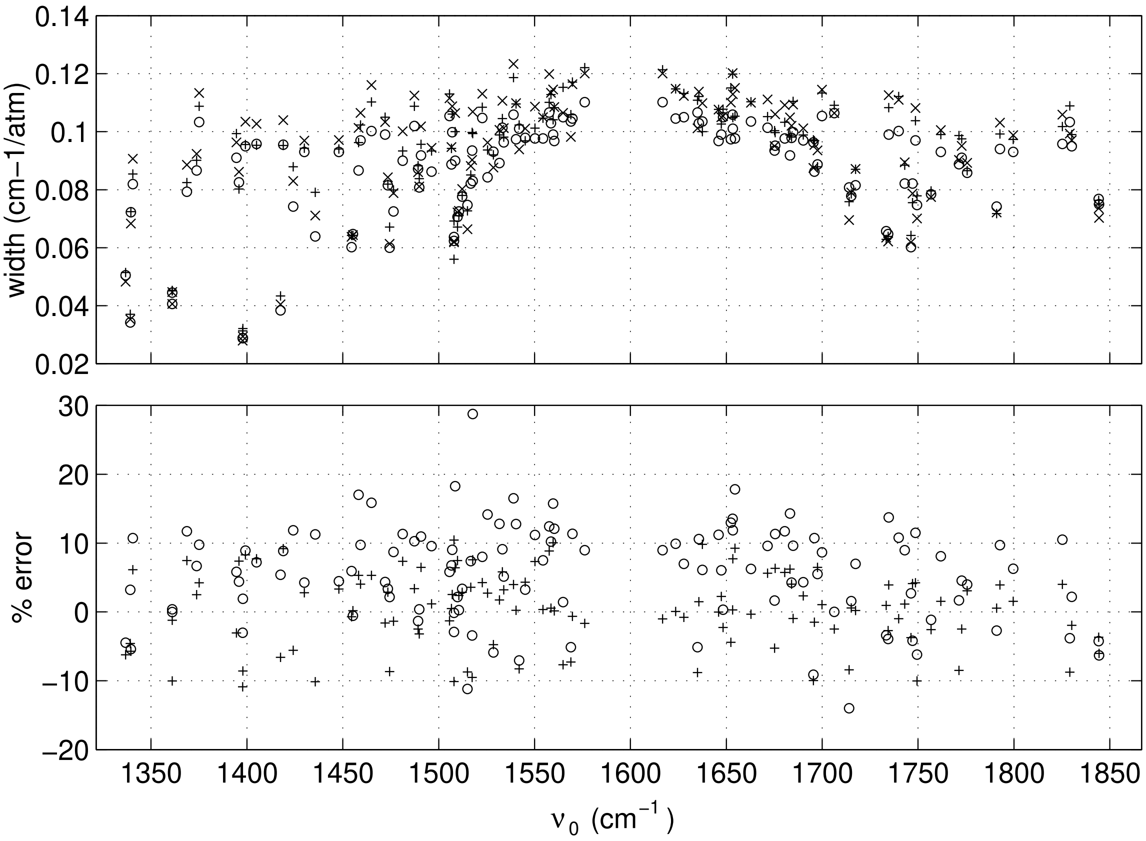

Figure 4.50: N_2 broadened widths for the strong low J $H_2^{16}O$ lines: +, Remedios; o, Toth's corresponding $H_2^{18}O$ values; x, LOD measurements. The bottom panel shows the percent errors (relative to the LOD measurements) of Toth's and Remedios' values.

widths, and the measured widths are shown in the figures. The similarity in the residuals shows the difficulty in determining accurate widths. For most cases, however, the residuals for Toth's widths are consistently worse than the others. As with the water vapor pressure determinations, the fits were complicated by the presence of fringes. A cosine function was again used to take care of these, but with little success. The analysis was also made difficult by narrow Doppler lines resulting from small amounts of pure water vapor in the FTS. Thus, for each transition, there are actually two spectral lines super-imposed, a Doppler limited line from within the FTS and a N_2-broadened

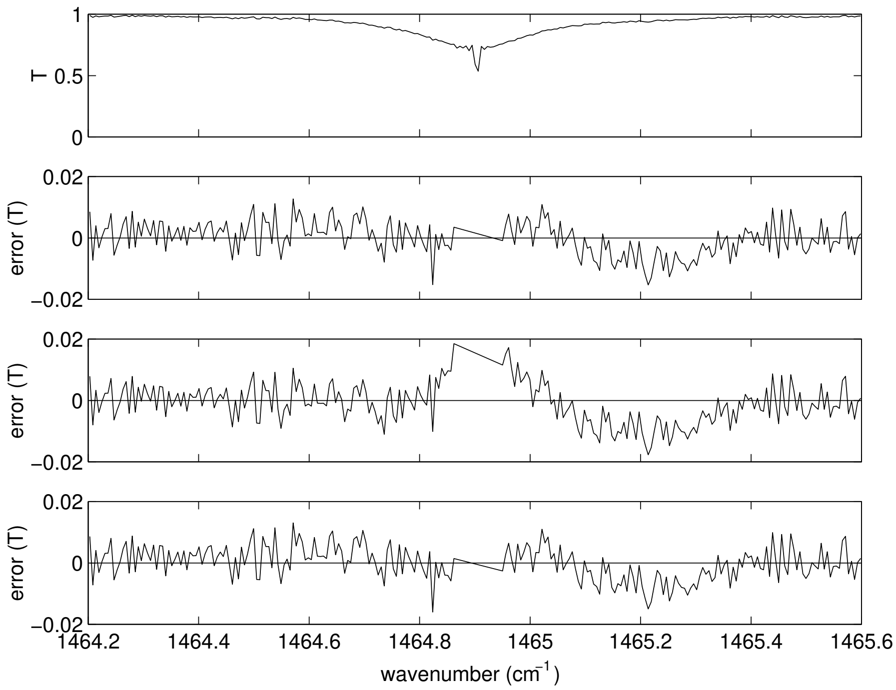

Figure 4.51: H_2O-N_2 width measurements for the 212 ← 321 line at ~1465 cm^{-1}. Raw data from file number 179 is shown in the top panel. The other panels are residuals from calculations using Remedios' width (0.1097 cm^{-1}/atm), Toth's width (0.1002 cm^{-1}/atm), and the fitted width (0.1111 cm^{-1}/atm).

Lorentz line from the absorption cell. The ringing of the high frequency Doppler lines corrupts the centers of the Lorentz lines. To account for this, the regions of the spectra near line centers are simply not included in the fits – enough of the spectra is excluded to be sure that the ringing does not effect the results. Results of this analysis were also tested by extracting the noise, fringes, and Doppler lines from the raw data and super-imposing them on calculated lines of known line widths and strengths. Fits were then performed in the usual manner. For all lines tested, the fitted widths were within 1% of the known widths.

4.6.3.2.4 Gamache's QFT calculations – intermediate J. For lines of intermediate strength (i.e. $5 \leq J \leq 8$), quantum Fourier transform (QFT) calculations by Gamache and

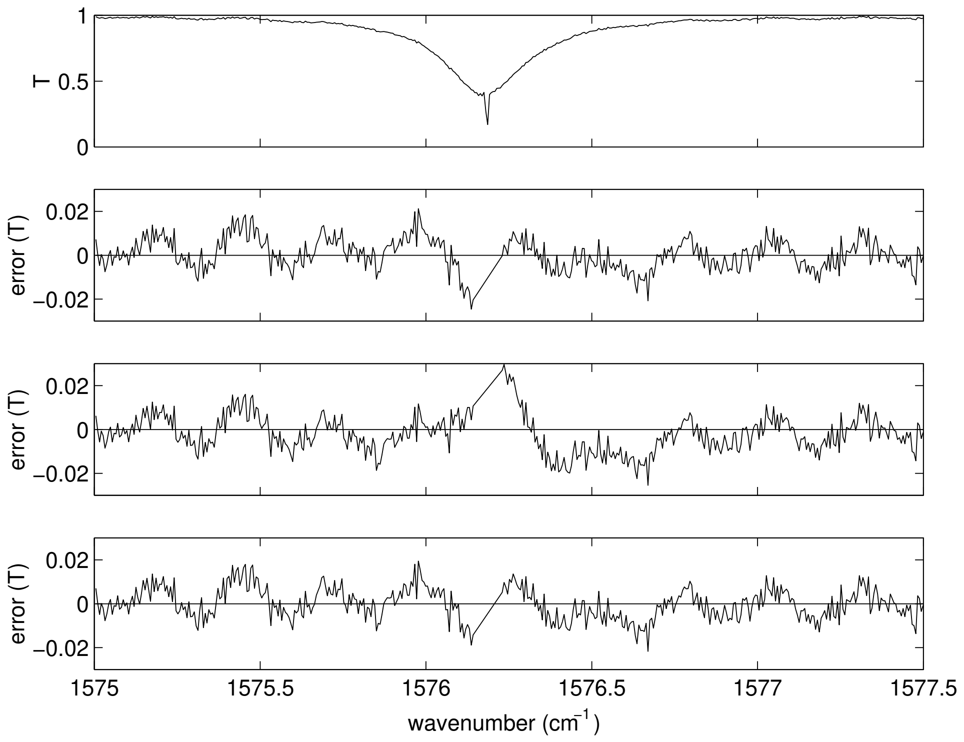

Figure 4.52: H_2O-N_2 width measurements for the 101 ← 110 line at ~1576 cm^{-1}. Raw data from file number 179 is shown in the top panel. The other panels are residuals from calculations using Remedios' width (0.1226 cm^{-1}/atm), Toth's width (0.1102 cm^{-1}/atm), and the fitted width (0.1201 cm^{-1}/atm).

Davies [8] are used. These were described briefly in Section 2.2. The corresponding air-broadening values are currently on HITRAN. Since the original calculations were performed for nitrogen and converted to broadening by air by multiplying by 0.9, the nitrogen broadened values are obtained by dividing the HITRAN values by 0.9.

4.6.3.2.5 HOD measurements – intermediate *J*. Many of the intermediate J $H_2^{16}O$ lines were also measured in this work using the HOD spectra used in the water vapor partial pressure determinations. These are shown in Figure 4.55. As for the H_2O pressure determinations, width fits were performed using individuals spectra and also using several spectra of various P_{N_2} simultaneously. The results shown in Figure 4.55

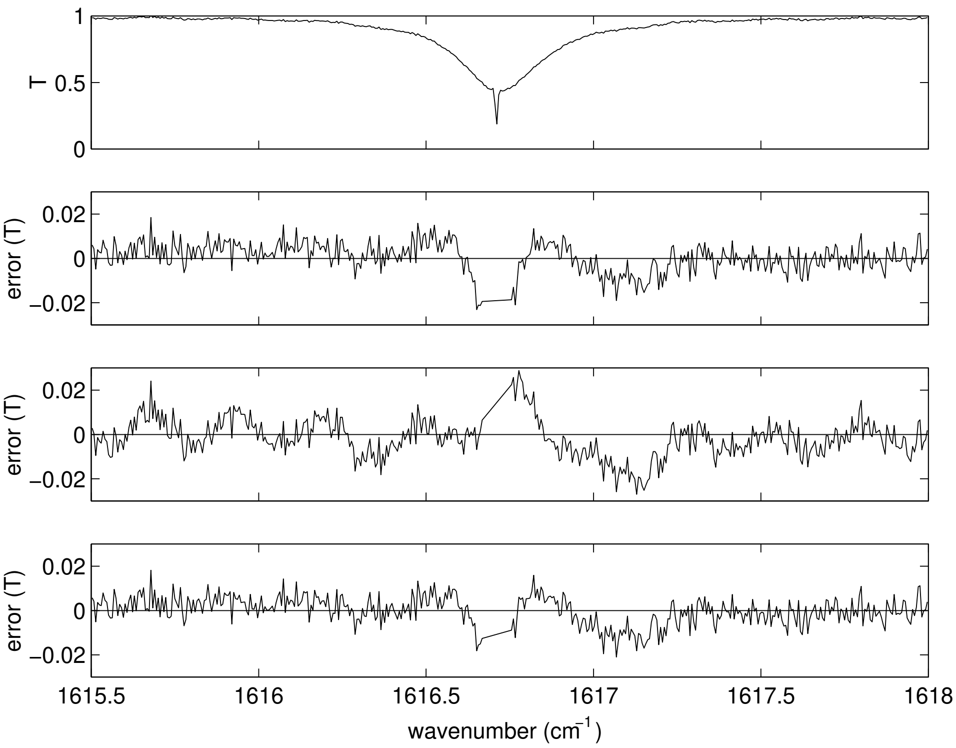

Figure 4.53: H_2O-N_2 width measurements for the 110 ← 101 line at ~1616 cm^{-1}. Raw data from file number 179 is shown in the top panel. The other panels are residuals from calculations using Remedios' width (0.1234 cm^{-1}/atm), Toth's width (0.1102 cm^{-1}/atm), and the fitted width (0.1196 cm^{-1}/atm).

are the mean values from all of the HOD spectra broadened with 500 torr or more of N_2. No general trends are observed for these lines. However, it appears that there is better agreement with Toth's values than with Gamache's calculations. This is not surprising since Gamache's calculations are not expected to be accurate at high J [8, 9].

4.6.3.2.6 Other lines. For all remaining lines, which are much weaker, the 1992 HITRAN air-broadened values are used, divided by a factor or 0.9 to convert them to nitrogen broadening.

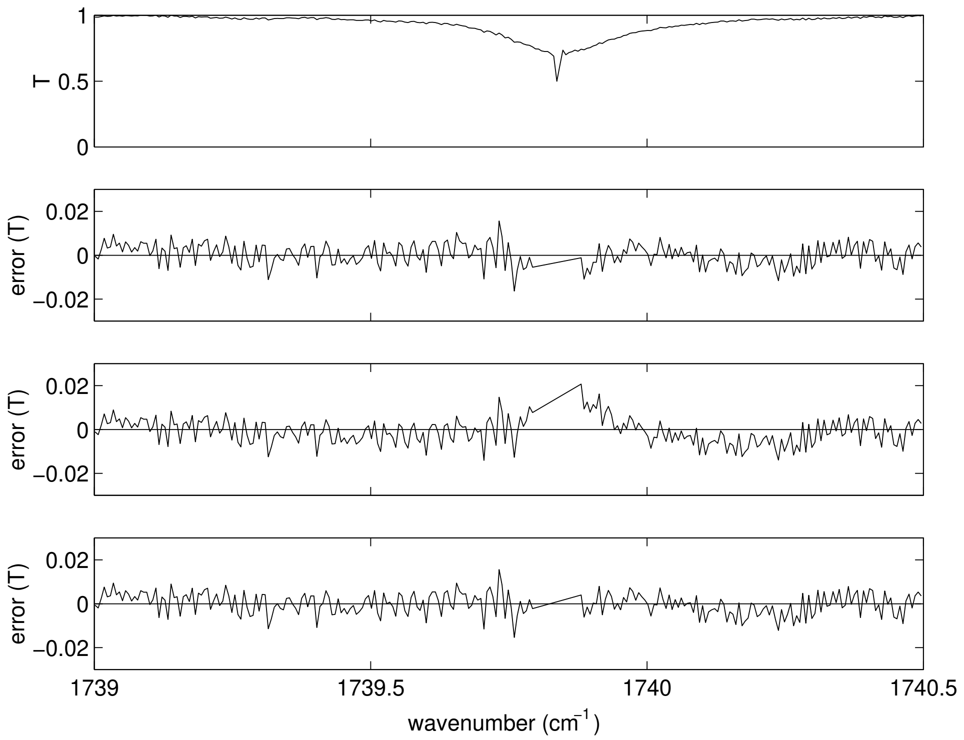

Figure 4.54: H_2O-N_2 width measurements for the 321 ← 212 line at ~1740 cm^{-1}. Raw data from file number 179 is shown in the top panel. The other panels are residuals from calculations using Remedios' width (0.1121 cm^{-1}/atm), Toth's width (0.1002 cm^{-1}/atm), and the fitted width (0.1092 cm^{-1}/atm).

4.6.3.2.7 Width Sets. Due to the uncertainty in the line widths, the continuum is analyzed with three different sets of widths. The first set, and what we feel is the most accurate set of widths, has been described above. This set of widths includes: strong low J $H_2^{16}O$ lines measured by Remedios, Gamache's QFT calculations for the intermediate strength lines, Toth's values for $H_2^{18}O$ and $H_2^{17}O$, and the HITRAN air-broadened values, divided by 0.9, for all remaining lines. The second set of widths is composed solely of Toth's measured values for the $H_2^{18}O$ and $H_2^{17}O$ measurements substituted in for all other lines, matching lines with identical rotational quantum numbers. The third set includes our LOD and HOD measurements, Toth's values for the $H_2^{18}O$ and

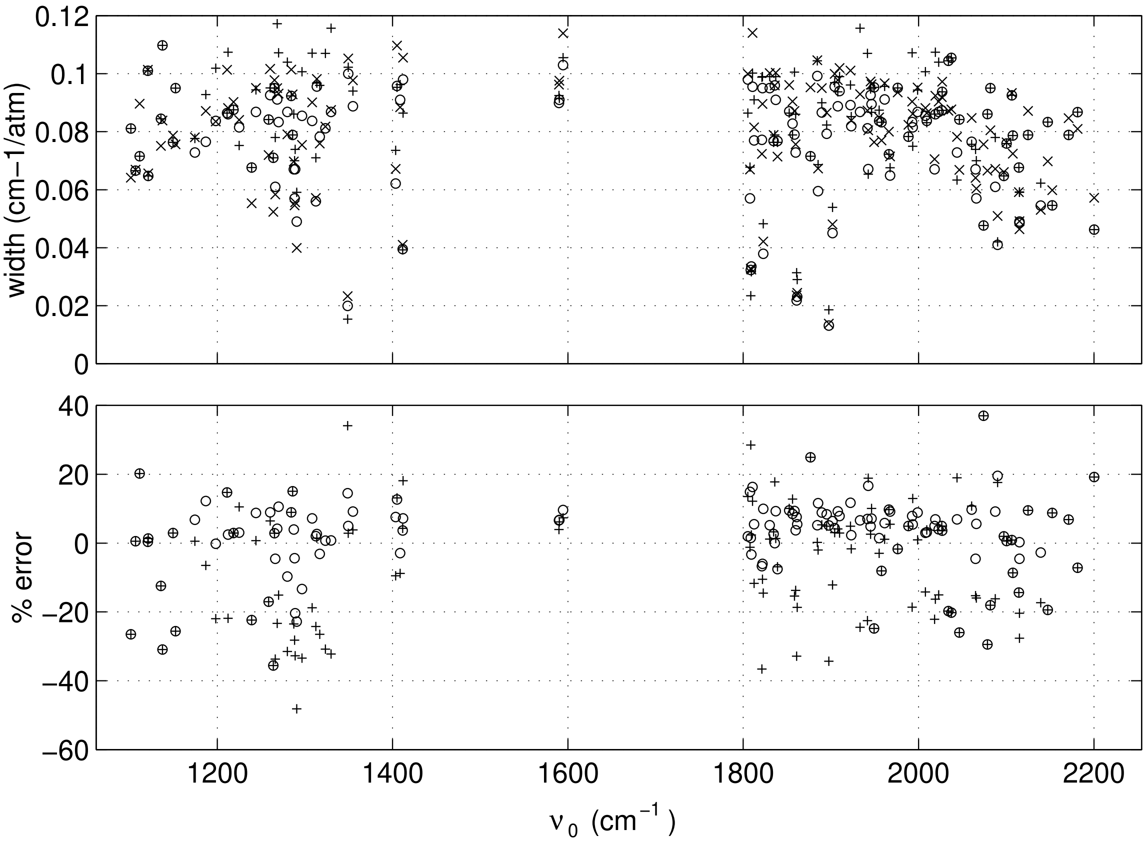

Figure 4.55: N_2 broadened widths for intermediate J $H_2^{16}O$ lines measured with the HOD spectra: +, HITRAN; o, Toth's corresponding $H_2^{18}O$ values; x, HOD measurements. The bottom panel shows the percent errors (relative to the HOD measurements) of Toth's and HITRAN's values.

$H_2^{17}O$ lines, and all other lines taken from HITRAN and divided by 0.9. These are referred to as width sets 1, 2, and 3 hereafter.

4.6.3.3 Air-broadened Line Widths

Although no air-broadened transmission spectra were collected in this work, the continuum results are applied to atmospheric data in Section 4.9, which requires accurate air-broadened widths. Air broadened widths are taken from measurements by Toth and from the HITRAN database.

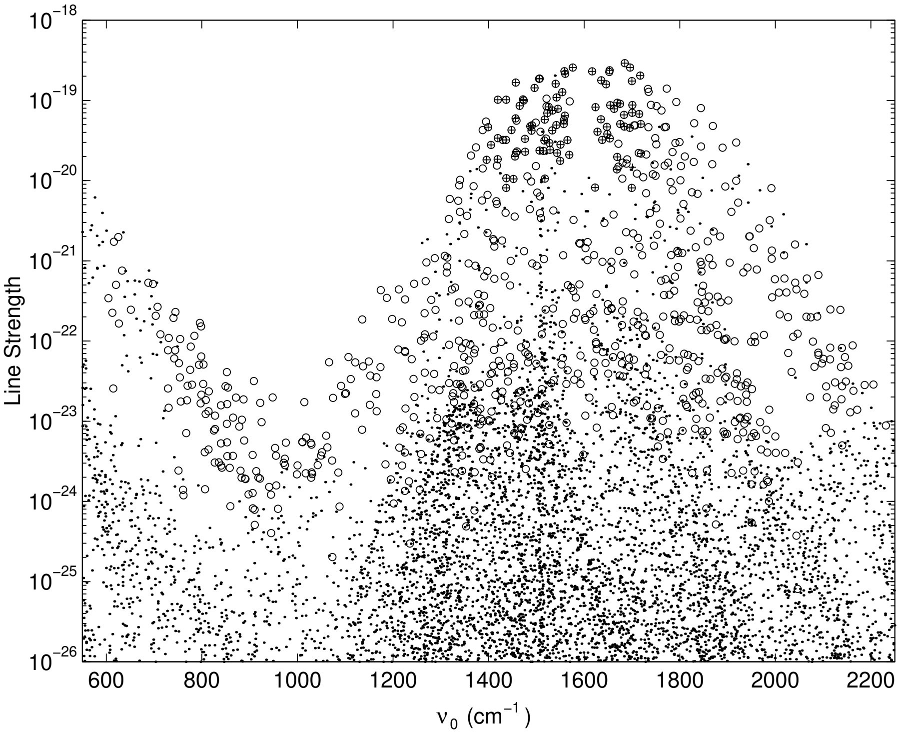

Figure 4.56: Sources of air-broadened widths: o, measured by Toth; +, measured by Remedios; ·, other HITRAN values.

HITRAN air widths are composed primarily of air-broadened measurements by J. J. Remedios for the stronger low J lines and Gamache's QFT calculations for nitrogen broadening converted to air by multiplication by 0.9 for most other significant lines. The lines measured by Remedios are the same ones he measured for nitrogen broadening.

Unlike nitrogen broadening, Toth was able to measure nearly every significant air-broadened width between 600 and 2200 cm^{-1}. These are shown in Figure 4.56. As with nitrogen broadening, no significant differences between the R and Q^R transitions and the P and Q^P transitions, nor any isotopic or vibrational dependences were observed. All values for similar rotational transitions were combined in the averaging process and smoothed values were obtained from plots of widths versus J for families

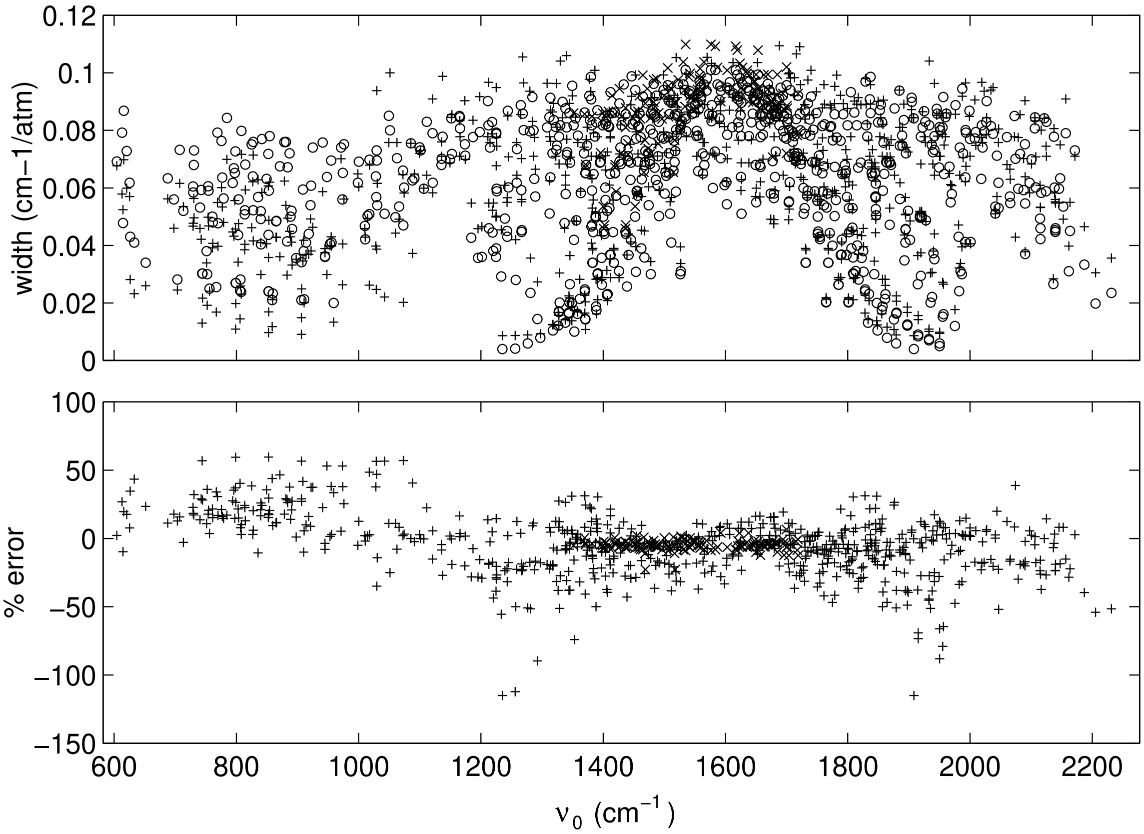

Figure 4.57: Air-broadened widths are shown in the top panel: o, measured by Toth; x, measured by Remedios; +, other HITRAN values. The bottom panel shows the percent difference between Toth's values and those of Remedios (x) and other HITRAN values (+).

of transitions.

Toth's and HITRAN's values are shown in Figure 4.57. Figure 4.58 contains only the strongest lines whos widths were measured by both Toth and Remedios. For these lines, Remedios' values are consistently ~10 percent greater than those of Toth.

4.6.3.4 O_2-broadened Line Widths

There are no reliable sources of measured O_2 broadened widths for the ν_2 band known to this author. A study of these width could be performed with file number 183. It

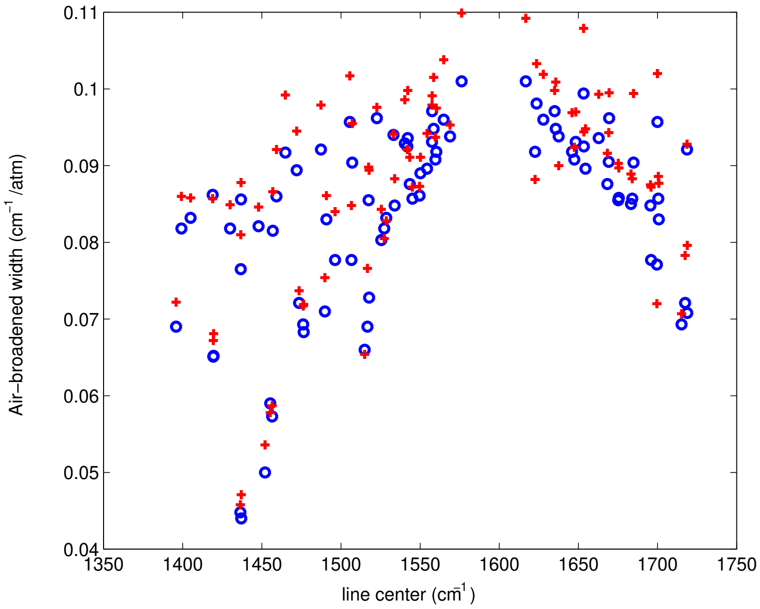

Figure 4.58: Air-broadened widths measured by Toth (o) and by Remedios (+).

is common to use oxygen broadened widths based on the ratio to nitrogen broadened widths for some well studied lines. For example, $\gamma_{O_2} = 0.75\gamma_{N_2}$ [105], $\gamma_{O_2} = 0.597\gamma_{N_2}$, $\gamma_{O_2} = 0.609\gamma_{N_2}$, and $\gamma_{O_2} = 0.627\gamma_{N_2}$ [9].

4.7 Microwindow Continuum Analysis

This section describes the analysis of the continuum coefficients in the microwindows. That is, in regions at least $\sim$1 cm^{-1} from any strong absorption lines. In regions of low absorption, such as in Figure 4.59, the lineshape is safely approximated as Lorentzian and the only errors are due to line parameters. In regions of high optical depth (Figure 4.60) larger errors, which are due to an inaccurate far-wing lineshape, are observed. By sampling the spectra in the microwindows, denoted in Figure 4.60 with asterisks, the far-wing effects of all lines leading to the observed deviations from Lorentz behavior can be characterized.

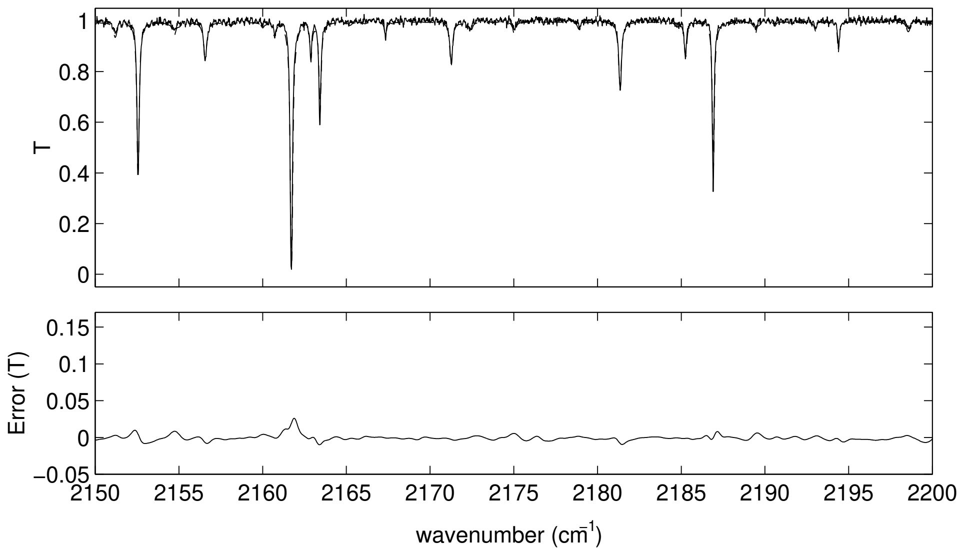

Figure 4.59: Sample spectra for the 2150–2200 cm^{-1} region. The top panel shows the raw data (solid curve) and a calculation (dashed curve) using the CKDv0 continuum model. The bottom panel shows the resulting error. Experimental parameters are: 14.5 torr H_2O, 800 torr N_2, 84.05 meter path length, 296K.

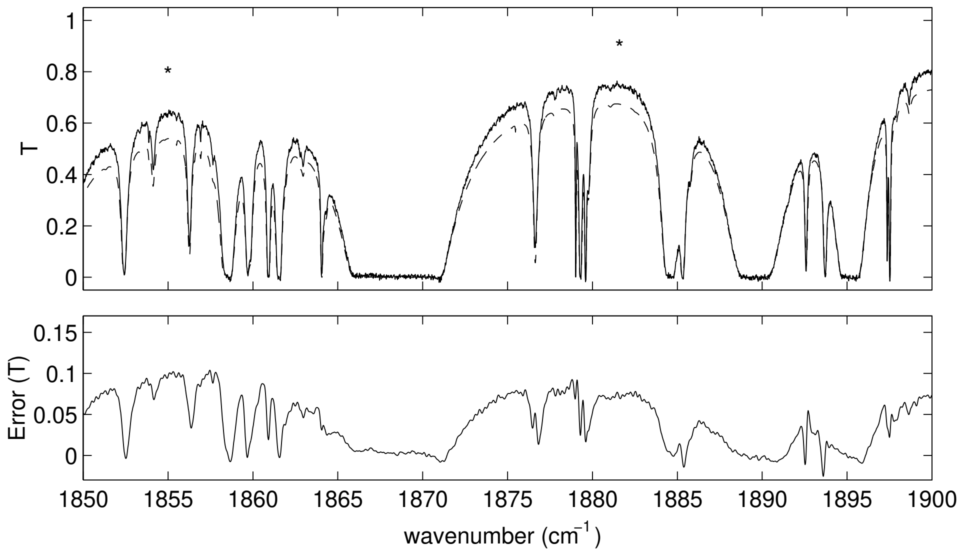

Figure 4.60: Sample spectra for the 1850–1900 cm^{-1} region. The top panel shows the raw data (solid curve) and a calculation (dashed curve) using the CKDv0 continuum model. The bottom panel shows the resulting error. Experimental parameters are: 14.5 torr H_2O, 800 torr N_2, 84.05 meter path length, 296K.

4.7.1 Analysis Methods

For a single spectrum, the continuum can be determined by simply subtracting the local absorption coefficient (Equation 4.1) from the total experimental absorption coefficient. This is referred to as the "simple subtraction method" from now on. Furthermore, in the wings of lines, the pressure dependencies of Equation 4.2 can be adopted and the continuum coefficients C_s^0 and C_f^0 can be determined. Alternatively, the continuum can be determined in the microwindows using several spectra by utilizing the pressure dependencies of Equation 4.2. This approach, which is referred to as the "slope method", decreases sensitivity to uncertainties in the 100% transmission baselines, since the fitted continuum coefficients only depend on the slope of k_{con} with pressure and not on the absolute value of the experimental continuum. For pure H_2O spectra, C_s^0 is proportional to the slope of the observed continuum absorption coefficient versus $P_{H_2O}^2$.

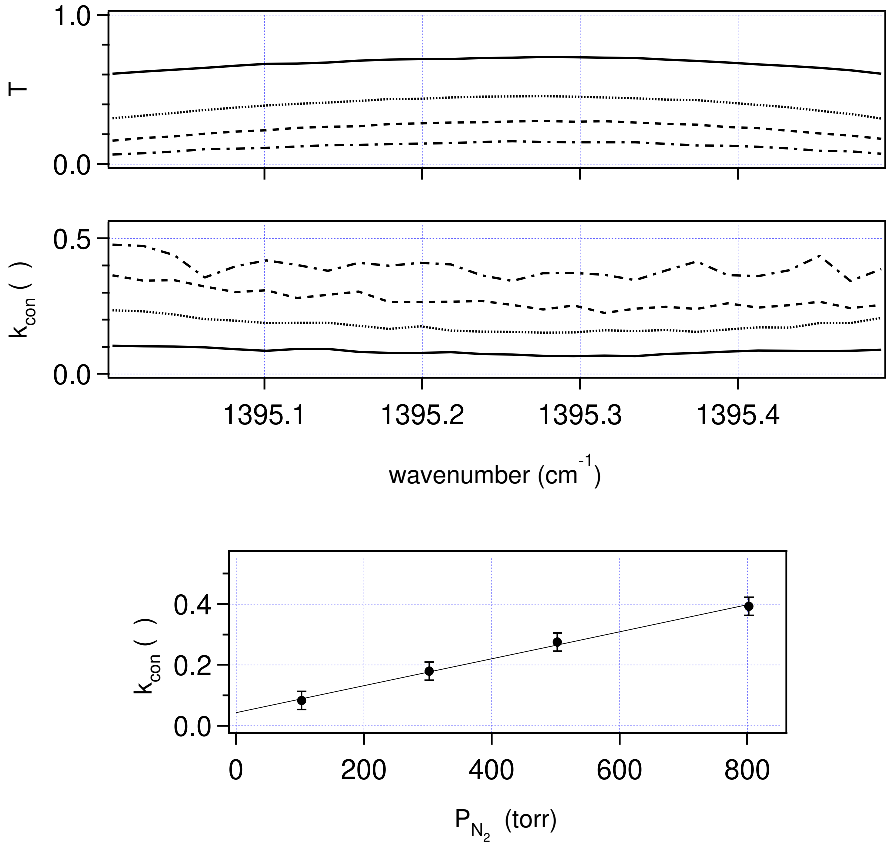

Figure 4.61: A sample slope method continuum retrieval from a set of nitrogen broadened spectra for a microwindow at ~1395 cm^{-1}. Experimental parameters are: 84 meter path length, 296K, 8.5 torr H_2O, 100 (solid curves), 300 (dotted curves), 500 (dashed curves), and 800 (dash-dot curves) torr N_2. C_f^0 is proportional to the slope of the straight line fitted to k_{con} versus P_{N_2}.

Similarly, for N_2-broadened spectra with the same H_2O partial pressure, C_f^0 is proportional to the slope of the observed continuum absorption coefficient versus P_{N_2} and C_s^0 is proportional to the y-intercept. The reported continuum coefficients come from least-squares fits for these slopes. The slope method is valid as long as the observation wavenumbers are not too close to any strong absorption lines such that the far-wing

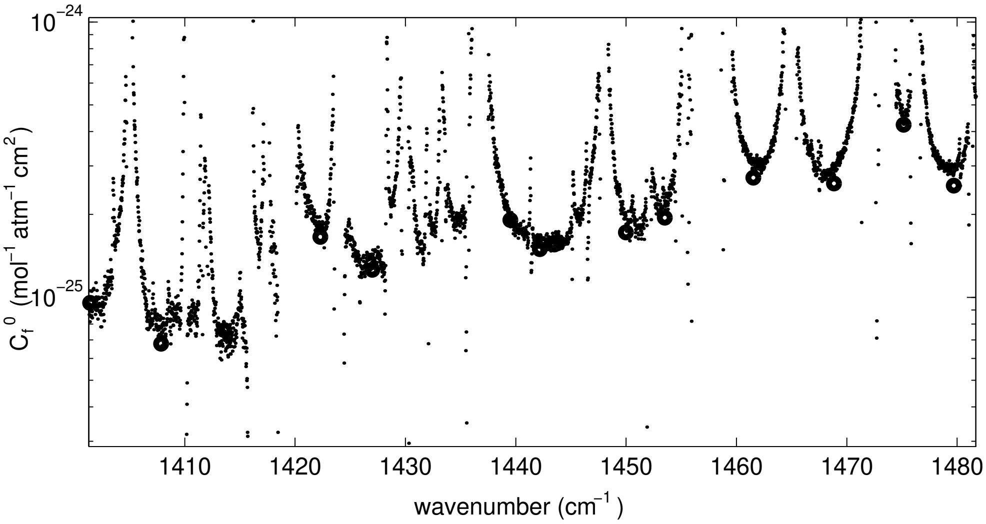

Figure 4.62: C_f^0 measurements using the simple subtraction method for file number 154 (dots) and the slope method (circles) for file numbers 151 through 154: 12 meter path length, 296K, 10 torr H_2O plus 100, 300, 500, and 800 torr N_2.

pressure dependencies no longer hold – the simple subtraction and slope methods results can always be compared to be sure that this is the case. A sample slope method measurement of C_f^0 from a set of nitrogen broadened spectra is shown in Figure 4.61. Sample continuum coefficients determined with both the simple subtraction and slope methods are shown in Figure 4.62.

4.7.2 Error Analysis

For a single spectrum, in any given window region, the uncertainty in the continuum absorption coefficient is mainly due to uncertainties in: (1) the H_2O pressure, (2) the

100% transmission baseline and, (3) the line parameters used to subtract off the local absorption contribution. Considerations 1 and 3 have been addressed in Sections 4.5 and 4.6. Baseline errors were characterized in Section 4.4, but are presented in more detail below.

4.7.2.1 Baseline Errors

The sensitivity of the derived continuum to uncertainties in the 100% transmission baseline was determined as follows. Instead of deriving the continuum from the slope method, it is calculated directly using the simple subtraction method. For the N_2 continuum this does require that you first measure the self continuum contribution so it can be subtracted from k_{con}. This method is prone to large errors since it is very sensitive to uncertainties in the 100% transmission baseline, especially in regions of low absorption. By comparing results obtained with this error-prone method to those using the slope method, in spectral regions where there is relatively low absorption, but enough to retrieve a reasonably accurate continuum, the uncertainty in the measured transmission baselines can be quantified. This is illustrated in Figure 4.63. The differences in these two measurements indicate that we have maximum baseline errors of roughly ~0.005 in transmission, which is very similar to the values determined in Section 4.4. This baseline error is used to determine errors in the continuum derived using the slope method. The impact of this error varies strongly with spectral region. In regions of strong absorption, the resulting errors in the retrieved continuum coefficients due to baseline errors are negligible compared to the uncertainty in the H_2O partial pressure. However, in regions of little absorption, the baseline error is potentially the main source of error in the coefficients. For example, at ~1350 cm^{-1}, a 0.005 baseline error in transmission translates into an error of ~ 20–30 % in C_f^0 for our optical depths.

A baseline error of 0.005 in transmission is propagated into the uncertainty of the

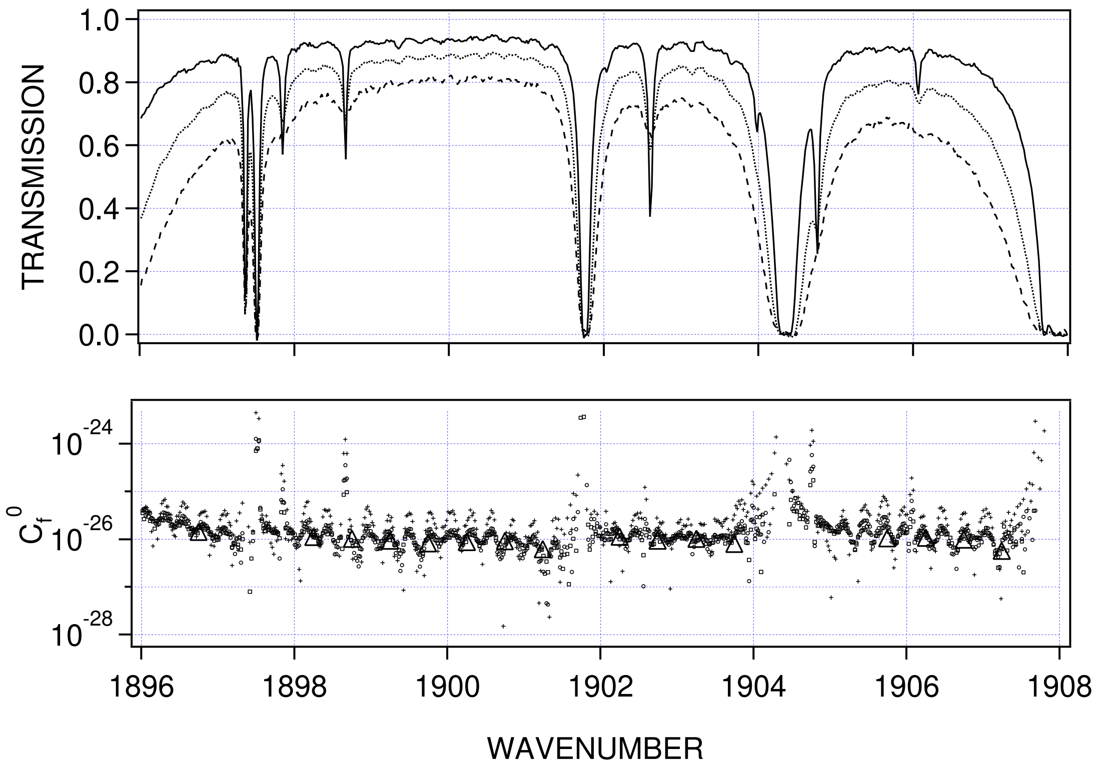

Figure 4.63: Baseline accuracy determined by comparing simple subtraction and slope methods. The top panel shows transmission spectra for 14.5 torr H_2O, 84 meter path length, 105 (solid curve), 400 (dotted curve), and 800 (dashed curve) torr N_2. The bottom panel shows the simple subtraction C_f^0's determined for each spectrum and the slope method results (triangles).

continuum coefficients reported here. This appears to be a good estimate for the low wavenumber band wing where the spectra are dominated by noise. However, in the high wavenumber wing, the signal-to-noise ratio is much greater and it appears that we may have overestimated the baseline error in this region, where we report large uncertainties despite the excellent agreement with Burch's measurements (see Section 4.7.4).

4.7.2.2 Synthetic Sensitivity Studies

Continuum retrievals from synthetic transmission spectra were performed to test the sensitivity of the retrieved C_f^0s to several factors. Synthetic spectra were computed using Clough's version 0 continuum model and a Lorentzian local lineshape. In addition, the spectra were subject to one or more of the following factors: (1) increased line widths (+10,+20%), (2) random noise (5,10%), and (3) 100% transmission baseline errors ($\pm$2% T). Retrievals were then performed in the regular fashion using unmodified line parameters. Because a Lorentzian local lineshape is used to compute the spectra, any errors in the retrieved continua are not due to errors in the lineshape, but only to the factors being tested. Retrieval errors for no modifications, line width errors, random noise, and baseline errors are shown in Figure 4.64.

Some conclusions from these studies are: (1) large random noise (10%) can cause significant errors in the retrieved coefficients – however, averaging over many spectra and over a ~0.5 cm^{-1} region can reduce these errors. Actual noise in the spectra is much smaller, on the order of 1–2%. (2) baseline errors don't cause scatter, but can cause large offsets (20-30%) in the retrieved C_f^0, especially far from the band center. (3) line width errors can cause large errors in the retrieved coefficients. (4) some combination of random noise and increased line widths *could* account for the observed scatter in C_f^0.

4.7.3 Total Error Budget

Simple propagation of errors is used to combine the sources of error in determining one standard deviation uncertainties in the reported continuum coefficients. These errors were calculated separately for each continuum coefficient reported. For example, for a series of pure spectra with various H_2O partial pressures, the continuum absorption coefficient is plotted versus $P_{H_2O}^2$, with each point having its own uncertainty dependent on (1) the baseline errors for the spectrum used to determine k_{con} for that point, (2) the uncertainty in the local absorption coefficient subtracted from that spectrum, and

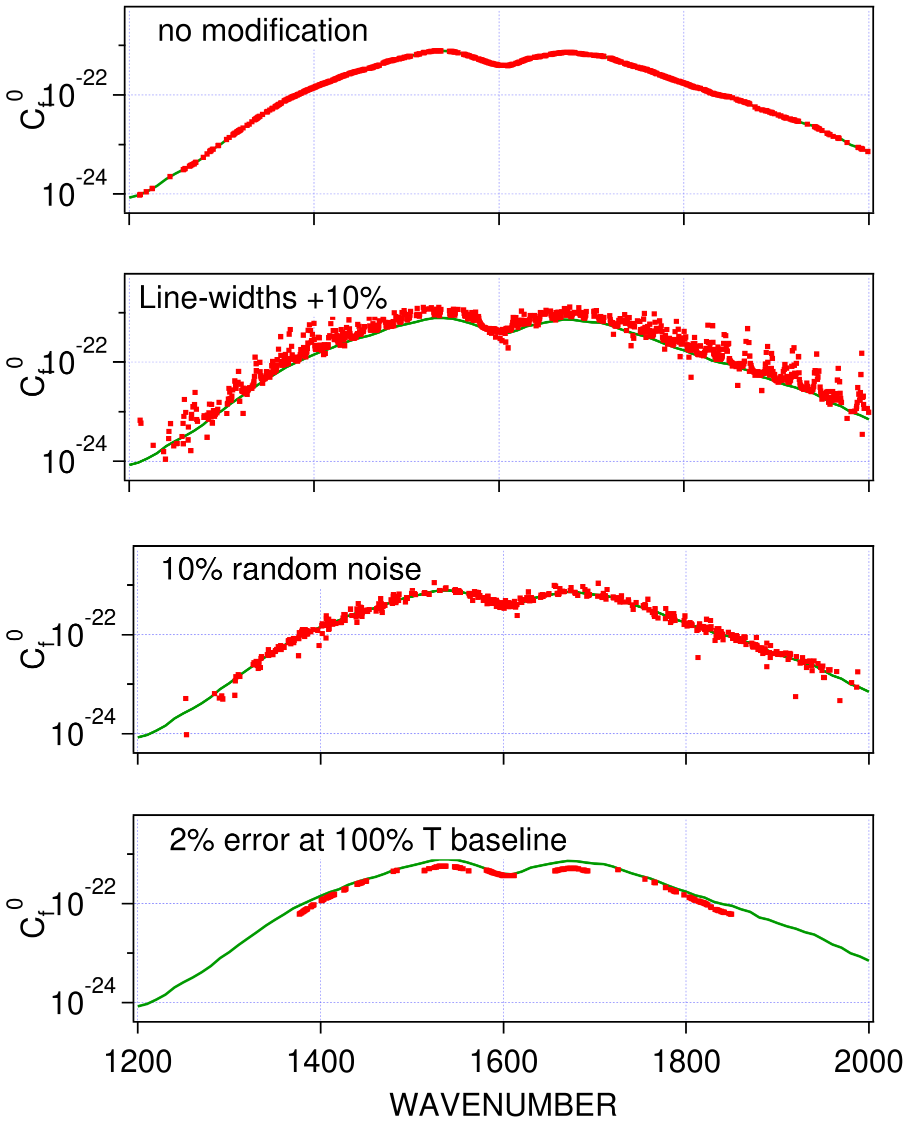

Figure 4.64: Sensitivity studies of C_f^0. The solid curve is the continuum model used in the calculations (CKDv0) and the dots are the retrieved coefficients. The modifications to the synthetic spectra are noted for each case.

(3) the uncertainty in P_{H_2O}. A weighted linear fit of this curve gives C_s^0 and its statistical uncertainty, which is combined with the uncertainty in C_s^0 from propagation of errors. This results in one retrieved value of the continuum coefficient and its uncertainty. We

then combine values for the same wavenumber region obtained from spectra taken at different pathlengths using a weighted mean, where the final error is a combination of the standard deviation of the mean and the propagation of errors uncertainty. The pure spectra were grouped and analyzed individually for pathlengths of 12, 44 and 84 meters. A final value for C_s^0 was derived from a weighted sum of these three measurements. For the N_2-broadened spectra, the spectra were grouped according to different pathlengths and H_2O pressures, resulting in 12 groups which were then combined into one final value of C_f^0 and its associated uncertainty.

The resulting errors in the reported continuum coefficients are smallest at the band center where baseline and line width errors are negligible. They increase at the peaks of the P and R branches, where the uncertainties in many strong absorption lines combine. They also increase in the band wings where lower optical depths make errors in the 100% baselines dominant. For self-broadening, the error in C_s^0 is roughly 7% at the band center and increases to ~50% at 1350 and 1950 cm^{-1}. For N_2-broadening, the error in C_f^0 is roughly 5% at the band center and increases to ~30% at 1325 and 1975 cm^{-1}.

4.7.4 Discussion of Results

The continuum coefficients determined using width set 1 (see Section 4.6) are presented in the following two sections and compared to various measurements and models for wavenumber regions within wide microwindows. Results for narrower microwindows are then presented and finally, the coefficients determined from width sets 1, 2, and 3 are compared.

4.7.4.1 Self-Broadened Continuum

Self-broadened continuum results are plotted in Figure 4.65 in semilog (top panel) and linear (bottom panel) format along with the measurements of Burch [79] and Clough's CKDv0 and CKDv2.1 models [84]. The theoretical calculations of Ma and Tipping [21] are also shown, although it should be emphasized that their published results are not directly applicable to the in-band continuum for several reasons. Continuum measurements are also included for a number of additional microwindows that Burch did not report. Our uncertainties are quite small between 1450 and 1900 cm^{-1}, on the order of 10%. In the edges of the band, these accuracies increase due to increased noise, especially at the lower wavenumbers, and due to lack of optical depth. Calculations using the impact approximation (Van Vleck-Huber) are also shown.

The most obvious difference between our results and those of Burch is at 1584.0 cm^{-1} where Burch's continuum is almost half of our result. Otherwise, we find general agreement with Burch. Indeed many of his measurements fall within the error bars of our results. In the high wavenumber wing, there is good agreement with Burch's measurements at 322K and with Clough's models. A comparison of our 296K data to Burch's 322K measurements shows no observable temperature dependence of C_s^0 in this region at the level of accuracy of the data. A blowup of the high wavenumber continuum in Figure 4.66 shows good agreement of our results with Clough's CKD models and with Burch's points.

These results suggest that the dip at the band center is not as drastic as seen by Burch. Burch's only point that follows this dip in the continuum is the one at 1584 cm^{-1}. Our measurement for this point is almost twice as large, resulting in a much less pronounced dip at band center. We cannot find any reason why our reported uncertainty in this region should be any larger and can only conclude that the difference is due to an error in Burch's measurement. Note that we also see rather large differences between our results and Burch's at the band center for the N_2-broadened continuum as well. Also note that in Figure 4.11, the dip in the total continuum is caused by the near-wing lineshape behavior (within 25 cm^{-1} of the line center), at least according to Clough's definition of the continuum.

As mentioned earlier, Ma and Tipping's theoretical calculations are not directly applicable to the in-band continuum. Their theory is by nature a far-wing theory and is

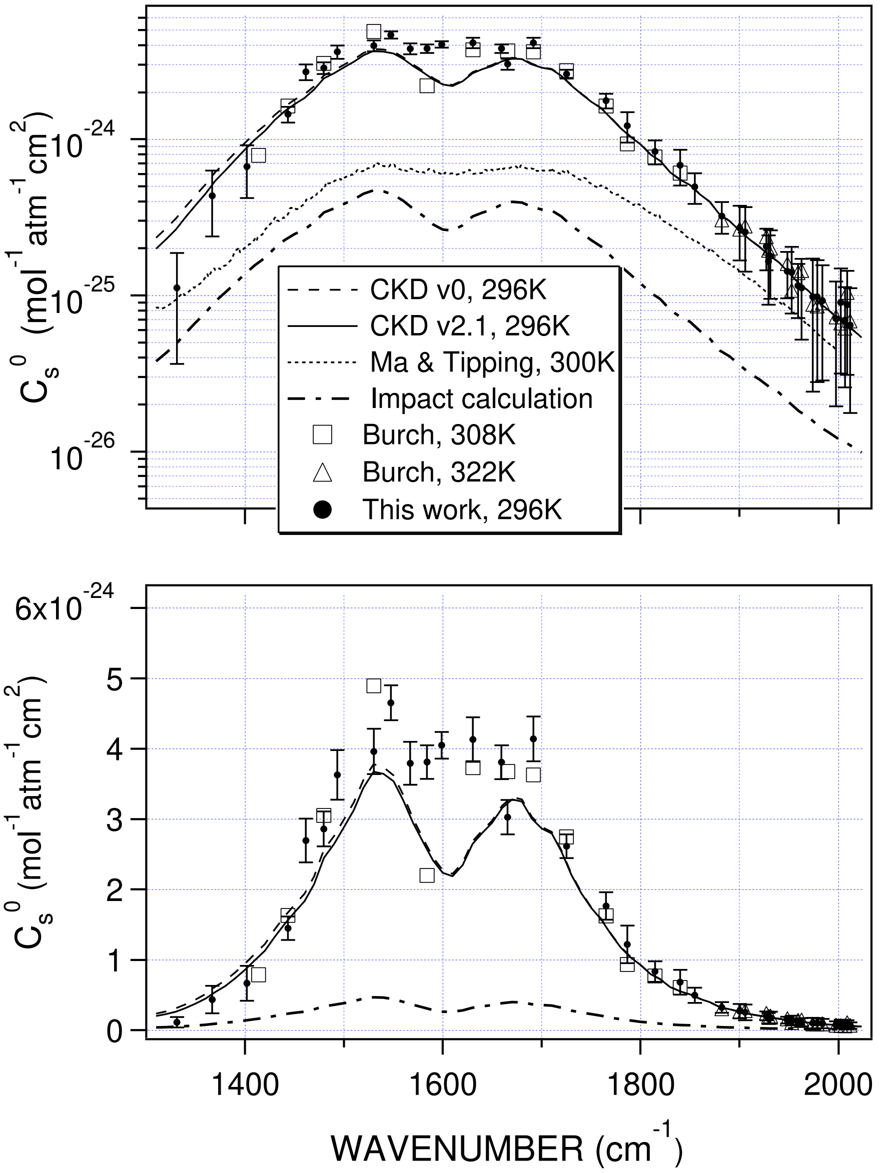

Figure 4.65: Self-broadened continuum coefficients from this work, Burch, CKD models, Ma and Tipping, and from impact theory.

least accurate close to line centers. Furthermore, they used a 25 cm^{-1} cutoff, so that contributions from lines within ± 25 cm^{-1} of line center were not adequately represented in these calculations. We have added the "basement" terms to their calculations

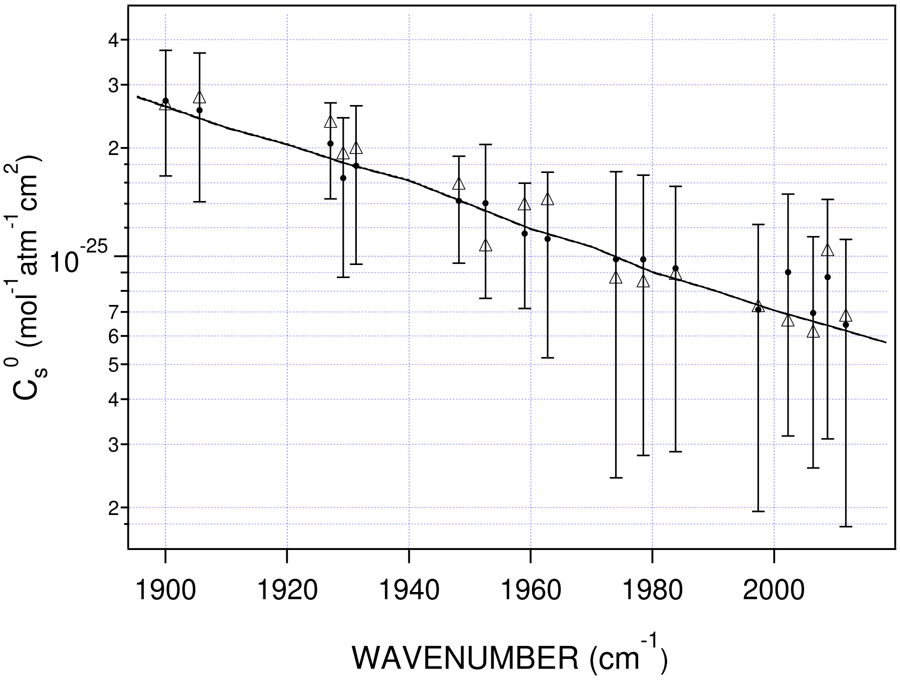

Figure 4.66: An expanded portion of Figure 4.65.

for consistency. In a very rough sense, Figure 4.11 shows that lines within 25 cm^{-1} contribute on the order of half the observed continuum, so it is not surprising that Ma and Tipping's results are so much smaller than our measurements. Their calculations do agree better with experiment in the wings of the band where the continuum is due almost entirely to the far-wings of lines.

4.7.4.2 N_2-broadened Continuum

N_2-broadened continuum results (determined with width set 1) are plotted in Figure 4.67 in semilog (top panel) and linear (bottom panel) format along with the measurements of Burch [79] and Clough's CKDv0 and CKDv2.1 models [84]. The theoretical calculations of Ma and Tipping are again included, keeping in mind that their calculations are really only applicable to the wings of the band, as previously discussed.

Impact calculations (Van Vleck-Huber) are also shown. These figures include measurements of C_f^0 in a few additional microwindows that Burch did not report. Our best results are located between 1450 and 1900 cm^{-1}, where the uncertainties are on the order of 10%. Just as for the self-broadened data the reported uncertainties in the band wings are dominated by the estimated 0.5% uncertainty in the 100% transmission level.

As with self-broadening, the largest discrepancy between these measurements and Burch's is the point at 1584 cm^{-1}, near the center of the band, where Burch's value is about 30% smaller than ours. From 1500 to 1700 cm^{-1} the N_2-broadened continuum values are all lower than Burch's. In this same region our results follow Clough's CKDv0 curve much better than CKDv2.1. Above 1700 cm^{-1} both our data and Burch's jumps between Clough's two models. Our results are in rough agreement with Burch except past 1950 cm^{-1} where our error bars start to get rather large. In this region, however, we do notice good agreement with the measurements of Theriault [93]. Above 1850 cm^{-1} all of Burch's points are for 353K, while our data is at 296K, so some disagreement is not unexpected. The overall agreement of our data with Burch above 1700 cm^{-1} proves that the continuum is indeed bumpy and that a smooth continuum like Clough's present models cannot adequately reproduce the data.

Below 1500 cm^{-1} there is rough agreement with Burch, except for the lowest wavenumber point at 1333.1 cm^{-1}, where our error bars become large. Although there are fewer microwindows on this side of the band, the measured continuum still bounces to some degree between Clough's CKDv0 and CKDv2.1. Below 1450 cm^{-1} our data seems to favor CKDv2.1 and therefore also shows general agreement with the atmospheric measurements [] which led to the changes in the CKD models in this region. This region has fewer wide microwindows, so we did not add many more points over what Burch used.

On the low wavenumber side of the band, our measurements are in general agreement with Theriault's results [93] for measurements at the exact centers of the microwindows. From ~1320 to 1360 cm^{-1}, our values for C_f^0 agree with those of Theriault

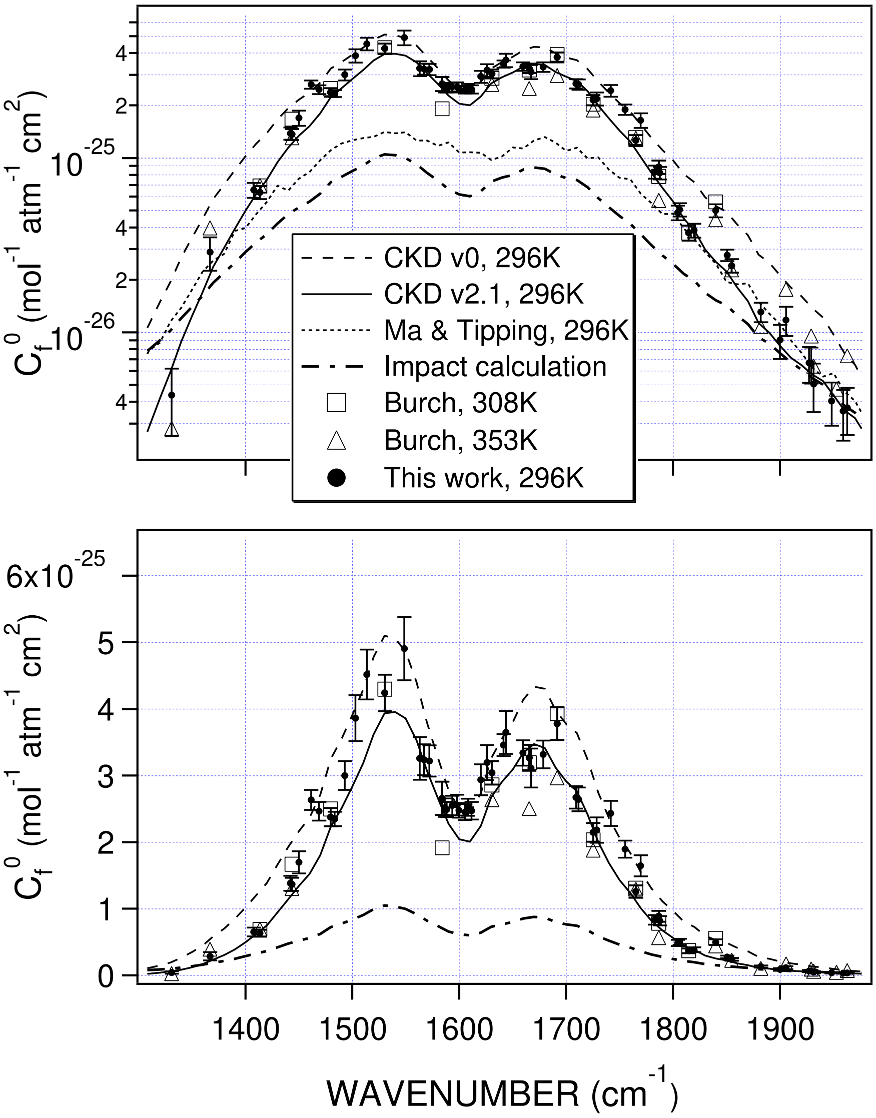

Figure 4.67: N_2-broadened continuum coefficients from this work, Burch, CKD models, Ma and Tipping, and from impact theory.

within experimental error. However, at Theriault's highest wavenumber in this region (~1381 cm^{-1}) our value is twice as large as Theriault's, with Clough's CKDv2.1 falling almost directly in-between the two measurements. On the high wavenumber side of the band, our results are in relatively good agreement with Burch's measurements and with CKDv2.1, all of which are consistently larger than Theriault's results.

4.7.5 Continuum in Narrower Microwindows

Our H_2O spectra contain a large number of microwindows that are not as wide as those used by Burch but are still relatively free of strong local absorption. In Figures 4.68 and 4.69 the measured values for C_s^0 and C_f^0 (determined with width set 1) for a number of additional microwindows are shown. These windows are loosely defined as spectral regions that contain a local transmission maximum that is at least 0.5 cm^{-1} wide, and is not too close to a very strong line. Since the ultimate goal is to reproduce the observed spectra, we eventually hope to develop a model that will work on any wavenumber grid. Examination of the continuum in these smaller microwindows using Clough's existing continuum definition is a natural first step.

The self-broadened results shown in Figure 4.68 suggests that the continuum becomes quite bumpy with wavenumber between the strong lines of the band. Most of the new points in this graph are larger than those in the original microwindows, indicating that near-wing super-Lorentz behavior by the local lines is playing an important role in the observed absorption coefficients. Note that our continuum is fairly smooth near the band center and in the band wings where there is an absence of strong lines.

The N_2-broadened continuum shown in Figure 4.69 is quite a bit bumpier than the self-continuum. Again, most of the added points have a larger continuum than those in the original larger microwindows.

4.7.6 Comparing Results from Width Sets 1, 2, and 3

The nitrogen broadened continuum coefficients determined using width set 1 (Remedios/Toth/Gamache widths), width set 2 (Toth), and width set 3 (LOD and HOD measurements/Gamache/Toth) are shown in Figure 4.70 for the narrow microwindows discussed in Section 4.7.5. The percent difference from the width set 1 results are shown

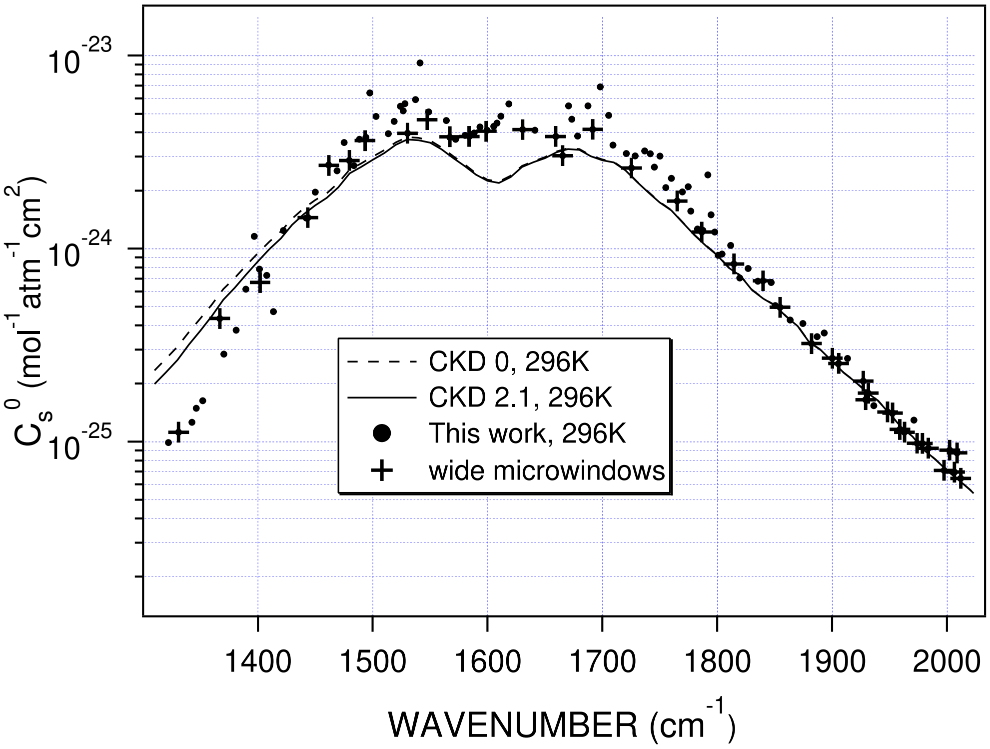

Figure 4.68: Self-broadened continuum coefficients from this work reported for a larger number of microwindows as discussed in section 4C.

in the bottom panel of the figure.

For the very wide microwindows, all three width sets yield essentially the same results due to the fact that these regions are relatively insensitive to the widths. This is especially true at the band center, where there are no strong lines between 1576 and 1616 cm^{-1}. This is a region where we have good optical depth and essentially no errors due to line parameters – this is where our results are expected to be most accurate.

In the narrower microwindows and on the edges of microwindows closer to strong lines, the effect of using different widths is apparent. Width set 2 (Toth's widths) contains widths which are almost consistently ~10 percent smaller than the other sets. This results in larger continuum coefficients for nearly every microwindow. However,

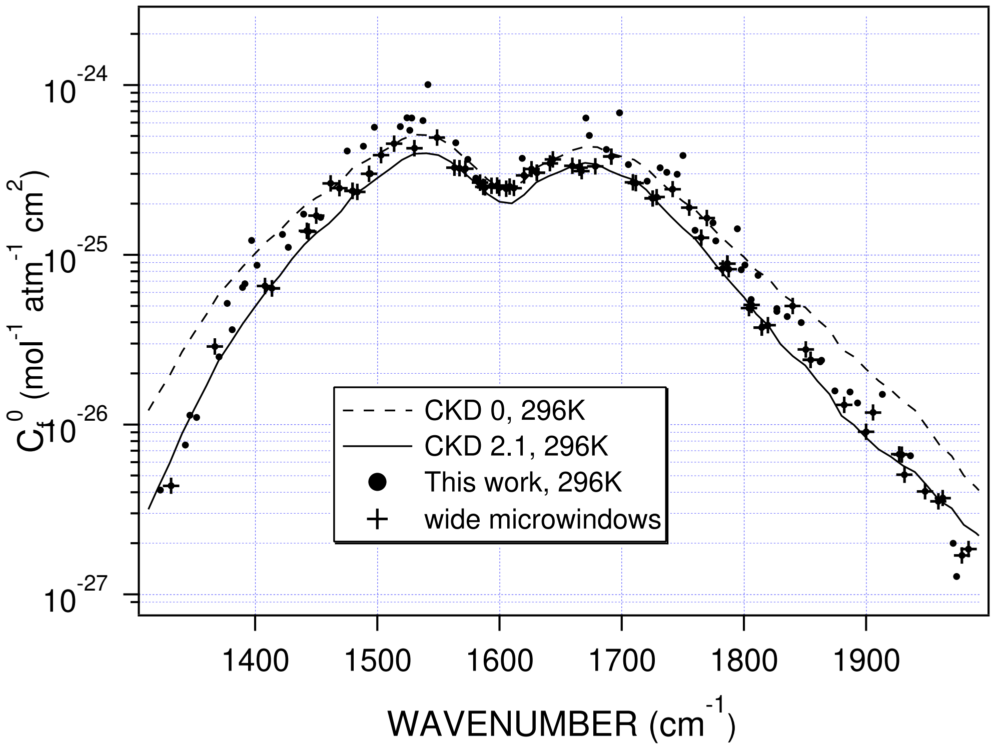

Figure 4.69: N_2-broadened continuum coefficients from this work reported for a larger number of microwindows discussed in section 4C.

the overall agreement between the results from different width sets leads to the conclusion that the bumpiness in the continuum coefficients is not due entirely to line width errors.

4.7.7 Calculations using Measured Continuum Coefficients

Sample calculations using CKDv0, CKDv2.1, and the microwindow continuum coefficients of this work are shown in Figures 4.72 through 4.74. For the calculations using the results of this work, the continuum coefficients are linearly interpolated in wavenumber between the measured microwindow points – this is illustrated in Figure 4.71. In this figure, the simple subtraction method (dots) and slope method results

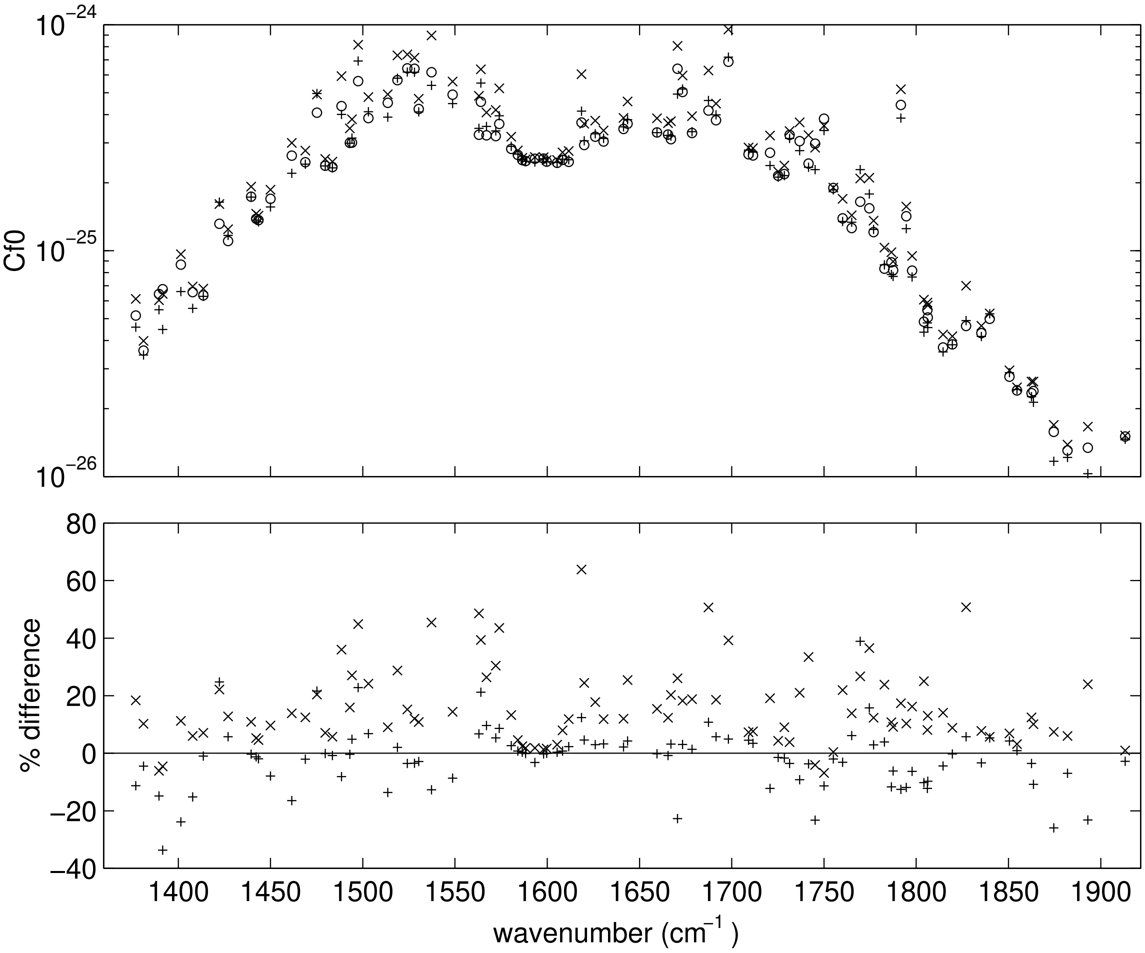

Figure 4.70: C_f^0 derived from width sets 1 (o), 2 (x) and 3 (+) are shown in the top panel. The percent difference from the width set 1 results are shown in the bottom panel.

(circles) are shown, as well as the linear interpolation between the microwindow points (solid line) used in the calculations. Just considering the microwindows, the resulting continuum is considerably bumpier than the CKD models. This is due to the cumulative effects of the near- and intermediate-wing non-Lorentz behavior of many lines. In all of the wide microwindows, the errors due to this work are zero. This is due to the fact that that the continuum coefficients used for these calculations were derived from the same spectra, but also shows that the analysis process has worked. The CKD

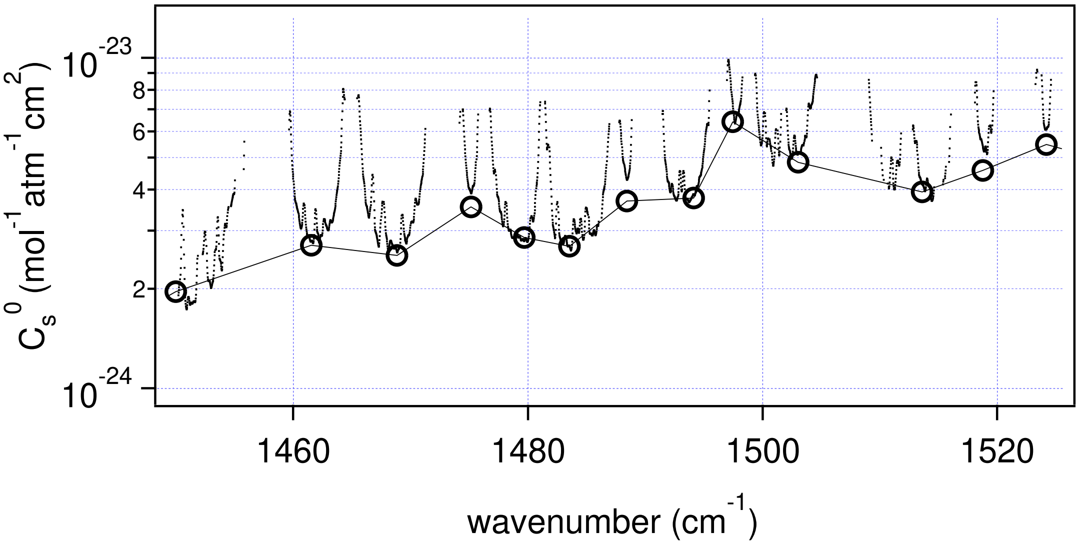

Figure 4.71: C_s^0 determined with the simple subtraction (dots) and slope (circles) methods. The solid line illustrates the interpolation between microwindows used in the calculations in Figures 4.72 through 4.74.

models do well in some regions, but not all – further suggesting that a smooth continuum model within the ν_2 band is not appropriate. Characterizing the continuum even closer to line centers is difficult due to the uncertainties in the line widths and optical depth – this is the focus of Section 4.8.

4.7.8 Conclusions

Experimental measurements of the ν_2 water vapor continuum coefficients have been determined and compared with the previous results of Burch *et.al.* In regions which are least sensitive to local line absorption, the coefficients are in general agreement with the earlier measurements as well as with the CKD models. For the nitrogen component, good agreement is found with CKDv2.1 in the wings of the band and with the original version CKDv0 at the band center. These results show that accurate modeling of the continuum within the band requires a more complex model; possibly super-Lorentz local lineshapes are required. In fact, it may be necessary to redefine the meaning of the "local" component of the continuum and use a non-Lorentzian local lineshape. In the following sections, the analysis is extended to denser wavenumber coverage in spectral regions closer to strong absorption lines. This requires great care because of the difficulty in differentiating between the effects of incorrect spectral lineshapes, strengths and widths.

4.7.9 Oxygen Broadened Spectra

Future work involves processing the high optical depth O_2 broadened spectra once accurate widths are obtained.

4.7.10 High N_2 Pressure Broadened Results

Continuum coefficients determined from the high N_2 pressure (1, 3, 5, 7 atmospheres) spectra are shown in Figure 4.75 along with the results from the lower pressures for the wide microwindow regions. These data were processed in the same manner as the low pressure spectra. For most points, there are no significant differences between the results, although the high pressure results are slightly lower for 3 to 4 points. Future work involves taking into account deviations from the ideal gas law when processing the data.

4.7.11 Low Temperature Spectra

Due to the low signal-to-noise ratios of the low temperature spectra and to the lack of accurate temperature dependent exponents for low temperature line widths, these spectra have not been analyzed.

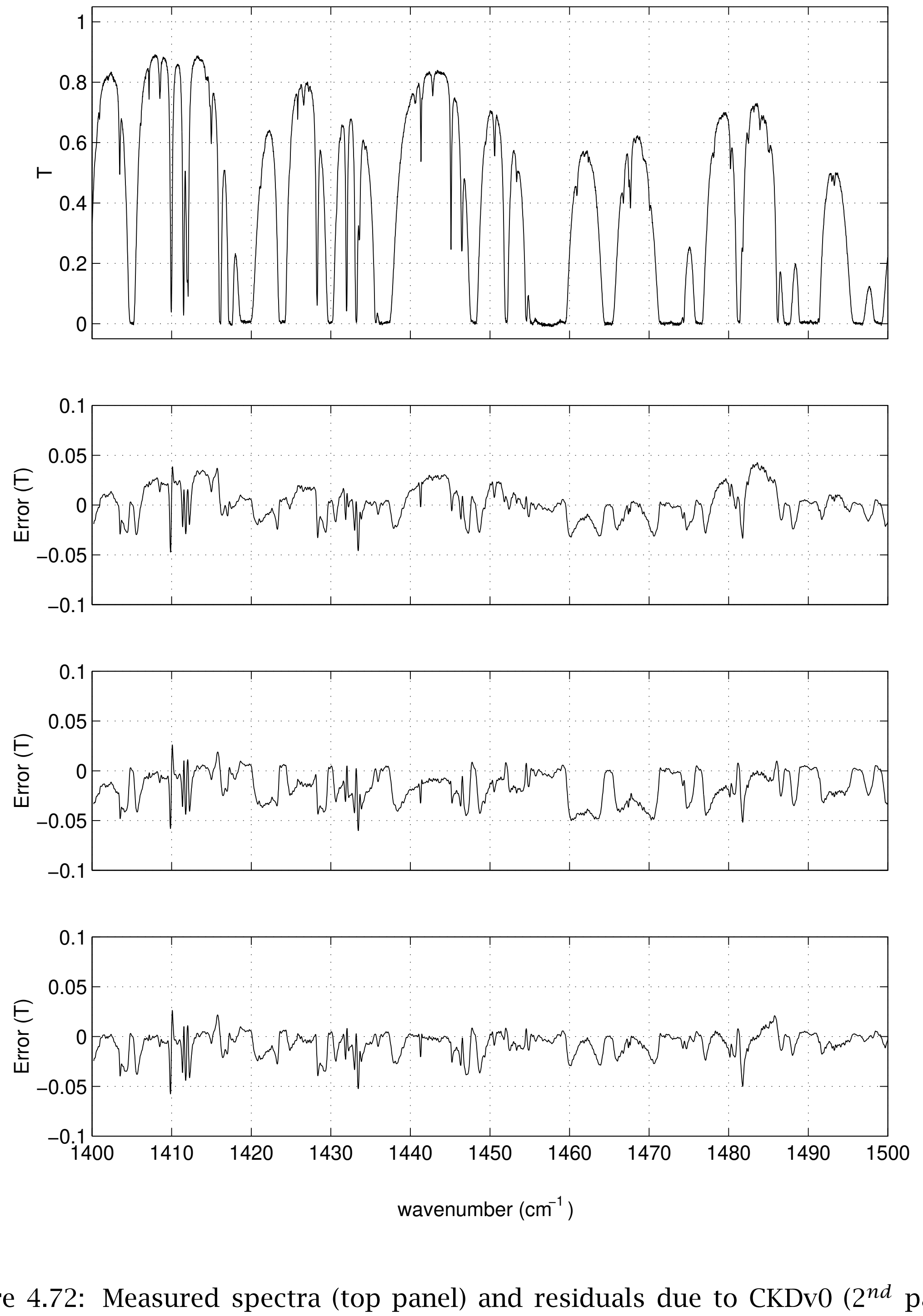

Figure 4.72: Measured spectra (top panel) and residuals due to CKDv0 (2^{nd} panel), CKDv2.1 (3^{rd} panel), and the microwindow continuum from this work (4^{th} panel) for 1400–1500 cm^{-1}. Experimental parameters are: 9.5 torr H_2O, 800 torr N_2, 12 meter path length, 296K.

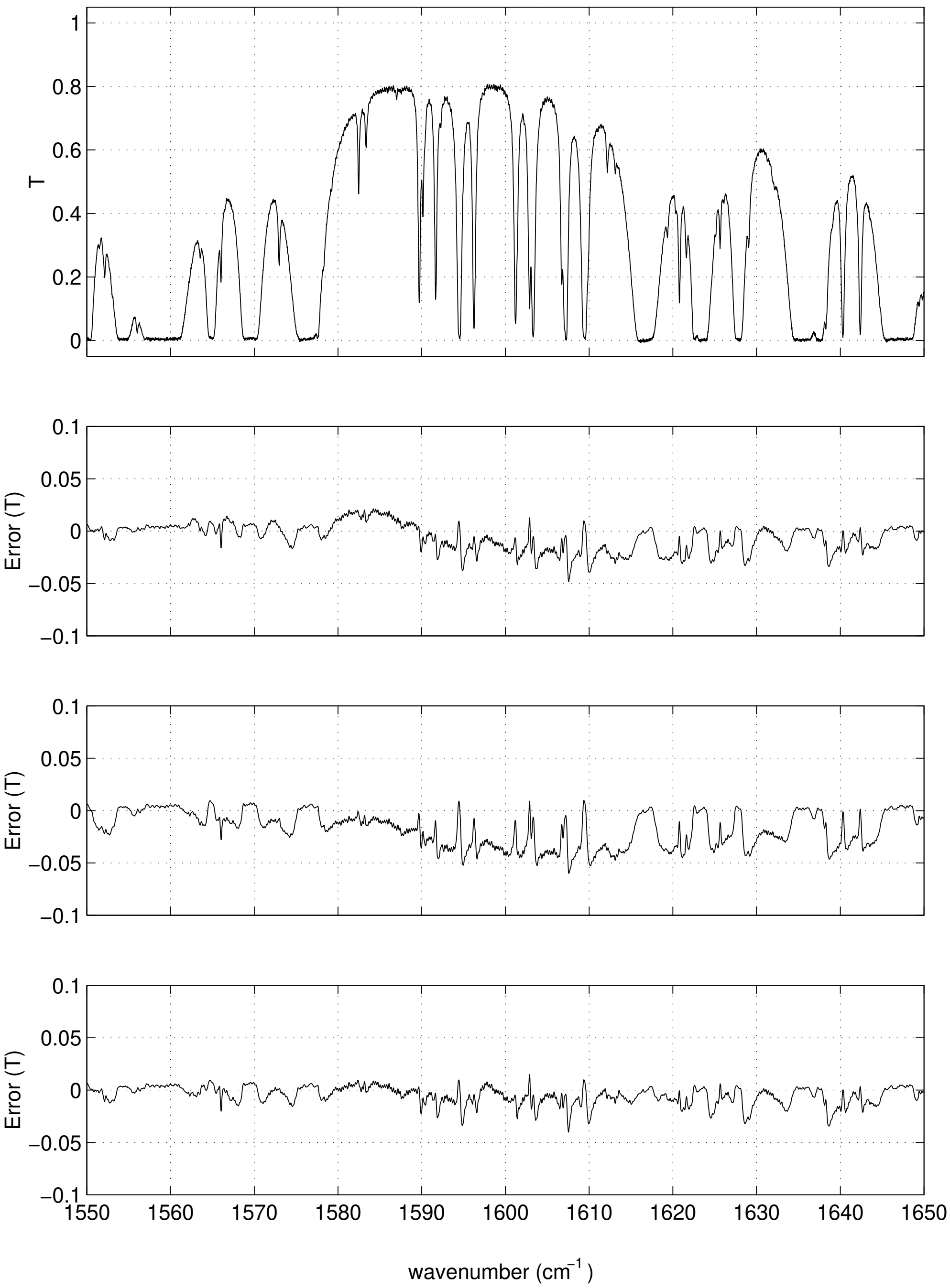

Figure 4.73: Measured spectra (top panel) and residuals due to CKDv0 (2^{nd} panel), CKDv2.1 (3^{rd} panel), and the microwindow continuum from this work (4^{th} panel) for 1550–1650 cm^{-1}. Experimental parameters are: 9.5 torr H_2O, 800 torr N_2, 12 meter path length, 296K.

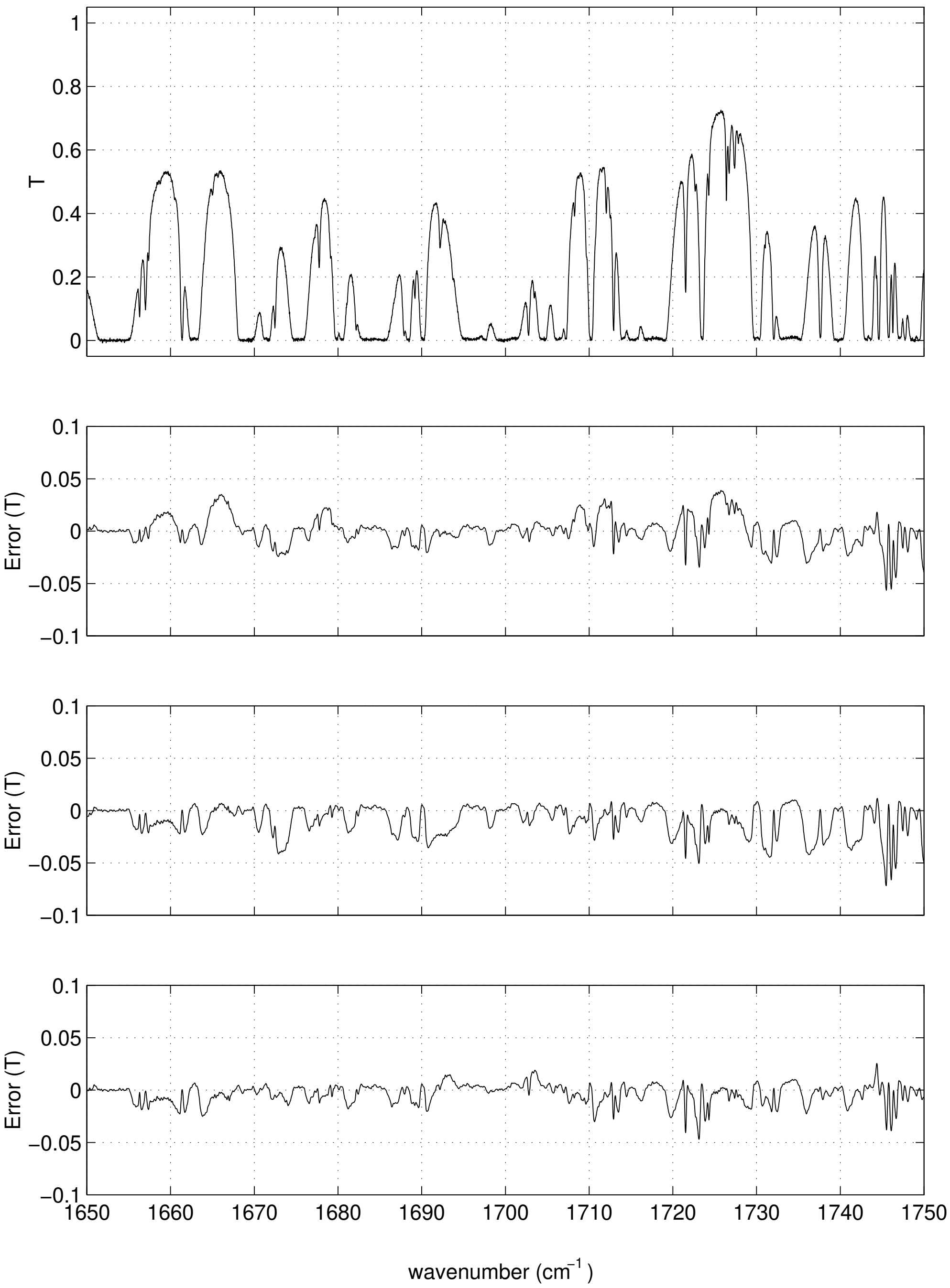

Figure 4.74: Measured spectra (top panel) and residuals due to CKDv0 (2^{nd} panel), CKDv2.1 (3^{rd} panel), and the microwindow continuum from this work (4^{th} panel) for 1650–1750 cm^{-1}. Experimental parameters are: 9.5 torr H_2O, 800 torr N_2, 12 meter path length, 296K.

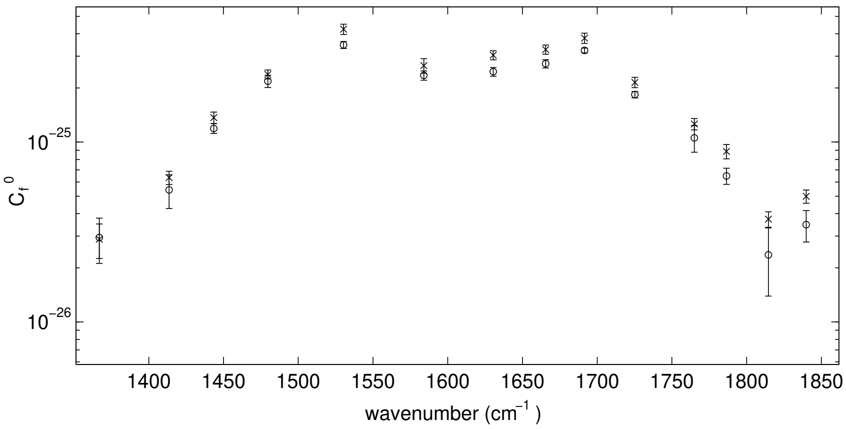

Figure 4.75: Continuum coefficients determined from the high N_2 pressure spectra (circles) and from the lower pressure spectra (x's).

4.8 Near-wing Analysis

This section describes the analysis of the near-wing (~0.5–3 cm^{-1}) lineshape behavior. With the high optical depth spectra used for the microwindow continuum analysis, the lineshape is probed in regions much further from line center than is with spectra used to measure the line parameters. For example, the low optical depth spectra have absorption greater than ~10% only 1 to 2 halfwidths (~0–0.3 cm^{-1}) from line center. The question to be answered then is: How far from line center can we assume the lineshape to be purely Lorentz ? Although the lineshape is known to be super-Lorentzian somewhere in the range ~20–100 cm^{-1} from line center, experimental deviations from Lorentz behavior within ~1-10 cm^{-1} of line center for isolated lines have not been confirmed.

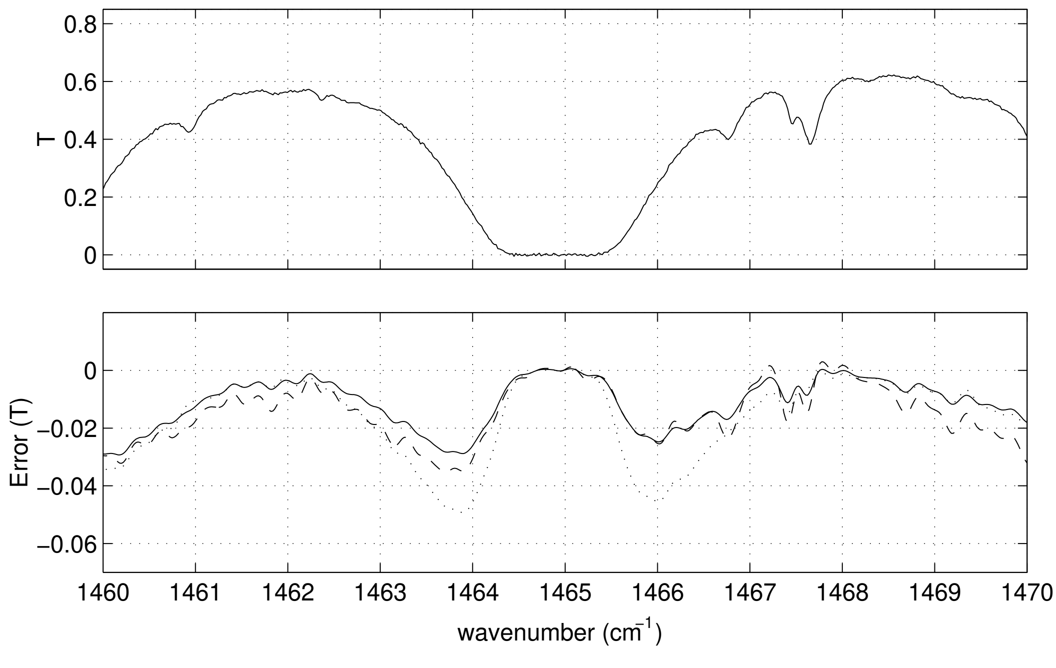

Figure 4.76: Measured spectra (top panel) and residuals due to a calculation using the microwindow continuum from this work (bottom panel) for 1460–1470 cm^{-1} using width sets 1 (solid curve), 2 (dashed curve), and 3 (dotted curve). Experimental parameters are: 9.5 torr H_2O, 800 torr N_2, 12 meter path length, 296K.

In Figures 4.72 through 4.74, the errors due to the results of this work show the same behavior for nearly every microwindow – a deficit of absorption on the edges of the microwindows, close to the centers of the strong lines. This is shown in more detail in Figure 4.76 for the 212 ← 321 line at ~1464.9 cm^{-1}. The errors at the centers of the microwindows on each side of the line (~1462.0 cm^{-1}, ~1468.5 cm^{-1}) are zero. Error curves are shown for calculations using each width set. In all cases, the spectrum shows super-Lorentzian behavior ~0.5 to ~3 cm^{-1} from line center. These errors arise because the continuum is due primarily to near-wing lineshape behavior within the ν_2 band. In other words, in this region the continuum coefficients can not be obtained by simply connecting the points between the sampled microwindows, as was done in the previous section. This approach is valid in window regions because the continuum is due to the far-wings of lines which vary slowly with wavenumber. Within the band, however, the continuum is dominated by near-wing lineshapes which contain much higher frequency components, leading to bumpy continuum coefficients. *Quantifying* this near-wing behavior is the subject of the rest of this section.

With higher optical depths, the contributions from neighboring lines becomes more important, as seen in Figure 4.77 for the 1455–1475 cm^{-1} region. The 212 ← 312 line, along with only a hand-full (~10) of other lines, is well suited for analyzing the lineshape under these conditions because it is somewhat isolated from other lines. Even for this line, however, the 212 ← 312 line is responsible for 90% of the total absorption within only ~1 cm^{-1} of line center. The following analysis is presented using mainly this line, but is representative of nearly all other lines studied. Lines for this analysis were chosen using several criteria including: (1) they do not overlap significantly with other neighboring lines, (2) their low optical depth Lorentz widths are known accurately, and (3) they are sufficiently broadened by N_2 to minimize errors in the self-broadened widths.

To characterize the near-wing lineshape, several approaches have been used. These

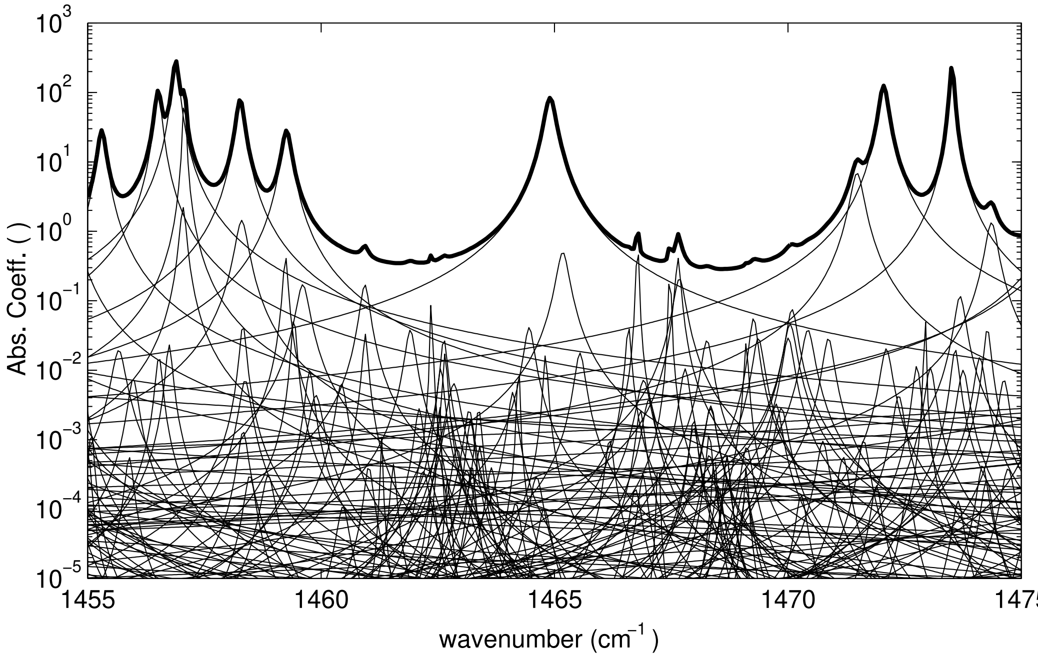

Figure 4.77: Contributions to the total absorption coefficient (thick line) from 1455–1475 cm^{-1}. Lines between 1430 – 1500 cm^{-1} are shown.

include (1) fitting the saturated high optical depth spectra for line widths and comparing to the low optical depth measurements and (2) studying the ratio of the experimental absorption coefficient to the Lorentz local absorption in regions dominated by only one spectral line. For all approaches, definite conclusions about the magnitude of the super-Lorentz behavior with these saturated transmission lines are difficult to make due to the difficulty in distinguishing between possible near-wing super-Lorentz behavior and errors in the line widths and strengths and/or errors in the optical depth.

4.8.1 Width Analysis

The increase in C_f^0 near strong lines (i.e. Figure 4.71) and the behavior shown in Figure 4.76 could be due to near-wing super-Lorentzian behavior, inaccurate line parameters, inaccurate optical depths, or some combination of these factors. Assuming

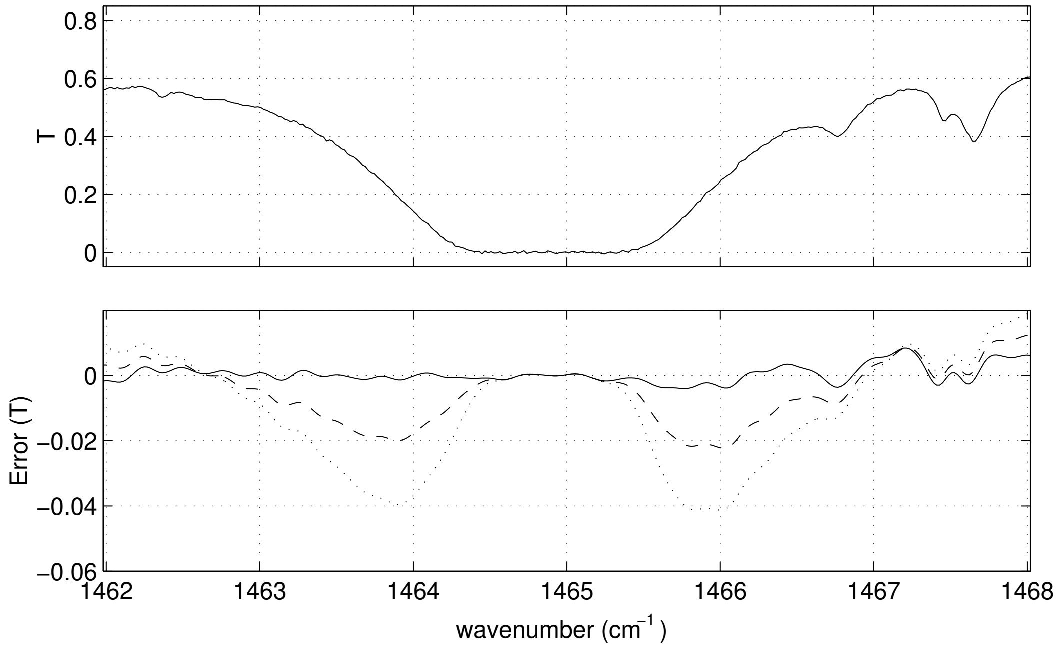

Figure 4.78: Measured spectra (top panel) and residuals (bottom panel) due to calculations using the fitted width (0.1219 cm^{-1}/atm, solid curve), the LOD fitted width (0.1111 cm^{-1}/atm, dashed curve), and Toth's width (0.1002 cm^{-1}/atm, dotted curve). Experimental parameters are: 9.5 torr H_2O, 800 torr N_2, 12 meter path length, 296K.

the behavior is due solely to line width errors, the widths of selected lines were adjusted to obtain agreement with the saturated, high optical depth spectra – an example is shown in Figure 4.78. To obtain agreement with the data, the line width had to be increased to 0.1219 cm^{-1}/atm for this line. That is, it had to be increased ~12% over the Lorentz width determined under optimum low optical depth conditions. If Toth's $H_2^{18}O$ widths are used, the effect is nearly twice as large. This general behavior is typical of all lines and all spectra examined.

It should be noted again that different parts of the spectral line are probed with these saturated lines than with spectra of lower optical depth. The lines are saturated within ~0.5 cm^{-1} of line center and have optimum optical depths ~1–2 cm^{-1} from line center. In this range, the lines can be considered as "far-wing" in that the width term in the denominator of the Lorentz shape is dominated by the frequency displacement term. For example, for a Lorentz width of 0.1 cm^{-1}/atm, a displacement of 1.5 cm^{-1} is 15 times larger than the total width for a pressure of 1 atmosphere. The lineshape is then proportional to $P_{H_2O}S\gamma/(\Delta\nu^2)$. This is significant because it implies the observed absorption has nearly the same functional dependence on the optical depth and the line width. In other words, for these saturated lines, it is difficult to differentiate between the lineshape and errors in the optical depth and widths.

Based on the excellent agreement of the Lorentz widths determined in this work with those of Remedios, we believe the accuracy of the widths is ~2–3%. The optical depths, determined from the H_2O partial pressure analysis, are known to ~3–4%. Thus, the ~10-12% increase in widths/optical depth needed to account for the excess of absorption observed 1–2 cm^{-1} from line centers is statistically significant. It is unlikely that the random optical depth and width errors combine additively to produce errors on the order of 10%. However, assuming that they do combine additively, a ~3–4% super-Lorentzian effect is still observed.

4.8.2 Ratio Analysis

In spectral regions dominated by a single line, the ratio of the experimental absorption coefficient to Lorentz, $k_{exp't}/k_{Lor}$, can be used to characterize the near-wing behavior. Examples are shown in Figures 4.79. (The fact that the ratios approach zero near line centers is caused by the saturation of the lines.) It is difficult to extract the behavior of a single line from this ratio due to the fact that $k_{exp't}$ contains the effects of all lines. To account for this, the microwindow continuum absorption is subtracted from the total experimental absorption and then ratioed to Lorentz – shown in the bottom panel of the figure. This ratio, $(k_{exp't} - k_{con})/k_{Lor}$, characterizes the near wing behavior more accurately, but is contaminated by k_{con}. That is, subtracting off k_{con} corrupts the ratio by effectively setting it equal to one in each microwindow. Furthermore, the microwindows in which the continuum is sampled are irregularly spaced throughout

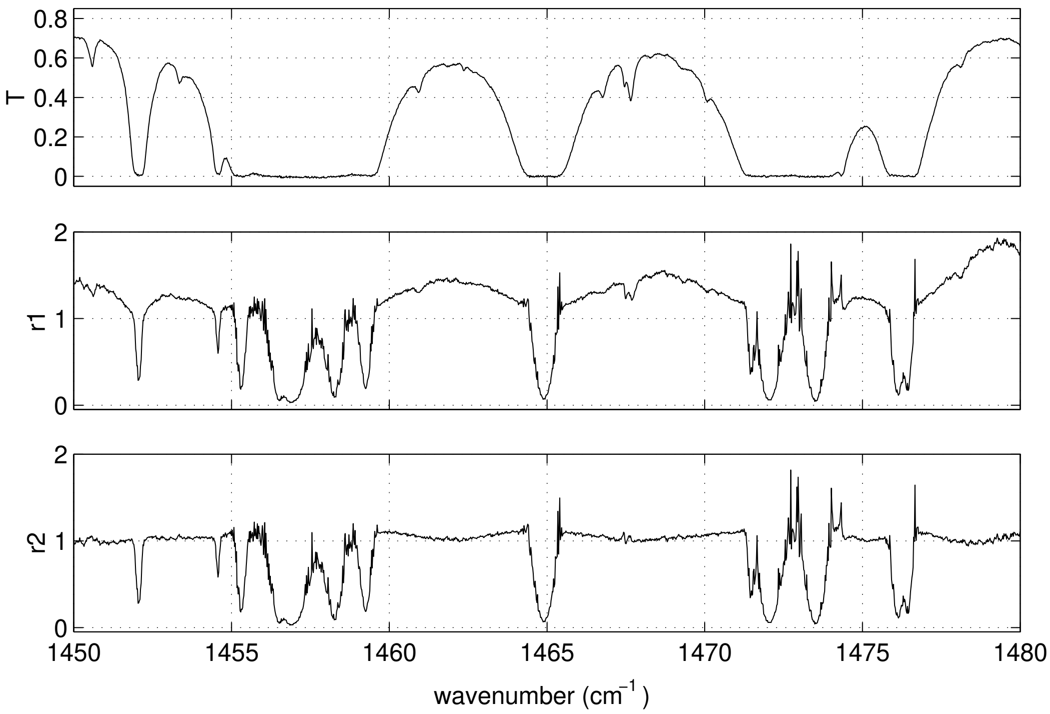

Figure 4.79: Measured spectra (top panel) and ratios of experimental absorption coefficient to Lorentz: $r1 = k_{exp't}/k_{Lor}$ and $r2 = (k_{exp't} - k_{con})/k_{Lor}$. Experimental parameters are: 9.5 torr H_2O, 800 torr N_2, 12 meter path length, 296K.

the band, resulting is slightly different ratios dependent upon how far a particular line is displaced from the nearest microwindow. A more consistent approach is presented in Section 4.10.

Ratios as a function of self- and broadening pressures and as a function of path length were examined to distinguish between line parameter errors and truly super-Lorentz lineshape behavior. Lines and spectra of varying optical depths were examined to probe the lineshape behavior over a range of regions from the line center – examples are shown in Figure 4.80. The information gained from examining these ratios is the same as from the width analysis – for nearly every line, a $\sim$10% super-Lorentz lineshape is observed.

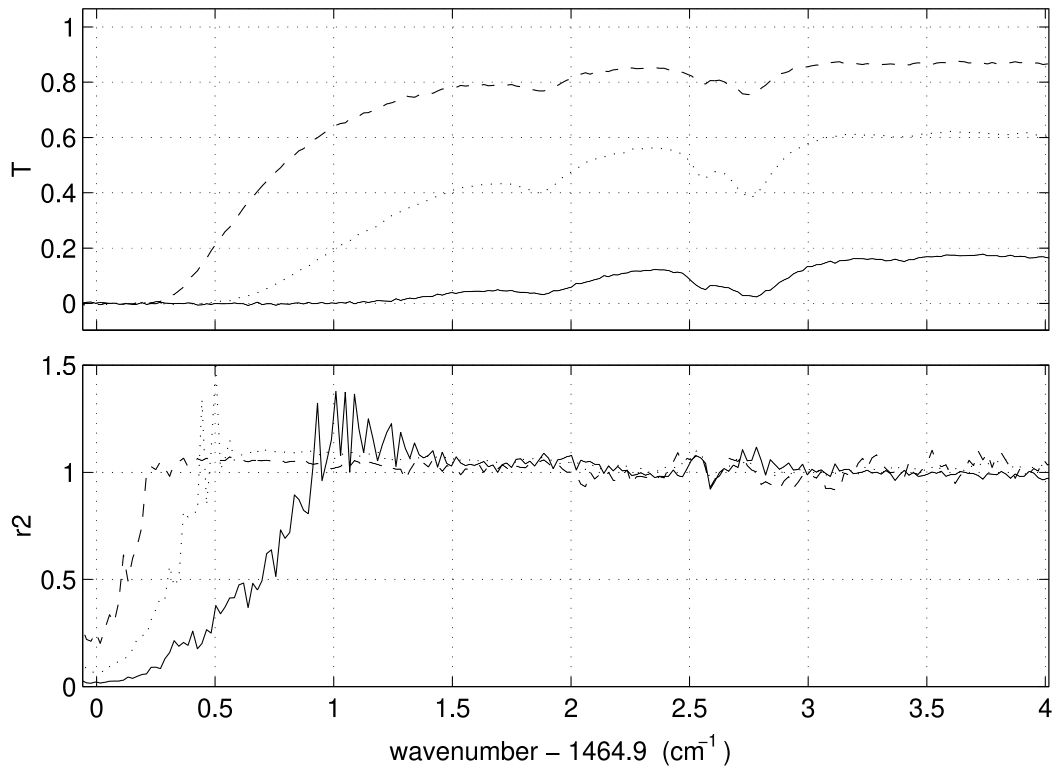

Figure 4.80: Measured spectra (top panel) and ratios of experimental absorption coefficient to Lorentz: $r2 = (k_{exp't} - k_{con})/k_{Lor}$. Experimental parameters are: (solid curve) 2.8 torr H_2O, 800 torr N_2, 12 meters, (dashed curve) 9.5 torr H_2O, 800 torr N_2, 12 meters, (dotted curve) 9.7 torr H_2O, 800 torr N_2, 44 meters.

A way of expressing this near-wing behavior, merely for empirical purposes, is useful for computational reasons. Based on the ratios, a near wing χ-function of the of the form:

$$\chi_{NW} = \begin{cases} 1 & \text{if } |\Delta\nu| \le 0.2\text{cm}^{-1}, \text{if } |\Delta\nu| \ge 3.0 \\ 1.1 - \frac{0.1}{2.8}(|\Delta\nu| - 0.2) & \text{if } 0.2 \le |\Delta\nu| \le 3.0 \end{cases}$$

could be appropriate. This form was chosen somewhat arbitrarily – the main goal is to simply represent the behavior observed in the ratios. χ_{NW} is equal to 1 within 0.2 cm^{-1} of line center due to a lack of spectra with optical depths suitable for probing this region.

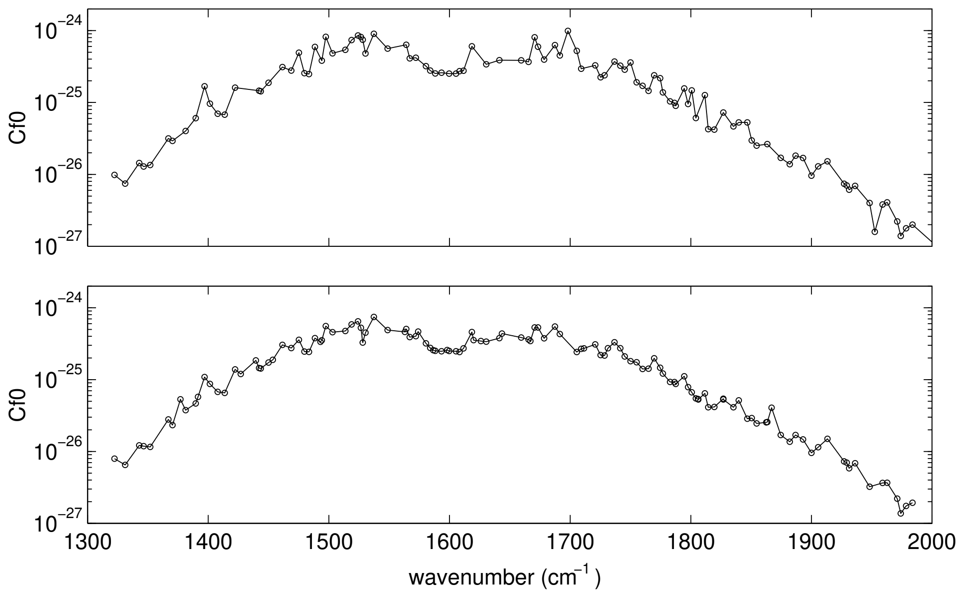

Figure 4.81: C_f^0 processed with a Lorentz local lineshape (top panel) and with a Lorentz$\cdot\chi_{NW}$ local lineshape (bottom panel).

The continuum coefficients were processed using a local lineshape of $k_{Lor}\chi_{NW}$. This is shown in Figure 4.81 along with results obtained using the standard Lorentz local lineshape. Including the high frequency components of the near-wing χ-function in the local calculations has indeed smoothed out the resulting continuum coefficients to a certain degree. Residuals for transmission spectra using χ_{NW} are shown in Figures 4.82 through 4.84. In most spectral regions, the addition of the near wing correction term improves the residuals on the edges of the strong lines.

4.8.3 Summary

Analyzing the continuum with the most accurate Lorentz widths (Remedios, this work) and optical depths, a systematic ~10% surplus of absorption is observed near line centers. Using Toth's $H_2^{18}O$ widths, this effect is nearly twice as large. The effect, which

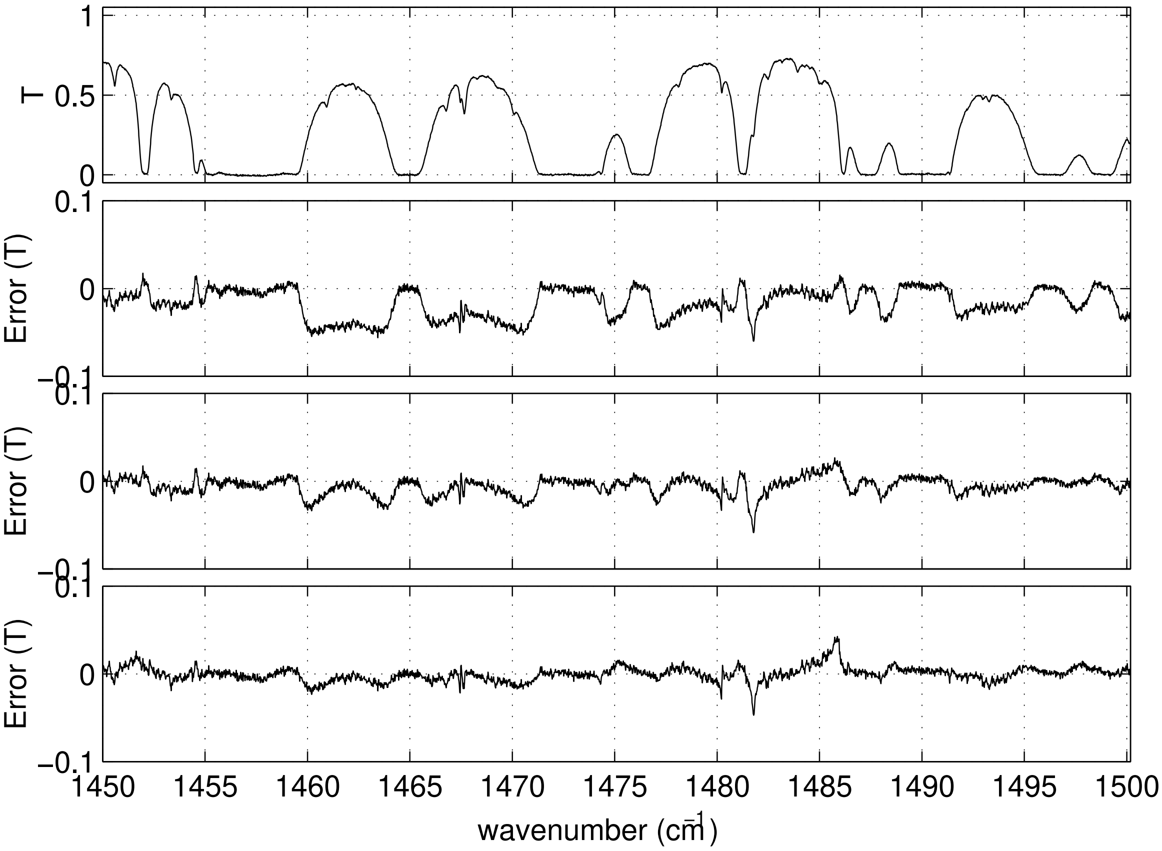

Figure 4.82: Measured spectra (top panel) and residuals due to CKDv2.1 (2^{nd} panel), the microwindow continuum results (3^{rd} panel), and the microwindow continuum plus the near-wing χ-function (4^{th} panel) for 1450–1500 cm^{-1}. Experimental parameters are: 9.5 torr H_2O, 800 torr N_2, 12 meter path length, 296K.

is seen for all lines examined, manifests itself in what appears to be a near-wing (~0.5–2.5 cm^{-1}) super-Lorentz lineshape. Alternatively, assuming that errors in line widths (2-3%) and optical depths (3-4%) combine additively to yield maximum errors, the super-Lorentz effect is reduced to ~2–3%. Clearly, more accurate width measurements are required before a conclusion can be made.

Based on the predictions of Ma and Tipping [21], the nitrogen broadened lineshape is only ~0.8% super-Lorentzian 3 cm^{-1} from line center [5]. Clough's CKDv0 χ-function

[5]Due to the far-wing nature of Ma and Tipping's theory and the way their results are expressed, this

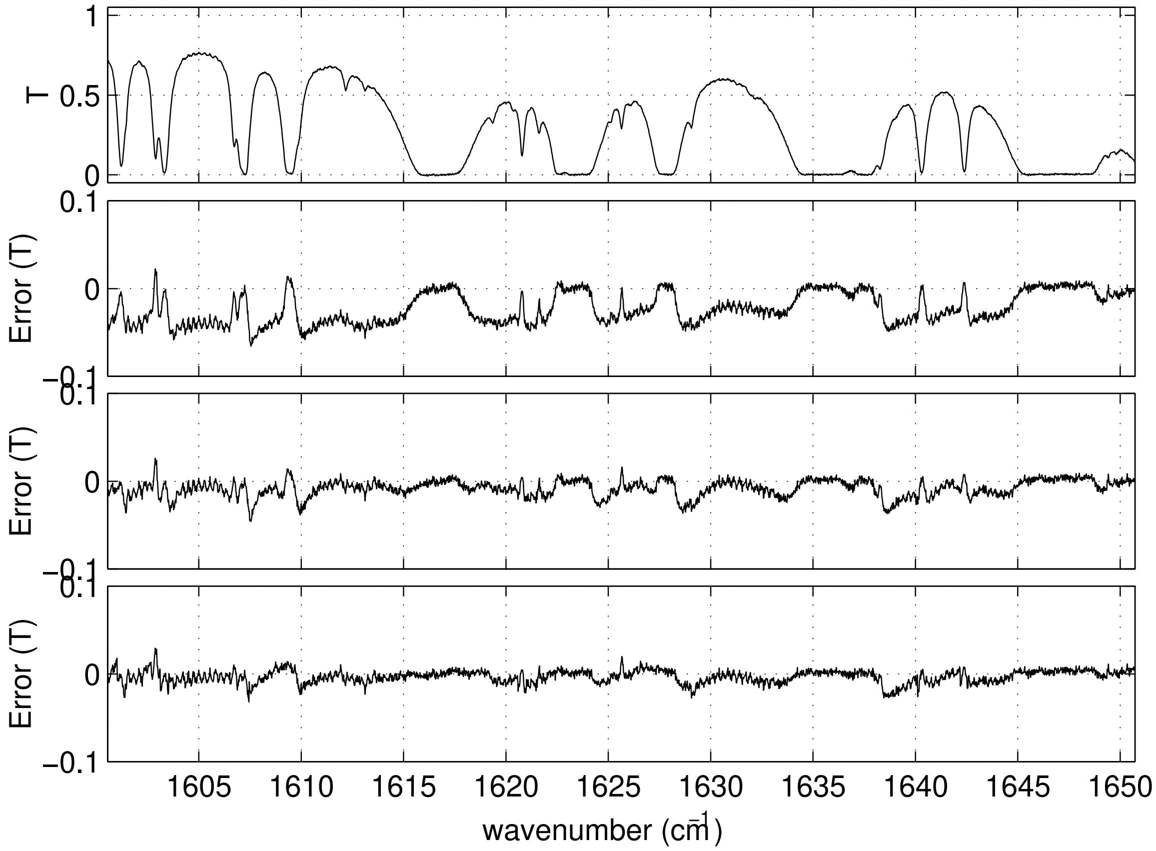

Figure 4.83: Measured spectra (top panel) and residuals due to CKDv2.1 (2^{nd} panel), the microwindow continuum results (3^{rd} panel), and the microwindow continuum plus the near-wing χ-function (4^{th} panel) for 1600–1650 cm^{-1}. Experimental parameters are: 9.5 torr H_2O, 800 torr N_2, 12 meter path length, 296K.

predicts a lineshape which is 1% super-Lorentz 1.0 cm^{-1} from line center, 2% super-Lorentz 1.5 cm^{-1} from line center, and 8% super-Lorentz 3.0 cm^{-1} from line center[6]. The near-wing super-Lorentz effect is therefore a small effect and our data is in reasonable agreement.

A pseudo near-wing χ-function has been derived from the spectra and applied to

value is only approximate

[6]These values are used only as an order-of magnitude of what kind of near-wing effect is expected – the near wing CKD χ-functions have not been verified.

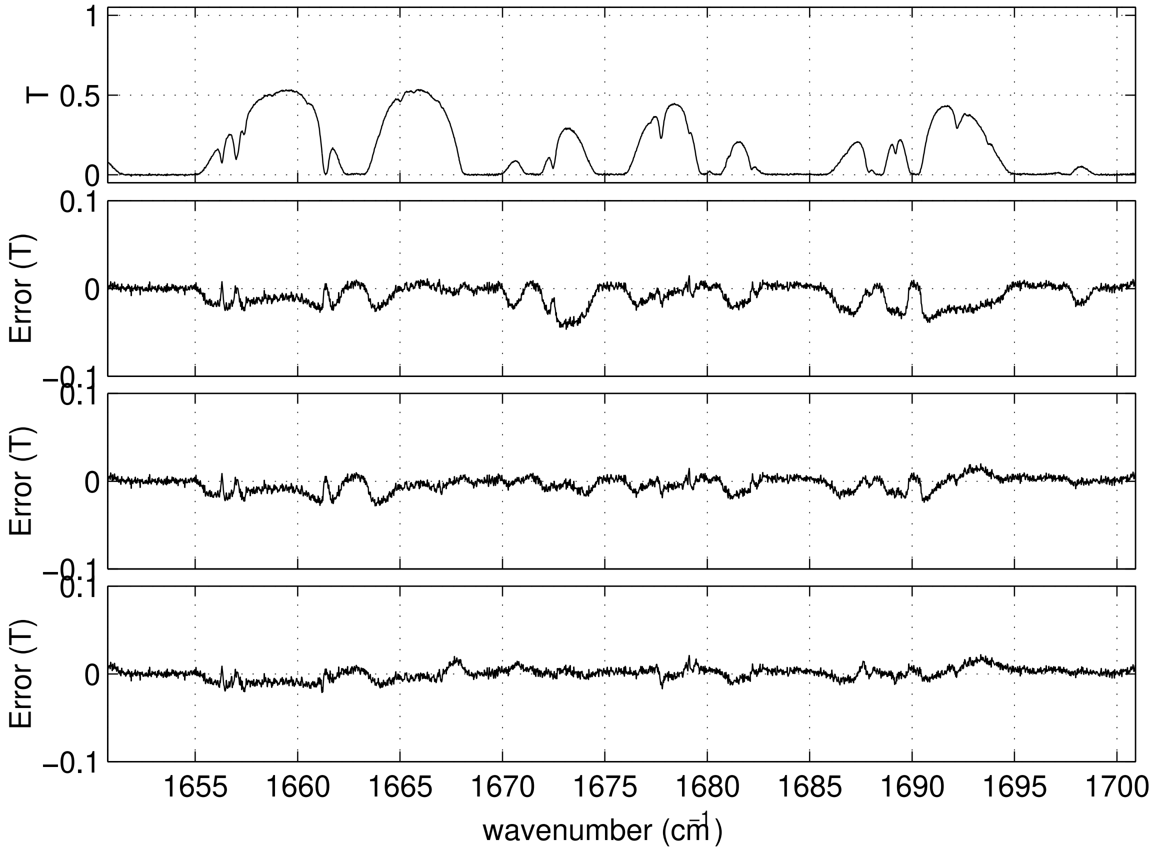

Figure 4.84: Measured spectra (top panel) and residuals due to CKDv2.1 (2^{nd} panel), the microwindow continuum results (3^{rd} panel), and the microwindow continuum plus the near-wing χ-function (4^{th} panel) for 1650–1700 cm^{-1}. Experimental parameters are: 9.5 torr H_2O, 800 torr N_2, 12 meter path length, 296K.

the continuum coefficients. Including the high frequency near-wing super-Lorentz behavior in the local calculations produces smoother continuum coefficients and also improves agreement with the spectra.

4.9 Application to Atmospheric Spectra

The results from the microwindow continuum and near-wing analyses (Sections 4.7 and 4.8) have been incorporated into a line-by-line radiative transfer code and compared to atmospheric radiance measurements from NASA's CAMEX (Convection and Moisture Experiment) campaign [24]. In particular, they are compared to a validated spectrum measured by the HIS (the University of Wisconsin's emission interferometer) during the "third northbound pass" of the high altitude ER-2 aircraft over the ocean offshore of Wallops Island, Virginia on September 29, 1993. The spectrum is referred to as "validated" because the state of the atmosphere (i.e. temperature, water vapor profiles, etc...) was accurately characterized with the use of other ground and balloon-based instruments at the time of the measurements. These include a ground based Raman LIDAR [] and several sets of radiosondes. (A complete description of CAMEX

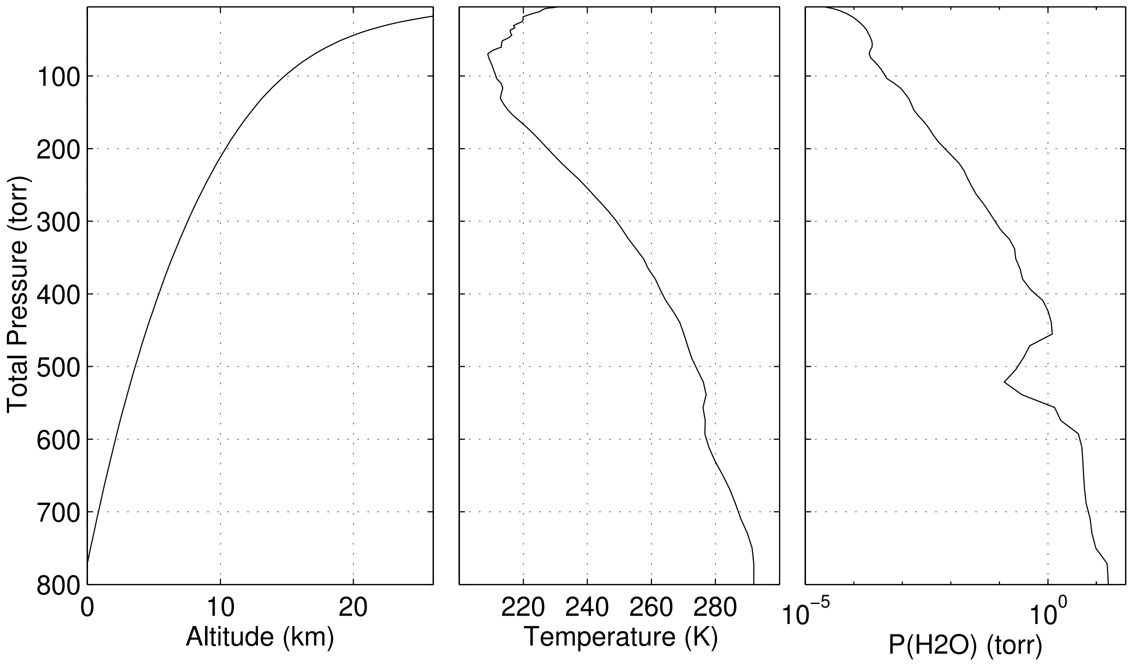

Figure 4.85: Altitude, temperature, and water vapor profiles used in the validated HIS spectrum calculations.

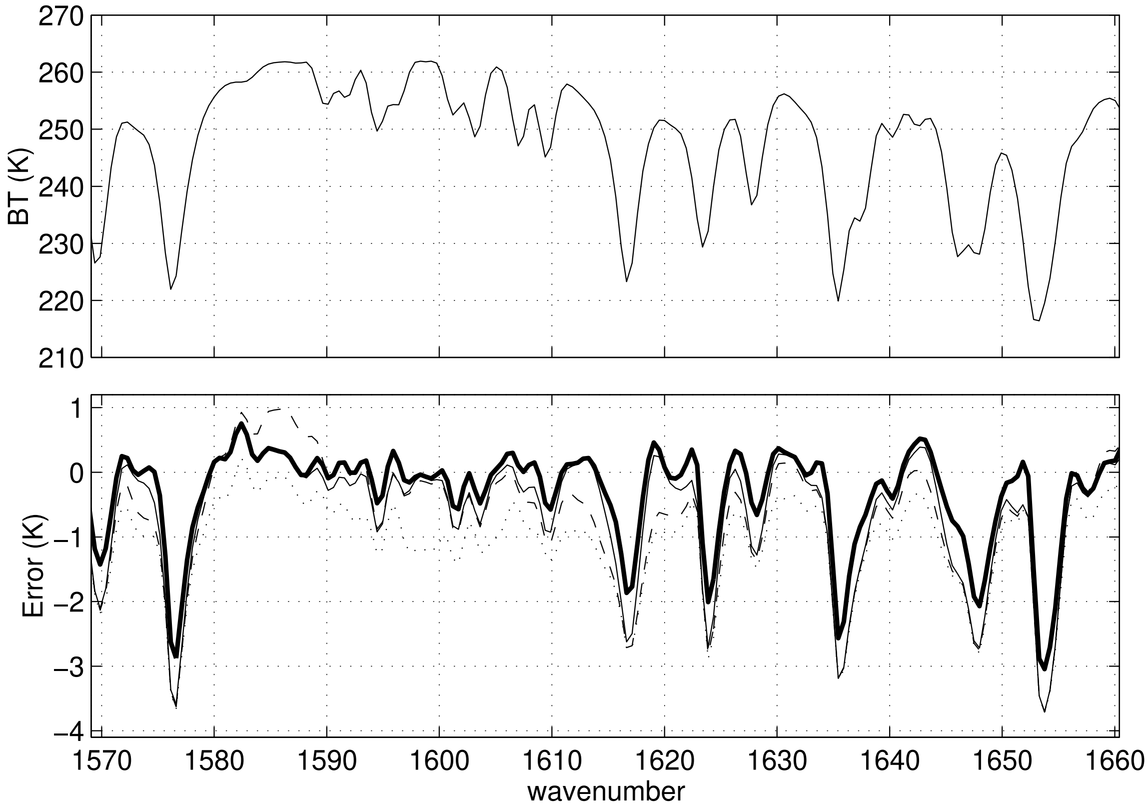

Figure 4.86: Validated HIS spectrum (top panel) and residuals (observed-calculated, bottom panel) for band 2. CKDv0 (dashed curve), CKDv2.1 (dotted curve), microwindow continuum from this work (solid curve), microwindow continuum plus χ_{NW} from this work (thick solid curve).

is given in Reference [24].) Furthermore, for this particular set of measurements, remarkably good agreement is found between the water vapor profiles determined with the radiosondes and with the Raman LIDAR. Thus, these spectra provide a useful test of our laboratory results.

The atmospheric profiles used in the calculations are shown in Figure 4.85. These were derived from the University of Wisconsin's "validated atmosphere" and processed using the AIRS 100 layer pressure levels. The aircraft was at an altitude of $\sim$20 km when the measurements were performed. Radiance calculations were performed using various continuum models and then apodized to the same resolution as the HIS instrument (~0.637 cm^{-1} for band 2). The calculations and measured spectra have been Beer apodized for presentation. For these calculations, Toth's air-broadened line widths (presented in Section 4.6) and the N_2-broadened continuum coefficients were used.

The measured spectrum and residuals (observed-calculated) are shown in Figure 4.86. The top panel shows the equivalent blackbody brightness temperature of the up-welling radiance as measured by the HIS. The bottom panel includes errors due to calculations using the CKD models and the results of this work. The band center region is shown in detail to illustrate the accuracy of the calculations using the results of this work. As described in Section 4.7, our results are expected to be most accurate in this region – the only major source of error is due to uncertainties in the water vapor partial pressures. Furthermore, this region of the HIS spectrum is most sensitive to the lower part of the troposphere (below ~400 torr total pressure, ~5–6 km) where the temperature and water vapor profiles are known most accurately. Based on the excellent agreement in-between the lines at band center, it appears that the water vapor partial pressures and microwindow continuum have been determined very accurately – to within the noise level of the HIS measurements. Like the laboratory spectra, these calculations show that CKDv0 is more accurate than CKDv2.1 at band center.

On line centers, larger errors up to ~3.5K are observed. The inclusion of the super-Lorentz χ-function along with the continuum results helps to improve these errors, but is clearly not the total solution. Accounting for these errors requires much larger widths (increased by factors of 3 to 4) or a much larger near-wing super-Lorentz χ-function, both of which are highly unlikely. Other possible sources of error are inaccurate width temperature exponents and/or inaccurate upper atmosphere water vapor amounts. More validated spectra need to be examined to resolve this problem.

To further examine the problem of distinguishing between line width errors and near-wing super-Lorentz behavior, calculations were also performed using N_2-broadened widths increased by 10 %. On the edges of strong lines, the resulting errors are almost identical to those obtained using χ_{NW}.

4.10 An Experimental χ-function

This section describes a more consistent and global approach for extracting the H_2O lineshape from the laboratory spectra. In Section 4.7, the effects of all lines were characterized in a form well suited for computation with the so-called "continuum" part of the lineshape. In Section 4.8, deviations from the Lorentz lineshape for small frequency displacements were presented by examining the ratios of the observed absorption coefficients to Lorentz in spectral regions dominated by one line. Both of these approaches have their advantages, but do not address the fundamental question: *What exactly is the H_2O lineshape?* In this section, the lineshape from near- to far-wing is determined via a non-linear least squares regression technique to multiple transmission spectra. The only assumption, one which is made in all existing theoretical treatments, is that every line has the same shape. [7]

4.10.1 Method

The absorption coefficient for a single transition is calculated using

$$k(\nu_0, \nu) = k_{VVH}(\nu_0, S, \gamma, \nu)\chi(\nu - \nu_0) \tag{4.11}$$

with

$$\chi(\nu - \nu_0) = \begin{cases} x_1 & \text{if} \quad 0 \le |\nu - \nu_0| < c_1 \\ x_2 & \text{if} \quad c_1 \le |\nu - \nu_0| < c_2 \\ x_3 & \text{if} \quad c_2 \le |\nu - \nu_0| < c_3 \\ & \text{etc...} \end{cases} \tag{4.12}$$

where k_{VVH} is the Van Vleck–Huber lineshape (Section 2.3.3.3) and c_i (cm^{-1}) are fixed constants. x_i are adjustable parameters which are determined by summing Equation

[7] At first, using the same shape for all lines appears to contradict the possibility of strong line-mixing effects. Mixing, however, is not expected to play a major role in the H_2O lineshape [16,106]. Calculations performed using a simple model similar to the one developed for CO_2 suggest that this is true.

4.11 over all necessary transitions and then minimizing the difference (via non-linear least squares) between a transmission spectrum and the calculation. There are no constraints imposed on the values of x_i. χ is therefore free to assume any form – it is merely a "binning" type function in which x_i are grouped according to their displacement from line center. The fact that no assumptions are made about the form of the χ-function is a significant advantage of this approach.

In order to satisfy detailed balance, χ is not an even function but is given by $\chi(-\nu) = \mathrm{e}^{-hc\nu/kT}\chi(\nu)$ as shown in Reference [13]. This modification is important only in the far-wing and window regions.

It should be emphasized that the absorption coefficients are not divided into local and continuum components with this method. For a single transition, the total lineshape is merely $k_{Lor}\chi$ for all wavenumber displacements. This is another advantage because all lines are treated consistently – the cumulative effects of distant lines are not grouped together in a bin called the continuum.

The main disadvantage of this method is that it is somewhat of an ill-posed problem. That is, there are potentially a very large number of solutions for χ which lead to the same behavior in the resulting absorption coefficients. In other words, in the example:

$$\sum_{i=1}^{200} k_{Lor}(\nu_i, \nu)\chi(\nu_i - \nu) = k(\nu) \tag{4.13}$$

there are many ways in which $k_{Lor}\chi_i$ can add up to equal $k(\nu)$. This is evident by considering Figure 4.77. There are advanced ways of constraining and "regularizing" these types of inverse source problems, but none are employed in the work presented here. Instead, a more ad-hoc approach is taken whereby different parts of χ are determined based on its sensitivity to different regions of the spectra. For example, the near-wing region of χ is determined using spectral regions which are most sensitive to the near-wing lineshape and relatively insensitive to the far-wing. The near-wing of χ is then held fixed and the far-wing determined using spectra more sensitive to the far-wing. Future work might include a more sophisticated approach of inverting an observed spectrum to determine χ.

This general approach is similar to that used by Clough when he determined the CKDv0 χ-functions (Section 4.2), but is different is several significant ways: (1) Clough used only Burch's measurements throughout the entire ν_2 band (roughly 20 points between 1300–1900 cm^{-1}), whereas entire spectra between 1100 and 2200 cm^{-1} of 0.040 cm^{-1} resolution are used in this work. This is important because Burch's points are all located at the centers of microwindows. (2) The CKDv0 χ-function was determined using a predetermined empirical form for the χ-function. In particular, the form of χ_{CKD} within 25 cm^{-1} of line center was an educated guess on how to interpolate between the Lorentz result at line center and the fitted values in the far-wing. This was done to simplify the procedure by constraining the behavior of the fit, and to yield results which were easily represented with only a few parameters. The drawback is that by constraining χ to a functional form, its actual behavior might be corrupted. And lastly (3) Clough determined his χ-function by fitting for continuum coefficients, not spectra. Of these differences, (1) and (2) are by far the most important. By using more data points and not assuming a functional form for χ, this method is more versatile and has the potential to provide more information than the CKDv0 χ-functions.

Some general concerns and more detailed information about how the least-squares fits are performed are described in the next few sections. Evaluations for self- and nitrogen-broadened spectra are then presented, along with detailed comparisons to the results of Clough and of Ma and Tipping and the resulting implications on the intermolecular forces involved in H_2O-H_2O and H_2O-N_2 interactions. This is followed by a proposed method for incorporating the results into a line-by-line code.

4.10.2 General Concerns

Concerns which arise when fitting for χ are: which spectral lines are needed in the calculations?, which wavenumber regions should be used?, how should χ be "binned"?

(i.e. what values of c_i should be used?), which line parameters to use?, and how accurate are the results ?

4.10.2.1 Which lines to use?

The choice of which spectral lines to use in the least-squares fit is important. If all spectral lines are used (~23,000 lines), the calculations take too long and the fit is even more ill-posed because lines which contribute essentially no absorption are allowed to float in the fit. To select lines which add a significant amount to the absorption for a particular wavenumber region and for a particular set of experimental conditions, the individual contributions to the total absorption are calculated for all ~23,000 lines using the CKDv0 lineshape at a point which is most sensitive to distant lines. This point is generally taken to be where the transmission is a maximum. For large wavenumber regions, lines selected for several of these points are combined. The lines are then sorted in ascending order according to their percent contribution to the total absorption. Lines which together provide 99 percent of the total absorption are used in the calculations. This typically reduces the number of lines to anywhere from 50 to 500 depending on the wavenumber region under examination. In general, spectral regions probing the far-wing lineshape require more lines than regions which probe the near-wing. In addition, all lines not selected but which are within ~5 cm^{-1} of the studied region are also used in the calculations regardless of their percent contribution to the total absorption. The contributions from all other lines are included in the calculations as background absorption, but their lineshapes are not allowed to vary.

4.10.2.2 Which spectral regions to use?

The choice of which spectral region to use depends upon what region of the χ-function is under investigation. This is determined primarily by intuition. For example, if the behavior of the χ-function very close to line center (0-~3 cm^{-1}) is of interest, a spectral region which is dominated primarily by the absorption of a single line is used. Alternatively, if the near and intermediate regions are of interest, the spectral regions at the peaks of the P- and R-branches yield the most information. Lastly, if the intermediate and far-wings are under investigation, the region at the very center of the band and in the wings of the band are used, for example. The choice of these regions can be correlated to the choice of c_i.

Furthermore, the fits can be performed using a single spectrum and one wavenumber region, a single spectrum and several spectral regions, several spectra with one or more spectral regions, or any combination. Performing the fits using several spectra simultaneously helps to constrain the solution by providing more data to fit. Using several spectral regions simultaneously also helps to determine all regions of the χ-function in a consistent manner.

4.10.2.3 What bins (c_i) to use?

The c_i are chosen according to what regions of χ are being determined and what spectral region is used. For the near-wing, c_i are generally closely spaced (i.e. c_1=0.1 cm^{-1}, c_2=0.2 cm^{-1}, c_3=0.3 cm^{-1}, c_4=0.4 cm^{-1}, etc...) in order to account for any high frequency components in the near-wing lineshape. In the intermediate wing, c_i are spaced further apart (i.e. 3–5 cm^{-1}). In the far-wing, the bins are generally 10 cm^{-1} wide. The wider bins can be used in the intermediate and far-wing because the Lorentz modulation of the lines contributing from these regions makes their contribution fairly smooth. Computationally, the number of bins is kept to a minimum to reduce computing times and to help constrain the fit.

Bins are included up to $\sim$100 cm^{-1} away from line center. The spectra used here are simply not sensitive to contributions from lines much further away. To extend the fitted χ-functions further into the far-wing, spectra of higher optical depth for the 5 and 10μm window regions must be used. Future work could involve the incorporation of Burch's window region measurements to provide this information.

4.10.2.4 Which line parameters to use?

The line parameters discussed in Section 4.6 are used for the calculations. Nitrogen broadened widths from width set 1 are used. The sensitivity of χ to the widths is important mainly for the near-wing portions of χ. Other regions ($|\nu - \nu_0| \gtrsim 2$ cm^{-1}) are also dependent on the widths, but the observed deviations from Lorentz are orders of magnitude greater than linewidth uncertainties.

4.10.2.5 How accurate are the results?

To determine the accuracy of the fitted χ-functions, several tests are performed. One basic concern is the overall agreement between the resulting calculated spectrum and the raw data. In general, this agreement is excellent. By itself, this result means almost nothing because of the ill-posed nature of the problem. In other words, getting good residuals does not mean that χ has been determined uniquely, and the χ-function cannot be used universally for other conditions and wavenumber regions. Therefore, the fits are performed under a variety of different conditions and regions. If the resulting χ-functions all have the same behavior, the uniqueness of the solution is more certain. This, in fact, is the case. Thus, by picking wavenumber regions with thought as to what part of the χ-function they are sensitive to, and by constraining the fits by using multiple optical depths, the fits are not entirely ill-posed and a reasonably unique and accurate result is achieved.

The uncertainty in the fitted χ-functions are estimated by comparing results from different optical depths for the same wavenumber region. They are also determined by adjusting the raw data by small amounts and seeing how sensitive the resulting χ-function is to these changes. As a final test, the spectra can be re-calculated with specific parts of the χ-function adjusted by nominal amounts (i.e. ±1 standard deviation) – the resulting calculations can then be compared to the raw data to see how sensitive the data is to that particular part of χ.

4.10.3 Sample Fits

To illustrate the methods described above, sample fits are shown for the 1435–1455 cm^{-1}, 1500–1700 cm^{-1}, 1460–1470 cm^{-1}, and 1575–1615 cm^{-1} regions. Unless otherwise noted, the starting values of x_i are 1.

4.10.3.1 The 1435–1455 cm^{-1} region

A sample fit for the near- and intermediate-wing χ-function is shown in Figures 4.87 and 4.88. For this example, the 1435–1455 cm^{-1} region of only one spectrum (file number 154: 9.5 torr H_2O, 800 torr N_2, 12 meter path length, 296K) is used. This spectrum is broadened with ~800 torr of N_2 and the resulting χ-function therefore contains very little contribution from self-broadening. This region contains several strong local absorption lines at ~1437.0 cm^{-1}, ~1447.5 cm^{-1}, and ~1452.0 cm^{-1} which provide information about the lineshape from ~0.5–3 cm^{-1} from line center. For this particular fit, the value of χ from 0–0.5 cm^{-1} was held fixed at 1 – the other near-wing regions, however, were free to assume any values. The chosen values of c_i are somewhat apparent in Figure 4.88 – they are fairly closely spaced in the near wing and increase to 3 cm^{-1} wide beyond 12 cm^{-1} from line center. The resulting χ-function is well-behaved in the near-wing region – the gradual increase for increasing displacements is very similar to that observed in the CKDv0 χ-function. The region from ~1440–1445 contains fewer contributions from nearby lines and is therefore sensitive to lines from 10 cm^{-1} to up to ~30 cm^{-1} away. Although there are lines ~30 cm^{-1} beyond the 1435-1455 cm^{-1} region included in the fit, their contributions are so weak that the fit is ill-determined beyond ~30 cm^{-1}.

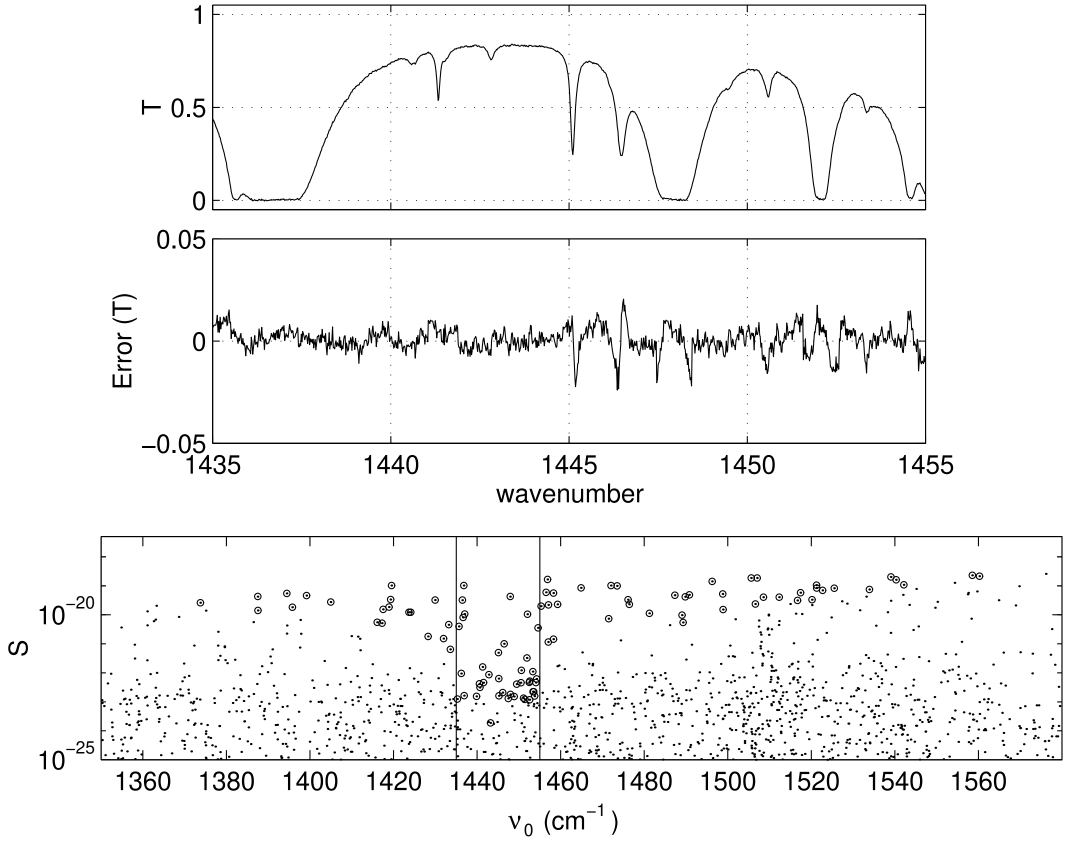

Figure 4.87: A sample χ-function fit using the 1435–1455 cm^{-1} region and file number 154 (9.5 torr H_2O, 800 torr N_2, 12 meter path length, 296K). Measured spectra and residuals (observed-fitted) are shown in the top two panels. The bottom panel displays the transitions included in the fit (circles) and other background lines (dots). The fitted χ-function is shown in Figure 4.88.

For this fit, and for nearly all others, the accuracy of the calculated spectrum is quite high. In Figure 4.87, the maximum errors are on the order of 0.02 in transmission and these are due partially to inaccurate line parameters of the weaker lines. The errors are generally much less than those obtained using the microwindow continuum (Section 4.7) or the microwindow continuum plus χ_{NW} (Section 4.8) approach. This is due primarily to the fact that with this method, the effects of all lines are treated consistently and, of course, because there are more free parameters. These free parameters, however, attain values which are consistent from one fit to another. There are some

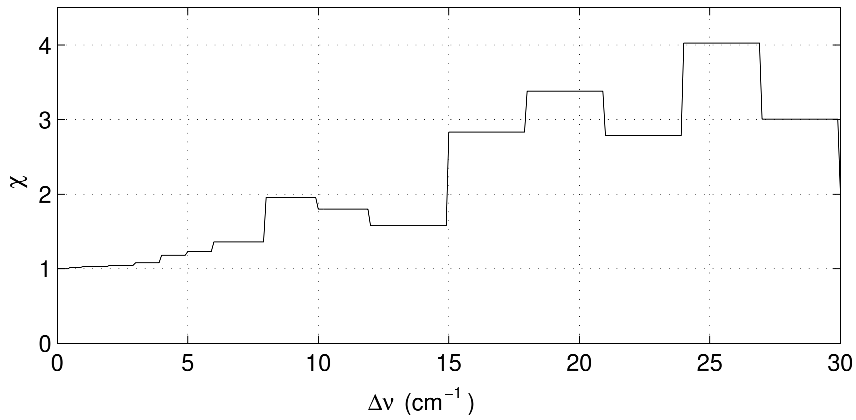

Figure 4.88: The fitted χ-function using the 1435–1455 cm^{-1} region and file number 154 (9.5 torr H_2O, 800 torr N_2, 12 meter path length, 296K) shown in Figure 4.87.

remaining errors near the edges of a few strong lines which are probably due to a combination of lineshape and width errors. However, for the most part, both the far-wing microwindow regions and the near-wing super-Lorentz behavior are accounted for very accurately.

4.10.3.2 The 1500–1700 cm^{-1} region

The 1500–1700 cm^{-1} region (Figures 4.89 and 4.90) is sensitive to nearly all parts of the lineshape up to ~100 cm^{-1} away. For the fit, all x_i were allowed to vary out to 100 cm^{-1} from line center, again using file number 154. The excellent agreement over this wide wavenumber range suggests that it is valid to assume that every line has the same lineshape. The quality of the residuals also suggests that if some type of parameterization which represents the behavior of the fitted lineshape were developed, the problems currently attributed to the water vapor continuum would be greatly reduced. Some unimportant errors due to unresolved lines are found near 1600 cm^{-1}.

4.10.3.3 The 1460–1470 cm^{-1} region

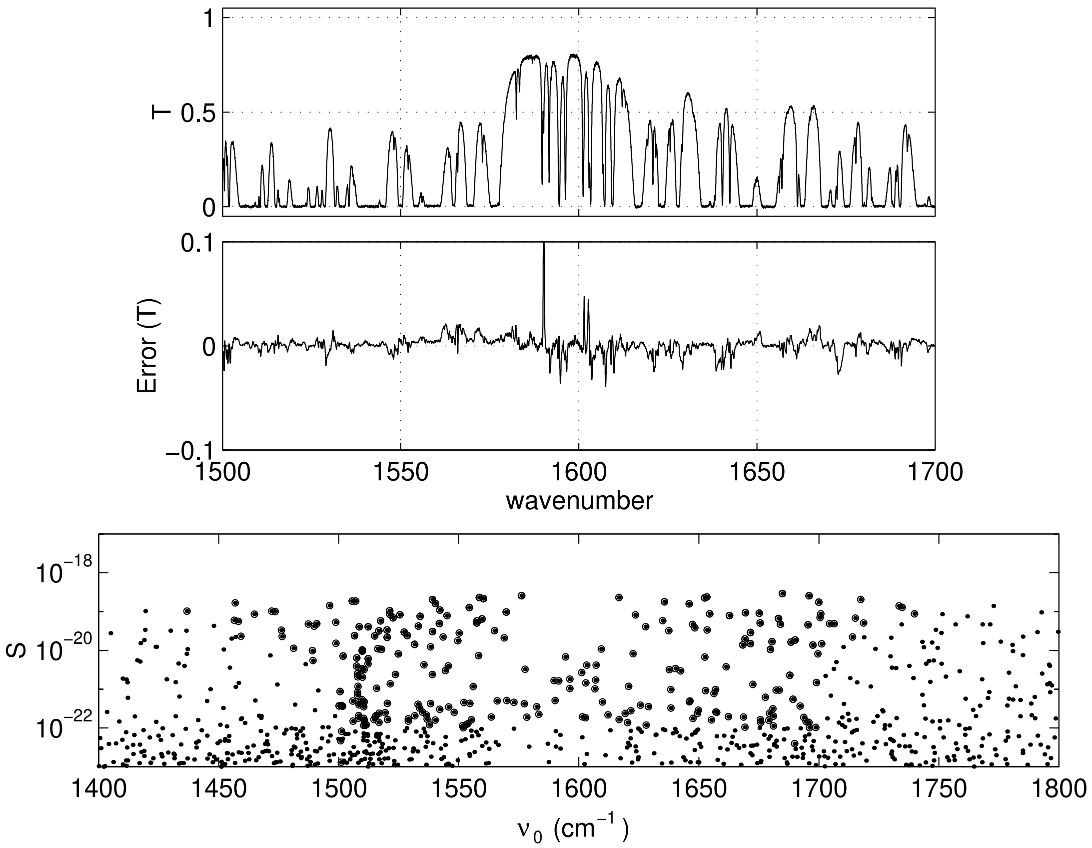

Figure 4.89: A sample χ-function fit using the 1500–1700 cm^{-1} region and file number 154 (9.5 torr H_2O, 800 torr N_2, 12 meter path length, 296K). Measured spectra and residuals (observed-fitted) are shown in the top two panels. The bottom panel displays the transitions included in the fit (circles) and other background lines (dots). The fitted χ-function is shown in Figure 4.90.

The fits shown in Figures 4.91 and 4.92 were performed using files 152, 153, and 154 (9.5 torr H_2O, 300, 500, 800 torr N_2, 12 meter path length, 296K). c_i are 0.1 cm^{-1} wide from 0 to 1 cm^{-1} from line center, 0.2 cm^{-1} wide from 1 to 2 cm^{-1}, and 0.5 cm^{-1} wide from 2 to 3 cm^{-1}. No constraints were imposed on the values of x_i. χ functions are shown in Figure 4.92 for results using N_2-broadened widths of set #1 and with the width of the 321 ← 212 line at 1464.9 cm^{-1} (the main line) increased by 10 %. The near line center behavior of the fitted χ-function determined with the increased width is

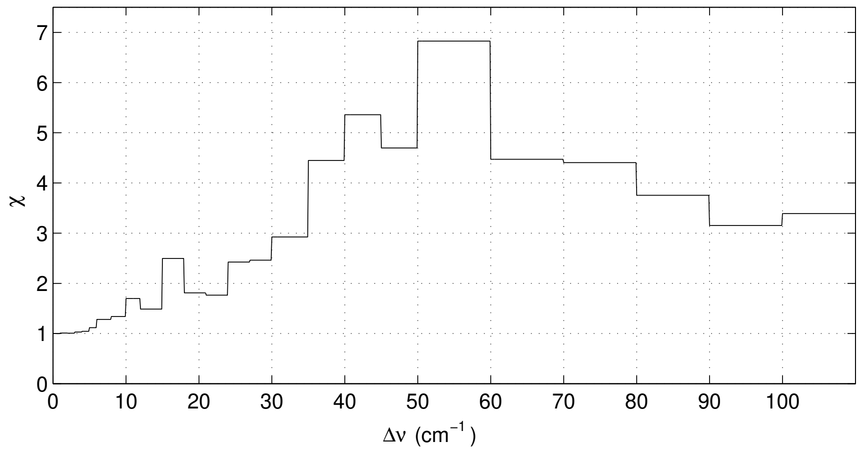

Figure 4.90: The fitted χ-function using the 1500–1700 cm^{-1} region and file number 154 (9.5 torr H_2O, 800 torr N_2, 12 meter path length) shown in Figure 4.89.

physically unrealistic near line center. These and other similar results provide further evidence that the near-wing super-Lorentz behavior, which was analyzed in detail in Section 4.8, is attributable to a non-Lorentz lineshape, not inaccurate line widths. The fact that the fitted χ-function (determined with width set # 1) goes to ~1 at line center explains why the low optical depth spectra, which are sensitive to only ~0.2 cm^{-1} from line center, behave purely Lorentzian and yet the high optical depth spectra with saturated lines appear to be ~10 % super-Lorentzian.

4.10.3.4 The 1575–1615 cm^{-1} region

Sample fits for the 1576–1616 cm^{-1} region are shown in Figures 4.93 and 4.94. This region is at the very center of the band, has few strong local absorption lines, and is therefore sensitive to lines from as far as 100 cm^{-1} away. The 110 ↔ 101 lines are also within this range and provide information about the near-wing. Results from 10 individual N_2-broadened spectra are shown in Figure 4.94 along with their mean and one standard deviation uncertainties. Again, all x_i were allowed to float. These results were obtained over a wide range of optical depths – the fact that their overall behavior

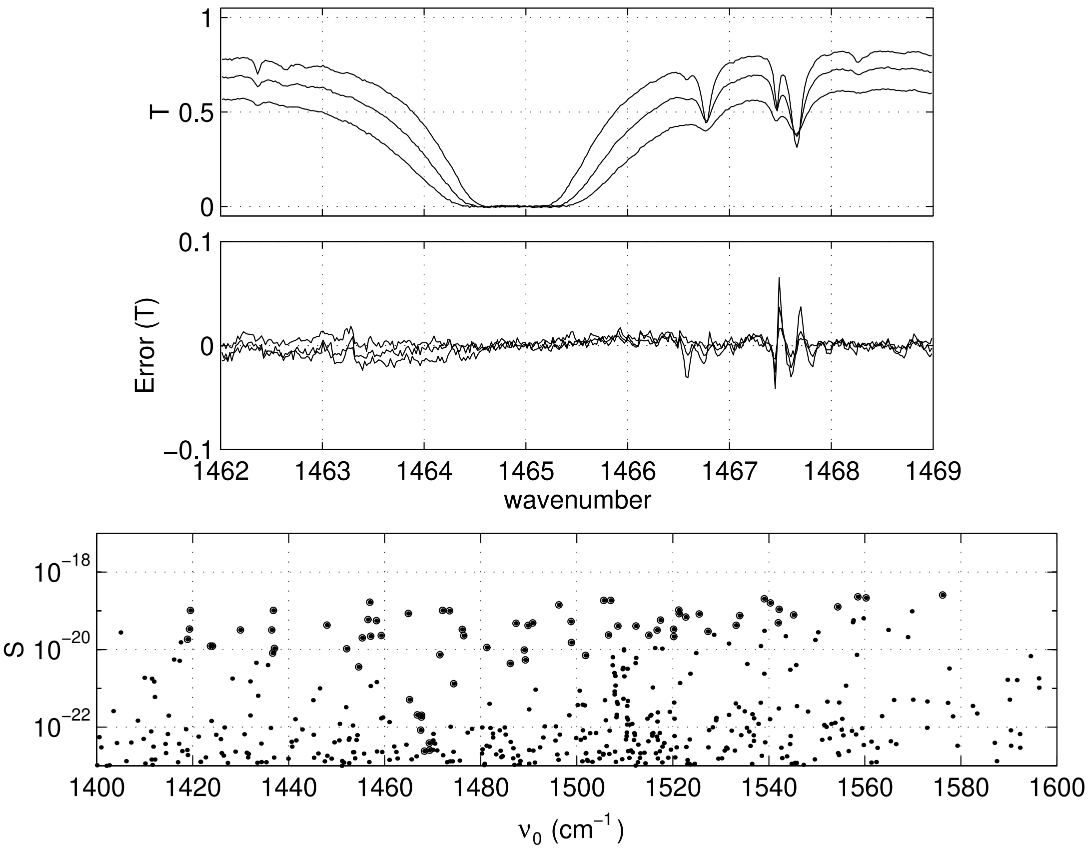

Figure 4.91: A sample χ-function fit using the 1460–1470 cm^{-1} region and file numbers 152, 153, and 154 (9.5 torr H_2O, 300, 500, 800 torr N_2, 12 meter path length, 296K). Measured spectra and residuals (observed-fitted) are shown in the top two panels. The bottom panel displays the transitions included in the fit (circles) and other background lines (dots). The fitted χ-function is shown in Figure 4.92.

is nearly the same implies that the fitted χ-function is fairly unique.

4.10.4 Results

The sample fits shown above yield slightly different results depending on the regions and spectra utilized. To make final determinations of χ, the following approach is used. The near wing (0–5 cm^{-1}) is first determined using spectral regions sensitive to only the near wing (such as those shown in the 1460–1470 cm^{-1} sample). The near

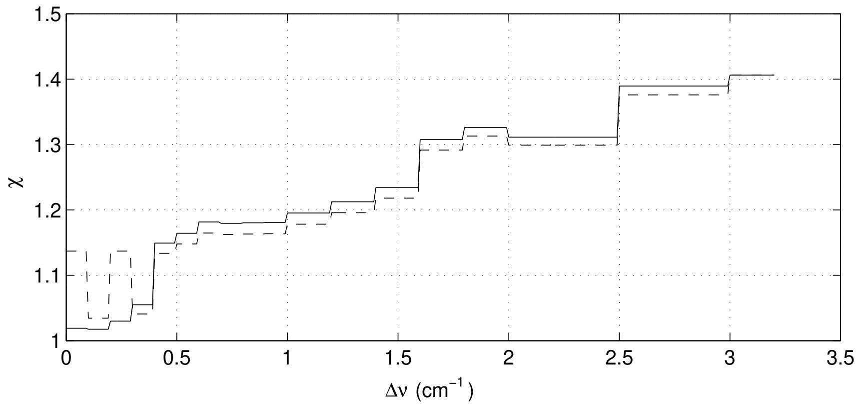

Figure 4.92: Fitted χ-functions from the 1460–1470 cm^{-1} region of file numbers 152, 153, and 154 (9.5 torr H_2O, 300, 500, 800 torr N_2, 12 meter path length) determined with the standard widths (solid curve) and the widths increased by 10 % (dashed curve).

wing χ is then held constant and the 5–20 cm^{-1} region χ obtained using the spectral regions such as 1435–1455 cm^{-1}, for example. Finally, the 20–100 cm^{-1} region of χ is determined using the 1575–1615 cm^{-1} and 1890–1930 cm^{-1} spectral regions. For self-broadening, all of the pure samples are used, while for N_2-broadening, all of the spectra broadened with 1 atmosphere of N_2 are used. Assuming fits from different spectra are weighted equally, uncertainties in χ are estimated by combining fits for a number of individual spectra. Because different spectra are more sensitive to different parts of the χ-function, the reported errors may be slightly over-estimated.

4.10.4.1 N_2-broadening

The final determination of the nitrogen broadened χ-function is shown in Figure 4.95 along with the CKDv0 χ-function and the results of Rosenkranz and Ma and Tipping. For these comparisons, Rosenkranz's and Ma and Tipping's χ-functions are scaled to equal 1 at 1 cm-1 from line center. (The questionable accuracy of these calculations in the near-wing was discussed in Section 4.2.) There are several conclusions

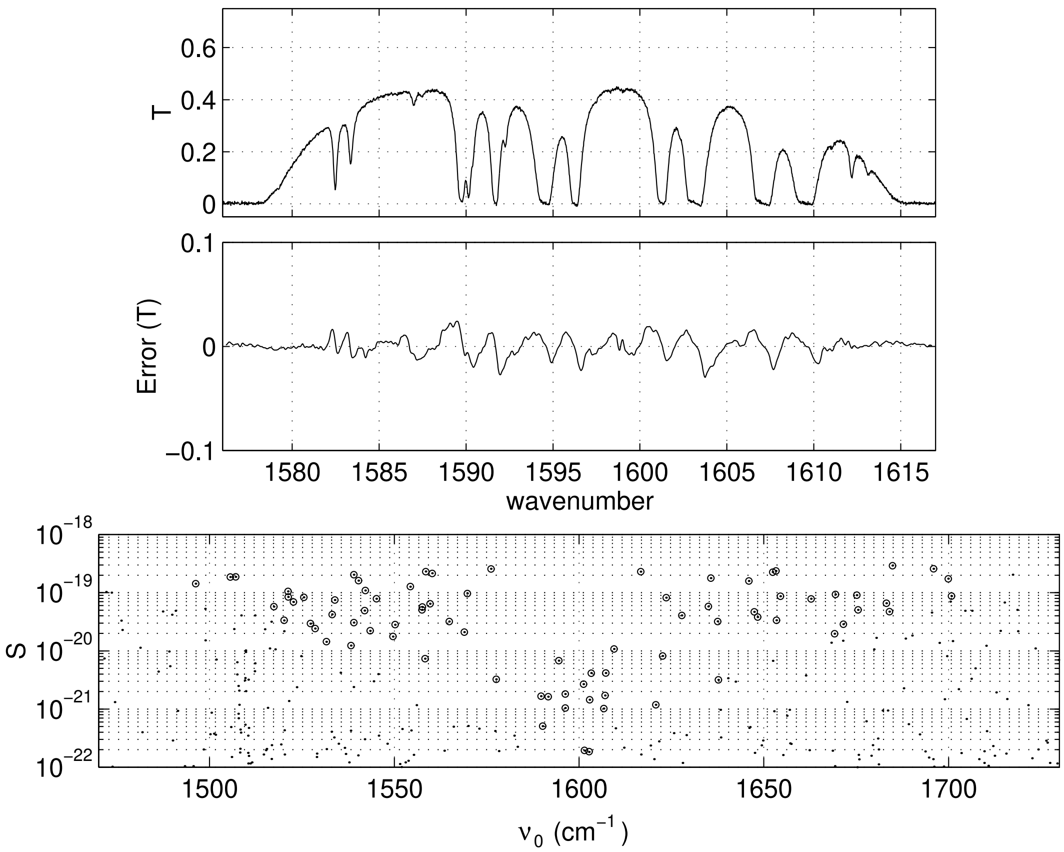

Figure 4.93: A sample χ-function fit using the 1576–1616 cm^{-1} region and file number 140 (9.7 torr H_2O, 800 torr N_2, 44 meter path length, 296K). Measured spectra and residuals (observed-fitted) are shown in the top two panels. The bottom panel displays the transitions included in the fit (circles) and other background lines (dots). The fitted χ-function is shown in Figure 4.94.

from these comparisons: (1) the near-wing super-Lorentz behavior is most likely attributable to a non-Lorentz lineshape, (2) Clough's CKDv0 χ-function agrees very well with the fitted results within ~15 cm^{-1} of line center, (3) Rosenkranz's and Ma and Tipping's χ-functions increase almost linearly with displacement from line center in the near wing but do not become as super-Lorentz as the other results in the intermediate region, and (4) the results of this work are significantly more super-Lorentz than the others ~30–70 cm^{-1} from line center. The significance of these points are discussed

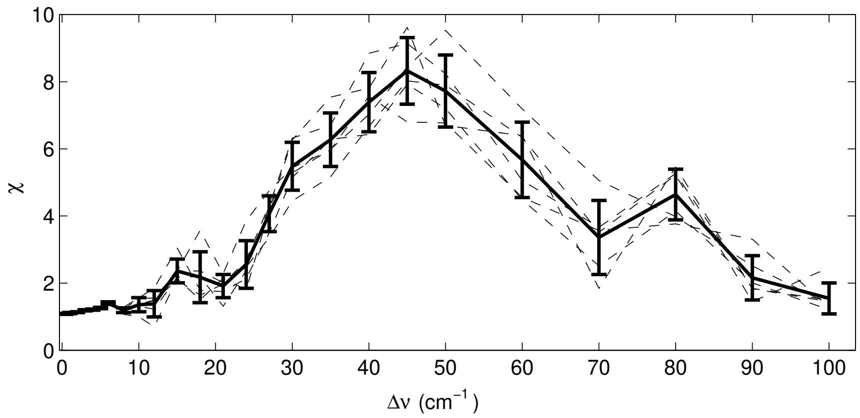

Figure 4.94: Fitted χ-functions using the 1576–1616 cm^{-1} region and various individual spectra (dashed curves) and their average (solid curve).

below.

The fitted results agree well with the CKDv0 χ-function within ~15 cm^{-1} of line center. This is not surprising since both results have been determined from in-band ν_2 experimental data which is very sensitive to this region of the lineshape. The functional form chosen for the CKDv0 lineshape within 25 cm^{-1} of line center appears to be adequate in representing the actual near-wing behavior.

Rosenkranz's and Ma and Tipping's χ-functions increase linearly with displacement from line center within ~15 cm^{-1} of line center, resulting in too much absorption in this region. Due to the statistical nature of their theory, these calculations are not accurate in the near wing.

In the intermediate wing (i.e. 30–75 cm^{-1} from line center) the results of this work are considerably more super-Lorentz than those of other investigators. This difference is much greater than any errors which could arise from ~10 % width errors. Clough was not able to predict this behavior because of the functional form adopted and because of the limited amount of in-band data used to optimize the CKDv0 χ-functions.

The super-Lorentz behavior implies that we are observing more intermediate range

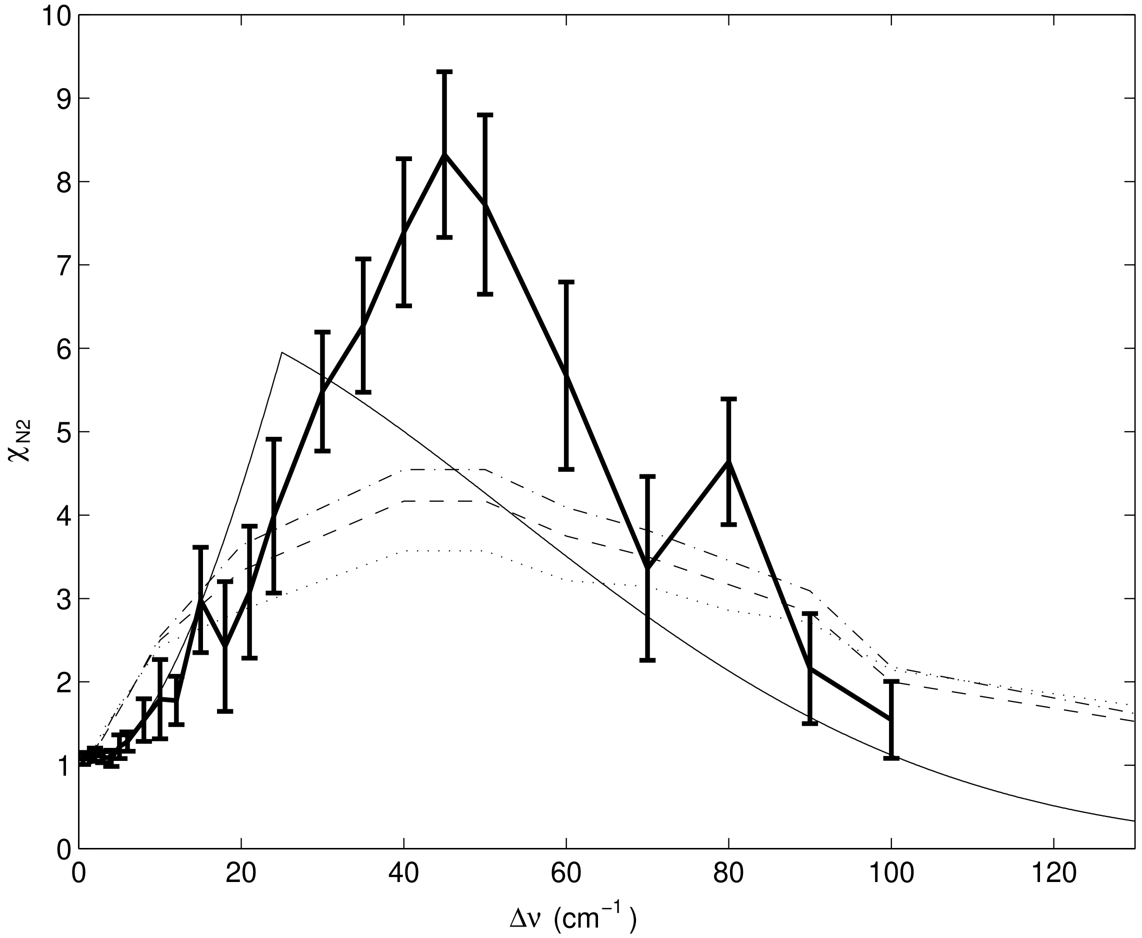

Figure 4.95: N_2-broadened χ functions from: this work (solid with error bars), CKDv0 (solid), Rosenkranz (dashed), and Ma and Tipping (dash-dot and dotted).

forces than are used in Rosenkranz's and Ma and Tipping's calculations. In other words, following the logic of Section 2.3.4.2, the super-Lorentz shape implies that the molecules' autocorrelation function contains more high frequency components which are attributed to a steeper/wider/deeper intermolecular potential, which in turn, is caused by additional intermolecular forces not included in their calculations. This result is not surprising given the simple intermolecular potentials (Lennard-Jones s-6 plus the leading multipole) used in the calculations. The lineshape does not provide specific information about these forces, but we conjecture that dispersion, induction, and/or lower order multipoles, which are expected to become important for medium range separations, are producing the extra forces we observe. All of these sources do produce net intermolecular attraction which leads to the observed super-Lorentz behavior.

In a recent study [107] of the H_2O–H_2 potential using a five dimensional, 48-term angular expansion of the anisotropy of the interaction, the intermolecular potential was found to be “generally more repulsive at short range and more attractive at long range” than a simpler dipole-atom potential after averaging over all H_2 orientations. In addition, forces for all separation distances “show strong angle dependence with a large contribution from electrostatic interactions”. The depth of the potential well was found to be three times deeper than the dipole–atom system. Qualitatively, these predictions agree with the finding of this work stated in the previous paragraph and should have the same applicability to the H_2O–N_2 system.

The smooth, physically reasonable super-Lorentz behavior we observe can clearly produce the bumpiness seen in the microwindow continuum coefficients (Figures 4.68 and 4.69).

Due to insufficient optical depth in the band wings, the N_2-broadened χ-function was not determined beyond $\sim$100 cm^{-1} of line center. Future work could involve using Burch’s window region measurements in conjunction with this data to extend the χ-function to $\sim$500 cm^{-1} from line center.

4.10.4.2 Self-broadening

The final determination of the self-broadened χ-function is shown in Figure 4.96. Again, Rosenkranz’s and Ma and Tipping’s calculations have been set to 1 at 1 cm^{-1} from line center for these comparisons. Due to unresolved lines and insufficient optical depth, the self-broadened χ-function has been determined to only 15 cm^{-1} from line center. Unlike the N_2-broadening results, the individual fitted χ-functions do not

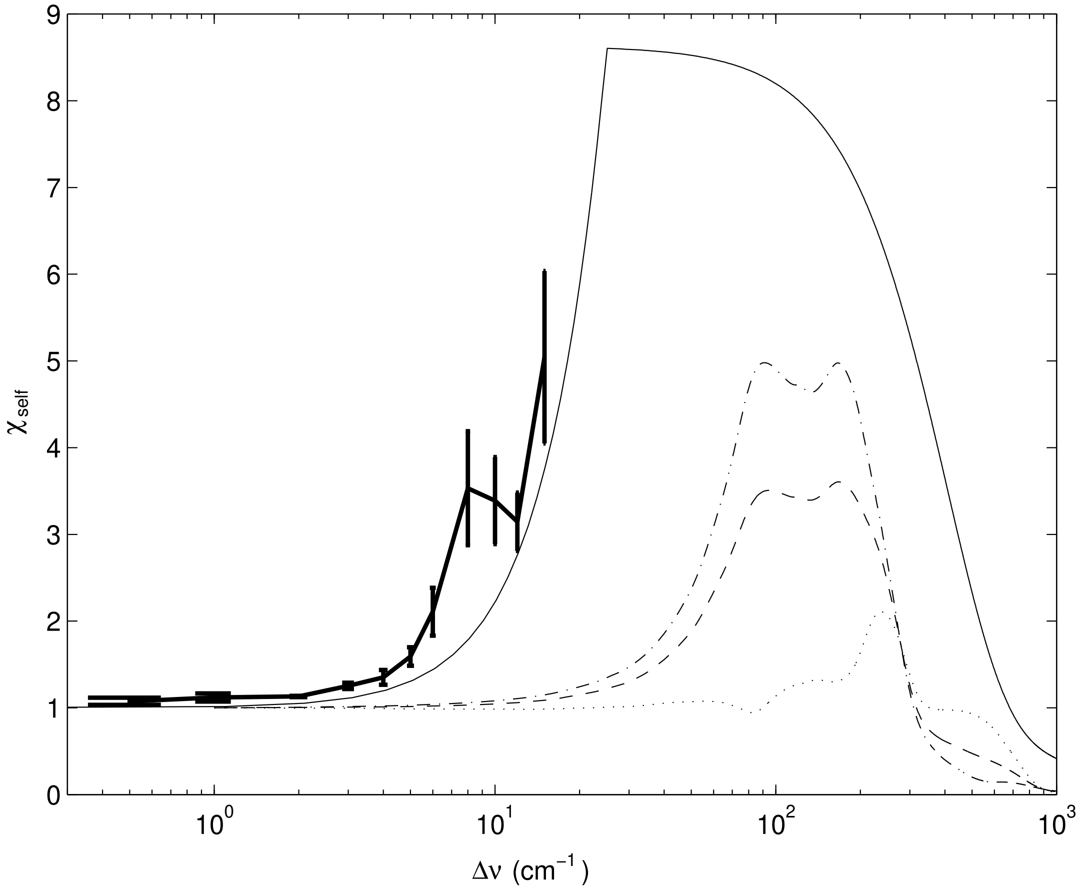

Figure 4.96: Self-broadened χ functions from: this work (solid with error bars), CKDv0 (solid), Rosenkranz (dashed), and Ma and Tipping (dash-dot and dotted).

converge on a final result beyond ~15 cm^{-1} from line center. However, from the results which are available, it is clear that the CKDv0 χ-function and the results of this work are in good agreement. Again, this is expected since both results have been determined from in-band data. Rosenkranz's and Ma and Tipping's calculations do not become significantly super-Lorentz until ~40 cm^{-1} from line center, in contrast to the fitted χ which reaches a value of 2 near 5 cm^{-1} from line center.

4.10.4.3 N_2- versus Self-Broadening

N_2 versus self broadened χ-functions are shown in Figure 4.97. As with the CKDv0

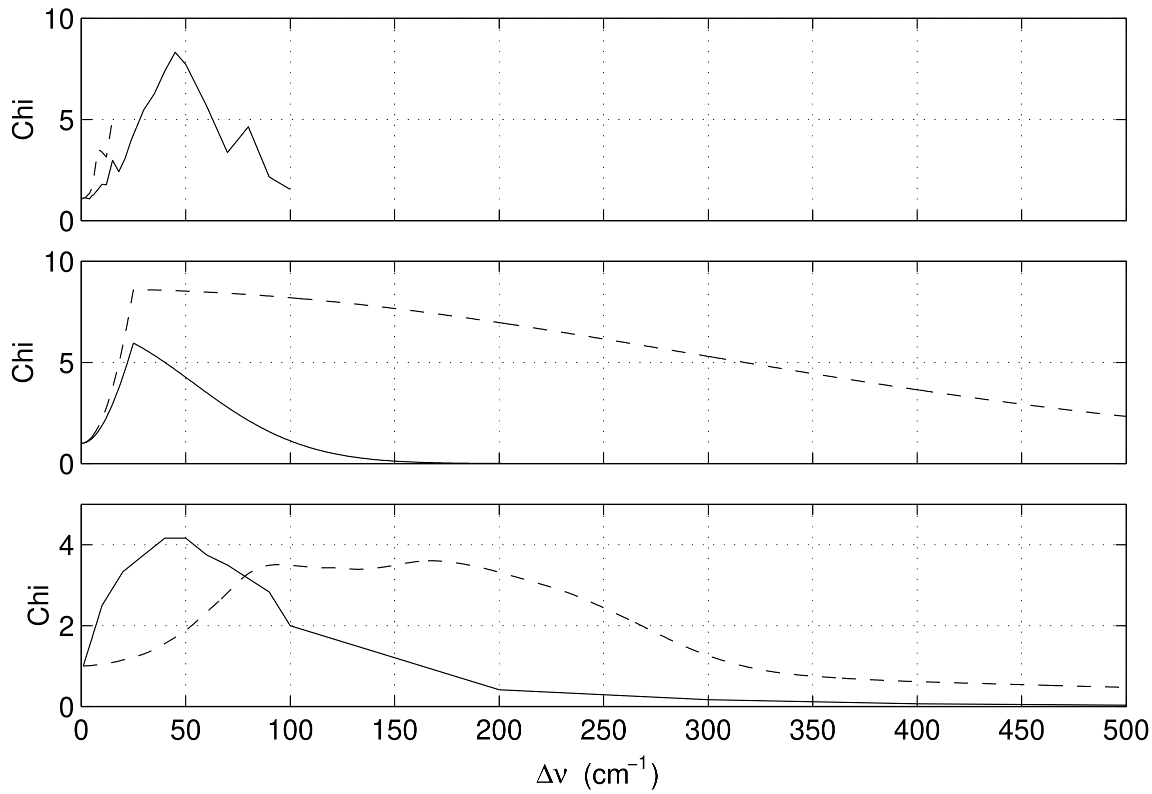

Figure 4.97: Self-(dashed curves) vs. N_2-(solid curves) broadened χ functions from: this work (top panel), CKDv0 (middle panel), and Rosenkranz (bottom panel).

χ-functions, the fitted χ-functions are greater for self-broadening than for N_2-broadening. This is somewhat expected since medium and long range dipole-dipole forces are stronger than dipole-quadrupole forces. Rosenkranz's and Ma and Tippping's results are difficult to compare due to their inaccuracies in the near-wing. Beyond ~ 75 cm^{-1} from line center, however, they also predict the lineshape to be greater for self-broadening than for N_2-broadening.

4.10.5 Parameterization

Using Equation 4.11 to compute absorption coefficients for all displacements from line center and all transitions is too slow computationally for most applications. Two methods for incorporating the results of this section into a faster algorithm while retaining the overall accuracy are proposed. The first parameterization uses a new near-wing local lineshape definition given by $K_{VVH}\chi$ within 25 cm^{-1} of line center along with a standard far-wing plus basement continuum look-up table. In order to obtain smooth continuum coefficients, it may be necessary to extend the local lineshape cuttoff to $\sim$40 cm^{-1}. The main point with this method is that the high frequency components of near-wing super-Lorentz must be included in the local calculation. The second parameterization uses a Lorentz local and a high frequency continuum look-up table which includes the near-wing super-Lorentz behavior and the far-wing components. With this approach, care must be taken when interpolating across the centers of strong absorption lines and to ensure that the far-wing pressure dependencies are valid. Both approaches were used in the line-by-line calculations presented in Section 4.9.

4.11 Summary

Research performed for the “continuum" absorption within the ν_2 band of H_2O has been outlined. Self-, N_2-, and O_2-broadened water vapor transmission spectra were collected using Fourier transform spectrometers and long path absorption cells. High and low optical depth spectra between 1100 and 2200 cm^{-1} were collected at resolutions of 2.00, 0.04, and 0.011 cm^{-1} for a variety of pressures and path lengths. Water vapor pressures of the high optical depth N_2-broadened samples were determined to within 3 to 4% using isolated spectral lines in the band wings.

Low optical depth spectra were used to measure the $H_2^{16}O$ fundamental ν_2 N_2-broadened line widths. Excellent agreement (2,3 %) is found with the measurements of Remedios. These widths are also found to be ~10 % greater than ν_2 $H_2^{18}O$ widths reported by Toth, indicating the first experimental observation of an isotopic width dependence for water vapor.

Self, N_2-, and high pressure N_2-broadened continuum coefficients have been determined from the high optical depth spectra in the microwindows using Clough's local lineshape definition. A full error analysis is presented, including baseline errors, absorber amounts, and line parameter errors. Good agreement is found with the previous laboratory measurements of Burch *et.al.*, except for several points at the band center where our values are greater. For N_2-broadening, our results are also in agreement with the CKDv0 continuum model at band center, with CKDv2.1 in the band wings, and with recent field measurements by the University of Wisconsin and J. M. Theriault in the 1200 cm^{-1} region. These results validate the accuracy of Burch's original measurements but also show that the continuum coefficients are not necessarily smooth as a function of wavenumber due to significant near-wing super-Lorentz lineshape behavior. These results have been incorporated into a line-by-line radiative transfer code and compared to validated atmospheric emission spectra. At the band center, where the results are most accurate, excellent agreement is found.

Using the most accurate line parameters, a systematic ~5-10 % surplus of absorption over Lorentz is observed ~0.5–3 cm^{-1} from line center for nearly all lines examined. This effect is nearly twice as large if Toth's $H_2^{18}O$ widths are used. Based on several types of analysis, we find several pieces of evidence supporting this conclusion. It should be emphasized, however, that this effect could be due, at least partially, to line width errors. An accurate and comprehensive analysis of the ν_2 H_2O line widths must be performed before more definite conclusions can be made.

Self- and N_2-broadened χ-functions have been determined from the spectra in a way such that no functional form for the lineshapes are assumed. For self-broadening, the lineshape is determined to 15 cm^{-1} from line center, while for N_2-broadening, the lineshape is determined to ~100 cm^{-1} from line center. In the near-wing, excellent agreement is found with Clough's χ-functions. Results clearly show that the intermediate N_2-broadened lineshape is extremely super-Lorentz, suggesting that dispersion and/or inductive forces must be addressed for medium range intermolecular separations. These results also show that the near-wing lineshape is more super-Lorentz for self-broadening than for N_2-broadening.

In all, this research has resulted in a better understanding of the in-band ν_2 continuum and in the near and intermediate wing H_2O lineshape.

4.12 Future Work

Listed below are some ideas which compliment this research.

- Obtain more accurate line widths for self-, N_2-, O_2-, and air-broadening, and for temperatures other than room temperature. A more conclusive analysis of the near-wing lineshape can then be performed.

- Test the continuum coefficients and fitted χ-functions with other independent laboratory and/or atmospheric data sets.

- If possible, incorporate the intermolecular potential into the χ-function fits and determine the potential directly.
- Use more sophisticated methods such as regularization to constrain the χ-function fits. Investigate techniques of forcing χ to be smooth without imposing a particular functional form. Also, conduct a more systematic error analysis.
- Determine the relationship between air-, N_2-, and O_2-broadened widths more accurately by measuring identical lines with the same instrument for the different perturbers.
- Once accurate widths are available, process the high optical depth O_2-broadened spectra to obtain continuum coefficients.
- Examine simpler systems such as HF-HF or HF-Ar to study super-Lorentz lineshape behavior.
- Incorporate the results of this work into a line-by-line radiative transfer code.
- Perform a study of a single H_2O absorption line (i.e. the $321 \leftarrow 212$ line at 1464.9 cm^{-1}) using a tunable diode laser. Examine the line width as a function of broadening pressure and verify near-wing super-Lorentz lineshape behavior.
- Examine more validated atmospheric spectra to determine the source of large errors observed at line centers.
- After incorporated into a line-by-line code, determine if new continuum coefficients improve atmospheric humidity profile retrievals.
- We encourage the use of more realistic potentials in future theoretical calculations.

Appendix A

Molecular Spectroscopy of CO_2

In order to understand the line-mixing theory developed in this study, it is useful to review the characteristics of various types of CO_2 absorption bands.

There are two important forms of internal energy which the CO_2 molecule can attain that play a role in the infrared region of the spectrum. These are, in order of increasing energy, rotational and vibrational energy.

A.1 Rotational Energy

CO_2 is a symmetric linear molecule and therefore has no permanent electric dipole moment. Certain modes of vibration, however, can make the electric charge distribution of the molecule asymmetric. This creates a dipole moment which allows for a strong coupling between an external electric field and the molecule, therefore allowing for radiative rotational-vibrational transitions. This vibration has corresponding energies which are much greater than the rotational energies and the two can be treated, to a large degree, as independent.

The rotational energies of a rigid, linear tri-atomic molecule such as CO_2 are given by

$$E_{rot}(J) = \frac{h^2}{8\pi^2 cI} J(J+1) = BJ(J+1) \tag{A.1}$$

where J can have integer values of 0,1,2,... B is the rotational constant and equals $\frac{h^2}{8\pi^2 cI}$, I, being the moment of inertia. h is Planck's constant and c is the speed of light.

In reality, the CO_2 molecule is not a rigid rotor, but experiences a very small stretching of the C=O bonds during rotation. This is due to the centrifugal forces which increase with increasing angular frequency. This effect causes a slight change in the moment of inertia and therefore distorts the rigid rotor energy levels. The energy levels of such a non-rigid rotor are

$$E_{rot}(J) = BJ(J+1) - D[J(J+1)]^2 \tag{A.2}$$

where $D \simeq \frac{4B^3}{\omega^2}$. Thus, D has an extremely small value and deviations from the rigid rotor approximation are found only at high J values.

Because these rotational transitions can accompany a vibrational transition as well, the moment of inertia is slightly dependent upon what mode of vibration the molecule is in. For this reason, B and D are dependent on the vibrational mode and the rotational energy expression must be written as

$$E_{rot}(J) = B_\nu J(J+1) - D_\nu[J(J+1)]^2 \tag{A.3}$$

Internuclear Distance	r(C=O)	1.1615 A(equilibrium)
Force Constants	k(ν_1)	16.8×10^5 dynes/cm
	k(ν_3)	14.2×10^5 dynes/cm
Masses	Mass (^{12}C)	12.011 amu
	Mass (^{16}O)	15.999 amu
Moment of Inertia	I(equilibrium)	71.67×10^{-40} g cm^2.
Rotational Constant	B(equilibrium)	0.3906 cm^{-1}

Table A.1: Some basic physical constants of CO_2

A.2 Vibrational Energy

The C=O bonds are not of a fixed length, but can be stretched and compressed slightly. O=C=O angle bending vibrations can also occur leading to deviations from a linear inter-nuclear axis. CO_2 is a symmetric linear triatomic molecule and therefore has four (3N-5) distinct orthogonal modes of vibration, represented by ν_1, ν_{2a}, ν_{2b}, and ν_3. The fundamental vibration wavenumbers of ν_1, ν_2, and ν_3 are 1388, 667, and 2349 cm^{-1}, respectively. ν_1 is a symmetric stretch and causes no change in the dipole moment and therefore can not produce radiative transitions by itself. ν_{2a} and ν_{2b} are degenerate bends. They represent the same kind of motion but are orthogonal because they act in perpendicular planes. They both produce a changing dipole moment and are therefore infrared "active". ν_3 is the asymmetric stretch and is also infrared "active". These vibrational modes are illustrated in Figure A.1.

Vibration spectra can be understood qualitatively assuming harmonic forces. Solving the time independent Schroedinger equation, the energy eigenvalues of this system are given by

$$E_\upsilon = h\nu_i(\upsilon + \frac{1}{2}) \tag{A.4}$$

where ν_i is the resonant frequency of any of the four vibrational modes and υ is the vibrational quantum number which can have integer values of 0,1,2 .... Classically, the fundamental frequencies, ν_i, can be calculated with $\nu_i = \frac{1}{2\pi}(\frac{k_i}{\mu})^{1/2}$, where μ is the reduced mass of the molecule.

More than one vibrational mode can be active at a given time. Neglecting any small interactions between the different vibrations, the total energy of vibration is given by

$$E_{\upsilon_1,\upsilon_2,\upsilon_3} = h\nu_1(\upsilon_1 + \frac{1}{2}) + h\nu_2(\upsilon_2 + \frac{1}{2}) + h\nu_3(\upsilon_3 + \frac{1}{2}) \tag{A.5}$$

The selection rule governing such transitions from one energy level to another is given by

$$\Delta\upsilon_i = \pm 1 \tag{A.6}$$

A vibrational transition is represented with the notation $v_1 v_2 \ell v_3 r \leftarrow v_1 v_2 \ell v_3 r$. The primed quantum numbers on the left correspond to the final state of the system and the ones on the right with the initial state. ℓ is the vibrational angular momentum quantum number (discussed later) and r is the Fermi resonating index. Fermi resonance occurs when a combination of vibrational modes have a resonant frequency very close to another mode and the states mix. Transitions which involve initial quantum numbers which are equal to zero are called fundamental bands, while those which involve excitations from states other than ν_1, ν_2, $\nu_3 = 0$ are called hot bands. For example, a transition from one quanta of ν_1 and one quanta of ν_3 to zero quanta of ν_1 and two quanta of ν_3 is represented as $00020 \leftarrow 10010$.

The calculation of these vibrational energy levels rests upon the assumption that the displacements are very small and therefore the quadratic terms of the potential energy are the only ones which need to be considered. We will use energy level values determined experimentally in this work and need not consider non rigid-rotor, non-harmonic terms in the energy level expressions any further.

A.3 Rotation-Vibration Interaction

So far, the rotation and vibration wavefunctions have been treated as totally independent. Because rotational energies are much smaller than vibrational energies, this is a very good approximation. Using the Born-Oppenheimer approximation, if the degrees of freedom of a wavefunction can be assumed to have little or no interaction, then the wavefunction can be broken up into a product of individual wavefunctions by a separation of variables. Since our wavefunction is a function of both rotational and vibrational motion and they are to a large degree independent, we can use the Born-Oppenheimer approximation. If Ψ_{tot}, Ψ_{rot}, and Ψ_{vib} are the total, rotational, and vibrational wavefunctions then we can assume that $\Psi_{tot} = \Psi_{rot}\Psi_{vib}$. As a result, the total energy of a molecule which is both rotating and vibrating is simply given by

$$E_{tot} = E_{rot} + E_{vib} \tag{A.7}$$

There are, however, some interactions which occur when a molecule is rotating while it is also vibrating. As shown earlier, the ν_1 and ν_3 vibrations involve displacements of nuclei which occur along the molecule's O=C=O linear axis. The ν_2 motion, however, involves displacements perpendicular to this axis. This perpendicular motion produces angular momentum about the O=C=O axis, called vibrational angular momentum. It is quantized and has a magnitude of $\ell\hbar$, where ℓ is the vibrational angular momentum quantum number. This adds to the total angular momentum, and if the molecule is also rotating, the rotational energy is given by

$$E_{rot}(J) = B_v[J(J+1) - \ell^2] - D_v[J(J+1) - \ell^2]^2 \tag{A.8}$$

which is doubly degenerate for $\ell = 1, 2, ...$. An important consequence of this vibrational angular momentum is that transitions which involve ν_2 are allowed to have ΔJ=0 rotational transitions. When a transition involves a change in υ_2, there is also a change in the molecule's vibrational angular momentum. Therefore, even when there is no change in the rotational angular momentum, there is still a change in the molecule's total angular momentum when there is a change in υ_2. Thus, a ΔJ=0 rotational transition, which also involves a change in υ_2, is allowed.

Vibrations involving zero quanta of ν_2, called Σ levels, have ℓ=0 and no vibrational angular momentum. Π levels have ℓ=1 and therefore have one quanta of angular momentum even when the molecule is not "rotating". The Π levels, therefore, do not have J=0 rotational energy levels. Similarly, Δ levels, which have ℓ=2, have neither the J=0 or J=1 rotational levels.

Doubly degenerate vibrational angular momentum states are formed from combinations of the degenerate ν_{2a} and ν_{2b} bending modes. This degeneracy is lifted, however, by the presence of Coriolis forces. If the motion of a particle is referred to in a uniformly rotating coordinate system, apart from the external forces, two additional accelerations appear. These are the centrifugal acceleration and the Coriolis acceleration. The centrifugal acceleration has already been dealt with and results in the D_ν terms of the rotational energy. The Coriolis force is given by

$$\vec{F}_{Coriolis} = 2m\vec{v} \times \vec{\omega} = 2m\nu\omega \sin\phi \tag{A.9}$$

where m is the mass of the nuclei , $\vec{v}$ is its velocity in the rotating reference frame, and ω is the frequency of rotation of that reference frame. ϕ is the angle between the axis of rotation and $\vec{v}$. Applying this force to a molecule which is rotating and also vibrating in mode ν_{2a}, we see that $\vec{v} \perp \vec{\omega}$ and $\vec{F}_{Coriolis} = 2m\nu\omega$. But for ν_{2b}, $\vec{v} \parallel \vec{\omega}$ and $\vec{F}_{Coriolis} = 0$. These forces are depicted in Figure A.2. This results in a small change in the moment of inertia for a molecule vibrating with ν_{2a} and its energies will therefore be slightly different from that of ν_{2b}. This splitting of the energy levels is called ℓ-type doubling.

A.4 Symmetry Requirements

Because of quantum mechanical symmetry requirements, not all energy levels of CO_2 are permitted. This is a result of Bose-Einstein statistics, which states that if a molecule is made up of two or more particles which are bosons, then their wavefunction should remain unchanged upon simultaneous exchange of those particles. This implies that the wavefunction should always be symmetric.

For the case of CO_2, exchange of the two oxygen atoms, which have spin=1 and are thus bosons, should produce an unchanged wavefunction, Ψ. This implies that the combination of the rotational and vibrational wavefunctions, Ψ_{rot} and Ψ_{vib}, must always combine to form a symmetric wavefunction. Therefore, if Ψ_{rot} is symmetric then Ψ_{vib} must also be symmetric. Similarly, if Ψ_{rot} is asymmetric then Ψ_{vib} must also be asymmetric.

The symmetry of rotational wavefunctions are determined by their J value: Ψ_{rot} is symmetric for even J and asymmetric for odd J. For molecules with a quanta of ν_2, ℓ-type doubling, as stated earlier, results in two vibrational levels for each J value, one level being symmetric and the other asymmetric, denoted by e and f respectively.

The result of these symmetry requirements is to eliminate some of the energy levels. For instance, a level which has a symmetric vibrational wavefunction and ℓ=0 will have only even J rotational levels. Likewise, an asymmetrical vibrational level with ℓ=0 will have only odd J rotational levels. A vibrational level with $\ell \neq 0$, however, will have both even and odd J rotational levels due to ℓ type doubling.

A.5 Parallel bands and P- and R-branches

A vibrational transition is usually accompanied by a group of rotational transitions as well. The superposition of many rotational spectral lines centered about a vibrational transition frequency is called a band. All of the CO_2 bands between 500 and 2500 cm^{-1} are shown in Figure A.3. Bands which do not involve a quanta of ν_2 are called parallel bands because the electric dipole oscillates parallel to the molecule's linear axis. The selection rules for such bands are

$$\Delta J = \pm 1 \quad \text{and} \quad \Delta \upsilon = \pm 1$$

The group of transitions which have ΔJ=+1 form a group of spectral lines called an R-branch and those with ΔJ=-1 form a P-branch. Because P-branch transitions involve a decrease in the molecule's rotational frequency by one quanta, the molecule experiences a smaller centrifugal force and its moment of inertia therefore decreases. This results in the spacing between adjacent P-branch lines getting larger as J increases. On the other hand, the moment of inertia increases for R-branch lines and they, as a result, get closer together as J increases. This effect can be so strong that the R-branch lines can in fact "turn-around" at high values of J and form what is known as a band-head. One particular example of this is the fundamental ν_3 with a band-head located at ~2397 cm^{-1} for $J \sim 108$. A typical parallel band exhibiting these characteristics is shown in Figure A.4 for the 00011 ← 00001 transition.

A.6 Perpendicular Bands and Q-branches

Bands which involve ν_2 are called perpendicular bands because the motion of the electric dipole moment is perpendicular to the molecule's linear axis. The selection rules for these bands are

$$\Delta J = 0, \pm 1 \quad \text{and} \quad \Delta \upsilon = \pm 1 \tag{A.10}$$

The ΔJ=+1 transitions form an R-branch and the ΔJ =-1 transitions form a P-branch. The transitions for ΔJ=0 is called a Q-branch. The spectral lines of a Q-branch are very close together because they involve no change in rotational energy (neglecting rotation due to vibrational angular momentum). The only factor which keeps all of these lines from being positioned at the vibrational transition frequency is the fact that the molecule's moment of inertia is slightly different between the initial and final vibrations. Thus the spacing between adjacent Q-branch lines in the rigid rotor approximation is directly proportional to this change in the moment of inertia:

$$\nu(J+1) - \nu(J) = \Delta B(2J+2) = (B_{final} - B_{initial})(2J+2) \tag{A.11}$$

Even at low pressures, these lines combine to form what looks like one very strong line since ΔB is generally very small. A typical spectrum of a perpendicular band is shown in Figure A.5 for the 10001 ← 01101 transition centered at 720 cm^{-1}. The energy levels and transitions of various bands are shown in Figures A.6 and A.7 for reference. Low pressure spectra of their Q-branches are also shown in Figures A.8 and A.9.

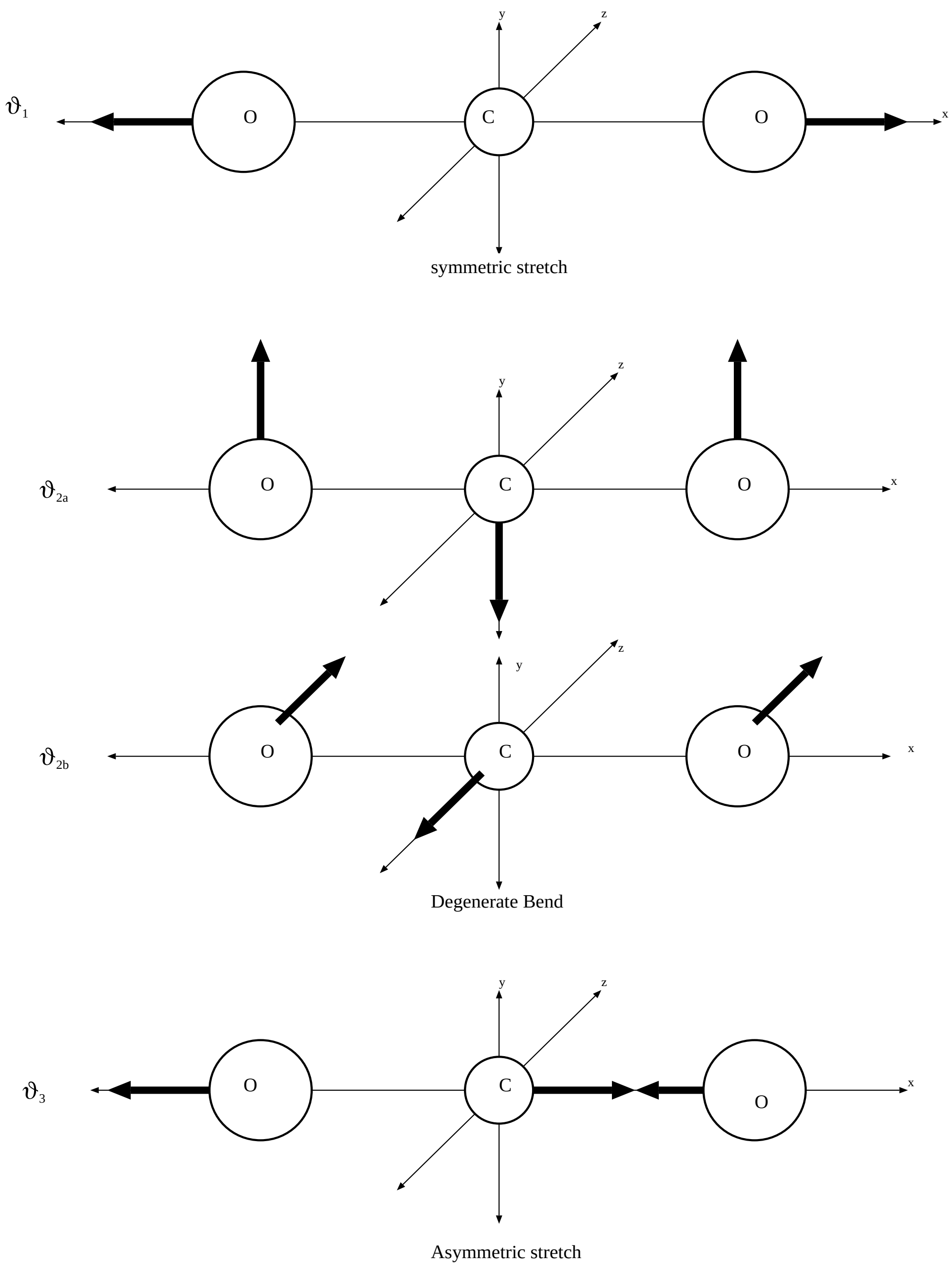

Figure A.1: The four vibrational modes of CO_2. ν_1 is the symmetric stretch ($\sim$1337 cm^{-1}). ν_{2a} and ν_{2b} (667 cm^{-1})are the two degenerate bends, and ν_3 (2349 cm^{-1}) is the asymmetric stretch. The bold arrows represent the displacement of the atoms from their equilibrium positions.

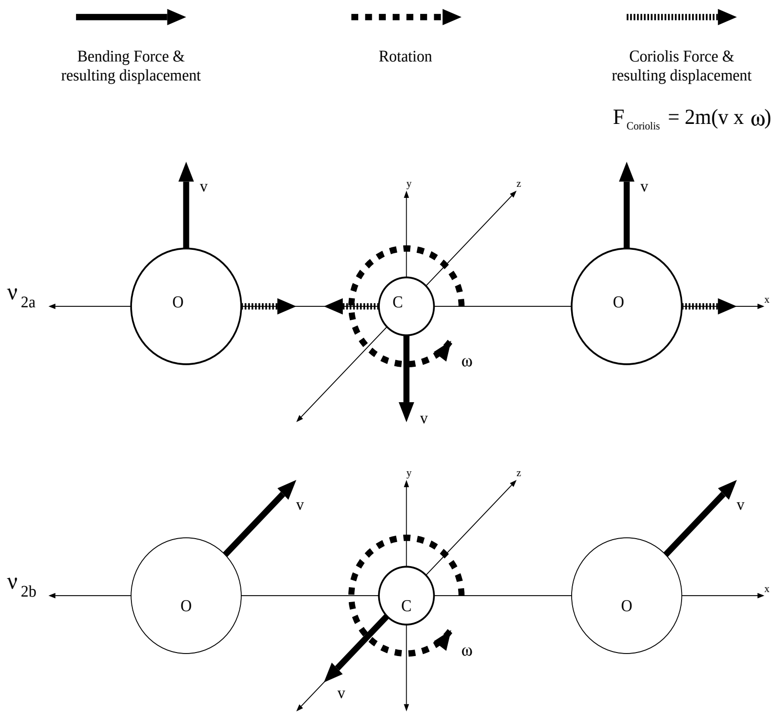

Figure A.2: ℓ-type doubling in the degenerate bends, ν_{2a} and ν_{2b}. For ν_{2a}, the axis of rotation is perpendicular to the motion of the nuclei and the Coriolis force is non-zero. For, ν_{2b}, the axis of rotation is parallel to the motion of the nuclei and the Coriolis force is zero. This results in a change of the moment of inertia for ν_{2a}, but not for ν_{2b}, and a splitting of their energy levels.

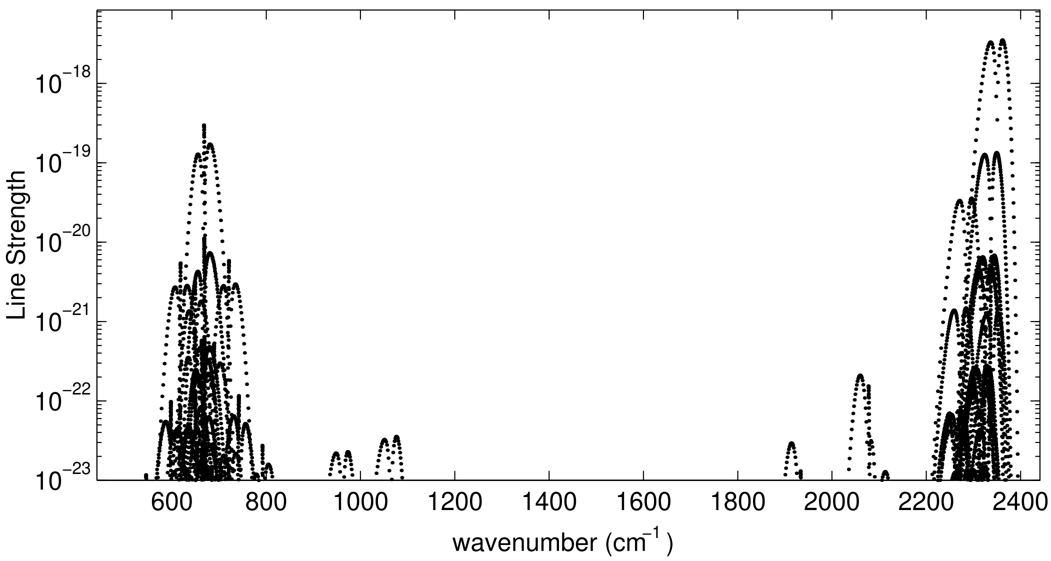

Figure A.3: CO_2 spectral lines for the entire mid-infrared region.

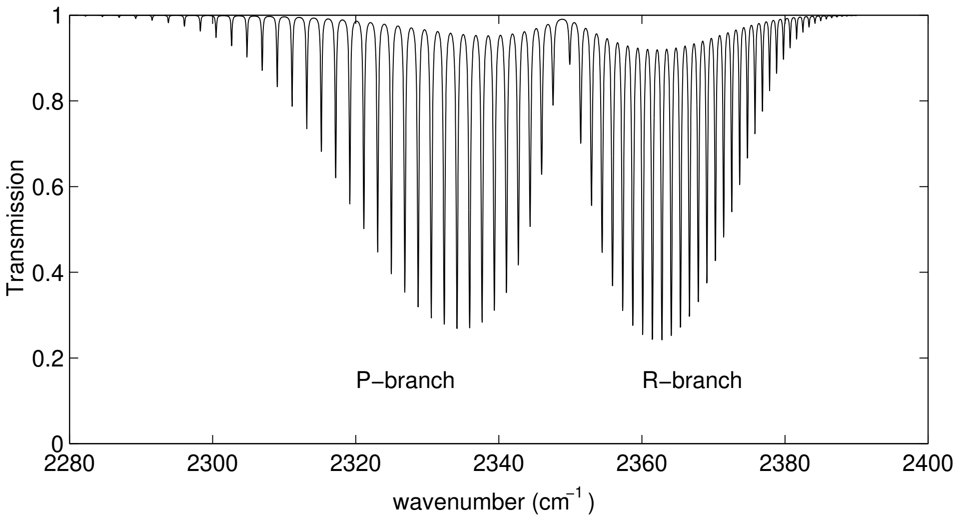

Figure A.4: A typical parallel band: the 00011 ← 00001 transition. This is the fundamental ν_3 transition centered at 2349 cm^{-1}. The overall shape of the P and R-branches is due to the degeneracy and statistical population of each level. Stretching of the O=C bonds due to centrifugal forces at high values of J causes the R-branch lines to get closer together and the P-branch lines to get further apart.

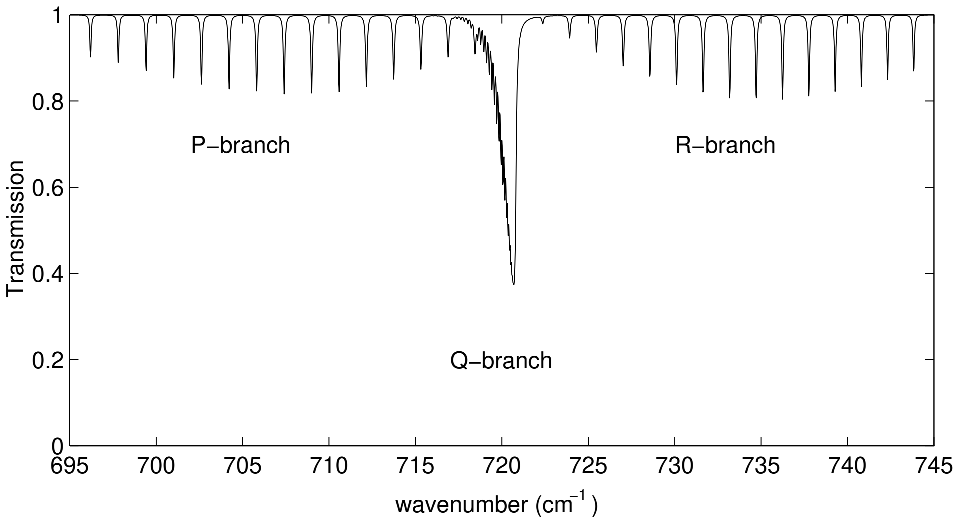

Figure A.5: A typical perpendicular band: the 10001 ← 01101 transition. The P and R-branches are similar to those of a parallel band. The Q-branch is positioned at the vibrational frequency of 720 cm^{-1} and is not just one spectral line, but many positioned right next to each other. The degeneracy of the Q-branch lines is lifted due to a change in the rotational constant between the initial and final vibrations.

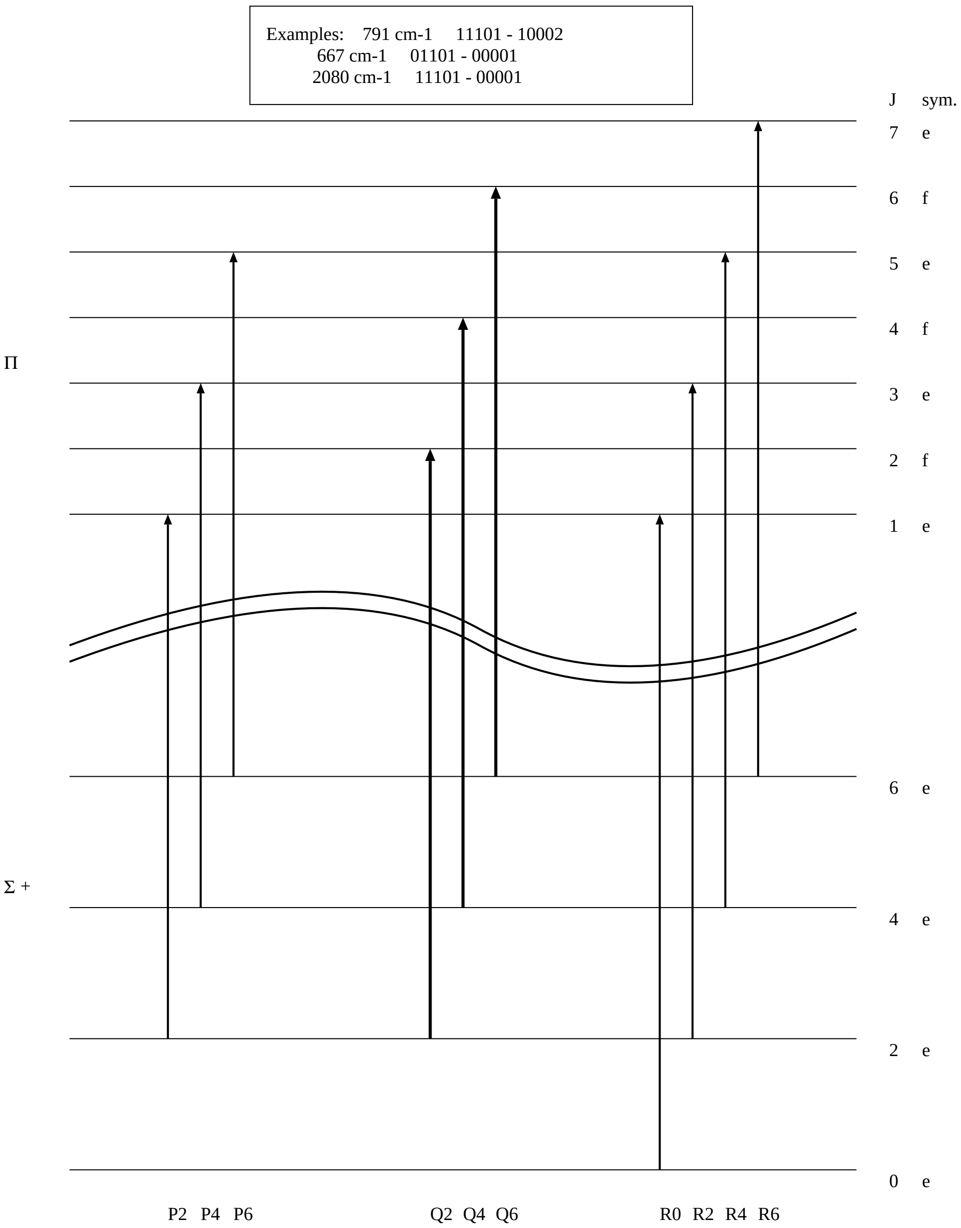

Figure A.6: The energy levels and transitions of a $\Pi \leftarrow \Sigma$ transition. In the Σ state, there is no vibrational angular momentum (ℓ =0) and therefore no ℓ-type doubling. The vibrational wavefunction is symmetric so the only remaining rotational energy levels are those of even J values. In the Π state, ℓ=1, resulting in ℓ -type doubling. Because the vibrational wavefunction is asymmetric, every symmetric ℓ-type doubled level does not exist, leaving one rotational level for each J value. Note that there is no J=0 level because ℓ=1.

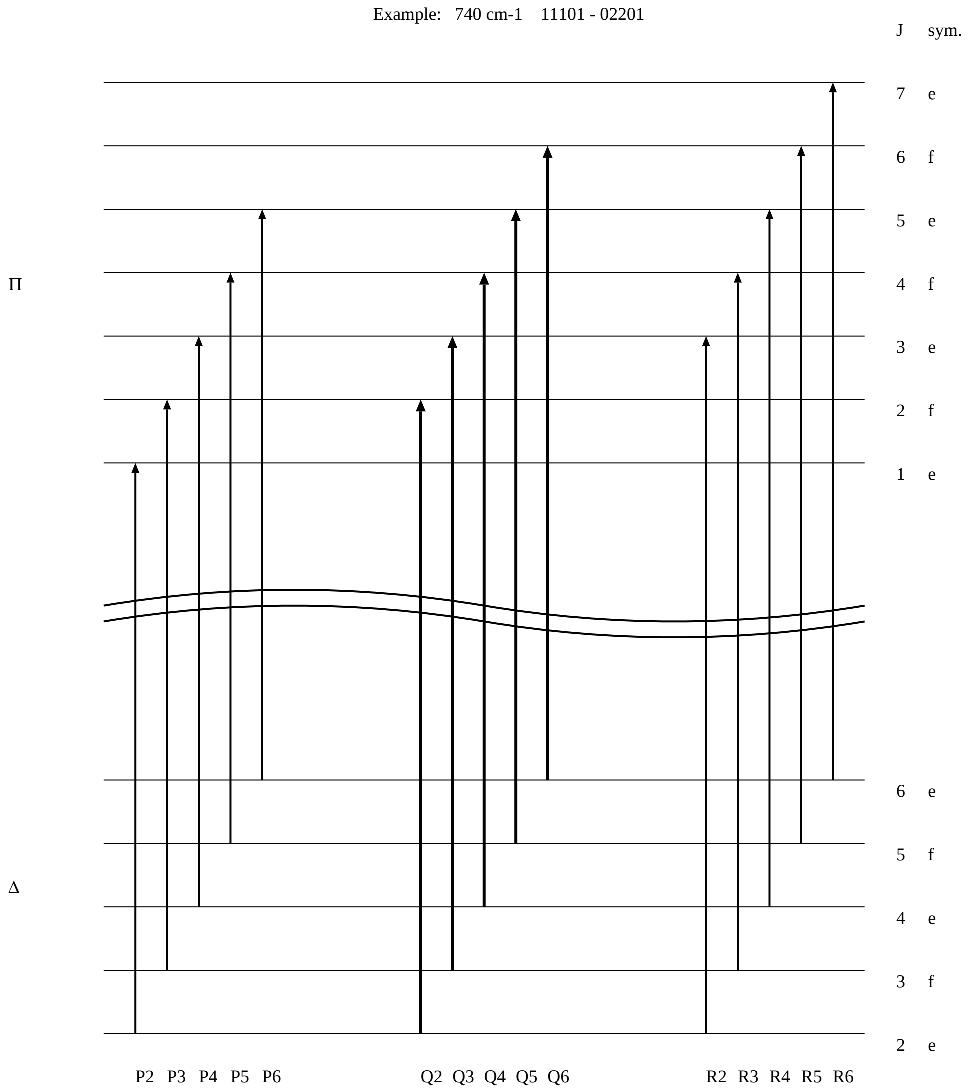

Figure A.7: The energy levels and transitions of a $\Pi \leftarrow \Delta$ transition. In both the Π and Δ states, $\ell \neq 0$, and therefore ℓ-type doubling occurs, resulting in a rotational level for each J value. For the Δ state, the J=0 and J=1 levels are missing because ℓ=2. In the Π state, ℓ=1 and the J=0 level is missing. All of the even J Q-branch transitions end in Π_f levels while all of the odd J transitions end in Π_e levels, resulting in a more complex line structure than for $\Pi \leftarrow \Sigma$ bands.

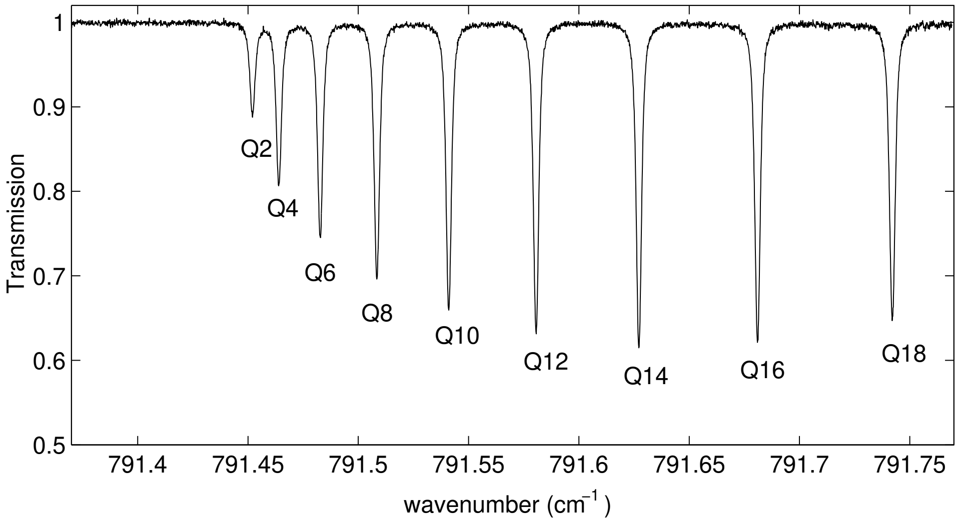

Figure A.8: A low pressure spectrum of the 791 cm^{-1} $\Pi \leftarrow \Sigma$ Q-branch. P(CO_2)=5 Torr, path length=4.17 m, T=294.5 K. The spectrum was measured with a tunable diode laser spectrometer at UMBC.

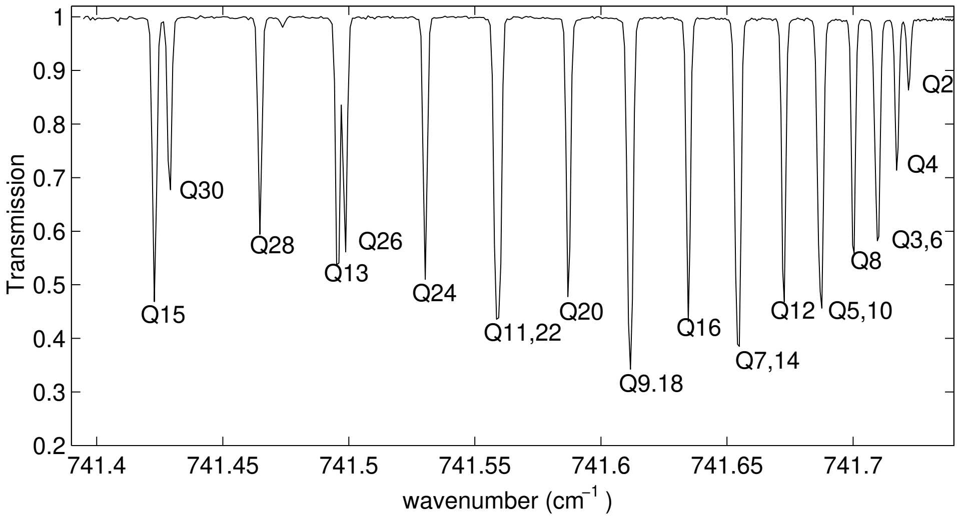

Figure A.9: A low pressure spectrum of the 741 cm^{-1} $\Pi \leftarrow \Delta$ Q-branch measured with a tunable diode laser at UMBC. P(CO_2)=0.33 Torr, path length=12.17 m, T=296 K. Unlike a $\Pi \leftarrow \Sigma$ Q-branch, $\Pi \leftarrow \Delta$ Q-branches consist of both even and odd J lines. The odd J lines show extreme overlap with every other even J line. (i.e. Q_3 overlaps Q_6, Q_5 overlaps Q_{10}, Q_7 overlaps Q_{14}, etc.)

Appendix B

Line-mixing in CO_2 Q-branches

This appendix is a review of line-mixing theory developed previously for CO_2 Q-branches [33]. Sections B.1 and B.2 describe the model as applied to $\Pi \leftarrow \Sigma$ and $\Pi \leftarrow \Delta$ bands, respectively. Section B.3 then describes the physical implications of the model.

B.1 Line-mixing in $\Pi \leftarrow \Sigma$ Q-branches

In order to calculate the line mixing absorption coefficient, the relaxation matrix, **W**, must first be evaluated. As described previously, this is accomplished by equating the linewidths as a function of J to the sum of all relaxation rates, $K_{j'j}$, which limit the lifetime of a transition via non-linear least-square fits to the known line-widths. In this manner, the free parameters a_1, a_2, and a_3 of $K_{j'j}$ are determined and the off diagonal elements of **W** can be evaluated. For the Q-branch of a $\Pi \leftarrow \Sigma$ vibrational transition, the diagonal elements of **W** are given by

$$W_{jj} \equiv \gamma_{Qj} = -\frac{1}{2}\left(\sum_{j'\neq j}^{even} K^{\Sigma}_{j'j} + \sum_{j'\neq j}^{all} K^{\Pi}_{j'j}\right) \tag{B.1}$$

Here, $K^{\Sigma}_{j'j}$ are the collisional relaxation rates of the Σ (ℓ=0) vibrational level and $K^{\Pi}_{j'j}$ are of the Π (ℓ=1) level. Due to nuclear symmetry requirements, the odd rotational levels of the Σ level are missing and the sum over $K^{\Sigma}_{j'j}$ therefore includes only states of even

j'. The sum in the Π level includes all values of j' except for the missing j'=0 level. These relaxation rates are illustrated in Figure B.1.

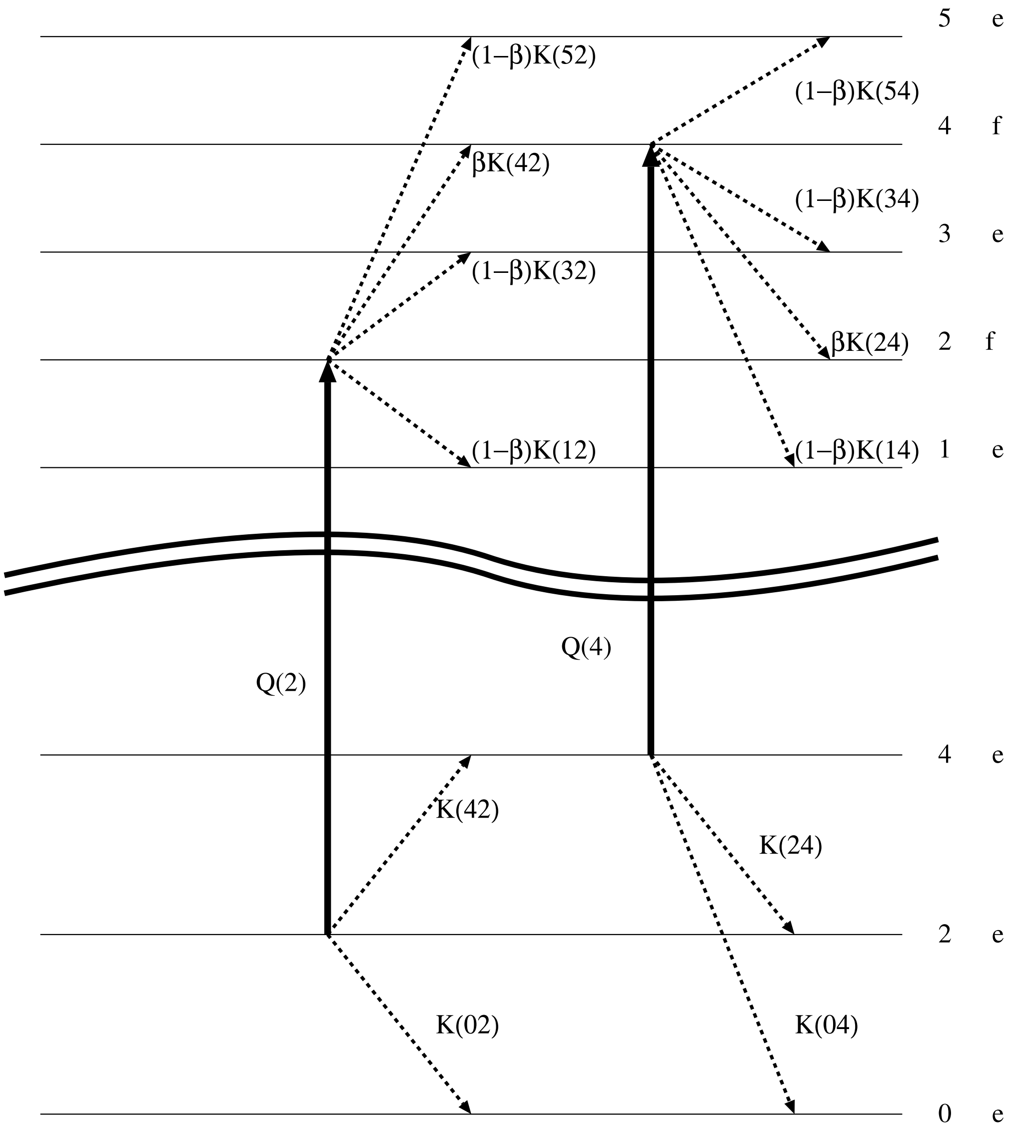

Figure B.1: Rotational relaxation rates, $K_{j'j}$, for several Q-branch lines of a $\Sigma \leftarrow \Pi$ transition. In our line-mixing model, Π rates connecting rotational levels of similar parity are multiplied by β and rates connecting levels of opposite parity are multiplied by $(1-\beta)$.

It is assumed that the total relaxation rate out of all rotational levels is the same for both upper and lower vibrational states. This is valid because the linewidths are independent of the vibrational levels involved in the transition. Since there are only half as many rotational levels in the Σ state as in the Π state, this assumption can only be satisfied if $\sum_{j'\neq j}^{even} K^{\Sigma}_{j'j} \approx 0.5 \sum_{j'\neq j}^{all} K^{\Pi}_{j'j}$. We also assume that the relaxation rates have the same functional form for K^{Σ} and K^{Π}. Taking these effects into account, Equation B.1 is re-written as

$$W_{jj} \equiv \gamma_{Qj} = -\frac{1}{2}\left(\sum_{j'\neq j}^{even} K^{\Sigma}_{j'j} + \frac{1}{2}\sum_{j'\neq j}^{all} K^{\Pi}_{j'j}\right) \tag{B.2}$$

Therefore, the *effective* individual relaxation rates out of Σ state J-levels are roughly twice as large as the corresponding rates in the Π state. For example, $K^{\Pi}_{42} \approx \frac{1}{2}K^{\Sigma}_{42}$. Line mixing can only occur if collisions couple the interacting spectral lines in both the upper and lower vibrational states. For example, in order for intensity to transfer from Q(4) to Q(2), collisions must couple the J=4 and J=2 rotational states in both the Σ and Π levels. The corresponding relaxation rates for these collisions are K^{Σ}_{24} and K^{Π}_{24}. To determine the off-diagonal elements of **W**, it is assumed that the amount of line mixing will be limited by the lesser of these two rates, and the off-diagonal elements of **W** are given by

$$W_{j'j} = -\frac{1}{2}K_{j'j} \tag{B.3}$$

Using Equations B.2 and B.3, the relaxation matrix and the line mixing absorption coefficient, $k_{mix}(\nu)$ can be calculated. Although these calculations provide a significant improvement over the Lorentz model, residual errors remain at the center of the Q-branches indicating that this model predicts too much mixing, especially for N_2-broadening.

To further improve this model, a β factor was introduced by Strow and Edwards [29] to differentiate between the collisional relaxation rates which connect states of similar and opposite rotational symmetry. With the β factor included, Equation B.2 becomes

$$W_{jj} \equiv \gamma_{Qj} = -\frac{1}{2}\left(\sum_{j'\neq j}^{even} K^{\Sigma(e\leftarrow e)}_{j'j}\right) - \frac{1}{2}\left(\sum_{j'\neq j}^{even} \beta K^{\Pi(f\leftarrow f)}_{j'j} + \sum_{j'\neq j}^{odd}(1-\beta)K^{\Pi(e\leftarrow f)}_{j'j}\right) \tag{B.4}$$

The superscript on $K_{j'j}$ now also denotes the symmetry of the levels involved. In the Π vibrational level, the relaxation rates have been divided into two groups. Those which connect rotational levels of similar symmetry are multiplied by β and those which connect levels of opposite symmetry are multiplied by $(1-\beta)$. The β factor is not needed in the Σ state simply because the odd rotational levels do not exist there. Therefore, *the effective β factor in the Σ state is 1*.

The amount of mixing between spectral lines is determined by the off-diagonal elements of **W**. Coupling collisions must occur in both upper and lower vibrational states during the transition for mixing to occur. For this band, this corresponds to relaxation rates of $K_{j'j}^{\Sigma(e\leftarrow e)}$ and $\beta K_{j'j}^{\Pi(f\leftarrow f)}$. As before, the off-diagonal elements of **W** are therefore equated to the lesser of them,

$$W_{j'j} = -\beta K_{j'j} \tag{B.5}$$

Note that for $\beta = \frac{1}{2}$, Equations B.4 and B.5 reduce to Equations B.2 and B.3. Introducing β can therefore be seen as a special case of the models presented earlier.

Since the relaxation matrix, **W**, represents the ensemble averaged interaction, an exact physical meaning for β is difficult to prescribe. However, β can be thought of as the relative probability of the occurrence of $(f \leftarrow f)$ collisions to that of $(e \leftarrow f)$ collisions. β satisfies the relation $0 \le \beta \le 1$.

Calculations for several $\Pi \leftarrow \Sigma$ Q-branches using this model have been performed by finding the optimum value of β (via non-linear least-square fits to observed spectra) which reduces the difference between the experimental and calculated transmission. The fitted values for β are different for self broadened CO_2 and N_2 broadened CO_2. For self broadened CO_2, using $\beta = \sim 0.5$ yields the best results. For CO_2 broadened with N_2, however, the best value for β was found to be ~ 0.61. For pure CO_2, since β was found to be 0.5, these results are very similar to those found without the β factor, with a maximum error in transmission of $\sim$ 1% for the experimental spectra studied. For N_2 broadened CO_2, the introduction of β reduced the maximum error in transmission from $\sim$ 3% to $\sim$ 1%. For this reason, the introduction of β is justified.

These results imply that $(e \leftarrow f)$ and $(f \leftarrow f)$ collisions are equally likely for CO_2-CO_2 interactions, at least averaged over lines that are dominant for room temperature spectra. However, for CO_2-N_2 interactions, the value of $\beta \sim 0.61$ implies that $(f \leftarrow f)$ collisions are more probable than $(e \leftarrow f)$ collisions.

B.2 Line-mixing in the $\Pi \leftarrow \Delta$ 740 cm^{-1} Q-branch

Line mixing for the 740 cm^{-1} $\Pi \leftarrow \Delta$ Q-branch has been calculated previously [31, 33] using methods similar to that of the $\Pi \leftarrow \Sigma$ bands discussed above. In this method, the relaxation rates are determined by

$$W_{jj} \equiv \gamma_{Qj} = -\frac{1}{2}\left(\frac{1}{2}\sum_{j' \neq j}^{all} K^{\Delta}_{j'j} + \frac{1}{2}\sum_{j' \neq j}^{all} K^{\Pi}_{j'j}\right) \tag{B.6}$$

where the sums are taken over all rotational levels (except for the missing $J = 0$ level of the Π state and the missing $J = 0$ and 1 levels of the Δ state).The off-diagonal elements of $\mathbf{W}$ are taken to be

$$W_{j'j} = -\frac{1}{2}K_{j'j} \tag{B.7}$$

The energy levels and relaxation rates for a $\Pi \leftarrow \Delta$ band are shown in Figure B.2. Again, although this model made significant improvements over Lorentz, it did not fully reproduce the observed spectra. This method over-estimated the amount of mixing by roughly a factor of two. It was speculated [31] that no mixing occurred between lines of similar symmetry, thereby using only half of the possible relaxation rates. Reducing the mixing by a factor of two can also be accomplished by simply dividing the off-diagonal elements of $\mathbf{W}$ by two. e.g. $W_{j'j} = -\frac{1}{4}K_{j'j}$. Although using this ad-hoc value of $\frac{1}{2}$ greatly improved the agreement with observed spectra, a reason for the factor of two was unknown [31].

Recent calculations [59] have also been performed for this band by using a model which does not allow line mixing to occur between spectral lines of opposite symmetry.

That is, line mixing was only allowed for even ΔJ collisional transitions. This has the overall effect of reducing the amount of mixing by a factor of two. This method was used for both nitrogen and self broadened CO_2. These calculations used Equations B.6 and B.7, but with the even-odd and odd-even elements of $\mathbf{W}$ set to zero. As expected, these results are similar to those where the factor of $\frac{1}{2}$ has been introduced. It should be pointed out however, that there is no justification for strictly forbidding line mixing between spectral lines which couple states of opposite rotational symmetry.

As for $\Sigma \leftarrow \Pi$ bands, the β factor was used [33] to improve the accuracy of the model. $\Pi \leftarrow \Delta$ bands differ from $\Pi \leftarrow \Sigma$ bands in that the lower vibrational level contains both even and odd rotational levels. The Δ level has two quanta of vibrational angular momentum ($\ell = 2$) and the rotational levels therefore experience ℓ-type doubling. Just as for the Π band, however, only one energy level is permitted for each J value due to nuclear symmetry requirements.

The method used to compute the diagonal elements of $\mathbf{W}$ followed the approach used for the $\Pi \leftarrow \Sigma$ bands, except the fact that both vibrational levels contain both even and odd rotational levels is taken into account. First, it was assumed that the same β factor can be used in both vibrational levels. This assumption implies that the magnitude of the vibrational angular momentum does not affect the symmetry properties of inelastic collisions. These factors lead to the following expression for the Q-branch line widths.

$$W_{jj} \equiv \gamma_{Qj} = -\frac{1}{2}\left(\sum_{j' \neq j} \beta K_{j'j}^{\Delta(e,f\leftarrow e,f)} + \sum_{j' \neq j}(1-\beta) K_{j'j}^{\Delta(e,f\leftarrow f,e)}\right) - \frac{1}{2}\left(\sum_{j' \neq j} \beta K_{j'j}^{\Pi(e,f\leftarrow e,f)} + \sum_{j' \neq j}(1-\beta) K_{j'j}^{\Pi(e,f\leftarrow f,e)}\right) \quad \text{(B.8)}$$

The sums in the Δ state include all j' except the missing j'=0 and j'=1 levels. The sum in the Π state includes all values except the missing j'=0 level. Note that Q-branch lines exist for all levels (except J=0,1), not just for even J as is the case for $\Pi \leftarrow \Sigma$ bands.

Mixing between various lines is determined by the relaxation rates: even lines mix with odd lines via the $(1-\beta)K^{\Pi(f\leftarrow e)}$ and $(1-\beta)K^{\Delta(e\leftarrow f)}$ terms ; odd lines mix with other odd lines via the $\beta K^{\Pi(e\leftarrow e)}$ and $\beta K^{\Delta(f\leftarrow f)}$ terms; even lines mix with other even lines via the $\beta K^{\Pi(f\leftarrow f)}$ and $\beta K^{\Delta(e\leftarrow e)}$ terms.

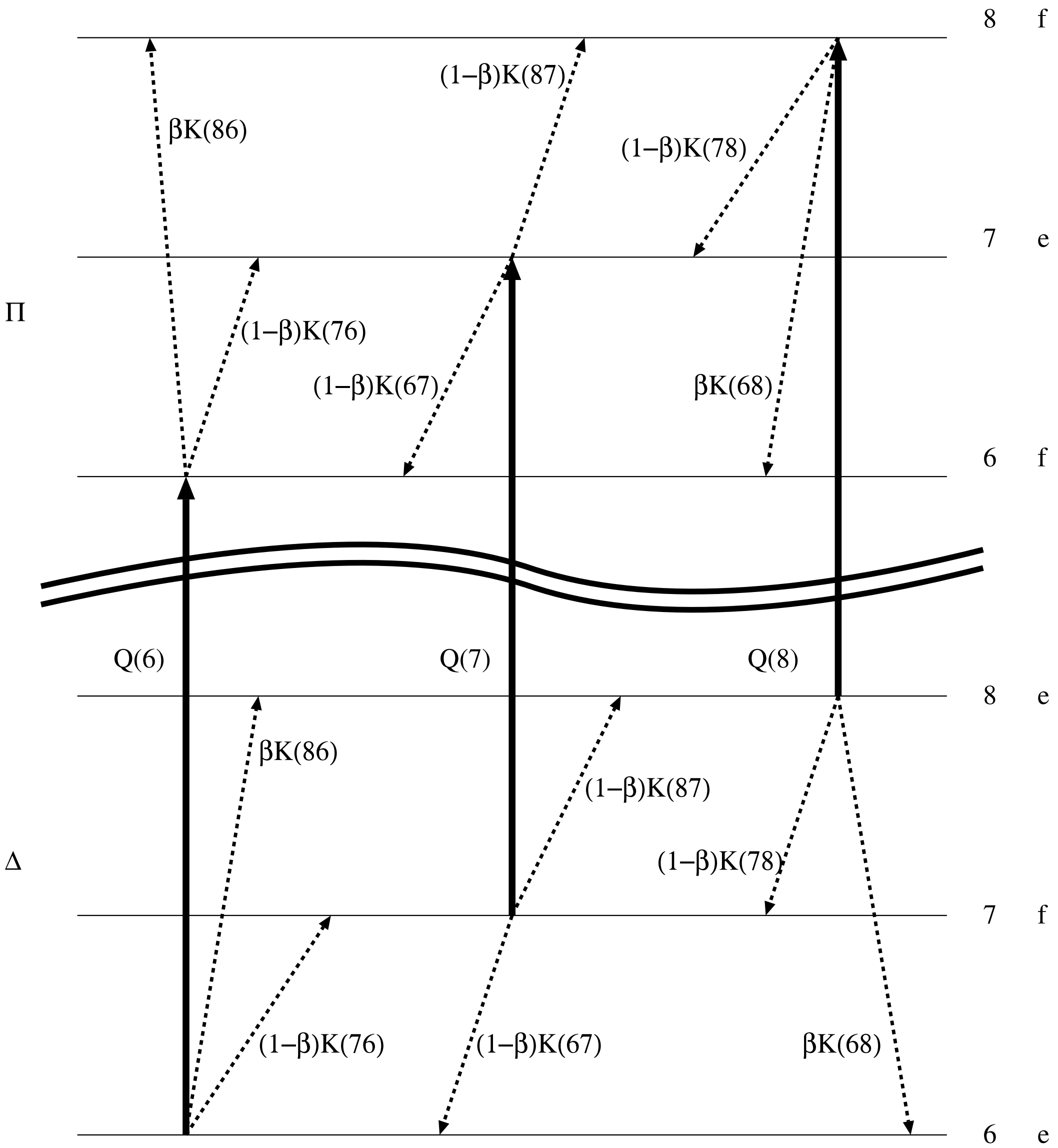

Figure B.2: Rotational relaxation rates, $K_{j'j}$, for several Q-branch lines of the 740 cm^{-1} $\Pi \leftarrow \Delta$ transition. Unlike a $\Pi \leftarrow \Sigma$ band, relaxation rates in both upper and lower vibrations are dependent on β.

In the above expression for the line widths, there is no differentiation made between $e \leftarrow f$ and $f \leftarrow e$ rates, or between $e \leftarrow e$ and $f \leftarrow f$ rates. It should also be noted, however, that when the splitting of rotational energy levels occurs due to ℓ-type doubling, the e levels always have higher energy than the f levels. Using this with the fact that even J Q-branch lines go from e to f and odd J lines go from f to e, it can be seen that even J Q-branch lines will be more closely spaced than odd J Q-branch lines. It is therefore likely that more mixing would occur between even Q-branch lines than odd Q-branch lines since the lines are energetically closer. Again, the total relaxation rate out of a particular rotational energy level is assumed to be independent of the vibrational level involved. Since the two vibrational levels involved here contain both even and odd rotational levels, their total sums are approximately equal. e.g.

$$\sum_{j' \neq j} \beta K_{j'j}^{\Delta(e,f \leftarrow e,f)} + \sum_{j' \neq j} (1-\beta) K_{j'j}^{\Delta(e,f \leftarrow f,e)} \approx \sum_{j' \neq j} \beta K_{j'j}^{\Pi(e,f \leftarrow e,f)} + \sum_{j' \neq j} (1-\beta) K_{j'j}^{\Pi(e,f \leftarrow f,e)} \quad \text{(B.9)}$$

and therefore no adjustments need to be made to Equation B.8 as was the case for $\Pi \leftarrow \Sigma$ bands.

At this point, we conjectured that since β has been treated as a probability in this model, the mixing should be determined by the probability that both collisions occur. Therefore, assuming the collisions in the upper and lower vibrational levels are independent, the probability that two lines mix are given by β^2 for mixing of states of similar symmetry and by $(1-\beta)^2$ for states of opposite symmetry. The mixing terms of $\mathbf{W}$ are then given by

$$W_{j'j} = -\beta^2 K_{j'j} \quad \text{(B.10)}$$

for even$\leftarrow$even and odd$\leftarrow$odd mixing and

$$W_{j'j} = -(1-\beta)^2 K_{j'j} \quad \text{(B.11)}$$

for even$\leftrightarrow$odd mixing. This is a consequence of the probabilistic nature of β. This result was not obvious for $\Pi \leftarrow \Sigma$ bands because there are no odd J levels in Σ states and therefore, the amount of mixing is determined solely by the β factor of the Π

band. For this model, however, since β is assumed to be the same for both vibrational levels in a $\Pi \leftarrow \Delta$ band, the mixing will be determined by the average β of both states. Calculations using **W** determined by Equations B.8, B.10, and B.11 greatly improved the agreement with the observed spectra, with maximum errors of ~1% (pure) and ~1.6% (foreign). Fitted values of β were determined to be ~0.5 for pure CO_2 and ~0.73 for N_2 broadened CO_2. Once again, it appeared that $e, f \leftarrow e, f$ collisions were just as likely to occur as $e, f \leftarrow f, e$ collisions for CO_2-CO_2 interactions. However, the value of $\beta =\sim 0.73$ for N_2 broadened CO_2 implies that CO_2 molecules tend to retain their original symmetry for collisions with N_2.

The final advancement in this model was to consider the case for which β is not assumed to be the same in the Π and Δ states. For the $\Pi \leftarrow \Sigma$ bands, there is no β factor for the Σ state simply because it has no odd rotational levels. Therefore, for the $\Pi \leftarrow \Sigma$ bands, the fitted values of β are due solely to the Π vibrational level. These values will be denoted as β_Π. Therefore, when dealing with $\Pi \leftarrow \Delta$ bands, the value of β_Π was held constant and the value of β due solely to the Δ band, β_Δ, was determined. Using this method, the effect of vibrational angular momentum on β is determined. Using these two different β's, Equations B.10 and B.11 become

$$W_{j'j} = -\beta_\Pi \beta_\Delta K_{j'j} \tag{B.12}$$

for even←even and odd←odd mixing and

$$W_{j'j} = -(1-\beta_\Pi)(1-\beta_\Delta) K_{j'j} \tag{B.13}$$

for even ↔ odd mixing. The corresponding expression for the linewidths is

$$W_{jj} \equiv \gamma_{Qj} = -\frac{1}{2}\left(\sum_{j' \neq j} \beta_\Delta K_{j'j}^{\Delta(e,f \leftarrow e,f)} + \sum_{j' \neq j} (1-\beta_\Delta) K_{j'j}^{\Delta(e,f \leftarrow f,e)}\right) - \frac{1}{2}\left(\sum_{j' \neq j} \beta_\Pi K_{j'j}^{\Pi(e,f \leftarrow e,f)} + \sum_{j' \neq j} (1-\beta_\Pi) K_{j'j}^{\Pi(e,f \leftarrow f,e)}\right) \tag{B.14}$$

For pure CO_2, β_Π was held constant at 0.5 and β_Δ was found to be ~0.51. For N_2 broadened CO_2, β_Π was held constant at 0.61 and β_Δ was found to be ~0.89.

B.3 Conclusions from Q-branch studies: Physical Implications of β

For calculations performed for pure samples of CO_2, done for both $\Pi \leftarrow \Sigma$ and $\Pi \leftarrow \Delta$ bands, it was determined that the optimum value for β is 0.5 ($\beta_\Pi =\sim 0.5, \beta_\Delta \sim 0.51$) . Therefore, within the assumptions of the model, it appears that $e, f \leftarrow e, f$ and $e, f \leftarrow f, e$ collisional transitions are equally probable. This means that when two CO_2 molecules collide, they are equally likely to keep the same rotational symmetry or switch to the opposite rotational symmetry.

For calculations performed for nitrogen broadened CO_2, the fitted values of β are greater than 0.5. This result implies that $e, f \leftarrow e, f$ collisional transitions are more probable than $e, f \leftarrow f, e$ transitions when a CO_2 molecule collides with a N_2 molecule. In other words, when a CO_2 molecule is perturbed by the smaller N_2 molecule, the CO_2 molecule is more likely to retain its original rotational symmetry. This result has not been reported by other experiments, although similar results have been predicted by Clary and Alexander for CO_2-He collisions [108]. Their theoretical work suggests that rotationally inelastic CO_2-He collisions will tend to conserve the vibrational angular momentum symmetry, although this conservation changes quite drastically with J. Previous line mixing calculations done by Strow on He-broadened CO_2 have yielded an optimum value for β_Π of ~0.75. Wen Ge [32] also found optimum values for β_Π to be ~0.5 for N_2O-N_2O collisions and ~0.7 for N_2O-He collisions [32]. In each case, β increases as the mass of the perturber decreases.

The propensity to conserve vibrational angular momentum appears to increase with increasing ℓ [108]. This is also supported by the results found here since the values of β have been calculated as ~0.61 for ℓ=1 and as ~0.89 for ℓ=2 for CO_2-N_2 collisions. It should be noted here that switching rotational symmetry is equivalent to making a transition from $-\ell$ to $+\ell$, or similarly, from one bending vibration (ν_2) to the other. Thus, as the amplitude of vibration increases with ℓ, it is less probable that the molecule will switch symmetry when perturbed by a nitrogen molecule.

Appendix C

1^{st}-order Mixing Coefficients for the ν_3 Band of CO_2

Below are tables of the temperature coefficients discussed in Section 3.7 for the first-order mixing coefficients of the CO_2 ν_3 band.

Table C.1: Temperature coefficients for the first-order mixing coefficients of the self-broadened fundamental ν_3 P-branch.

J_P	A	B	C	D
2	-7.1156823e-02	5.6551065e-05	-1.3075512e-07	1.6167598e-10
4	-3.2381752e-02	-8.6907582e-06	8.5104618e-08	-2.5574469e-10
6	-1.6940599e-02	-3.0333182e-05	1.4897368e-07	-3.7451115e-10
8	-8.3649130e-03	-4.0419650e-05	1.7466520e-07	-4.1887155e-10
10	-2.8956092e-03	-4.5650213e-05	1.8498913e-07	-4.3306383e-10
12	8.7797471e-04	-4.8891008e-05	1.9694092e-07	-4.8173238e-10
14	3.6157253e-03	-5.0147973e-05	1.8829808e-07	-4.2884705e-10
16	5.6468761e-03	-5.0555951e-05	1.8431107e-07	-4.1331435e-10
18	7.1883106e-03	-5.0431348e-05	1.7990362e-07	-4.0148716e-10
20	8.3732790e-03	-4.9900847e-05	1.7420745e-07	-3.8543313e-10
22	9.2922131e-03	-4.9127587e-05	1.6812949e-07	-3.6892467e-10

continued on next page

continued from previous page

J_P	A	B	C	D
24	1.0003005e-02	-4.8175431e-05	1.6182590e-07	-3.5223724e-10
26	1.0555661e-02	-4.7111095e-05	1.5543943e-07	-3.3545098e-10
28	1.0982714e-02	-4.5974728e-05	1.4901013e-07	-3.1839403e-10
30	1.1305985e-02	-4.4813800e-05	1.4304159e-07	-3.0392554e-10
32	1.1542660e-02	-4.3611136e-05	1.3700663e-07	-2.8871967e-10
34	1.1715400e-02	-4.2400809e-05	1.3114211e-07	-2.7404209e-10
36	1.1835584e-02	-4.1209556e-05	1.2552321e-07	-2.6004875e-10
38	1.1904585e-02	-4.0025660e-05	1.2023649e-07	-2.4763396e-10
40	1.1936408e-02	-3.8849728e-05	1.1484026e-07	-2.3367204e-10
42	1.1937037e-02	-3.7703415e-05	1.0979907e-07	-2.2126025e-10
44	1.1910158e-02	-3.6581825e-05	1.0498675e-07	-2.0952840e-10
46	1.1861722e-02	-3.5491489e-05	1.0038066e-07	-1.9835009e-10
48	1.1792618e-02	-3.4425109e-05	9.5950194e-08	-1.8761931e-10
50	1.1708518e-02	-3.3362513e-05	9.0887208e-08	-1.7104469e-10
52	1.1613101e-02	-3.2383903e-05	8.7650244e-08	-1.6763041e-10
54	1.1505763e-02	-3.1364731e-05	8.3122267e-08	-1.5576679e-10
56	1.1391187e-02	-3.0445034e-05	7.9619233e-08	-1.4692145e-10
58	1.1268351e-02	-2.9548253e-05	7.6443178e-08	-1.4070169e-10
60	1.1139637e-02	-2.8666599e-05	7.3096418e-08	-1.3297165e-10
62	1.1005128e-02	-2.7818199e-05	6.9990235e-08	-1.2611032e-10
64	1.0865292e-02	-2.6979450e-05	6.6728456e-08	-1.1799993e-10
66	1.0725719e-02	-2.6178462e-05	6.3749667e-08	-1.1103339e-10
68	1.0583696e-02	-2.5405959e-05	6.0908159e-08	-1.0443202e-10
70	1.0438517e-02	-2.4651847e-05	5.8129495e-08	-9.7795531e-11
72	1.0294954e-02	-2.3939277e-05	5.5901761e-08	-9.4420235e-11
74	1.0151853e-02	-2.3231019e-05	5.3064048e-08	-8.6370330e-11
76	1.0006611e-02	-2.2555417e-05	5.0674694e-08	-8.0923253e-11
78	9.8611484e-03	-2.1898259e-05	4.8374577e-08	-7.5711938e-11
80	9.7187360e-03	-2.1269603e-05	4.6189123e-08	-7.0780275e-11
82	9.5745952e-03	-2.0655454e-05	4.4075966e-08	-6.6042481e-11

continued on next page

continued from previous page

J_P	A	B	C	D
84	9.4336277e-03	-2.0066587e-05	4.2072147e-08	-6.1575905e-11
86	9.2928053e-03	-1.9493572e-05	4.0137342e-08	-5.7362304e-11
88	9.1538958e-03	-1.8941207e-05	3.8292932e-08	-5.3213467e-11
90	9.0174592e-03	-1.8406664e-05	3.6521903e-08	-4.9310282e-11
92	8.8828055e-03	-1.7887814e-05	3.4771450e-08	-4.5155849e-11
94	8.7498568e-03	-1.7389747e-05	3.3211489e-08	-4.1932982e-11
96	8.6182849e-03	-1.6900620e-05	3.1651787e-08	-3.8272796e-11
98	8.4895690e-03	-1.6427487e-05	3.0305657e-08	-3.5081789e-11
100	8.3633165e-03	-1.5947297e-05	2.9176179e-08	-3.2078876e-11
102	8.2418252e-03	-1.5400570e-05	2.8557462e-08	-3.0421292e-11
104	8.1433102e-03	-1.4556202e-05	2.8718270e-08	-3.2231294e-11
106	8.1729909e-03	-1.2390613e-05	2.7952157e-08	-3.8606079e-11
108	9.5216594e-03	-4.0613116e-06	5.1336045e-09	-6.2938705e-12

Table C.2: Temperature coefficients for the first-order mixing coefficients of the N_2-broadened fundamental ν_3 P-branch.

J_P	A	B	C	D
2	-6.4230226e-02	6.0700849e-05	-1.4335982e-07	2.4968151e-10
4	-3.1830847e-02	3.2808154e-06	5.2888213e-08	-1.8330568e-10
6	-1.7744024e-02	-2.0986084e-05	1.2962923e-07	-3.4666272e-10
8	-9.4546666e-03	-3.4571270e-05	1.6921705e-07	-4.2730327e-10
10	-3.9261750e-03	-4.2981966e-05	1.9124267e-07	-4.6902790e-10
12	2.6082706e-05	-4.8422127e-05	2.0360032e-07	-4.8990213e-10
14	2.9970054e-03	-5.2366939e-05	2.0913469e-07	-4.7690384e-10
16	5.2720706e-03	-5.4679829e-05	2.1377596e-07	-5.0017920e-10
18	7.0512613e-03	-5.6026305e-05	2.1332841e-07	-4.9368986e-10
20	8.4614046e-03	-5.6700899e-05	2.1099505e-07	-4.8347799e-10
22	9.5898004e-03	-5.6892133e-05	2.0744872e-07	-4.7131612e-10

continued on next page

continued from previous page

J_P	A	B	C	D
24	1.0493843e-02	-5.6703795e-05	2.0288277e-07	-4.5662887e-10
26	1.1223346e-02	-5.6233944e-05	1.9772599e-07	-4.4132967e-10
28	1.1811789e-02	-5.5554529e-05	1.9216012e-07	-4.2546062e-10
30	1.2281725e-02	-5.4713886e-05	1.8633243e-07	-4.0932654e-10
32	1.2651332e-02	-5.3733567e-05	1.8033345e-07	-3.9345720e-10
34	1.2944459e-02	-5.2660015e-05	1.7416053e-07	-3.7675617e-10
36	1.3173782e-02	-5.1531087e-05	1.6798728e-07	-3.6019227e-10
38	1.3341150e-02	-5.0344399e-05	1.6198279e-07	-3.4514827e-10
40	1.3461433e-02	-4.9118419e-05	1.5593324e-07	-3.2968853e-10
42	1.3541759e-02	-4.7876782e-05	1.5004310e-07	-3.1489542e-10
44	1.3586200e-02	-4.6617287e-05	1.4422637e-07	-3.0033277e-10
46	1.3601686e-02	-4.5356027e-05	1.3845726e-07	-2.8546532e-10
48	1.3589379e-02	-4.4097633e-05	1.3303867e-07	-2.7267413e-10
50	1.3556144e-02	-4.2845839e-05	1.2772766e-07	-2.6005660e-10
52	1.3505121e-02	-4.1608772e-05	1.2251174e-07	-2.4727359e-10
54	1.3437822e-02	-4.0386696e-05	1.1748290e-07	-2.3520241e-10
56	1.3357434e-02	-3.9186042e-05	1.1261846e-07	-2.2356563e-10
58	1.3264418e-02	-3.8008581e-05	1.0799236e-07	-2.1283359e-10
60	1.3161585e-02	-3.6852830e-05	1.0343709e-07	-2.0190267e-10
62	1.3049080e-02	-3.5724276e-05	9.9101821e-08	-1.9175050e-10
64	1.2927329e-02	-3.4613685e-05	9.4906505e-08	-1.8198898e-10
66	1.2803044e-02	-3.3537228e-05	9.0892962e-08	-1.7269408e-10
68	1.2673406e-02	-3.2489379e-05	8.7031340e-08	-1.6375807e-10
70	1.2537633e-02	-3.1464515e-05	8.3336687e-08	-1.5533844e-10
72	1.2401299e-02	-3.0470811e-05	7.9784736e-08	-1.4723931e-10
74	1.2263311e-02	-2.9507103e-05	7.6361690e-08	-1.3948945e-10
76	1.2120933e-02	-2.8574145e-05	7.3136893e-08	-1.3218402e-10
78	1.1976156e-02	-2.7661985e-05	7.0005488e-08	-1.2513810e-10
80	1.1833134e-02	-2.6785740e-05	6.7030264e-08	-1.1846759e-10
82	1.1686221e-02	-2.5929892e-05	6.4251011e-08	-1.1280463e-10

continued on next page

continued from previous page

J_P	A	B	C	D
84	1.1541520e-02	-2.5104540e-05	6.1429388e-08	-1.0598345e-10
86	1.1395379e-02	-2.4303770e-05	5.8809672e-08	-1.0016722e-10
88	1.1249922e-02	-2.3528268e-05	5.6301203e-08	-9.4601770e-11
90	1.1106031e-02	-2.2779356e-05	5.3905051e-08	-8.9269376e-11
92	1.0963009e-02	-2.2054981e-05	5.1614366e-08	-8.4119376e-11
94	1.0820732e-02	-2.1354470e-05	4.9442574e-08	-7.9153489e-11
96	1.0678983e-02	-2.0673196e-05	4.7397258e-08	-7.4295885e-11
98	1.0539471e-02	-2.0008276e-05	4.5551923e-08	-6.9630428e-11
100	1.0402051e-02	-1.9337754e-05	4.4041418e-08	-6.5353967e-11
102	1.0269732e-02	-1.8583330e-05	4.3216059e-08	-6.3190240e-11
104	1.0165419e-02	-1.7460970e-05	4.3211251e-08	-6.5194525e-11
106	1.0215793e-02	-1.4819966e-05	4.1364900e-08	-7.0884391e-11
108	1.1759136e-02	-6.1690241e-06	1.2941576e-08	-2.2458218e-11

Table C.3: Temperature coefficients for the first-order mixing coefficients of the self-broadened fundamental ν_3 R-branch.

J_R	A	B	C	D
0	6.8376662e-02	-7.5302534e-05	2.4642443e-07	-5.3746817e-10
2	4.9541571e-02	-1.9690176e-05	1.7533833e-08	2.0117053e-11
4	2.8667550e-02	1.7697695e-05	-1.1327427e-07	3.1333826e-10
6	1.7108353e-02	3.6051388e-05	-1.7053463e-07	4.3241782e-10
8	9.5931456e-03	4.6963566e-05	-2.0086285e-07	4.8998623e-10
10	4.2256528e-03	5.4138120e-05	-2.1829698e-07	5.1919050e-10
12	1.4496082e-04	5.9157525e-05	-2.2858979e-07	5.3279601e-10
14	-3.0719231e-03	6.2411729e-05	-2.3399558e-07	5.5186854e-10
16	-5.7063567e-03	6.5144733e-05	-2.3643478e-07	5.3365129e-10
18	-7.9235168e-03	6.7276957e-05	-2.3806521e-07	5.2992651e-10
20	-9.8270800e-03	6.8963789e-05	-2.3851019e-07	5.2407901e-10

continued on next page

continued from previous page

J_R	A	B	C	D
22	-1.1490019e-02	7.0330360e-05	-2.3817474e-07	5.1701134e-10
24	-1.2963898e-02	7.1453476e-05	-2.3723573e-07	5.0877682e-10
26	-1.4289734e-02	7.2400184e-05	-2.3594285e-07	5.0019453e-10
28	-1.5496009e-02	7.3225306e-05	-2.3443774e-07	4.9142555e-10
30	-1.6599998e-02	7.3944598e-05	-2.3275256e-07	4.8251075e-10
32	-1.7628198e-02	7.4596868e-05	-2.3124437e-07	4.7533120e-10
34	-1.8600383e-02	7.5227865e-05	-2.2959736e-07	4.6702108e-10
36	-1.9510217e-02	7.5785373e-05	-2.2741745e-07	4.5641258e-10
38	-2.0377870e-02	7.6329295e-05	-2.2555978e-07	4.4757163e-10
40	-2.1222537e-02	7.6892837e-05	-2.2385263e-07	4.3932824e-10
42	-2.2041625e-02	7.7459989e-05	-2.2219967e-07	4.3126912e-10
44	-2.2845479e-02	7.8060150e-05	-2.2069044e-07	4.2356872e-10
46	-2.3632806e-02	7.8681637e-05	-2.1926217e-07	4.1608308e-10
48	-2.4413274e-02	7.9326798e-05	-2.1792534e-07	4.0885561e-10
50	-2.5201828e-02	8.0032377e-05	-2.1683897e-07	4.0231413e-10
52	-2.5999477e-02	8.0791572e-05	-2.1569192e-07	3.9514226e-10
54	-2.6800499e-02	8.1609270e-05	-2.1478627e-07	3.8864244e-10
56	-2.7618568e-02	8.2499212e-05	-2.1405200e-07	3.8247217e-10
58	-2.8457566e-02	8.3476152e-05	-2.1351939e-07	3.7664297e-10
60	-2.9318963e-02	8.4517644e-05	-2.1309365e-07	3.7093359e-10
62	-3.0223992e-02	8.5686059e-05	-2.1295567e-07	3.6581815e-10
64	-3.1162091e-02	8.6958688e-05	-2.1296785e-07	3.6055802e-10
66	-3.2143745e-02	8.8357764e-05	-2.1323920e-07	3.5580189e-10
68	-3.3176094e-02	8.9884640e-05	-2.1372019e-07	3.5125824e-10
70	-3.4274021e-02	9.1586052e-05	-2.1452362e-07	3.4712887e-10
72	-3.5434926e-02	9.3445125e-05	-2.1556555e-07	3.4317277e-10
74	-3.6680443e-02	9.5517203e-05	-2.1697094e-07	3.3961946e-10
76	-3.8011834e-02	9.7808319e-05	-2.1874847e-07	3.3656337e-10
78	-3.9446584e-02	1.0034743e-04	-2.2085670e-07	3.3346820e-10
80	-4.1003228e-02	1.0319397e-04	-2.2348259e-07	3.3100823e-10

continued on next page

continued from previous page

J_R	A	B	C	D
82	-4.2689831e-02	1.0635348e-04	-2.2655831e-07	3.2885098e-10
84	-4.4543804e-02	1.0991989e-04	-2.3025182e-07	3.2717352e-10
86	-4.6577704e-02	1.1395000e-04	-2.3465476e-07	3.2604544e-10
88	-4.8818326e-02	1.1847156e-04	-2.3972190e-07	3.2519134e-10
90	-5.1334471e-02	1.2368690e-04	-2.4584871e-07	3.2502495e-10
92	-5.4133924e-02	1.2963497e-04	-2.5302593e-07	3.2514222e-10
94	-5.7303720e-02	1.3651648e-04	-2.6161590e-07	3.2551017e-10
96	-6.0919864e-02	1.4457354e-04	-2.7223141e-07	3.2615394e-10
98	-6.5060678e-02	1.5398931e-04	-2.8587250e-07	3.2800235e-10
100	-6.9894378e-02	1.6502703e-04	-3.0476838e-07	3.3263489e-10
102	-7.5614910e-02	1.7734761e-04	-3.3422089e-07	3.5568606e-10
104	-8.2736685e-02	1.8795730e-04	-3.8139308e-07	4.3469504e-10
106	-9.3442465e-02	1.8013979e-04	-4.2324459e-07	5.9783036e-10
108	-1.2958418e-01	6.5671403e-05	-8.7051026e-08	6.8273526e-11

Table C.4: Temperature coefficients for the first-order mixing coefficients of the N_2-broadened fundamental ν_3 R-branch.

J_R	A	B	C	D
0	6.1070381e-02	-6.9014289e-05	2.1060076e-07	-4.4276983e-10
2	4.7484249e-02	-3.0638449e-05	4.7200644e-08	-4.4987019e-11
4	2.8994215e-02	5.6534622e-06	-8.1914443e-08	2.4835074e-10
6	1.8085824e-02	2.6956099e-05	-1.5233212e-07	4.0232745e-10
8	1.0692312e-02	4.1257140e-05	-1.9666237e-07	4.9563643e-10
10	5.2389569e-03	5.1621210e-05	-2.2685932e-07	5.5691183e-10
12	9.8101282e-04	5.9482580e-05	-2.4791115e-07	5.9594188e-10
14	-2.4597175e-03	6.5093398e-05	-2.5740453e-07	6.0463894e-10
16	-5.3327897e-03	7.0172577e-05	-2.7293599e-07	6.3763396e-10
18	-7.7962631e-03	7.4249160e-05	-2.8136660e-07	6.4948871e-10

continued on next page

continued from previous page

J_R	A	B	C	D
20	-9.9484878e-03	7.7657389e-05	-2.8768601e-07	6.5702749e-10
22	-1.1859349e-02	8.0548755e-05	-2.9236970e-07	6.6110578e-10
24	-1.3578926e-02	8.3028892e-05	-2.9579539e-07	6.6259338e-10
26	-1.5147509e-02	8.5184318e-05	-2.9824272e-07	6.6208731e-10
28	-1.6593527e-02	8.7090475e-05	-2.9998506e-07	6.6024592e-10
30	-1.7934260e-02	8.8779468e-05	-3.0117026e-07	6.5747631e-10
32	-1.9195856e-02	9.0270110e-05	-3.0159556e-07	6.5269528e-10
34	-2.0399866e-02	9.1672359e-05	-3.0190971e-07	6.4804622e-10
36	-2.1539816e-02	9.2947504e-05	-3.0188803e-07	6.4278074e-10
38	-2.2635456e-02	9.4115357e-05	-3.0156522e-07	6.3693947e-10
40	-2.3707885e-02	9.5246756e-05	-3.0117113e-07	6.3101321e-10
42	-2.4754523e-02	9.6330179e-05	-3.0069649e-07	6.2508550e-10
44	-2.5786510e-02	9.7394974e-05	-3.0012071e-07	6.1874230e-10
46	-2.6802672e-02	9.8441244e-05	-2.9955939e-07	6.1259965e-10
48	-2.7813142e-02	9.9472846e-05	-2.9896329e-07	6.0640547e-10
50	-2.8834360e-02	1.0053428e-04	-2.9849807e-07	6.0060261e-10
52	-2.9868852e-02	1.0164186e-04	-2.9808280e-07	5.9463167e-10
54	-3.0909666e-02	1.0277696e-04	-2.9779138e-07	5.8903296e-10
56	-3.1972144e-02	1.0397027e-04	-2.9765643e-07	5.8371979e-10
58	-3.3061237e-02	1.0524394e-04	-2.9775732e-07	5.7876333e-10
60	-3.4178381e-02	1.0657221e-04	-2.9800249e-07	5.7440056e-10
62	-3.5348159e-02	1.0802903e-04	-2.9846210e-07	5.6987742e-10
64	-3.6559668e-02	1.0960647e-04	-2.9935104e-07	5.6632361e-10
66	-3.7824530e-02	1.1130379e-04	-3.0041291e-07	5.6321461e-10
68	-3.9151571e-02	1.1315808e-04	-3.0199481e-07	5.6136429e-10
70	-4.0558255e-02	1.1519152e-04	-3.0363135e-07	5.5797690e-10
72	-4.2042513e-02	1.1741729e-04	-3.0585592e-07	5.5629735e-10
74	-4.3629789e-02	1.1989531e-04	-3.0863940e-07	5.5549308e-10
76	-4.5322479e-02	1.2263098e-04	-3.1195735e-07	5.5542932e-10
78	-4.7141394e-02	1.2566770e-04	-3.1587646e-07	5.5614164e-10

continued on next page

continued from previous page

J_R	A	B	C	D
80	-4.9109266e-02	1.2907506e-04	-3.2056230e-07	5.5791323e-10
82	-5.1236327e-02	1.3286425e-04	-3.2597594e-07	5.6056583e-10
84	-5.3567395e-02	1.3715470e-04	-3.3237633e-07	5.6446772e-10
86	-5.6119219e-02	1.4201247e-04	-3.3989148e-07	5.6974245e-10
88	-5.8923624e-02	1.4748255e-04	-3.4852138e-07	5.7619779e-10
90	-6.2063929e-02	1.5381389e-04	-3.5881727e-07	5.8441172e-10
92	-6.5551818e-02	1.6105481e-04	-3.7084697e-07	5.9418722e-10
94	-6.9491202e-02	1.6945982e-04	-3.8509480e-07	6.0511417e-10
96	-7.3975935e-02	1.7932838e-04	-4.0259655e-07	6.1820509e-10
98	-7.9101807e-02	1.9087827e-04	-4.2465868e-07	6.3403135e-10
100	-8.5073385e-02	2.0444113e-04	-4.5485319e-07	6.5861722e-10
102	-9.2130354e-02	2.1953756e-04	-4.9947362e-07	7.1161327e-10
104	-1.0090363e-01	2.3259086e-04	-5.6589894e-07	8.3995453e-10
106	-1.1399182e-01	2.2509141e-04	-6.1759971e-07	1.0510625e-09
108	-1.5575851e-01	1.1489084e-04	-2.2676936e-07	3.6990359e-10

Appendix D

Molecular Spectroscopy of H_2O

Unlike CO_2, H_2O is not a linear molecule; it is bent with an H-O-H angle of ~104.5deg. It has three unique (and relatively small) principle moments of inertia (I_a, I_b, I_c) and is classified as an asymmetric top, with a high degree of asymmetry. The resulting vibration-rotation spectrum is very random in nature and the line positions and strengths follow no simple sequential scheme as for CO_2. Consequently, despite its apparently simple structure, H_2O is far from trivial to model theoretically. Some basic physical parameters of H_2O are listed in Table D for reference. The vibrational and rotational energies of H_2O will be reviewed only briefly in the following sections; for a more detailed analysis, the reader is directed to Herzberg [109], Townes and Schawlow [110], Allen and Cross [111], or Goody [112].

D.1 Rotational Energies

In the rigid rotor approximation, the rotational energies of an asymmetric rotor are

$$E_r(J) = \frac{1}{2}(A+C)J(J+1) + \frac{1}{2}(A-C)E(J, K_A - K_C, \kappa) \tag{D.1}$$

where J is the total angular momentum quantum number, $A = \frac{h}{8\pi^2 cI_A}$, $B = \frac{h}{8\pi^2 cI_B}$, and $C = \frac{h}{8\pi^2 cI_C}$. K_A and K_C are the components of angular momentum along the unique

Internuclear Distance	r(H-O)	0.9600 A(equilibrium)
H-O-H angle	∠HOH	104.5 degrees
Force Constants †	k_1	7.66 $\times 10^5$ dynes/cm
	k_{12}	-0.097 $\times 10^5$ dynes/cm
	$\frac{k_\delta}{\ell^2}$	0.703 $\times 10^5$ dynes/cm
Masses	m(^{1}H)	1.008 amu
	m(^{16}O)	15.999 amu
Moments of Inertia	I_A	1.01 $\times$ 10^{-40} g cm^2.
	I_B	1.93 $\times$ 10^{-40} g cm^2.
	I_C	3.01 $\times$ 10^{-40} g cm^2.
Rotational Constants	A	27.79 cm^{-1}
	B	14.51 cm^{-1}
	C	9.29 cm^{-1}

Table D.1: Some basic physical constants of H_2O. †: from Herzberg [109], p 187

symmetry axis of the molecule in the prolate ($A > B = C$) and oblate ($A < B = C$) symmetric top limits. $K_A - K_C$ represents the interpolation between the energy levels of the prolate and oblate limits. K_A and K_C are therefore not true quantum numbers for H_2O. In fact there is no set of quantum numbers which specify the state and also have some convenient physical meaning. Nevertheless, asymmetric top energy levels can be described by noting J and the values of K_A and K_C in the prolate and oblate top limits. $\kappa = \frac{2B-A-C}{A-C}$ is Ray's asymmetry factor and equals ~-0.43 for H_2O (κ=-1 for a prolate symmetric top and κ=+1 for an oblate symmetric top.) The values of $E(J, K_A - K_C, \kappa)$ vary for different molecules and different amounts of asymmetry and are available in the literature. Closed expressions for $E(J, K_A - K_C, \kappa)$ are obtainable only for the lowest values of J; some of these are listed in Table D.2. Values of E_R for low values of J are listed in D.3.

JK_AK_C	$E(J, K_A - K_C, \kappa)$
0 0 0	0
1 1 0	$\kappa + 1$
1 1 1	0
1 0 1	$\kappa - 1$
2 2 0	$2(\kappa + \sqrt{\kappa^2 + 3})$
2 2 1	$\kappa + 3$
2 1 1	4κ
2 1 2	$\kappa - 3$
2 0 2	$2(\kappa - \sqrt{\kappa^2 + 3})$
3 3 0	$5\kappa + 3 + 2\sqrt{4\kappa^2 - 6\kappa + 6}$
3 3 1	$2(\kappa + \sqrt{\kappa^2 + 15})$
3 2 1	$5\kappa - 3 + 2\sqrt{4\kappa^2 + 6\kappa + 6}$
3 2 2	4κ
3 1 2	$5\kappa + 3 - 2\sqrt{4\kappa^2 - 6\kappa + 6}$
3 1 3	$2(\kappa - \sqrt{\kappa^2 + 15})$
3 0 3	$5\kappa - 3 - 2\sqrt{4\kappa^2 + 6\kappa + 6}$
4 4 1	$5\kappa + 5 + 2\sqrt{4\kappa^2 - 10\kappa + 22}$
4 3 1	$10\kappa + 2\sqrt{9\kappa^2 + 7}$
4 3 2	$5\kappa - 5 + 2\sqrt{4\kappa^2 + 10\kappa + 22}$
4 2 3	$5\kappa + 5 - 2\sqrt{4\kappa^2 - 10\kappa + 22}$
4 1 3	$10\kappa - 2\sqrt{9\kappa^2 + 7}$
4 1 4	$5\kappa - 5 - 2\sqrt{4\kappa^2 + 10\kappa + 22}$

Table D.2: Some values of the energy parameter, $E(J, K_A{-}K_C, \kappa)$, for asymmetric rotors.

D.2 Vibrational Energies

H_2O has $3N = 9$ degrees of freedom. Three of these are for translation and three are for rotation, leaving $3N - 6 = 3$ degrees of freedom for vibration. The fundamental modes of vibration, ν_1, ν_2, and ν_3, are illustrated in Figure D.1. The symmetric bond stretch, ν_1, is somewhat of a misnomer and involves a small amount of angle bending; the angle increases slightly as the bonds stretch. Likewise, the angle bending vibration, ν_2, involves some bond stretching; the bonds contracting as the angle opens up. The

JK_AK_C	E_R
0 0 0	0
1 1 0	$A+B$
1 1 1	$A+C$
1 0 1	$B+C$
2 2 0	$2A+2B+2C+2\sqrt{(B-C)^2+(A-C)(A-B)}$
2 2 1	$4A+B+C$
2 1 1	$A+4B+C$
2 1 2	$A+B+4C$
2 0 2	$2A+2B+2C-2\sqrt{(B-C)^2+(A-C)(A-B)}$
3 3 0	$5A+5B+2C+2\sqrt{4(A-B)^2+(A-C)(B-C)}$
3 3 1	$5A+2B+2C+2\sqrt{4(A-C)^2+(A-B)(B-C)}$
3 2 1	$2A+5B+5C+2\sqrt{4(B-C)^2+(A-B)(A-C)}$
3 2 2	$4A+4B+4C$
3 1 2	$5A+5B+2C-2\sqrt{4(A-B)^2+(A-C)(B-C)}$
3 1 3	$5A+2B+2C-2\sqrt{4(A-C)^2+(A-B)(B-C)}$
3 0 3	$2A+5B+5C-2\sqrt{4(B-C)^2+(A-B)(A-C)}$
4 4 1	$10A+5B+5C+2\sqrt{4(B-C)^2+9(A-C)(A-B)}$
4 3 1	$5A+10B+5C+2\sqrt{4(A-C)^2-9(A-B)(B-C)}$
4 3 2	$5A+5B+10C+2\sqrt{4(A-B)^2+9(A-C)(B-C)}$
4 2 3	$10A+5B+5C-2\sqrt{4(B-C)^2+9(A-C)(A-B)}$
4 1 3	$5A+10B+5C-2\sqrt{4(A-C)^2-9(A-B)(B-C)}$
4 1 4	$5A+5B+10C-2\sqrt{4(A-B)^2+9(A-C)(B-C)}$

Table D.3: Some closed solutions for the rigid rotor rotational energy levels of asymmetric tops.

asymmetric stretch, ν_3, however, is a pure stretch and involves no change in the bond angle. The very small mixing between bond stretching and angle bending for H_2O is due to the very light mass of the hydrogen atoms. All three modes result in a change in the dipole moment and therefore result in infrared absorption. The fundamental ν_2 is centered at ~1595 cm^{-1}, approximately halfway between the pure rotational band and a group a bands from ~2700–3700 cm^{-1} due to $2\nu_2$, ν_1, and ν_3. ν_2 is therefore somewhat isolated from the other two modes. Weaker bands due to $H_2^{18}O$, $H_2^{17}O$ and hot bands, however, must be considered. The percent isotopic abundances of $H_2^{16}O$, $H_2^{18}O$, and $H_2^{17}O$ are 99.73, 0.2039, and 0.0373 % respectively. The $H_2^{18}O$ and $H_2^{17}O$ lines centers are shifted on the order of -10 to -1 cm^{-1} from the corresponding $H_2^{16}O$ values.

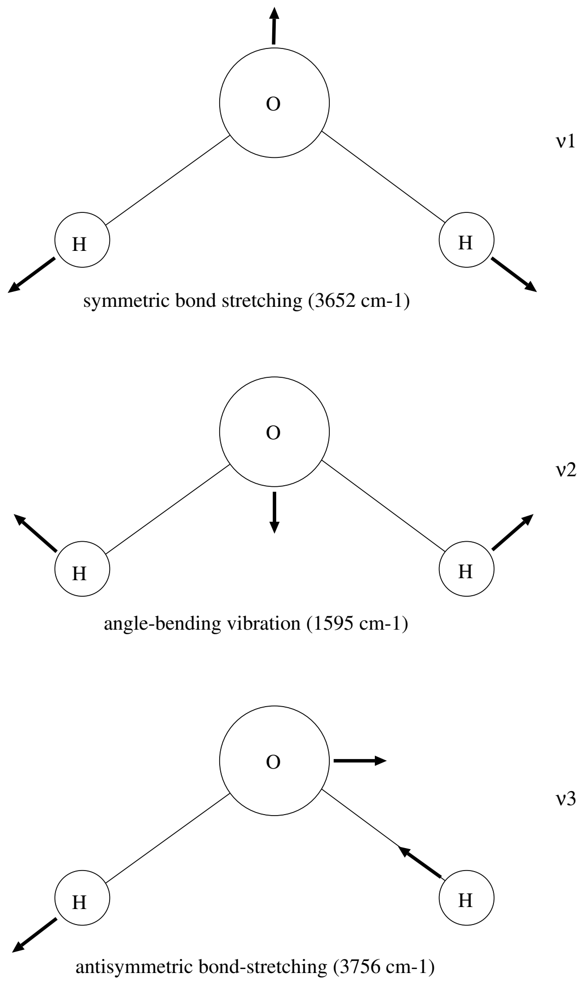

Figure D.1: Vibrational modes of H_2O. The thicker arrows represent the displacement of the nuclei from their equilibrium positions, which have been drawn approximately to scale for maximum displacement for one quantum of excitation.

D.3 Vibration-Rotation Bands

The addition of vibration and centrifugal distortion further complicate the calculation of these energies. Unlike linear molecules and symmetric tops, centrifugal distortion can play a very large role in determining energy levels. This is even more important for light molecules such as H_2O where centrifugal distortions can account for up to $\sim$10% of the observed rotational energy [110]. Because of this, a Hamiltonian that includes high order perturbation terms must be employed, namely

$$H_R^{AS} = H_2^{AS} + H_4^{AS} + H_6^{AS} + \ldots \tag{D.2}$$

with

$$\begin{aligned}
H_2^{AS} &= \tfrac{1}{2}(X^{AS} + Y^{AS})J^2 + [Z^{AS} - \tfrac{1}{2}(X^{AS} + Y^{AS})]J_z^2 + \tfrac{1}{4}(X^{AS} - Y^{AS})(J_+^2 + J_-^2) \\
H_4^{AS} &= -\Delta_J J^4 - \Delta_{JK} J^2 J_Z^2 - \Delta_K J_Z^4 - \delta_J J^2 (J_+^2 + J_-^2) - \tfrac{1}{2}\delta_K [J_Z^2 (J_+^2 + J_-^2) + (J_+^2 + J_-^2) J_Z^2] \\
H_6^{AS} &= H_J J^6 + H_{JK} J^4 J_Z^2 + H_{KJ} J^2 J_Z^4 + H_K J_Z^6 + h_J J^4 (J_+^2 + J_-^2) \\
&\quad + \tfrac{1}{2} h_{JK} J^2 [J_Z^2 (J_+^2 + J_-^2) + (J_+^2 + J_-^2) J_Z^2] + \tfrac{1}{2} h_K [J_Z^4 (J_+^2 + J_-^2) + (J_+^2 + J_-^2) J_Z^4] \\
H_8^{AS} &= L_J J^8 + L_{JJK} J^6 J_Z^2 + L_{JK} J^4 J_Z^4 + L_{KKJ} J^2 J_Z^6 + L_K J_Z^8 + \ell_J J^6 (J_+^2 + J_-^2) \\
&\quad + \tfrac{1}{2}\ell_{JK} J^4 [J_Z^2 (J_+^2 + J_-^2) + (J_+^2 + J_-^2) J_Z^2] + \tfrac{1}{2}\ell_{KJ} J^2 [J_Z^4 (J_+^2 + J_-^2) + (J_+^2 + J_-^2) J_Z^4] \\
&\quad + \tfrac{1}{2}\ell_K [J_Z^6 (J_+^2 + J_-^2) + (J_+^2 + J_-^2) J_Z^6]
\end{aligned} \tag{D.3}$$

Interested readers are referred to Strow [113] or Flaud [114], for example, for further explanation.

Asymmetric rotor spectra are further complicated by the complex selection rules and transition probability distributions. See the references given at the beginning of this section for a detailed discussion. For the ν_2 band of H_2O ("a B-type" transition), the selection rules are

$$\Delta J = 0, \pm 1, \pm 3 \quad \Delta K_A, \Delta K_C = \pm 1, \pm 3, \pm 5 \tag{D.4}$$

with ΔJ=0,$\pm$1 being the strongest transitions. Combining the selection rules with the rotation-vibration energy levels, energy level diagrams for the ν_2 band are shown in

Figures D.2 through D.4. Stick spectra showing line strength versus line center for the near-infrared and infrared regions are also shown in Figure D.5. The line positions and strengths used in this study are taken from the 1992 HITRAN database which consists of approximately 23,000 transitions for $H_2^{16}O$, $H_2^{18}O$, and $H_2^{17}O$ between 0 and 4000 cm^{-1}.

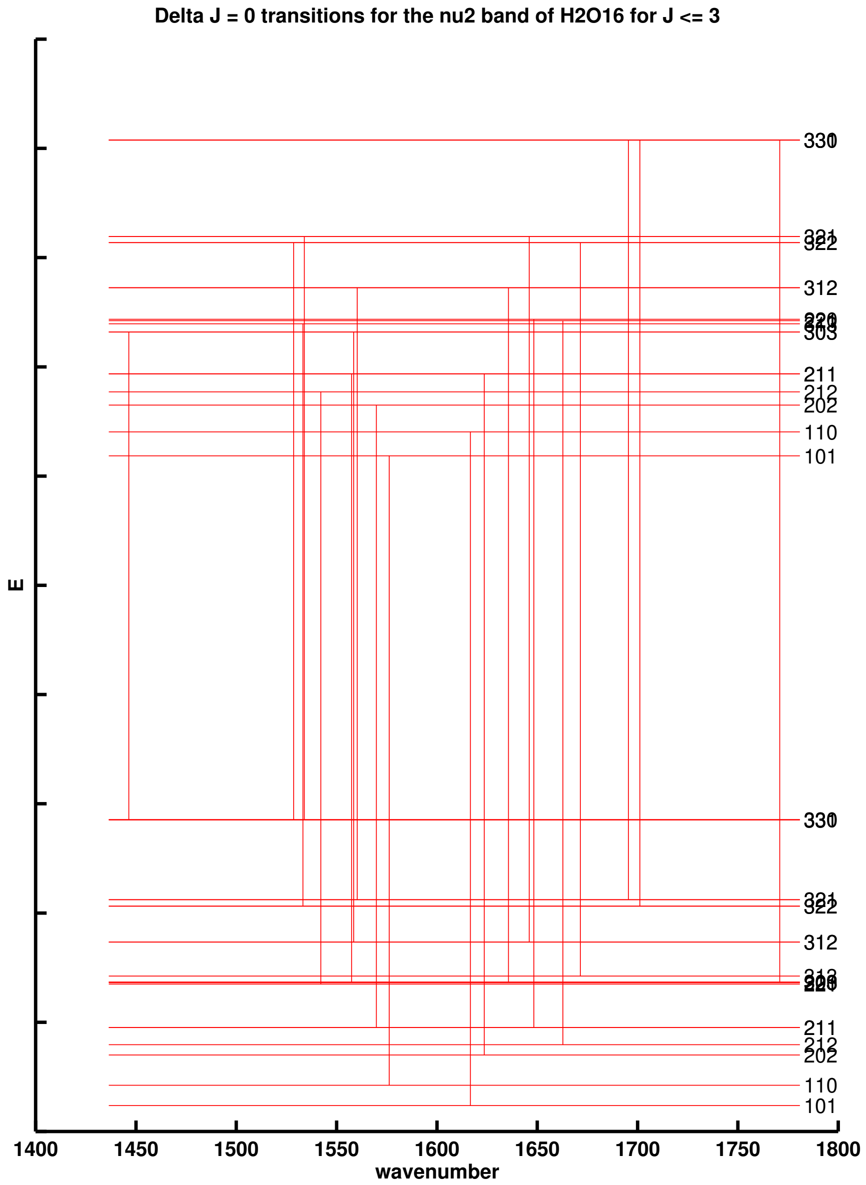

Figure D.2: Fundamental ν_2 $H_2^{16}O$ transitions for ΔJ=0 and $|J| \leq 3$.

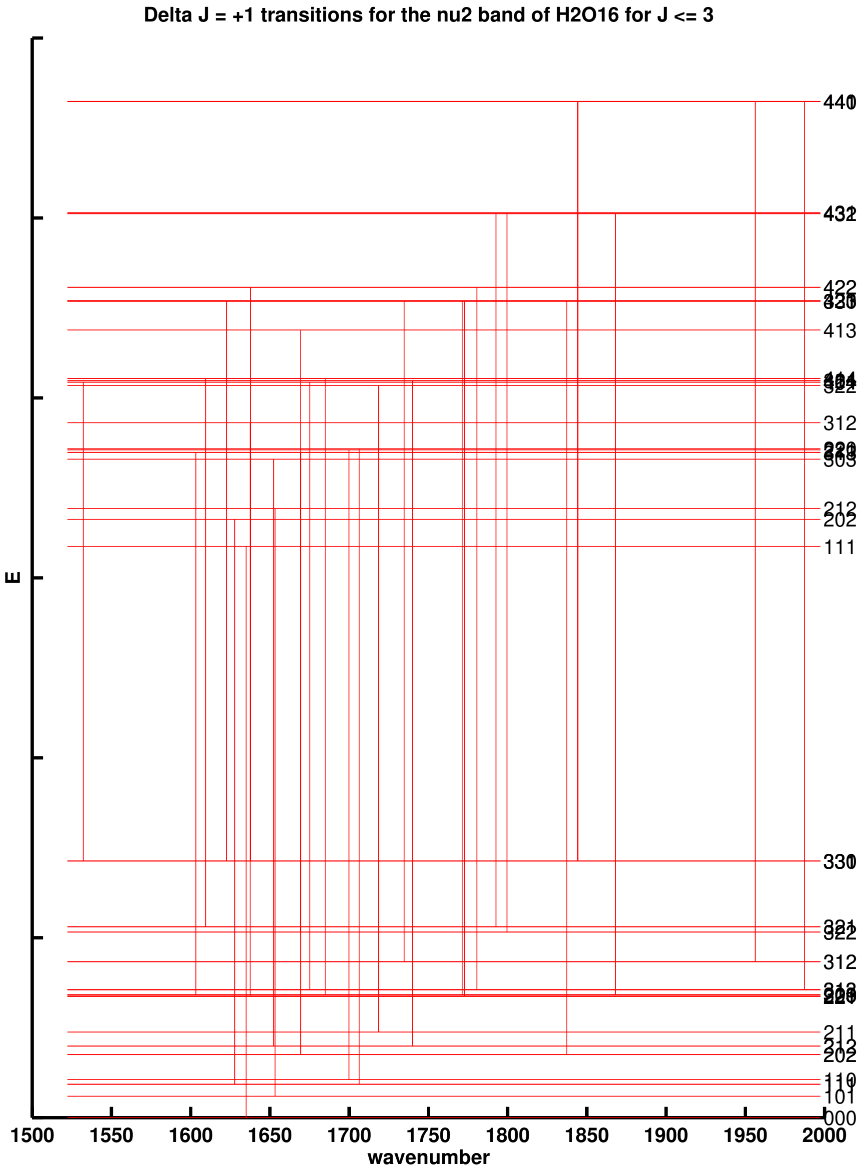

Figure D.3: Fundamental ν_2 $H_2^{16}O$ transitions for ΔJ=1 and $|J| \leq 3$.

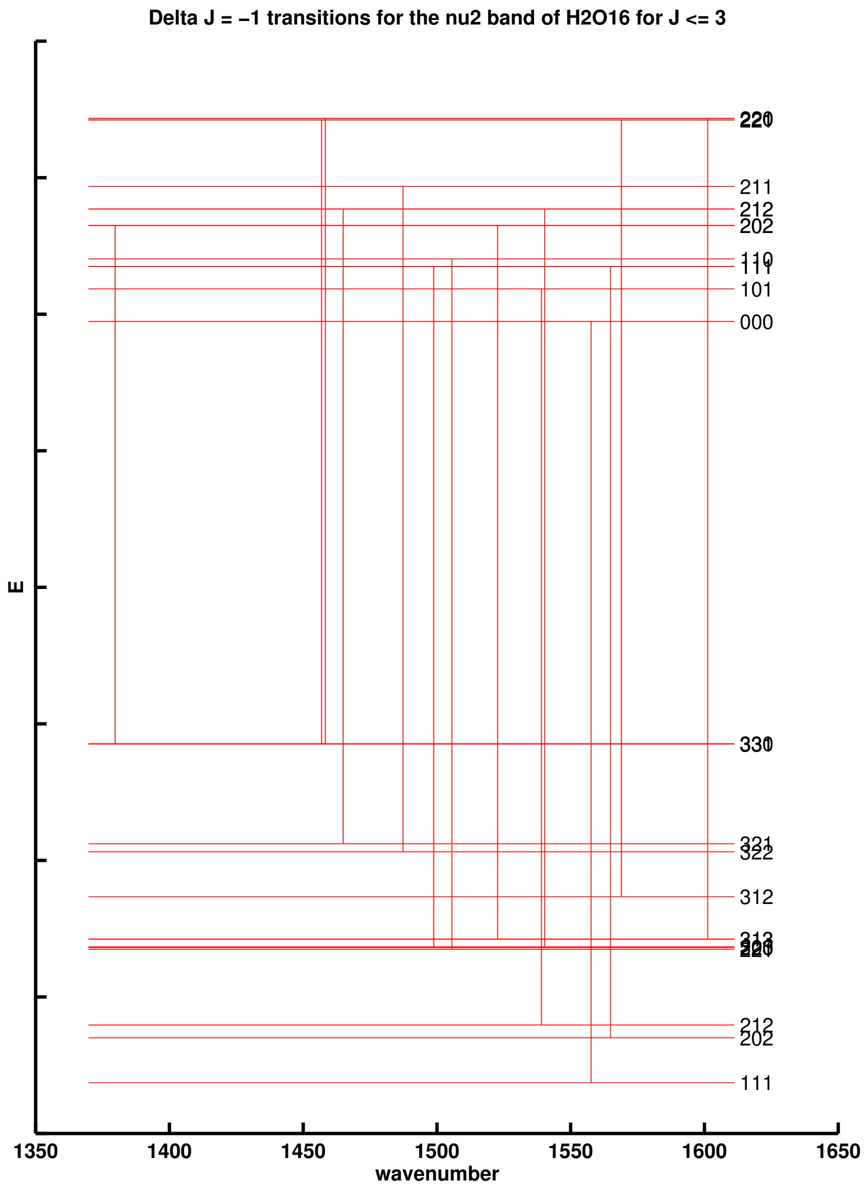

Figure D.4: Fundamental ν_2 $H_2^{16}O$ transitions for ΔJ=-1 and $|J| \leq 3$.

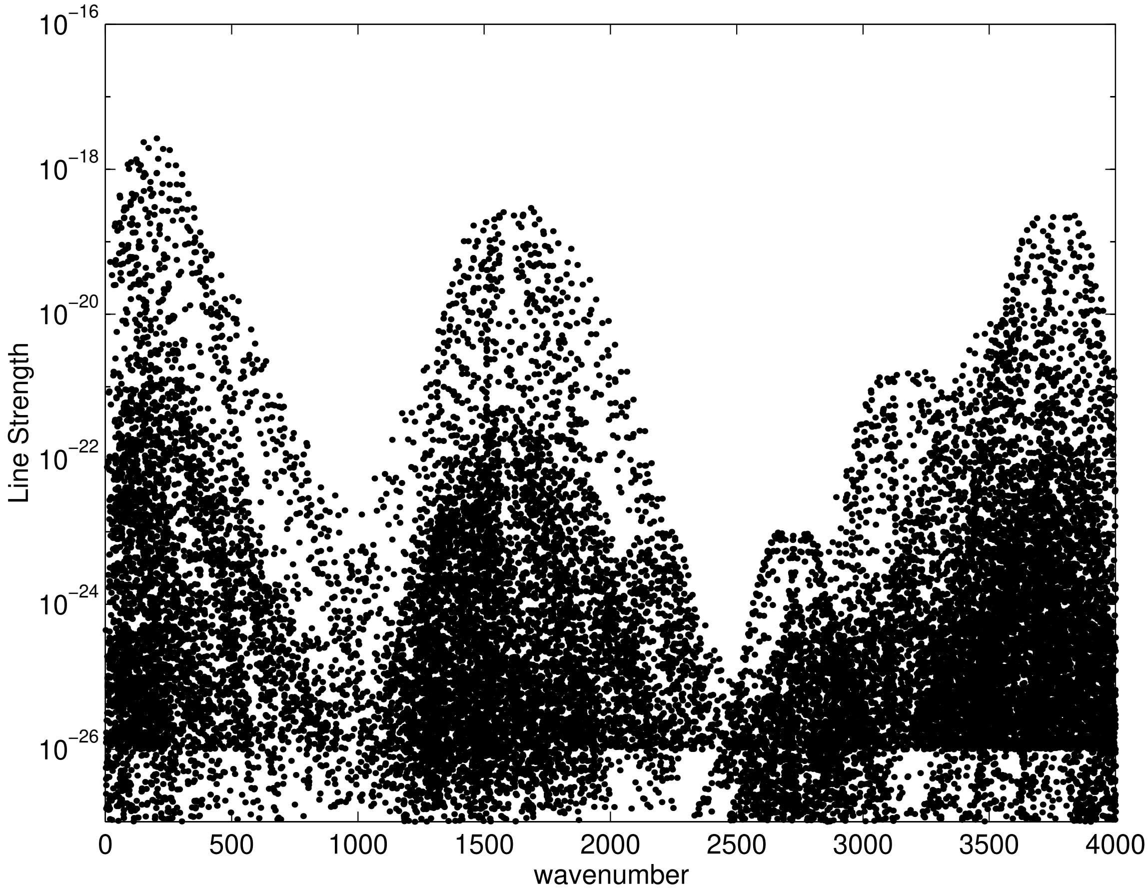

Figure D.5: $H_2^{16}O$, $H_2^{18}O$, and $H_2^{17}O$ spectral lines between 0 and 4000 cm^{-1}. The pure rotation (0 cm^{-1}), ν_2 (1600 cm^{-1}), ν_1 of HDO (2720 cm^{-1}), $2\nu_2$ (2720 cm^{-1}), ν_1 (3660 cm^{-1}), and ν_3 (3760 cm^{-1}) bands of $H_2^{16}O$ are evident in the figure.

Bibliography

[1] H. H. Aumann and R. J. Pagano. Atmospheric Infrared Sounder on the Earth Observing System. *Opt. Eng.*, 33:776, 1994.

[2] D. Gaffen and W. Elliot. Water Vapor in the Climate System. Technical report, American Geophysical Union, 1995.

[3] L. S. Rothman, R. R. Gamache, R. H. Tipping, C. P. Rinsland, M. A. H. Smith, C. Benner, V. M. Devi, J. M. Flaud, C. C. Peyret, A. Perrin, A. Goldman, S. T. Massiea, L. R. Brown, and R. A. Toth. The HITRAN Molecular Database: editions of 1991 and 1992. *J. Quant. Spectrosc. Radiat. Transfer*, 48:469, 1992.

[4] L. S. Rothman, R. R. Gamache, A. Goldman, L. R. Brown, R. A. Toth, H. M. Pickett, R. L. Poynter, J. M. Flaud, C. C. Peyret, A. Barbe, N. Husson, C. P. Rinsland, and M. A. H. Smith. The HITRAN Database: 1986 edition. *Appl. Opt.*, 26:4058, 1987.

[5] R. G. Breene. Line width. *Handbuch der Physik*, 27:19, 1956.

[6] R. R. Gamache, R. L. Hawkins, and L. S. Rothman. Total internal partition sums in the temperature range 700-3000 K: Atmospheric linear molecules. *J. Mol. Spectrosc.*, 142:205, 1990.

[7] Lui Zheng. An infrared spectral line shape study of CO_2 using diode lasers. Master's thesis, University of Maryland Baltimore County, 1989.

[8] R. R. Gamache and R. W. Davies. Theoretical calculations of N_2-broadened halfwidths of H_2O using quantum Fourier transform theory. *Appl. Opt.*, 22:4013, 1983.

[9] R. R. Gamache, J. M. Hartmann, and L. Rosenmann. Collisional broadening survey of water vapor lines - I. A survey of experimental results. *J. Quant. Spectrosc. Radiat. Transfer*, 52:481, 1994.

[10] S. G. Rautian and I. I. Sobel'man. The effect of collisions on the doppler broadening of spectral lines. *Sov. Phy. Ups.*, 9:701, 1967.

[11] J. H. Van Vleck and V. F. Weisskopf. On the shape of collision-broadened lines. *Rev. Mod. Phys.*, 17:227, 1945.

[12] J. H. Van Vleck and D. L. Huber. Absorption, emission, and linebreadths: A semihistorical perspective. *Rev. Mod. Phys.*, 49:939, 1977.

[13] Q. Ma and R. H. Tipping. The detailed balance requirement and general empirical formalisms for continuum absorption. *J. Quant. Spectrosc. Radiat. Transfer*, 51:751, 1994.

[14] M. E. Thomas and R. J. Nordstrom. The N_2-broadened water vapor absorption line shape and infrared continuum absorption - I. Theoretical development. *J. Quant. Spectrosc. Radiat. Transfer*, 28:81, 1982.

[15] M. Rigby, E. Smith, W. Wakeham, and G. Maitland. *The Forces Between Molecules*. Oxford University Press, 1986.

[16] P. W. Rosenkranz. Pressure broadening of rotational bands. II. Water vapor from 300 to 1100 cm^{-1}. *J. Chem. Phys.*, 87:163, 1987.

[17] C. Roche, A. Ernesti, and J. Hutson. An evaluation of existing potential energy surfaces for CO_2-Ar: Pressure broadening and high resolution spectroscopy of van der Waals complexes. *J. Chem. Phys.*, 104:2156–2166, 1996.

[18] L. Monchick. Modern quantum kinetic theory and spectral line shapes. *Johns Hopkins APL Tech. Dig.*, 12:246, 1991.

[19] S. Green. Ability to predict molecular rotation-vibration line shapes. In *AIP Conf. Proc., Spectral Line Shapes*, 1994.

[20] T. R. Phillips, S. Maluendes, and S. Green. Collisional excitation of H_2O by H_2 molecules. in preparation.

[21] R. H. Tipping and Q. Ma. Theory of the water vapor continuum and validations. *Atmos. Res.*, 36:69, 1995. and references therein.

[22] H. E. Revercomb, H. Bujis, H. B. Howell, D. D. LaPorte, W. L. Smith, , and L. A. Sromovsky. Radiometric calibration of IR Fourier transform spectrometers: Solution to a problem with the High-resolution Interferometer Sounder. *Appl. Opt.*, 27:3210, 1988.

[23] W. L. Smith, H. E. Revercomb, H. B. Howell, H. L. Huang, R. O. Knuteson, E. W. Koenig, D. D. LaPorte, S. Silverman, L. A. Sromovsky, and H. M. Woolf. GHIS-The GOES High-Resolution Interferometer Sounder. *J. Appl. Met.*, 29:1189, 1990.

[24] V. L. Griffin, A. R. Guillory, M. Susko, and J. E. Arnold. Operations summary for the Convection And Moisture EXperiment (CAMEX). Technical report, NASA TM-108445, 1994.

[25] L. L. Strow. Rotational collisional narrowing in an infrared CO_2 Q branch studied with a tunable diode laser. *J. Chem. Phys.*, 84:1149, 1986.

[26] B. Gentry and L. L. Strow. Line mixing in a CO_2 Q branch observed with a tunable diode laser. *J. Chem. Phys.*, 86:5722, 1987.

[27] L. L. Strow and A. S. Pine. Q-branch line mixing in N_2O: Effects of ℓ-type doubling. *J. Chem. Phys.*, 89:1427, 1988.

[28] L. L. Strow and D. Reuter. Effect of line mixing on atmospheric brightness temperatures near 15 μm. *Appl. Opt.*, 27:872, 1988.

[29] D. P. Edwards and L. L. Strow. Spectral line shape considerations for limb temperature sounders. *J. Geophys. Res.*, 96:20859, 1991.

[30] C. P. Rinsland and L. L. Strow. Line mixing effects in solar occultation spectra of the lower stratosphere: measurements and comparisons with calculations for the 1932 cm^{-1} Q branch. *Appl. Opt.*, 28:457, 1989.

[31] S. E. Hannon. A tunable diode laser study of infrared CO_2 spectra. Master's thesis, University of Maryland Baltimore County, 1990.

[32] Wen Ge. Rotational cross relaxation in N_2O-N_2O and N_2O-He collisions observed via Q-branch line mixing. Master's thesis, University of Maryland Baltimore County, 1992.

[33] D. C. Tobin. Carbon dioxide lineshapes in $\Pi \leftarrow \Sigma$ and $\Pi \leftarrow \Delta$ vibrational transitions. Master's thesis, University of Maryland Baltimore County, 1993.

[34] R. Le Doucen, C. Cousin, C. Boulet, and A. Henry. Temperature dependence of the absorption in the region beyond the 4.3μm band head of CO_2: 1: Pure CO_2 case. *Appl. Opt.*, 24:897, 1985.

[35] C. Cousin, R. Le Doucen, C. Boulet, and A. Henry. Temperature dependence of the absorption in the region beyond the 4.3μm band head of CO_2: 2: N_2 and O_2 broadening. *Appl. Opt.*, 24:3899, 1985.

[36] S. A. Clough, F. X. Kneizys, L. S. Rothman, and W. O. Gallery. Atmospheric spectra transmittance and radiance: FASCODE1B. *SPIE Atmospheric Transmission*, 277:152, 1981.

[37] D. P. Edwards. *GENLN2: A general line-by-line atmospheric transmittance and radiance model.* NCAR, Boulder, CO, 1992.

[38] C. Cousin, R. Le Doucen, J. P. Houdeau, C. Boulet, and A. Henry. Air broadened linewidths, intensities, and spectral line shapes for CO_2 at 4.3μm in the region of the ATMS instrument. *Appl. Opt.*, 25:2434, 1986.

[39] K. R. Rao and A. Weber. *Spectroscopy of the Earth's Atmosphere and Interstellar Medium*, chapter 4. Acedemic Press, 1992.

[40] C. Cousin, R. Le Doucen, C. Boulet, A. Henry, and D. Robert. Line coupling in the temperature and frequency dependencies of absorption in the microwindows of the 4.3μm CO_2 band. *J. Quant. Spectros. Radiat. Transfer*, 36:521, 1986.

[41] J. Boissoles, C. Boulet, L. Bonamy, and R. Robert. Calculation of absorption in the microwindows of the 4.3μm CO_2 band from an ECS scaling analysis. *J. Quant. Spectrosc. Radiat. Transfer*, 42:509, 1989.

[42] L. Bonamy, D. Robert, J. Boissoles, and C. Boulet. Determination of ECS scaling parameters for CO_2-CO_2 and CO_2-N_2. *J. Quant. Spectrosc. Radiat. Transfer*, 45:305, 1991.

[43] C. Boulet, J. Boissoles, and D. Robert. Collisionally induced population transfer effect in infrared absorption spectra. I. A line-by-line coupling theory from resonances to the far wings. *J. Chem. Phys.*, 89:625, 1988.

[44] J. Boissoles, V. Menoux, R. Le Doucen, and C. Boulet. Collisionally induced population transfer effect in infrared absorption spectra. II. the wing of the Ar-broadened ν_3 band of CO_2. *J. Chem. Phys.*, 91:2163, 1989.

[45] E. W. Smith. Absorption and dispersion in the O_2 microwave spectrum at atmospheric pressures. *J. Chem. Phys.*, 74:6658, 1981.

[46] P. W. Rosenkranz. Interference coefficients for overlapping oxygen lines in air. *J. Quant. Spectrosc. Radiat. Transfer*, 39:287, 1988.

[47] G. Birnbaum. Theory of collision-induced line shapes- absorption and light scattering at low densities. *Adv. Chem. Phys.*, 51:53, 1982.

[48] M. Baranger. Simplified quantum mechanical theory of pressure broadening. *Phys. Rev.*, 111:481, 1958.

[49] A. Ben-Reuven. Spectral line shapes in gases in the binary approximation. *Adv. Chem. Phys.*, 33:235, 1975.

[50] U. Fano. Pressure broadening as a prototype of relaxation. *Phys. Rev.*, 131:259, 1958.

[51] A. C. Kolb and H. Griem. Theory of line broadening in multiplet spectra. *Phys. Rev.*, 111:514, 1958.

[52] R. G. Gordon. Semiclassical theory of spectra and relaxation in molecular gases. *J. Chem. Physics*, 45:1649, 1966.

[53] M. Baranger. Simplified quantum mechanical theory of pressure broadening. *Phys. Rev.*, 111:494, 1958.

[54] A. Ben-Reuven. Impact broadening of microwave spectra. *Phys. Rev*, 145:7–22, 1966.

[55] R. G. Gordon and R. P. McGinnis. Line shapes in molecular spectra. *J. Chem. Physics*, 49:2455–2456, 1968.

[56] P. W. Rosenkranz. Shape of the 5mm oxygen band in the atmosphere. *IEEE Trans. Antennas Propag.*, 23:498, 1975.

[57] T. A. Brunner and D. Pritchard. Fitting laws for rotationally inelastic collisions. In *Advances in Chemical Physics*, volume 50, pages 589–641. John Wiley & Sons, 1982.

[58] G. Millot J.I. Steinfeld, P. Ruttenberg. Scaling laws for inelastic collision processes in diatomic molecules. *J. Phys. Chem*, 95:9638, 1991.

[59] M. M. Margottin, A. Henry, and A. Valentin. Line mixing in the Q branches of the $\nu_1 + \nu_2$ band of nitrous oxide and of the (1110)-(0220) band of carbon dioxide. *J. Chem. Phys.*, 96:1715, 1992.

[60] L. L. Strow, D. C. Tobin, and S. E Hannon. A compilation of first-order line-mixing coefficients for CO_2 Q-branches. *J. Quant. Spectrosc. and Radiat. Transfer*, 52:281, 1994.

[61] D. C. Tobin, L. L. Strow, and S. E. Hannon. Line mixing in $\Pi \leftarrow \Sigma$ and $\Pi \leftarrow \Delta$ CO_2 Q-branches. in preparation.

[62] D. C. Tobin, L. L. Strow, S. E. Hannon, and J. W. C. Johns. A combined line mixing and duration-of-collision spectral lineshape model for CO_2 at 4.3 and 15μm. in preparation.

[63] G. Birnbaum and E. R. Cohen. Theory of line shape on pressure-induced absorption. *Canadian J. Phys.*, 54:593, 1976.

[64] G. Birnbaum. The shape of collision broadened lines from resonance to the far wing. *J. Quant. Spectrosc. Radiat. Transfer*, 21:597, 1979.

[65] J. W. C. Johns. private communication, 01/28/92. 4.3μm CO_2 spectra, 1992.

[66] L. S. Rothman, R. L. Hawkins, and R. B. Wattson. Energy levels, intensities, and linewidths of atmospheric carbon dioxide bands. *J. Quant. Spectrosc. Radiat. Transfer*, 48:537, 1992.

[67] R. R. Gamache, L. Rosenmann, and J. M. Hartmann. unpublished results.

[68] R. G. Ellingson, J. Ellis, and S. Fels. The intercomparison of radiation codes in climate models: longwave results. *J. Geophys. Res.*, 96:8929–8953, 1991.

[69] D. E. Burch. Continuum absorption by atmospheric H_2O. *SPIE Atmospheric Transmission*, 277:28, 1981.

[70] W. B. Grant. Water vapor absorption coefficients in the 8-13μm spectral region: A critical review. *Appl. Opt.*, 29:451, 1990.

[71] L. L. Gordley, B. T. Marshall, and D. A. Chu. LINEPAK: Algorithms for modeling spectral transmittance and radiance. *J. Quant. Spectrosc. Radiat. Transfer*, 52:563, 1994.

[72] S. A. Clough, F. X. Kneizys, and R. W. Davies. Line shape and the water vapor continuum. *Atmos. Res.*, 23:229, 1989.

[73] C. G. Kilsby, D. P. Edwards, R. W. Saunders, and J. S. Foot. Water vapor continuum absorption in the tropics: Aircraft measurements and model comparisons. *Q. J. R. Meteorol. Soc.*, 118:715–748, 1992.

[74] N. N. Shchelkanov, Yu A. Pkhalagov, and V. N. Uzhegov. Field investigations of the water vapor continuum absorption near 10.6μm. *Atm. Oceanic Opt.*, 5:431–434, 1992.

[75] S. J. English, C. Guillou, C. Prigent, and D. C. Jones. Aircraft measurements of water vapour continuum absorption at millimeter wavelengths. *Q. J. R. Meteorol. Soc.*, 120:603–625, 1994.

[76] S. D. Rudman, R. W. Saunders, C. G. Kilsby, and P. J. Minnett. Water vapor continuum measurements in mid-latitudes: Aircraft measurements and model comparisons. *Q. J. R. Meteorol. Soc.*, 120:795–807, 1994.

[77] M. E. Thomas. Infrared and millimeter wavelength continuum absorption in the atmospheric windows: Measurements and models. *Infrared Phys.*, 30:161, 1990.

[78] D. E. Burch, D. A. Gryvnak, and R. R. Patty. Absorption of infrared radiation by CO_2 and H_2O. Experimental techniques. *J. Opt. Soc. Am. B*, 57:885, 1967.

[79] D. E. Burch. Continuum absorption by H_2O. Technical Report AFGL-TR-81-0300, AFGL, 1982.

[80] D. E. Burch and R. L. Alt. Continuum absorption by H_2O in the 700-1200 cm^{-1} and 2400-2800 cm^{-1} windows. Technical Report AFGL-TR-84-0128, AFGL, 1984.

[81] D. E. Burch. Absorption by H_2O in narrow windows between 3000 and 4200 cm^{-1}. Technical Report AFGL-TR-85-0036, AFGL, 1985.

[82] S. A. Clough, F. X. Kneizys, R. W. Davies, R. R. Gamache, and R. H. Tipping. *Atmospheric Water Vapor*, chapter 2. Acedemic Press, Inc., 1980.

[83] P. W. Anderson and P. R. Weiss. Pressure broadening in the microwave and infrared regions. *Rev. Mod. Phys.*, 25:269, 1953.

[84] S. A. Clough. The water vapor continuum and its role in remote sensing. In *Optical Remote Sensing of the Atmosphere*, Salt Lake City, UT, February 1995.

[85] R. W. Davies, R. H. Tipping, and S. A. Clough. Dipole autocorrelation function for molecular pressure broadening: A quantum theory which satisfies the fluctuation-dissipation theorem. *Phys. Rev. A*, 26:3378, 1982.

[86] P. W. Rosenkranz. Pressure broadening of rotational bands. I. A statistical theory. *J. Chem. Phys.*, 83:6139, 1985.

[87] Q. Ma and R. H. Tipping. The atmospheric water continuum in the infrared: Extension of the statistical theory of Rosenkranz. *J. Chem. Phys.*, 93:7066, 1990.

[88] Q. Ma and R. H. Tipping. Water vapor continuum in the millimeter spectral region. *J. Chem. Phys.*, 93:6127, 1990.

[89] Q. Ma and R. H. Tipping. A far wing line shape theory and its application to the water continuum absorption in the infrared region. I. *J. Chem. Phys.*, 95:6290, 1991.

[90] Q. Ma and R. H. Tipping. A far wing line shape theory and its application to the water vibrational bands (II). *J. Chem. Phys.*, 96:8655, 1992.

[91] Q. Ma and R. H. Tipping. A far wing line shape theory and its application to the foreign-broadened water continuum absorption (III). *J. Chem. Phys.*, 97:818, 1992.

[92] Q. Ma and R. H. Tipping. A near-wing correction to the quasistatic far-wing line shape theory. *J. Chem. Phys.*, 100:2537, 1994.

[93] J. M. Theriault, P. L. Roney, D. St.-Germain, H. E. Revercomb, R. O. Knuteson, and W. L. Smith. Analysis of the FASCODE model and its H_2O continuum based on long path atmospheric transmission measurements in the 4.5-11.5um region. *Appl. Opt.*, 33:323, 1994.

[94] S. A. Clough, R. D. Worsham, W. L. Smith, H. E. Revercomb, R. O. Knuteson, G. P. Anderson, M. L. Hoke, and F. X. Kneizys. Validation of FASCODE calculations with HIS spectral radiance measurements. In *IRS Proceedings*, Lille France, August 1988.

[95] H. E. Revercomb, R. O. Knuteson, W. L. Smith, H. M. Woolf, and H. B. Howell. Spectroscopic inference from HIS measurements of atmospheric thermal emission. *Optical Remote Sensing of the Atmosphere, OSA Digest Series*, 4:590, 1990.

[96] H. E. Revercomb, W. L. Smith, R. O. Knuteson, H. M. Woolf, and H. B. Howell. Comparison of FASCODE spectra with HIS observations. In *Annual Review Conference on Atmospheric Transmission Models*, 1989.

[97] L. L. Strow, D. C. Tobin, and S. E. Hannon. private calculations, 07/95. CAMEX/HIS calculations with CKD 2.1, 1995.

[98] D. C. Tobin, L. L. Strow, W. J. Lafferty, and Wm. B. Wm. Olson. Experimental investigation of the self- and N_2- broadened continuum within the ν_2 band of water vapor. *Appl. Opt.* accepted 01/24/96.

[99] M. E. Thomas, 1993. private communication.

[100] R. A. Toth. ν_2 band of $H_2^{16}O$ line strengths and transition frequencies. *J. Opt. Soc. Am. B*, 8:2236, 1991.

[101] R. A. Toth. private communication, 10/13/94. self-broadened H_2O widths, 1994.

[102] J. J. Remedios. *Experimental Determinations of the Air- and N_2- broadened Line Widths of Strong Lines in the ν_2 Band of $H_2^{16}O$: Line Widths and their Temperature Dependences between 243K and 298K.* PhD thesis, Oxford University, 1990.

[103] R. R. Gamache, 1995. private communication.

[104] *1990 ASA Workshop*, Moscow, 1990. Proceedings Introduction and Overview.

[105] R. J. Nordstrom, M. E. M.E.Thomas, J. C. Peterson, E. K. Damon, and R. K. Long. Effects of oxygen addition on pressure-broadened water vapor absorption in the 10μm region. *Appl. Opt.*, 17:2724, 1978.

[106] K. S. Lam. Application of pressure broadening theory to the calculation of atmospheric oxygen and water vapor microwave absorption. *J. Quant. Spectrosc. Radiat. Transfer*, 17:351, 1977.

[107] T. R. Phillips, S. Maluendes, A. D. McLean, and S. Green. Anisotropic rigid rotor potential energy function for H_2O–H_2. *J. Chem. Phys.*, 101:5824, 1994.

[108] M. H. Alexander and D. C. Clary. Propensity rules in rotationally inelastic collisions of CO_2. *Chem. Phys. Lett.*, 98:319–323, 1983.

[109] G. Herzberg. *Infrared and Raman Spectra of Polyatomic Molecules.* Van Nostrand Reinhold Co., 1945.

[110] C. H. Townes and A. L. Schawlow. *Microwave Spectroscopy*. McGraw-Hill Book Co., 1955.

[111] H. C. Allen and P. C. Cross. *Molecular Vib-Rotors*. Johns Wiley and Sons, Inc., 1963.

[112] R. M. Goody. *Atmospheric Radiation*. Oxford University Press, 1989.

[113] L. L. Strow. *A high resolution spectroscopic study of the ν_2 band of hydrogen sulfide and the 1-0 band of hydrogen iodide*. PhD thesis, University of Maryland College Park, 1981.

[114] J. M. Flaud and C. Camy-Peyret. *Atmospheric Water Vapor*, chapter 1. Acedemic Press, 1980.